Computational modelling and simulation of rat heart electromechanics – from (smoothed) finite element methods towards a ligand-receptor model

Computergestützte Modellierung und Simulation der Elektromechanik des Rattenherzens – von (geglätteten) Finite-Elemente-Methoden zu einem Ligand-Rezeptor-Modell

Der Technischen Fakultät
der Friedrich-Alexander-Universität
Erlangen-Nürnberg

zur

Erlangung des Doktorgrades Dr.-Ing.

Denisa Martonová

aus Poprad in der Slowakei

Abstract

Nowadays, computational modelling and simulation have become powerful tools in medical sciences due to their considerable potential to assist clinicians in diagnosing the source of a disease, the kind of a therapy, or in training for a surgical operation. The focus of this thesis is on modelling and simulation of cardiac electromechanics. The importance is highlighted by the fact that cardiovascular diseases are currently the main cause of death worldwide. Despite rapid development in the last decades, cardiac modelling and simulations are still the subject of intensive research. It remains a challenging task to create an efficient computational heart model including all necessary ingredients.

The overall aim of the present doctoral thesis is to develop a robust and accurate computational model of rat cardiac electromechanics, which is calibrated with experimental data. This cumulative thesis is presented as a compilation of six journal publications and one conference proceeding, which are grouped into four research contribution parts. To begin, the work is focused on creating a novel material model for passive cardiac mechanics. It is calibrated with experimental data in healthy rat cardiac tissue and in tissue 14 days after an induced myocardial infarction. The simulation results using the derived parameters show a close agreement with the experimental data. Then, using the suggested model and the determined parameters, it is studied how a weakened heart, suffering from a restrictive cardiomyopathy, may be supported from the outside by applying an external support pressure. Based on the simulation model, the optimal support pressure needed for the restoration of the healthy left-ventricular ejection fraction and end-diastolic volume is computed for different stages of ventricular fibrosis. Further, apart from the improvements on the material modelling level, the thesis focuses on a novel numerical method for the simulation of cardiac mechanics, i.e. multiple smoothed finite element methods are extended for the modelling and simulation of active cardiac contraction. It turned out that the method is very suitable for the simulation of the cardiac cycle. This is due to its ability to significantly reduce the volumetric locking problem, being present when large deformations occur, nearly incompressible material is utilised and the computational domain is discretised with tetrahedrons. Finally, in addition to the continuum approach on the organ-scale level, a cell-scale level two-state receptor binding model is established to investigate the influence of diverse hormone secretion patterns

as well as to determine the optimal drug dose in order to restore the reference cellular responsiveness, being decreased under various pathological conditions. A possible inclusion into the established heart model is discussed.

Kurzfassung

Heutzutage sind die computergestützte Modellierung und Simulation zu einem leistungsstarken Werkzeug in der Medizin geworden, das beispielsweise Ärzten bei der Krankheitsdiagnostik, bei der Bestimmung der Therapie oder beim Training für einen chirurgischen Eingriff helfen kann. Der Schwerpunkt dieser Arbeit liegt auf der Modellierung und Simulation der Elektromechanik des Herzens. Die Bedeutung wird durch die Tatsache unterstrichen, dass Herz-Kreislauf-Erkrankungen derzeit weltweit die Haupttodesursache darstellen. Trotz einer rasanten Entwicklung in den letzten Jahrzehnten sind die Modellierung und Simulation des Herzens immer noch Gegenstand intensiver Forschung. Es bleibt eine herausfordernde Aufgabe, ein effizientes computergestütztes Herzmodell zu erstellen, das alle notwendigen Bestandteile enthält.

Das übergeordnete Ziel der vorliegenden Dissertation ist die Entwicklung eines robusten und genauen Rechenmodells der Elektromechanik des Rattenherzens, das mit experimentellen Daten kalibriert wird. Diese kumulative Dissertation wird als eine Zusammenstellung von sechs begutachteten Journalpublikationen und einem Konferenzproceeding präsentiert, die in vier Forschungskategorien gruppiert sind. Zunächst konzentriert sich die Arbeit auf die Erstellung eines Materialmodells für passive Herzmechanik. Es wird mit experimentellen Daten von gesundem Rattenherzgewebe und von Rattenherzgewebe 14 Tage nach einem induzierten Herzinfarkt kalibriert. Die Simulationsergebnisse unter Verwendung der gewonnen Parameter zeigen eine gute Übereinstimmung mit den experimentellen Daten. Anschließend wird mit dem vorgeschlagenen Modell und den bestimmten Parametern untersucht, wie ein geschwächtes Herz, das an einer restriktiven Kardiomyopathie leidet, durch Anwendung eines externen Unterstützungsdrucks von außen unterstützt werden kann. Auf der Grundlage des Simulationsmodells wird ein optimaler Unterstützungsdruck, der für die Wiederherstellung der gesunden linksventrikulären Ejektionsfraktion und des enddiastolischen Volumens erforderlich ist, für verschiedene Stadien der ventrikulären Fibrose bestimmt. Neben den Verbesserungen auf der Materialmodellierungsebene fokussiert sich die Arbeit auf eine neuartige numerische Methode zur Simulation der Herzmechanik. Es werden mehrere geglättete Finite-Elemente-Methoden für die Modellierung und Simulation der aktiven Herzkontraktion erweitert. Es hat sich gezeigt, dass die Methoden sehr gut

für die Simulation eines Herzzyklus geeignet sind. Dies ist auf deren Fähigkeit zurückzuführen, das Problem des volumetrischen Lockings erheblich zu reduzieren. Es tritt bei großen Verformungen auf, insbesondere falls ein nahezu inkompressibles Material verwendet wird und das Berechnungsgebiet mit Tetraedern diskretisiert wird. Schließlich wird neben dem Kontinuum-Ansatz auf der Organ-Ebene ein Zwei-Zustands-Ligand-Rezeptor-Bindungsmodell auf der Zell-Ebene erstellt, um den Einfluss verschiedener Hormonsekretionsmuster zu untersuchen und die optimale Medikamentendosis zur Wiederherstellung des Referenzwertes der zellulären Responsivität zu bestimmen, die unter verschiedenen pathologischen Bedingungen verringert ist. Eine mögliche Einbeziehung in das etablierte Herzmodell wird diskutiert.

Contents

List of symbols and abbreviations

Abbreviations

2D	two-dimensional
3D	three-dimensional
BC	boundary condition
C3D10	ten-node tetrahedral element
C3D4	four-node tetrahedral element
CaAD	cardiac assist device
CS	cardiac surgery
CT	computer tomography
CVD	cardiovascular disease
DCCD	direct cardiac compression device
DOF	degree of freedom
EDP	end-diastolic pressure
EDV	end-diastolic volume
EF	ejection fraction
ES-FEM	edge-based smoothed finite element method
ESV	end-systolic volume
FAU	Friedrich-Alexander-Universität Erlangen-Nürnberg
FEM	finite element method
FS-FEM	face-based smoothed finite element method
G-protein	guanine nucleotide-binding-protein

GPCR	G-protein-coupled receptors
H8	eight-node hexaheral element
HO	Holzapfel-Ogden model
LDRBM	Laplace-Dirichlet-rule-based-method
LTD	Institute of Applied Dynamics
LV	left ventricle
LVAD	left ventricular assist device
MBT	Institute of Biomedical Technologies
MI	myocardial infarction
MRI	magnetic resonance imaging
NH	Neo-Hookean model
NS-FEM	node-based smoothed finite element method
PC	pediatric cardiology
PFN	Purkinje fibre network
PTH	parathyroid hormone
S-FEM	smoothed finite element method
UEL	user element subroutine

Mathematical symbols and operators

$(\bullet)^{\mathrm{T}}$	transpose operator
$\approx$	approximately equals sign
A	assembly operator
δ	Dirac measure
$\Delta(\bullet)$	increment
δ_{ij}	Kronecker delta
$\dot{(\bullet)}$	material time derivative

∇	gradient operator
$\otimes$	tensor product
∂	partial derivative operator
Lin^+	set of all tensors $\mathbf{T}$ with $\det \mathbf{T} > 0$
$\mathcal{E}$	Euclidian space
$\det(\bullet)$	determinant
Div	divergence operator with respect to the reference coordinates
$\mathbb{R}$	real numbers

Mechanical and electrophysiological quantities

α	cellular activity
α_R	cellular responsiveness
$\boldsymbol{\sigma}$	Cauchy stress tensor
$\boldsymbol{b}$	spatial body force field
$\boldsymbol{f}_0, \boldsymbol{s}_0, \boldsymbol{n}_0$	fibre, sheet, normal directions in reference configuration
$\boldsymbol{T}$	surface traction vector
$(\bullet)^\diamond$	isochoric part of a quantity
$\mathbf{I}$	identity tensor
$\mathbf{D}$	conductivity tensor
$\mathbf{C}$	right Cauchy-Green deformation tensor
$\mathbf{P}$	first Piola-Kirchhof stress tensor
$\mathbf{S}$	second Piola-Kirchhof stress tensor
$\mathbf{S}_{act}$	active part of the second Piola-Kirchhof stress tensor
$\mathbf{S}_{pas}$	passive part of the second Piola-Kirchhof stress tensor
Φ	transmembrane potential
Ψ	strain energy function

ρ	spatial density field
ρ_0	material density field
T	active muscle tension
W	smoothing function
φ_t	deformation map
φ	motion
$\mathbf{F}$	deformation gradient
$\boldsymbol{u}$	displacement vector
$\boldsymbol{X}$	position vector in reference configuration
$\boldsymbol{x}$	position vector in deformed configuration

List of Figures

List of Tables

Part I

Introduction and Background

1 Introduction

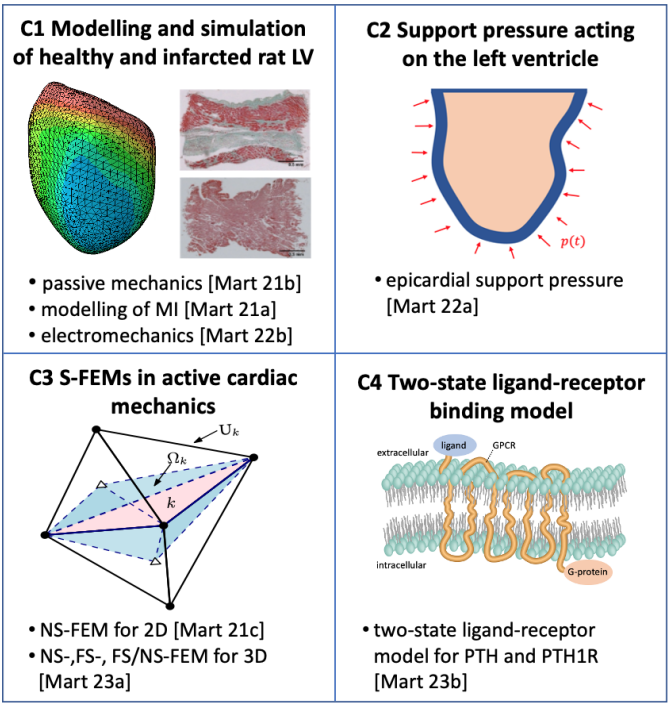

Figure 1.1: Four main research contributions (C1-C4).

This cumulative doctoral thesis presents a series of publications which are thematically grouped into research contributions in four areas (C1-C4) as illustrated in Figure 1.1: Firstly (C1), the focus is put on the modelling and simulation of a healthy rat left ventricle (LV) and a LV after myocardial infarction (MI). In particular, it is aimed to establish a novel material model for the passive cardiac mechanics involving experimental observations in healthy rat myocardial tissue and in tissue 14 days after MI. Secondly (C2), based on the model proposed and the parameters obtained in the first part, it is

investigated how a weakened heart, e.g. after MI, can be supported from outside by applying an external support pressure. Thirdly (C3), in addition to the standard numerical method of finite elements (FEM), various smoothed finite element methods (S-FEMs) [Liu07, Liu16] are extended for the simulation of active cardiac mechanics. Fourthly (C4), besides the continuum approach on the organ-scale-level in the previous parts, a cell-scale-level two-state receptor binding model is developed. Furthermore, the doctoral researcher contributed as a co-author to two journal publications regarding the development of the fibre orientation definition based on the Laplace-Dirichlet-rule-based-methods (LDRBMs). Details on the research contributions are presented in Part II.

In this chapter, a brief introduction to the state of the art for relevant topics is given as well as the motivation and formulation of the objectives in each of the research contributions. The chapter concludes with the presentation of the thesis outline.

1.1 Motivation and state of the art

The heart is one of the principal organs in humans and animals. Aristotle (384-322 before Christ) even identified it as the most important one [Clar63]. Undoubtedly, the heart has several essential functions such as pumping oxygenated blood through the whole body and hence delivering nutrients to each single cell as well as enabling excretion of the waste metabolic products and regulating the blood pressure. It is therefore not surprising, that any pathological condition in the cardiovascular system has serious impacts on the overall body function. The great importance of the well-functioning cardiovascular system is highlighted by the fact that cardiovascular diseases (CVDs) remain the leading cause of death worldwide [WHO20, Wilk17]. Nowadays, many cardiovascular pathologies are well studied, also thanks to the advances in imaging techniques such as echocardiography, computer tomography (CT) or magnetic resonance imaging (MRI). But, it is still challenging to diagnose and treat them in the early stages. However, in the last decades, computational models have become a powerful tool to better understand, diagnose and treat various CVDs [Lope15, Nied19, Peir21]. They provide a promising investigation opportunity which is non-invasive, cheaper and faster than clinical studies. So far, numerous heart models have been developed to simulate electromechanically coupled cardiac function, e.g. [Gökt10, Serm06, Bail15, Duon19] study pathologies [Berb15, Sáez16], investigate the arrhythmogenic influence of drugs [SC18], propose the best therapy strategy [Tray17, Boyl19, Lang22] and further guide cardiac assist device (CaAD) design [McCo13, AB18, Hirs19, Mart22a]. In the

latest clinical studies, computational simulations have been shown to correspond to clinical predictions or even outperform them [Yama22, O'Ha22].

Modelling of heart and CaAD (C1, C2) However, it is a challenging task to create a computational heart model including all necessary ingredients such as an adequate model for the passive and active tissue mechanics, fibre orientation, electrophysiology, boundary conditions (BCs) or blood flow. Although in the last decades, extensive research regarding the mechanical behaviour and electrophysiology in cardiac tissue has been done, it is still not fully clear what are the adequate material parameters for a cardiac simulation. In particular, the parameters greatly vary among the species [Doko02, Ahma18, Somm15, Mart21b] and are mostly characterised for humans. However, the aim is to build a computational model of a rat heart, more precisely left ventricle (LV). Such an animal computational model is motivated by our collaboration with the Pediatric Cardiology (PC), the Cardiac Surgery (CS) and the Institute of Biomedical Technologies (MBT) of the Friedrich-Alexander-Universität Erlangen-Nürnberg (FAU), for more details see Section 3.1.1. The abundance of experimental data for rats makes it relatively simple to validate the simulations. Furthermore, computer simulations can minimise the number of laboratory studies, which are frequently conducted in rodents [Mila14]. For example, the development of CaADs requires a challenging parameter optimisation which is easier to perform in computational simulations before the actual animal experiments.

Based on these rationales, the objectives of the first research contribution *Modelling and simulation of healthy and infarcted rat left ventricles* (C1) are derived, namely

C1-1 creation of a computational model of healthy and infarcted rat left ventricle,
C1-2 calibration of the model with experimentally derived parameters, partially measurements from the collaboration partners (passive mechanics for healthy and infarcted rat myocardium) and partially from the literature,
C1-3 comparison of existing models for active contraction in a fully electromechanically coupled simulation and comparison of the results with experimental data.

Besides the model for a contracting myocardium, computational models are beneficial in the development of CaADs which can greatly improve the life quality for patients suffering from different CVDs. They cover different types of mechanical pumping systems, known as left ventricular assist devices (LVADs),

which have been developed during the last several decades [Han19]. They are utilised as an invasive type of treatment to directly promote blood circulation. In general, these systems work to bypass the diseased heart. LVADs can thereby ease the burden on the heart and serve as either a short- to medium-term bridge to treat cardiac insufficiency until a possible transplantation (bridge-to-transplantation) or as a permanent solution (destination treatment). Thanks to the fast development of novel devices and advances in post-surgery survival, the functional capability of LVADs is approaching those of heart transplantation. However, there are still numerous issues to be considered when a LVAD is implanted. They include bleeding, thrombosis, strokes, and infections [Han19, Lima18]. The majority of these issues are caused by direct blood contact with a LVAD. Different possibilities how to prevent such a direct blood contact have been proposed. These approaches are commonly referred to as direct cardiac compression devices (DCCDs). In the first bridge-to-transplantation therapy, a pneumatic compression cup was used [Lowe91]. It was followed by numerous other creative techniques, e.g. [Artr99, Roch17, Jags18, Hord19]. The review articles [Han19, Oz02] provide a more detailed overview of available DCCDs. The pressure generated by these devices operates on the epicardial surface, which is the common principle of all DCCDs. In theory, a diseased heart can be supported solely in the diastole (via a negative pressure facilitating the diastolic filling), solely in the systole (via positive pressure increasing the cardiac output), or during both cardiac phases. However, most DCCDs only work during systole by compressing the heart and elevating the ejection.

To proceed towards closing this gap, the objectives of the second research contribution *Support pressure acting on the left ventricle* (C2) are

C2-1 creation of a computational model for restrictive cardiomyopathy at different stages based on C1 as an example for a diseased heart,
C2-2 investigation whether the application of support pressure (generated by an arbitrary DCCD) on the LV during both, the diastolic and systolic phases, is able to normalise the ejection fraction (EF) and left ventricular end-diastolic pressure (EDP),
C2-3 optimisation how much support pressure is needed to normalise EF and EDP in the diseased LV and what is its temporal evolution.

The focus of C2 is not put on modelling of a particular CaAD which may be done in the future, see Chapter 8 and Conclusion in [Mart22a].

Numerical approximation (C3) Most frequently, FEM is used to numerically approximate the solution of the addressed problem given in equations (2.12) and

(2.16) [Lope15, Nied19, Peir21]. However, FEM models require an adequate input geometry which can be very complex if biological (and in particular cardiac) tissue is simulated. As tetrahedral (or triangular) mesh can be generated automatically, e.g. with Delaunay triangulation, it is convenient to discretise complex computational domains with tetrahedrons [Bail14, Ross14, Serm06, Duon19]. But, simulations based on tetrahedral meshes in combination with nearly incompressible materials and linear shape functions suffer from volumetric locking and therefore produce overly stiff solutions [Jian14, Liu19, Kada19]. On the one hand, higher-order elements can be utilised, but the computational cost increases significantly. On the other hand, hexahedral elements were shown to produce more accurate solutions in cardiac mechanics [DO16]. However, the mesh generation for complex geometries requires a significant effort, because, in general, it cannot be performed automatically.

To overcome these challenges, an alternative numerical technique, a group of smoothed finite element methods, has been proposed by Liu and co-workers [Liu07]. These methods combine FEM and specific techniques from meshless methods, in particular, strain smoothing over a designed smoothing domain (SD). Depending on the SD type, different S-FEMs exist, e.g. cell-based S-FEM (CS-FEM) [Liu07], node-based S-FEM (NS-FEM) [Liu09a], edge-based S-FEM (ES-FEM) for both two-dimensional (2D) and three-dimensional (3D) problems [Liu09b] and face-based S-FEM (FS-FEM) for 3D problems [NT09, Duon14]. Additionally, selective FS/NS-FEM and ES/NS-FEM are proposed for nearly incompressible materials, where FS-FEM is used for the isochoric part and NS-FEM for the volumetric part [Nguy07, Jian14].

In the reviews [Liu19, Zeng18], the advantages and applications of S-FEMs are summarised. The most important benefits are: Firstly, S-FEMs are softer than linear FEM using the same mesh size and therefore resistant to volumetric locking. Secondly, they are less sensitive to mesh distortion which often occurs in the presence of large deformations. Thirdly, they are primarily developed for tetrahedral meshes which can be generated automatically.

In the last years, S-FEMs have been applied in different fields of mechanics. Recently, also biomechanics became a promising field of application for reasons corresponding to the S-FEMs' benefits mentioned above: Firstly, biological tissues are often modelled as nearly incompressible materials, suffering from volumetric locking. Secondly, large deformations often need to be simulated. Thirdly, geometries are usually complex and it is beneficial to discretise them with tetrahedrons. Previous works [Duon14, Duon15, Yao12, Wu20, Yan22, Wu23, Jian15a, Jian15b] have demonstrated that S-FEMs perform accurate at low computational cost, can reduce or overcome volumetric locking and are robust to mesh distortion. See the Introduction in [Mart23a] for more

details and a review of current applications in biomechanics in general. For the simulation of cardiac mechanics, FS/NS-FEM has only been applied to passive diastolic filling in [Jian15a]. Originally, S-FEMs have been implemented within in-house solvers. Some later works used solvers such as Abaqus, Julia and *code_aster* for a particular S-FEM. The reader is referred to Section 5.1.1 for a complete overview of available implementations. So far, implementations in the commercial software Abaqus for NS-FEM, FS-FEM and FS/NS-FEM in 3D are available neither in its element library nor as user element subroutines (UELs).

Based on these research gaps, the objective of the third research contribution *S-FEMs towards active cardiac mechanics* (C3) are derived, namely

C3-1 extension of different S-FEMs for active cardiac mechanics on benchmark geometry and rat LV,
C3-2 implementation of NS-FEM, FS-FEM, FS/NS-FEM as UELs in the commercial software Abaqus,
C3-3 comparison of linear and quadratic FEM and various S-FEMs regarding the accuracy and computational cost.

Receptor models (C4) The fourth research contribution was established during the doctoral researcher's stay at Queensland University of Technology in Brisbane, Australia (from May to August 2022). The connection to the cardiac modelling and simulation is a future possibility to include a cellular model into multiscale cardiac simulation. The hosting university provides great expertise in cellular modelling with a focus on bone (re)modelling. Therefore, the developed ligand-receptor binding model is exemplarily applied to the parathyroid hormone (PTH), mainly influencing bone metabolism, and the effects of its secretion and dosing (administration via subcutaneous injection) patterns on bone cellular activity are investigated. This model builds a fundamental framework for different hormone receptors with a similar structure, including adrenergic receptors in the heart, for example, β-receptors. Their stimulation influences both, cardiac output and heart remodelling processes [Woo12, Wang18].

The objectives of the fourth research contribution *Two-state ligand-receptor binding model* (C4) are

C4-1 investigation and numerical implementation of the two-state ligand-receptor binding model and its exemplary application for PTH and its receptor PTH1R,

C4-2 investigation of cellular activity function being able to distinguish various aspects of the stimulation signals, including peak dose, time of ligand exposure and exposure period,
C4-3 formulation and solving of various optimisation problems to determine the optimal secretion pattern of the hormone as well as dosing pattern in case of external drug administration.

1.2 Thesis outline

The present doctoral thesis is divided into two parts comprising several chapters. Part I introduces the objectives and theoretical background to access the research contributions. In Chapter 2, the fundamentals needed for understanding the presented publications in a broader context, are summarised. Firstly, they cover a necessary technical base, i.e. continuum mechanics, cardiac modelling and numerical approximation and optimisation techniques. Secondly, relevant basics in the anatomy and physiology of the heart and regarding the ligand-receptor models in pharmacology are introduced.

In Part II, four thematically grouped research contributions are presented in detail (Chapters 3 - 6). Additionally, a fifth group to which the doctoral researcher contributed as co-author, is briefly introduced in Chapter 7. At the end of each of Chapters 3 - 7, a summary of the relevant publications within each research contribution is given, the role of the doctoral researcher for the respective publications is specified and the main findings in each publication are highlighted. Finally, Chapter 8 summarises the findings, discusses the limitations and motivates an outlook on future prospects. In the Appendix, the doctoral researcher's publications are shown in their originally published form.

2 Fundamentals

This chapter briefly introduces the basics of continuum mechanics, the finite element method and smoothed finite element methods as well as the essential biological background.

2.1 Continuum mechanical approach in cardiac modelling

Continuum mechanics is the commonly utilised concept for the modelling of soft tissue biomechanics. Using this framework, biological tissues are viewed as a continuum and the possible presence of small discrete particles is transferred to the general behaviour of the continuum. In this section, based on [Gurt81, Gonz08, Holz00], the fundamentals of continuum mechanics are introduced. In particular, the focus is put on the basic equations of finite deformations and the relevant mechanical quantities. In the following, geometrically and materially nonlinear large displacement problems are considered. Throughout the thesis, vectors are denoted in italic boldface and tensors are denoted in boldface.

2.1.1 Kinematics

Let $\mathcal{E}$ be an Euclidean space ($\mathcal{E} = \mathbb{R}^3$ in the attached publications, except [Mart21c] where $\mathcal{E} = \mathbb{R}^2$), Ω_0 an open regular subspace of $\mathcal{E}$, called the reference configuration, $\boldsymbol{X} \in \Omega_0$ a material point and $t \in [t_0, t_f]$ the time (t_0 and t_f are the initial and final times of the motion, respectively). A bijective map

$$\begin{aligned} \varphi_t : \Omega_0 &\to \mathcal{E} \\ \boldsymbol{X} &\mapsto \boldsymbol{x} \end{aligned} \tag{2.1}$$

such that $\det \nabla \varphi_t > 0$ is called a deformation map at time t. A motion or a placement of the vector $\boldsymbol{X}$, is defined as

$$\begin{aligned} \varphi : \Omega_0 \times \mathbb{R} &\to \mathcal{E} \\ (\boldsymbol{X}, t) &\mapsto \boldsymbol{x}, \end{aligned} \tag{2.2}$$

such that $\varphi(\cdot, t)$ is a deformation for each fixed time $t \in [t_0, t_f]$, i.e. a motion is a smooth one-parameter family of deformations with the parameter t. We write $\boldsymbol{x} = \varphi(\boldsymbol{X}, t)$ for a point in space occupied by the material point $\boldsymbol{X}$ at time t and $\Omega_t = \varphi(\Omega_0, t)$ for a space occupied by the body at time t. For a fixed time t, the vector

$$\boldsymbol{u}(\boldsymbol{X}) = \varphi_t(\boldsymbol{X}) - \boldsymbol{X} \quad \in \mathcal{E} \tag{2.3}$$

is called the displacement of a material point $\boldsymbol{X}$. The deformation gradient, mapping line elements, e.g. fibres, from the reference to the deformed configuration, is defined as

$$\mathbf{F}(\boldsymbol{X}) = \nabla \varphi_t(\boldsymbol{X}) = \nabla \boldsymbol{u}(\boldsymbol{X}) + \mathbf{I} \quad \in \mathrm{Lin}^+ \tag{2.4}$$

with the determinant $J = \det \mathbf{F}$ and the identity tensor $\mathbf{I}$.

2.1.2 Balance equations

Using the Localisation theorem [Gurt81], the balance equations are given in the local forms. In this work, all balance equations are formulated in the material form. For the corresponding spatial formulation, the reader is referred to the literature, e.g. [Gurt81, Gonz08]. In the following, a closed system isolated from the surroundings is considered. However, in reality, biological structures such as the heart interact with other organs and receive external energy in the form of nutrients. Nevertheless, modelling the heart as an open system is a challenging task and is out of the scope of this thesis. The following balance equations are to be fulfilled in general:

Conservation of mass In a closed system, the total mass is constant during the motion φ, namely

$$J\rho(\varphi(\boldsymbol{X}, t), t) = \rho_0(\boldsymbol{X}), \quad \forall \boldsymbol{X} \in \Omega_0, \quad \forall t \geq t_0, \tag{2.5}$$

where $\rho(\boldsymbol{x}, t)$ and $\rho_0(\boldsymbol{X})$ are the spatial and material mass density fields, respectively.

Balance of linear momentum The resultant external force acting on a body equals the time rate of its linear momentum. By applying the Divergence theorem and Cauchy theorem, we obtain

$$\rho_0 \ddot{\varphi} = \mathrm{Div}\mathbf{P}(\boldsymbol{X}, t) + \rho_0 \boldsymbol{b}(\varphi(\boldsymbol{X}, t), t), \quad \forall \boldsymbol{X} \in \Omega_0, \quad \forall t \geq t_0, \tag{2.6}$$

where $\boldsymbol{b}(\boldsymbol{x}, t)$ is the spatial body force field and $\mathbf{P}$ is the first Piola-Kirchhoff stress tensor. If there is no acceleration, i.e. $\ddot{\varphi} = 0$, (2.6) is reduced to the Cauchy's equation of static equilibrium, namely

$$0 = \mathrm{Div}\mathbf{P}(\boldsymbol{X}, t) + \rho_0 \boldsymbol{b}(\varphi(\boldsymbol{X}, t), t) \quad \forall \boldsymbol{X} \in \Omega_0, \quad \forall t \geq t_0, \tag{2.7}$$

In the following, a quasi-static analysis is performed and therefore, (2.7) is to be fulfilled.

Balance of angular momentum The resultant torque acting on a body equals the time rate of its angular momentum. Using the Localisation theorem, Divergence theorem as well as equations (2.5) and (2.6), see e.g. [Gonz08], the balance of angular momentum yields

$$\mathbf{P}\mathbf{F}^{\mathrm{T}} = \mathbf{F}\mathbf{P}^{\mathrm{T}} \quad \forall \boldsymbol{X} \in \Omega_0, \quad t \geq t_0. \tag{2.8}$$

The symmetry of the second Piola Kirchhoff stress $\mathbf{S} = \mathbf{F}^{-1}\mathbf{P}$ and the Cauchy stress $\boldsymbol{\sigma} = J^{-1}\mathbf{P}\mathbf{F}^{\mathrm{T}}$ is therefore retrieved via the conservation of the angular momentum (2.8). Conversely, if the second Piola Kirchhoff and Cauchy stress tensors are symmetric, the balance of angular momentum is automatically fulfilled.

2.1.3 Constitutive models

The relationship between the stress in a material, represented by a stress measure $\mathbf{P}$, $\mathbf{S}$ or $\boldsymbol{\sigma}$ and the deformation of the material, represented by $\mathbf{F}$, is characterised via a constitutive model. It is assumed that the material behaviour is hyperelastic nearly incompressible and contractile. Based on [Tike22], the viscosity is neglected in the present thesis. To model the contractility of the myocardium, the stress measures are decomposed into two parts. More precisely, in the following, the second Piola-Kirchhoff stress $\mathbf{S}$ is considered and it is given as

$$\mathbf{S} = \mathbf{S}_{pas} + \mathbf{S}_{act}, \tag{2.9}$$

where $\mathbf{S}_{pas}$ is the passive part and $\mathbf{S}_{act}$ is the active part.

Due to the assumed hyperelasticity and near-incompressibility, the passive part is obtained as

$$\mathbf{S}_{pas}(\mathbf{C}) = 2\frac{\partial \Psi}{\partial \mathbf{C}}, \tag{2.10}$$

where $\mathbf{C}$ is the right Cauchy stress tensor and Ψ is a strain energy function of a nearly incompressible material. The latter is decomposed as

$$\Psi = \Psi_{iso}(\mathbf{C}^{\diamond}) + \Psi_{vol}(J), \tag{2.11}$$

where Ψ_{iso} is the isochoric part and $\Psi_{vol} = \kappa(J-1)^2$ is the volumetric part with the bulk modulus κ. Further, $\mathbf{C}^{\diamond} = \mathbf{F}^{\diamond \mathrm{T}}\mathbf{F}^{\diamond}$ and $\mathbf{F}^{\diamond} = J^{-1/3}\mathbf{F}$ denote the isochoric right Cauchy-Green tensor and isochoric deformation gradient, respectively, i.e. $\det \mathbf{C}^{\diamond} = \det \mathbf{F}^{\diamond} = 1$. The near-incompressibility of the material is achieved via a penalisation of the volumetric term. This approach is advantageous in the computational setting due to its straightforward implementation.

In the relevant publications, for Ψ_{iso}, different models are taken into account. In [Mart21a, Mart21b, Mart22a, Mart22b], the widely accepted Holzapfel-Ogden (HO) orthotropic model, mimicking the myocardial microstructures, is used [Holz09]. For benchmark problems in [Mart21c], a Neo-Hookean (NH) model is utilised, whereas in [Mart21b], a mixture model for the infarcted cardiac tissue is proposed. This model assumes HO model for the intact myocardium and a transversely isotropic model for the infarcted tissue. For an overview of the constitutive models used in cardiac mechanics, the reader is referred to the Introduction in [Mart21b].

2.1.4 Cardiac modelling

One of the thesis' objectives (C1-1) is to develop a computational model of the rat left ventricle which can be calibrated with parameters derived from experiments performed by our collaboration partners (PC, CS and MBT at FAU). In order to preserve consistency in the notation in the attached publications, the external mechanical body force $\boldsymbol{b}$ weighted by the reference volume ρ_0 in (2.6) is denoted by $\boldsymbol{F}^{\varphi}$ and the relationship between the first and second Piola-Kirchhof stress $\mathbf{P} = \mathbf{FS}$ is used. The reference configuration $\Omega_0 \subset \mathbb{R}^3$ corresponds to a three-dimensional model of a rat LV at time $t_0 = 0$.

Governing equations and constitutive models

The mechanical field equation is a static version of the balance of linear momentum, see (2.7), together with the BCs on the boundaries Γ_{φ} and Γ_T

$$\begin{aligned} \boldsymbol{0} &= \mathrm{Div}[\mathbf{FS}] + \boldsymbol{F}^{\varphi} \quad \text{in } \Omega_0, \\ \boldsymbol{\varphi}(\boldsymbol{X},t) &= \bar{\boldsymbol{\varphi}} \text{ in } \Gamma_{\varphi}, \quad \boldsymbol{T}(\boldsymbol{X},t) = \bar{\boldsymbol{T}} \quad \text{in } \Gamma_T, \end{aligned} \tag{2.12}$$

where $\mathbf{F}$ is the deformation gradient, $\mathbf{S}$ is the second Piola–Kirchhoff stress tensor, $\boldsymbol{F}^{\varphi}$ is the external mechanical body force, $\boldsymbol{\varphi}$ is the placement (see (2.2)) and $\boldsymbol{T}$ the surface traction vector. The prescribed values on the boundaries are denoted by bars, see Figure 2.1 for a schematic overview of the BCs. In [Mart21b, Mart22b, Mart22a], additionally, the Windkessel model described in Appendix E in [Mart22b] serves as a mechanical pressure BC.

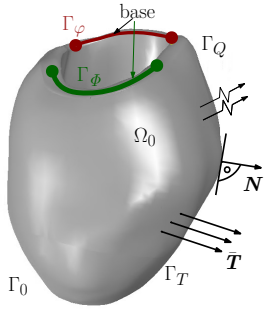

Figure 2.1: Rat left ventricle with prescribed mechanical and electrical BCs, from [Duon19].

Each material model of a fibre-reinforced tissue such as the myocardium has to account for the microstructure created by the network of these fibres. Based on the mechanical experiments on myocardia in humans and other mammals [Somm15, Ahma18, Doko02, Mart21b], myocardial tissue is assumed to be orthotropic with distinct fibre $\boldsymbol{f}_0$, sheet $\boldsymbol{s}_0$ and sheet-normal $\boldsymbol{n}_0$ directions which build a local orthonormal basis, see Figure 2.2. Its numerical implementation within a FEM framework is not straightforward and influences the simulation results as shown in [Holz22, Holz23]. In the present work, the material orientation is assumed to be generated by a LDRBM according to [Wong14].

The contraction of a rat LV in the attached publications is modelled either as a fully electromechanically coupled problem [Mart22b, Mart21a] or as a mechanical problem in which a temporal evolution of the active stress, based on a phenomenological model, is prescribed [Mart21c, Mart22a]. In both considered models, the total stress is additively decomposed into the passive part $\mathbf{S}_{pas}$ and the active part $\mathbf{S}_{act}$, namely

$$\mathbf{S} = \mathbf{S}_{pas}(\mathbf{C}) + \mathbf{S}_{act}(\boldsymbol{f}_0, \boldsymbol{n}_0, \bullet), \tag{2.13}$$

where $\boldsymbol{f}_0$ and $\boldsymbol{n}_0$ are the reference fibre and sheet-normal direction along which the contraction is induced. If electrophysiology is omitted, the evolution of the

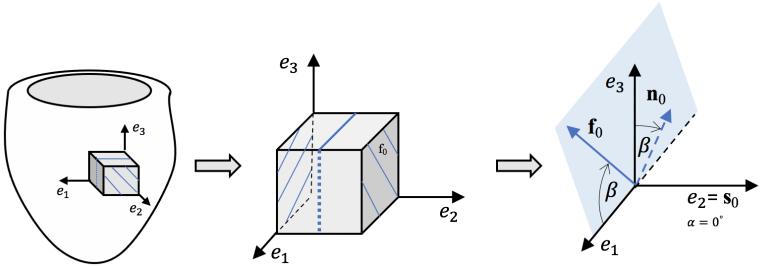

Figure 2.2: Local fibre orientation in the myocardium, from [Mart21b].

active stress can be described by the following time-dependent function

$$\mathbf{S}_{act} = \mathbf{S}_{act}(\boldsymbol{f}_0, \boldsymbol{n}_0, t) = T(t)(\boldsymbol{f}_0 \otimes \boldsymbol{f}_0 + \nu \boldsymbol{n}_0 \otimes \boldsymbol{n}_0), \tag{2.14}$$

where T denotes the active muscle tension and ν is the weighting factor accounting for experimentally observed reduced contraction in the cross-fibre direction [Lin98]. In [Mart21c], the model according to [Gucc93] is used whereas in [Mart22a], the model according to [Pfal19] is utilised. In the latter, the end-diastolic and peak-systolic times can be set as input directly. When the electromechanically coupled problem is considered [Mart21a, Mart22b], the active stress is dependent on the transmembrane potential Φ, i.e.

$$\mathbf{S}_{act} = \mathbf{S}_{act}(\boldsymbol{f}_0, \boldsymbol{n}_0, \Phi). \tag{2.15}$$

The reader is referred to Section 2 and Appendix B in [Mart22b] for two different models, based on a pure stress and a stress-strain approach, and more details regarding (2.15). In both considered models, however, an additional differential equation, describing the spatio-temporal evolution of the transmembrane potential Φ needs to be solved, namely

$$\begin{aligned} &\dot{\Phi} = \mathrm{Div}[\boldsymbol{Q}] + F^{\Phi} \quad \text{in } \Omega_0 \quad \text{and} \\ &\Phi(\boldsymbol{X}, t) = \bar{\Phi} \quad \text{in } \Gamma_{\Phi}, \quad \boldsymbol{Q}(\boldsymbol{X}, t) \cdot \boldsymbol{N} = \bar{\boldsymbol{Q}} \quad \text{in } \Gamma_Q, \end{aligned} \tag{2.16}$$

where $F^{\Phi} = F_e^{\Phi} + F_m^{\Phi}$ is the non-linear current for the electrical excitation, consisting of the purely electrical part F_e^{Φ} and electromechanical part F_m^{Φ}, $\dot{\Phi}$ denotes the material time derivative of the transmembrane potential and the flux is $\boldsymbol{Q} = \mathbf{D} \cdot \nabla \Phi$ with the anisotropic conductivity tensor $\mathbf{D} = d_{iso}\mathbf{I} + d_{ani}\boldsymbol{f}_0 \otimes \boldsymbol{f}_0$, where $\boldsymbol{f}_0$ is the reference fibre orientation [Gökt10]. Further, $\boldsymbol{N}$ is the unit normal vector pointing outwards of surface Γ_Q. BCs are defined on the boundaries Γ_{Φ} and Γ_Q. See Figure 2.1 and [Duon19] for a more detailed description and visualisation of the BCs. In [Mart22b], additionally, the

Purkinje fibre network (PFN) [SC16] serves as an electrical BC. The constitutive model for the electrical source term F_e^{Φ} is according to the phenomenological model proposed by [Alie96]. Its description can be found in Appendix C in [Mart22b] or in the original work.

In order to achieve a fully coupled system, the mechanically induced electrical source term F_m^{Φ}, commonly known as mechanoelectrical feedback (MEF), is modelled. The author refers to Appendix D in [Mart22b] for the constitutive equation.

2.2 Numerical methods

This section introduces two numerical methods for solving the (electro)mechanical problem given in (2.12) and (2.16). Firstly, the well-known finite element method is briefly introduced. This section aims to provide an overview and to define the used notation. For a complete introduction including mathematical derivation and proofs, the reader is referred to the literature, e.g. [Hugh00, Bath06, Wrig01, Bely13]. Secondly, the basic idea of an alternative method, the smoothed finite element method, is presented. For a more detailed background of this method, see [Liu16].

2.2.1 Finite element method

The weak forms of the balance equations (2.12) and (2.16) are required for solving the problem with the FEM. By multiplying (2.12) and (2.16) with vector- and scalar-valued test functions η and $\xi \in C^1(\Omega_0)$, respectively, integration over the reference domain Ω_0, using integration by parts, the Divergence theorem and BC given in (2.12) and (2.16), we obtain the following weak form

$$\mathbf{0} = \int_{\Omega_0} \nabla\eta : (\mathbf{FS})\mathrm{d}V - \int_{\partial\Omega_0} \eta\bar{\boldsymbol{T}}\mathrm{d}A - \int_{\Omega_0} \eta\boldsymbol{F}^{\varphi}\mathrm{d}V, \tag{2.17}$$

$$0 = \int_{\Omega_0} \xi\dot{\Phi}\mathrm{d}V + \int_{\Omega_0} \nabla\xi \cdot \mathbf{Q}\mathrm{d}V - \int_{\partial\Omega_0} \xi\bar{\boldsymbol{Q}}\mathrm{d}A - \int_{\Omega_0} \xi F^{\Phi}\mathrm{d}V. \tag{2.18}$$

To solve the above nonlinear equations numerically, discretisation and linearisation are required. It is worth noting, that the order of these operations can

be arbitrarily chosen. We start with the spatial discretisation of the domain Ω_0 into n_{el} finite elements such that the following approximation holds

$$\Omega_0 \approx \Omega_0^h = \bigcup_{e=1}^{n_{el}} \Omega_e, \quad \Omega_i \cap \Omega_j = \emptyset \quad \text{for } i \neq j. \tag{2.19}$$

By splitting (2.17) and (2.18) elementwise, the discrete weak forms are derived according to the following concept

$$\int_{\Omega_0} (\bullet)\, \mathrm{d}V \approx \int_{\Omega_0^h} (\bullet)\, \mathrm{d}V = \mathop{\mathrm{A}}_{e=1}^{n_{el}} \int_{\Omega_e} (\bullet)\, \mathrm{d}V, \tag{2.20}$$

where the assembly operator $\mathrm{A}_{e=1}^{n_{el}}$ ensures that the contributions of the element nodes i are assigned to the correct global node I. To formulate the specific discrete weak forms of (2.12) and (2.16), elementwise approximations of the test functions η^e and ξ^e and their gradient $\nabla\eta^e$ are needed, namely

$$\eta^e = \sum_{i=1}^{nn} N_i \eta_i, \quad \nabla\eta^e = \sum_{i=1}^{nn} N_i \otimes \nabla\eta_i, \tag{2.21}$$

$$\xi^e = \sum_{i=1}^{nn} N_i \xi_i, \quad \nabla\xi^e = \sum_{i=1}^{nn} N_i \otimes \nabla\xi_i, \tag{2.22}$$

where nn is the number of nodes in the element Ω_e and N_i are the nodal shape functions. Further, based on the isoparametric concept, all quantities are approximated in the same way. In particular, the displacement in (2.3) is approximated as $\boldsymbol{u}^e = \sum_{i=1}^{nn} N_i \boldsymbol{u}_i$. Note that if linear shape functions are used, the deformation gradient is constant over the element, i.e.

$$F_{kl}^e(\boldsymbol{X}) = \frac{\partial u_k^e(\boldsymbol{X})}{\partial X_l} + \delta_{kl} = \sum_{i=1}^{nn} \frac{\partial N_i}{\partial X_l} (\boldsymbol{u}_i^e)_k + \delta_{kl} \quad \forall \boldsymbol{X} \in \Omega_e. \tag{2.23}$$

The discrete weak forms are then given as

$$\boldsymbol{r}_I^{\varphi} := \mathop{\mathrm{A}}_{e=1}^{n_{el}} \left(\int_{\Omega_e} (\mathbf{FS}) \nabla N_i \mathrm{d}V - \int_{\partial\Omega_e} N_i \bar{\boldsymbol{T}} \mathrm{d}A - \int_{\Omega_e} N_i \boldsymbol{F}^{\varphi} \mathrm{d}V \right) = \mathbf{0}, \tag{2.24}$$

$$r_I^{\Phi} := \mathop{\mathrm{A}}_{e=1}^{n_{el}} \left(\int_{\Omega_e} N_i \dot{\Phi} \mathrm{d}V + \int_{\Omega_e} \nabla N_i \boldsymbol{Q} \mathrm{d}V - \int_{\partial\Omega_e} N_i \bar{\boldsymbol{Q}} \mathrm{d}A - \int_{\Omega_e} N_i F^{\Phi} \mathrm{d}V \right) = 0 \tag{2.25}$$

and have to hold for each node i/I in the elementwise/global numbering, respectively. Therefore, we obtain the following nonlinear equation which has to be fulfilled

$$\boldsymbol{r}(\varphi, \Phi) := (\boldsymbol{r}^{\varphi}(\varphi, \Phi), \boldsymbol{r}^{\Phi}(\varphi, \Phi)) = \mathbf{0}. \tag{2.26}$$

To solve (2.26) numerically, commonly and in particular in the attached publications, the iterative Newton-Rhapsod method is utilised in each load step of the quasi-static analysis. This method is based on the linearisation of the discrete global residual $\boldsymbol{r}$ given in (2.26). Using Taylor expansion after the assembling procedure, the following equations are to be fulfilled at each increment m of the Newton-Rhapson method

$$\boldsymbol{r}^{\varphi}_{m+1} = \boldsymbol{r}^{\varphi}_{m} + \frac{\partial \boldsymbol{r}^{\varphi}_{m}(\varphi, \Phi)}{\partial \varphi}\Delta\varphi + \frac{\partial \boldsymbol{r}^{\varphi}(\varphi, \Phi)}{\partial \Phi}\Delta\Phi = \boldsymbol{r}^{\varphi}_{m} + \mathbf{K}^{\varphi\varphi}_{m}\Delta\varphi + \mathbf{K}^{\varphi\Phi}_{m}\Delta\Phi = \mathbf{0}, \tag{2.27}$$

$$\boldsymbol{r}^{\Phi}_{m+1} = \boldsymbol{r}^{\Phi}_{m} + \frac{\partial \boldsymbol{r}^{\Phi}_{m}(\varphi, \Phi)}{\partial \varphi}\Delta\varphi + \frac{\partial \boldsymbol{r}^{\Phi}(\varphi, \Phi)}{\partial \Phi}\Delta\Phi = \boldsymbol{r}^{\Phi}_{m} + \mathbf{K}^{\Phi\varphi}_{m}\Delta\varphi + \mathbf{K}^{\Phi\Phi}_{m}\Delta\Phi = \mathbf{0}, \tag{2.28}$$

where $(\Delta\varphi, \Delta\Phi)$ is the incremental update of the solution. At each increment, the above equations can be summarised as follows

$$\begin{bmatrix} \mathbf{K}^{\varphi\varphi}_{m} & \mathbf{K}^{\varphi\Phi}_{m} \\ \mathbf{K}^{\Phi\varphi}_{m} & \mathbf{K}^{\Phi\Phi}_{m} \end{bmatrix} \cdot \begin{bmatrix} \Delta\varphi \\ \Delta\Phi \end{bmatrix} = \mathbf{K}_{m} \cdot \begin{bmatrix} \Delta\varphi \\ \Delta\Phi \end{bmatrix} = \begin{bmatrix} -\boldsymbol{r}^{\varphi}_{m} \\ -\boldsymbol{r}^{\Phi}_{m} \end{bmatrix}, \tag{2.29}$$

where $\mathbf{K}_m$ is the global stiffness matrix at the increment m. The resulting system of linear equations can be solved numerically and the incremental updates of the solution are computed as

$$\varphi_{m+1} = \varphi_{m} + \Delta\varphi, \tag{2.30}$$

$$\Phi_{m+1} = \Phi_{m} + \Delta\Phi. \tag{2.31}$$

The iterations are performed until the residuals $\boldsymbol{r}^{\varphi}_{m+1}$ and $\boldsymbol{r}^{\Phi}_{m+1}$ reach a given tolerance and we can proceed to a next load step.

2.2.2 Smoothed finite element methods

In the classical FEM, as described in the previous Section 2.2.1, the so-called compatible strain field (i.e. deformation gradient in large deformation analysis) in (2.23) is immediately used to compute stress in a finite element, using (2.13). In S-FEMs, after the evaluation of the compatible strain field, it is modified by a strain smoothing operation. The strain is smoothed over a

designed SD, see Figure 2.3 for SDs in 3D for NS-FEM and FS-FEM. In NS-FEM, the SD associated with the node k is created by connecting the node k to the mid-edge points, centroids of adjacent tetrahedron's faces and centroids of the adjacent tetrahedrons (Figure 2.3(a)). In FS-FEM, the SD associated with the face k is created by connecting three nodes of the face to the centroids of the adjacent tetrahedrons as shown in Figure 2.3(b). For 2D, the reader is referred to [Mart21c]. For the relation between a SD Ω_k and a user element U_k, the reader is referred to Section 5.1.1.

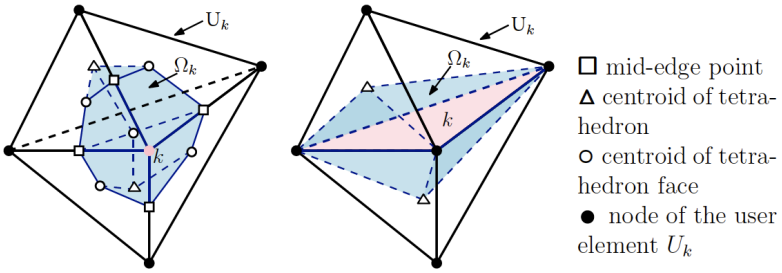

(a) NS-FEM (b) FS-FEM

Figure 2.3: Smoothing domains in 3D for NS-FEM (a) and FS-FEM (b). In blue, the SDs Ω_k around the node k respectively the face k are highlighted. The user element in Abaqus U_k (black line) is built of n_k^e adjacent elements of the original mesh. Note that for (a), if the node $k \notin \Gamma_0$ then $n_k^e > 2$ and consequently, the highlighted blue domain is a subdomain of the SD Ω_k and the displayed two tetrahedral elements (black colour) are a subpart of the user element U_k. For (b), if the face $k \notin \Gamma_0$ then $n_k^e = 2$ and the user element U_k is displayed in black colour.

To numerically solve (2.12) with a S-FEM, initially, the undeformed computational domain Ω_0 bounded by Γ_0 is discretised into non-overlapping elements in the same way as in the FEM, see (2.19). Subsequently, it is subdivided into a finite number of non-overlapping SDs Ω_k with boundary Γ_k, i.e. $\Omega_0^h = \cup_{k=1}^{n_{sd}} \Omega_k$, where n_{sd} is the number of SDs and $\Omega_i \cap \Omega_j = \emptyset$ for $i \neq j$. In general, S-FEMs can be applied for arbitrary n-sided polygonal elements [Wu23a], including linear triangular elements in 2D and linear tetrahedral elements in 3D, which are of the main interest in the present thesis. For these elements, the strain field is evaluated in exactly the same way as in the FEM and then smoothed (i.e. averaged) by convolution with a smoothing function $W(\boldsymbol{X}_k - \boldsymbol{X})$ associated

with a material point $\boldsymbol{X}_k \in \Omega_k$. The smoothing function W has to satisfy the positivity and unity properties [Liu19], i.e.

$$W(\boldsymbol{X}_k - \boldsymbol{X})\mathrm{d}V \geq 1, \quad \int_{\Omega_k} W(\boldsymbol{X}_k - \boldsymbol{X})\mathrm{d}V = 1. \tag{2.32}$$

Most commonly, a simple Heaviside step function is utilised. Using this assumption and the property that SDs are disjoint and therefore each $\boldsymbol{X} \in \Omega_0$ can be uniquely associated with a SD Ω_k, the smoothing function W is constant on the SD Ω_k and can be rewritten as in [Mart21c, Mart23a], namely

$$W(\boldsymbol{X}_k - \boldsymbol{X}) = W_k(\boldsymbol{X}) = \begin{cases} 1/V_k & \text{if } \boldsymbol{X} \in \Omega_k \\ 0 & \text{else} \end{cases} \quad \text{with } V_k = \int_{\Omega_k} \mathrm{d}V. \tag{2.33}$$

For linear shape functions N_α^e for the node α on the tetrahedral element Ω_e, the smoothed deformation gradient $\bar{\mathbf{F}}^k$ on the SD Ω_k is constant for all $\boldsymbol{X} \in \Omega_k$ and takes the form

$$\begin{aligned} \bar{\mathrm{F}}_{ij}^k &= \int_{\Omega_k} \frac{\partial u_i(\boldsymbol{X})}{\partial X_j} W_k(\boldsymbol{X})\mathrm{d}V + \delta_{ij} = \frac{1}{n_n^e} \sum_{e=1}^{n_k^e} \int_{\Omega_e} \frac{\partial u_i(\boldsymbol{X})}{\partial X_j} W_k(\boldsymbol{X})\mathrm{d}V + \delta_{ij} \\ &= \frac{1}{n_n^e V_k} \sum_{e=1}^{n_k^e} \frac{\partial u_i(\boldsymbol{X})}{\partial X_j} V_e + \delta_{ij} = \frac{1}{n_n^e V_k} \sum_{e=1}^{n_k^e} \sum_{\alpha=1}^{n_n^e} \frac{\partial N_\alpha}{\partial X_j} (\boldsymbol{u}_\alpha)_i V_e + \delta_{ij}, \end{aligned} \tag{2.34}$$

where V_e is the reference volume of the element Ω_e, n_k^e is the number of elements connected to the node k in NS-FEM or face k in FS-FEM, n_n^e denotes the number of nodes in one element ($n_n^e = 3$ for triangular [Mart21c], $n_n^e = 4$ for tetrahedral mesh [Mart23a]) and δ_{ij} is the Kronecker delta. Consequently, the smoothed right Cauchy-Green tensor $\bar{\mathbf{C}}^k = \bar{\mathbf{F}}^{k\,T} \bar{\mathbf{F}}^k$ and the second Piola–Kirchhoff stress tensor $\bar{\mathbf{S}}^k$ are computed on a SD. Furthermore, the fibre orientation on the SD $\bar{\boldsymbol{f}}_0^k = (\bar{x}_1^k, \bar{x}_2^k, \bar{x}_3^k)$ is given as

$$\bar{x}_i^k = \frac{1}{n_k^e} \sum_{e=1}^{n_k^e} x_i^e \quad i \in \{1, 2, 3\}, \tag{2.35}$$

where x_i^e is the i-th component of the local fibre orientation on the element Ω_e. The stiffness matrix and the residual vector are computed analogously to the nonlinear FEM, but integration is performed over the SDs rather than over elements.

Convergence property Let $\bar{\boldsymbol{u}}$ and $\boldsymbol{u}$ be the solutions of a S-FEM and the FEM, respectively. When $n_{sd} \to \infty$, then $\bar{\boldsymbol{u}}$ converges to $\boldsymbol{u}$.

To prove this statement, let's discretise $\Omega_0^h = \cup_{k \in n_{sd}} \Omega_k$, let's associate Ω_k with a material point $\boldsymbol{X}_k \in \Omega_k$ and let $n_{sd} \to \infty$. Then $V_k = \int_{\Omega_k} \mathrm{d}V \to 0$ and the smoothing function $W(\boldsymbol{X}_k - \boldsymbol{X})$ with the properties (2.32) converges to the Dirac measure δ, in particular with the following two properties [Liu16]

(1) $\delta(\boldsymbol{X}_k - \boldsymbol{X}) = 0$ if $\boldsymbol{X}_k \neq \boldsymbol{X}$

(2) $\delta(\boldsymbol{X}_k - \boldsymbol{X}) = 1$ if $\boldsymbol{X}_k = \boldsymbol{X}$

For $V_k \to 0$ and $(\boldsymbol{X}_k - \boldsymbol{X}) \to \boldsymbol{0}$, using (2.34), we consequently obtain

$$\bar{\mathbf{F}}(\boldsymbol{X}_k) = \int_{\{\boldsymbol{X}_k\}} (\mathbf{F}(\boldsymbol{X}) - \mathbf{I}) \mathrm{d}\delta(\boldsymbol{X}_k - \boldsymbol{X}) + \mathbf{I} = \mathbf{F}(\boldsymbol{X}_k) \tag{2.36}$$

Hence, the smoothed stress, residual vector and stiffness matrix converge to those obtained in FEM. This eventually implies that if S-FEM is associated with a certain number of nodes (NS-FEM), edges (ES-FEM) or faces (FS-FEM) going to infinity, then, because $\boldsymbol{u}$ converges to the exact solution (well-known property of FEM), $\bar{\boldsymbol{u}}$ does it as well.

2.2.3 Numerical optimisation

In [Mart21b, Mart22a, Mart23b], optimisation problems are solved in order to fit the model parameters, determine the optimal support pressure and to find the optimal glandular secretion or drug dosing patterns, respectively. In the following, a general optimisation problem is introduced.

Let $f(\boldsymbol{x})$ be an objective function, i.e. a scalar function of $\boldsymbol{x} \in \mathbb{R}^n$ that we want to minimise (or maximise). The constraint optimisation problem is given as

$$\begin{aligned} \min_{\boldsymbol{x}} f(\boldsymbol{x}) \quad \text{subject to} \quad & c_i(\boldsymbol{x}) = 0,\ i \in \mathcal{E}, \\ & c_i(\boldsymbol{x}) \leq 0, i \in \mathcal{F}, \end{aligned} \tag{2.37}$$

where $\boldsymbol{x} \in \mathbb{R}^n$ is the vector of unknown parameters, c_i are constraint functions, defining certain restrictions that the unknown vector $\boldsymbol{x}$ has to satisfy.

In general, either stochastic or deterministic algorithms can be utilised to solve the problem (2.37) numerically. While stochastic methods can be used

if some quantities are unknown or uncertain, deterministic methods require that the model is completely known. In this work, only the latter methods are considered.

To find the best curve fit in [Mart21b], the MATLAB function *lsqcurvefit* using the trust-region-reflective algorithms is utilised. For mathematical background see e.g. [Conn00]. Providing the constitutive model $F(\boldsymbol{x}, xdata_i)$ and the measured values $ydata_i$, the following constrained optimisation problem is solved

$$\min_{\boldsymbol{x}} f(\boldsymbol{x}) = \min_{\boldsymbol{x}} \sum_{i=1}^{n} (F(\boldsymbol{x}, xdata_i) - ydata_i)^2 \quad \boldsymbol{lb} \leq \boldsymbol{x} \leq \boldsymbol{ub}, \tag{2.38}$$

where $\boldsymbol{xdata}$, $\boldsymbol{ydata} \in \mathbb{R}^n$ have the components $xdata_i$, $ydata_i \in \mathbb{R}$, n is the number of the measured values and $\boldsymbol{lb}$, $\boldsymbol{ub} \in \mathbb{R}^n$ are the lower and upper bounds for the unknown model parameters, respectively. See (26) in [Mart21b] for the specific form of (2.38).

The constraint optimisation problems in (15) and (20) in [Mart23b] can be rewritten into unconstrained optimisation problems (18) and (21), i.e. (2.37) without the constraint functions c_i. Therefore, the MATLAB function *fminsearch* using the computationally efficient Nelder–Mead simplex method [Neld65, Laga98] can be used. In this algorithm, a simplex of $n+1$ points for $\boldsymbol{x} \in \mathbb{R}^n$ is created. It initially makes a simplex around the initial guess $\boldsymbol{x}_0$. Then, the simplex is repeatedly modified until the stopping criterion is reached. For details see the original publications.

2.3 Basic biological background

This section aims to introduce a very basic biological background and the terminology which is essential to follow the attached publications. For a deeper understanding of the biological and physiological background, the reader is referred to the literature, e.g. [Katz10, Ande04, Klab11] for cardiac physiology and [Weis96, Graw12, Lauf96] for ligand-receptor binding models in pharmacology.

2.3.1 Heart anatomy and physiology

Throughout the thesis, a four-chamber heart, which is present in all mammals, is considered. Its main functions are pumping blood into the systemic circulation,

controlling the heart rate, maintaining the blood pressure and enabling the excretion of the waste metabolic products.

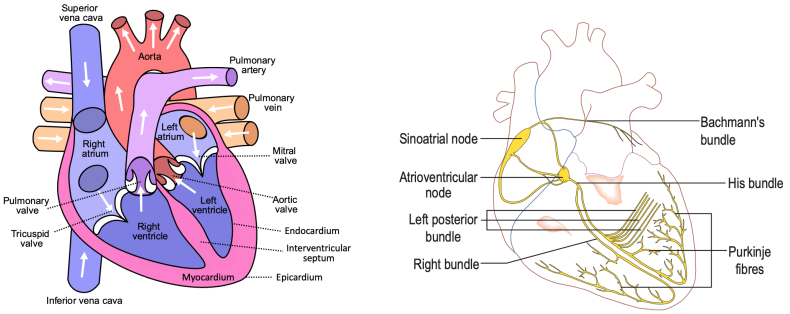

(a) (b)

Figure 2.4: (a) Schematic structure of the heart anatomy[1]. (b) Schematic overview of the heart electrical conduction system [2].

The heart can be separated into four chambers, the right and left atria and the right and left ventricles, as displayed in Figure 2.4(a). The right atrium receives deoxygenated blood from the venae cavae superior and inferior, whereas the left atrium receives oxygenated blood from the pulmonary vein. The anatomical separation of the heart into a left and right component is made possible by the interatrial and interventricular septa. Each component has two chambers that are connected by atrioventricular valves – the mitral valve on the left side and the tricuspid valve on the right side. Two other valves, pulmonary and aortic, are located between the right ventricle and the pulmonary artery and between the left ventricle and the aorta, respectively.

The cardiac tissue is made up of three layers: The middle and thickest muscular layer is called myocardium, and mainly consists of cells responsible for generating the contractile force in the heart, i.e. cardiomyocytes. The myocardial cells also carry electrical impulses and act as a framework for the heart chambers. In the chambers, a thin layer of smooth additional tissue, the endocardium, separates the myocardium from the hollow areas. Similarly, the outer layer of the heart is referred to as epicardium, which makes up part of the pericardium. The latter surrounds and protects the heart and holds it in place.

[1] elaborated from https://commons.wikimedia.org/w/index.php?curid=830253
[2] elaborated from https://commons.wikimedia.org/w/index.php?curid=10197958

During the cardiac cycle, two main phases are distinguished, the systole and the diastole. Both phases can be further subdivided into two phases. The systole begins with the isovolumetric contraction of both ventricles, the atrioventricular valves remain closed and therefore a rapid increase in the ventricular blood pressure occurs. When the pressures in the right/left ventricles exceed the pressures in the pulmonary artery/aorta, the pulmonary/aortic valves open, the blood is pumped into the circulatory system and the ventricular volume is reduced (ejection phase). If the pressure of the ventricles and arteries is equal, the pulmonary/aortic valves close and the diastole begins. Initially, the isovolumetric relaxation takes place, i.e. pressure in the ventricles is decreased until it drops under the atrial pressure, the ventricular volume is preserved. Subsequently, the atrioventricular valves open and the blood from the atria starts to flow into the ventricles (ventricular filling). In Figure 2.5, all phases are schematically shown in the form of a so-called pressure-volume loop of the LV.

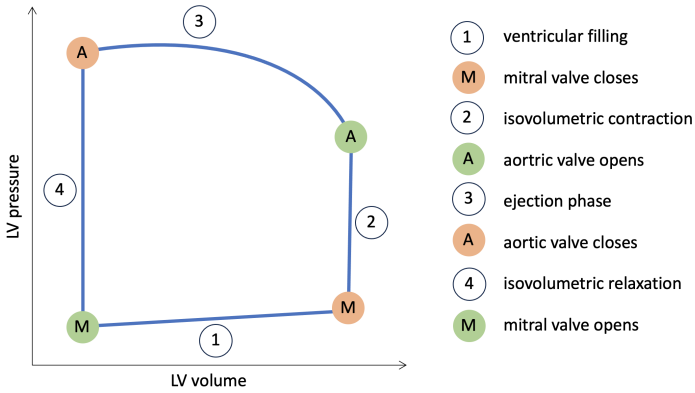

Figure 2.5: Schematic representation of a left-ventricular pressure-volume loop displaying four phases of the cardiac cycle: ventricular filling, isovolumetric contraction, ejection phase and isovolumetric relaxation.

The whole cardiac cycle is controlled by the electrical conduction system of the heart, whose key elements are depicted in Figure 2.4(b). The sinoatrial node is where the pacemaking electrical signal first appears. Then, the signal continues via the myocardium of the right atrium to the left atrium via specialised inter-atrial bundle connections. Then, it continues to the atrioventricular node where the signal is delayed until the atrial contraction is completed. Subsequently, the signal is travelling through the His bundle to the atrioventricular septum,

where it is split into the left and right bundle and ends in the PFN in the subendocardial layer. The signal transmurally travels from the endocardium to the epicardium, via the interaction of the PFN with the cardiomyocytes.

Specific features of rat heart All mammals have structurally similar hearts as described above. However, the present thesis focuses on modelling and simulation of a rat heart and thus, some specific characteristics of a rat heart in comparison to a human heart are listed in Table 2.1. In particular, a small rat heart works at much higher frequencies than the human heart. This inverse relationship between the heart or body weight and the heart rate is due to a larger metabolic rate in small animals. It is necessary because due to a larger surface area to volume ratio in small animals, more energy is needed in order to keep the body temperature constant [Nouj04].

Table 2.1: Comparison of basic characteristics of human and rat hearts [Treu17, Øste10].

characteristic	human	rat
body weight (kg)	50 - 86	0.225 – 0.52
heart weight (g)	200 - 350	0.5 - 2.5
heart weight (% of body weight)	0.40 - 0.45	0.20 - 0.50
heart rate (bpm)	80 - 120	300 - 500
blood flow rate ($l \cdot min^{-1}$)	4.5 - 5.0	0.07 - 0.08
systolic pressure (mmHg)	120	84 - 184
diastolic pressure (mmHg)	80	58 -145

2.3.2 Ligand-receptor binding models

To present a fundamental background for C4, in the following, the focus is put on guanine nucleotide-binding (G)-protein-coupled receptors (GPCRs) which build the largest receptor family in eukaryotes. They mediate a response to a variety of extracellular signalling molecules, including hormones, local mediators, and neurotransmitters. Some examples of GPCRs include PTH receptors in osteoblasts and renal cells, regulating calcium homeostasis; α- and β-adrenergic and angiotensin receptors, found predominantly in the heart and regulating for example cardiac contractility, heart rate and cardiac remodelling; prostaglandin receptors, found mainly in the brain and modulating the inflammation processes; or rhodopsin receptors in the retina, triggering the phototransduction.

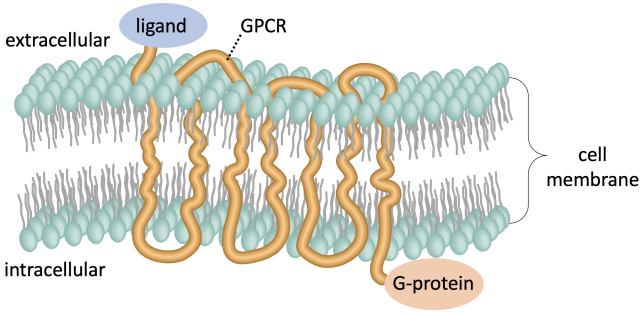

Figure 2.6: A schematic representation of a G-protein-coupled receptor snaking seven times through the cell membrane[3].

Despite the diversity of signalling molecules that can be bound to a GPCR, all these receptors have a similar structure: each receptor consists of a single polypeptide chain that snakes back and forth through the cell membrane seven times as schematically depicted in Figure 2.6. When a ligand binds to a GPCR, it leads to a conformational change in the GPCR. This modification then triggers the interaction between the GPCR and a nearby G-protein which subsequently changes its conformation as well and activates other molecules in the cell. To model the binding between a ligand and its receptor, many different models exist, see e.g. [Weis96]. The simplest model is a two-element model consisting only of a ligand and a receptor. The binding of a ligand activates the receptor and leads to an active ligand-receptor complex. However, this simple model does not describe the whole ligand-receptor binding process correctly [Leff95]. For example, it neglects the differences between the active and inactive receptor states, R_a and R_i, respectively, see Figure 2.7(a). A more complex, but also a more realistic model, known as a two-state receptor model (Figure 2.7(b)), assumes that the receptor can be present in two conformational states. These correspond to an active (or nondesensitised) receptor state (R_a), and an inactive (or desensitised) receptor state (R_i), which differ by their capability of eliciting a cellular response upon binding of the ligand. Both receptor states are able to bind to the ligand L to form active and inactive ligand-receptor complexes $C_a = LR_a$ and $C_i = LR_i$, respectively [Leff95]. This widely accepted model [Leff95] is also utilised in [Mart23b], see Chapter 6. Theoretically, both above models can be seen as submodels of an even more complex model, i.e. the ternary model, see Figure 2.7(c). They include a third component, G-protein which acts as an intermediary between the receptor

[3]elaborated from https://commons.wikimedia.org/wiki/File:202304_G_protein-coupled_receptor.svg

and its ligand. It is assumed that the receptor possesses two binding sides, one for the ligand and one for the G-protein. As shown in [Weis96], different intermediate stages can be assumed.

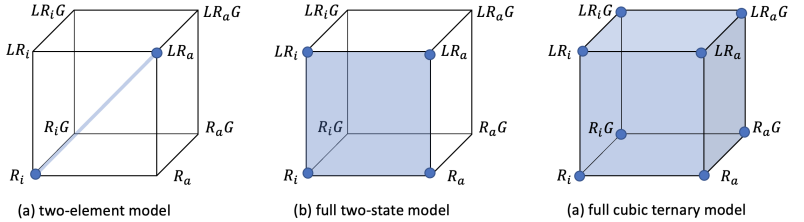

Figure 2.7: Ligand-receptor binding models: A representative two-element (a) and full two-state (b) receptor models are schematically shown as submodels of the full cubic ternary model (c). Relevant parts of the model are highlighted in blue. Reconstructed according to [Weis96].

Part II

Research Contributions

The present doctoral thesis is a compilation of six journal publications and one conference proceeding (see Appendix for their originally published versions), covering various aspects of biomechanics with the main focus on modelling and simulation of rat cardiac electromechanics. The publications span from the organs-scale model of a rat heart to a cell-level two-state ligand-receptor binding model. This chapter thematically orders the publications into five groups of research contributions. In the first four groups (C1-C4), visually summarised in Figure 1.1, the doctoral researcher contributed as the first (main) author whereas in the fifth group, the contribution is as a co-author. At the end of each subsection, the relevant publications are listed and the original abstract, the role of the doctoral researcher and the main highlights of the publication are shown. The publications are attached in the Appendix in their originally published form.

3 Modelling and simulation of healthy and infarcted rat left ventricles (C1)

3.1 Introduction to C1

3.1.1 Experimental work

The experimental part of the work is carried out at Pediatric Cardiology, Cardiac Surgery and Institute of Biomedical Technologies of FAU. The tested animals, Sprague Dawley rats, are divided into control, sham and infarcted groups. A MI in the last group is induced via permanent ligation of the left anterior descending coronary artery as described in [Mart21b]. After the operation, the rats (control, sham and infarcted) underwent MRI and echocardiography examination to keep track of physiological parameters, in particular heart rate, EF, deformation and wall thickness. These measured values are used for simulation validation in [Mart22b]. To investigate the passive mechanical properties of the healthy and infarcted rat LVs, uniaxial extension tests on tissue samples were performed using *MyoRobot* [Haug18, Haug19] as described in Section 2 in [Mart21b]. Based on the histological staining of the tested samples, see Figure 1.1 left upper box or Figure 7 in [Mart21b], the amount of fibrosis was quantified and further used for the fitting of the parameter needed for the computational simulation.

3.1.2 Cardiac modelling and simulation

The modelling and simulation part of the work is performed at LTD and is the core part of the present thesis. The basis is an electromechanically coupled simulation model of the rat LV using FEM.

First, a passive material model for healthy and infarcted tissue is developed in [Mart21b], the workflow is depicted in Figure 3.1. After the mechanical testing and histological staining, see Section 3.1.1, a modified HO constitutive law is calibrated with the experimental data in combination with the published

data. In the proposed model, the infarcted tissue is additively decomposed into intact myocardium and fibrotic scar, see Figure 1.1 left upper box for the histological samples. The amount of fibrosis obtained from the histology serves as a weighting factor, i.e.

$$\Psi_{pas} = (1 - fib)\, \Psi^m_{pas} + fib\, \Psi^s_{pas}, \quad \mathbf{S}_{pas} = (1 - fib)\, \mathbf{S}^m_{pas} + fib\, \mathbf{S}^s_{pas}, \quad (3.1)$$

where the superscripts m and s represent the quantities associated with the healthy myocardial tissue and the scar structure after MI, respectively. The orthotropic HO strain energy function [Holz09] is denoted by Ψ^m and Ψ^s is a transversal isotropic strain energy function, taking into account the direction of the collagen fibres building the scar. Finally, a passive end-diastolic filling of a rat LV is simulated with both, the fitted parameters and previously published material parameters. The experimental results demonstrate that the stress in an infarcted myocardium is significantly higher than in a healthy one, see Figure 8 in [Mart21b].

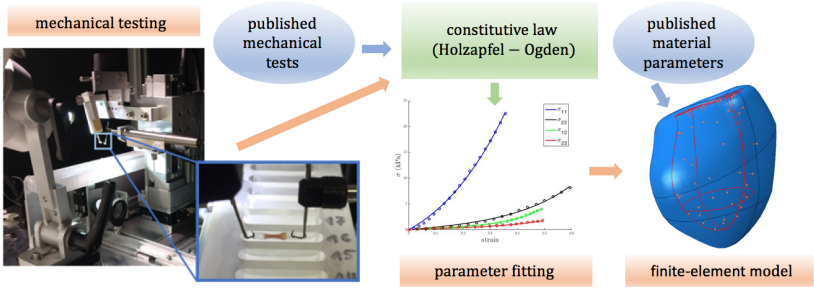

Figure 3.1: Workflow in publication [Mart21b]: Firstly, mechanical testing on healthy and infarcted tissue samples from rat LVs is performed; secondly, modified Holzapfel-Ogden constitutive law is calibrated with the experimental data in combination with the published data. Finally, the passive end-diastolic filling of a rat LV is simulated with both, the fitted parameters and with previously published material parameters.

Secondly, in [Mart21a], the passive material model is extended for an active contraction, which is as well scaled by the amount of fibrosis, namely

$$\mathbf{S} = (1 - fib)\, (\mathbf{S}^m_{act} + \mathbf{S}^m_{pas}) + fib\, \mathbf{S}^s_{pas}, \quad (3.2)$$

assuming that only the healthy myocardium can actively contract [Berb15]. It is shown that the passive material parameters obtained in [Mart21b] greatly

improve the simulation results, in particular, the EFs are close to the experimentally reported values in [Jegg06].

Thirdly, within this research contribution, two different approaches for the electromechanically coupled simulation model, pure stress [Gökt10] and stress-strain approach [Gökt14], are compared with the experimental data (end-diastolic volume, end-systolic volume, EF, wall thickness, myocardial volume) as well as among each other regarding the regional differences in the active stress [Mart22a].

3.2 Summary of publications within C1

3.2.1 Passive mechanical properties in healthy and infarcted rat left ventricle characterised via a mixture model

[Mart21b] D. Martonová, M. Alkassar, J. Seufert, D. Holz, M. T. Duong, B. Reischl, O. Friedrich, and S. Leyendecker. Passive mechanical properties in healthy and infarcted rat left ventricle characterised via a mixture model. *Journal of the Mechanical Behavior of Biomedical Materials*, 119:104430, 2021.

Abstract *During the cardiac cycle, electrical excitation is coupled with mechanical response of the myocardium. Besides the active contraction, passive mechanics plays an important role, and its behaviour differs in healthy and diseased hearts as well as among different animal species. The aim of this study is the characterisation of passive mechanical properties in healthy and infarcted rat myocardium by means of mechanical testing and subsequent parameter fitting. Elasticity assessments via uniaxial extension tests are performed on healthy and infarcted tissue samples from left ventricular rat myocardium. In order to fully characterise the orthotropic cardiac tissue, our experimental data are combined with other previously published tests in rats – shear tests on healthy myocardium and equibiaxial tests on infarcted tissue. In a first step, we calibrate the Holzapfel-Ogden strain energy function in the healthy case. So far, this orthotropic constitutive law for the passive myocardium has been fitted to experimental data in several species, however there is a lack of an appropriate parameter set for the rat. With our determined parameters, a finite element simulation of the end-diastolic filling is performed. In a second step, we propose a model for the infarcted tissue. It is represented as a mixture of intact myocardium and a transversely isotropic scar structure. In our mechanical*

experiments, the tissue after myocardial infarction shows significantly stiffer behaviour than in the healthy case, and the stiffness correlates with the amount of fibrosis. A similar relationship is observed in the computational simulation of the end-diastolic filling. We conclude that our new proposed material model can capture the behaviour of two kinds of tissues – healthy and infarcted rat myocardium, and its calibration with the fitted parameters represents the experimental data well.

Author contribution The first author contributed in the following tasks:

- conceptualisation
- methodology
- software
- formal analysis
- writing - original draft
- visualisation

Highlights

- stiffness of the rat myocardium positively correlates with the amount of fibrosis
- scar tissue yields anisotropy in rat LV after MI
- mixture material model of healthy and infarcted rat myocardium
- calibration of modified Holzapfel-Ogden strain energy function with experimental data
- finite element simulation of end-diastolic filling with varying infarction size

3.2.2 Influence of passive mechanical properties in healthy and infarcted rat myocardium on the cardiac cycle

[Mart21a] D. Martonová, M. Alkassar, J. Seufert, D. Holz, M. Tuan Duong, B. Reischl, O. Friedrich, and S. Leyendecker. Influence of passive mechanical properties in healthy and infarcted rat myocardium on the cardiac cycle. *PAMM*, 21(1):e202100054, 2021.

Abstract *Passive mechanics plays an important role during the electromechanically coupled cardiac cycle and its behaviour strongly changes after myocardial infarction. In the present work, the cardiac tissue is modelled as a mixture of an active orthotropic intact myocardium and a passive transversely isotropic fibrotic scar structure. We apply the constitutive model on the fully electromechanically coupled simulation of a cardiac cycle using a generic geometry of a rat left ventricle. Finally, the ejection fractions for various parameter sets based on the fitting to experimental data in different animal species as well as for a varying amount of fibrosis are compared. We show that both, the choice of species-specific passive material parameters and the amount of fibrosis, have a significant influence on the cardiac performance measured by the ejection fraction of the left ventricle.*

Author contribution The first author contributed in the following tasks:

- conceptualisation
- methodology
- software
- formal analysis
- writing - original draft
- visualisation

Highlights

- passive material parameters highly influence whole cardiac cycle
- cardiac simulation at different fibrosis stages
- fibrosis as scaling factor for passive and active cardiac cycle

3.2.3 Comparison of stress and stress–strain approaches for the active contraction in a rat cardiac cycle model

[Mart22b] D. Martonová, D. Holz, J. Seufert, M. T. Duong, M. Alkassar, and S. Leyendecker. Comparison of stress and stress–strain approaches for the active contraction in a rat cardiac cycle model. *Journal of Biomechanics*, 134:110980, 2022.

Abstract *In the last decades, different strategies to model the active electromechanically coupled behaviour of the cardiac tissue were proposed in order to simulate electromechanics of the heart under healthy and pathological conditions. The main objective of this work is to compare two approaches for modelling the active contraction during the electromechanically coupled rat cardiac cycle – the stress and the stress–strain approach. Firstly, a cylindrical benchmark is considered and secondly, for a generic model of a rat left ventricle, a simulation including the Windkessel model, excitation via Purkinje fibre network and mechano-electrical feedback is performed. The model is calibrated with experimental data for rats, partly from own measurements via cardiac ultrasound, partly from the literature. Further, possibilities to reach higher ejection fractions are discussed and considered for an exemplary rat left ventricle. Within each approach, we observe regionally different active stresses and fibre stretches. Moreover, the transmural active stress and fibre stretch distribution is influenced by the pressure load on the endocardial surface. The active stress approach is not sensitive to the fibre stretch and transmurally varying fibre stretch in the left ventricular domain is observed. The active stress–strain approach leads to transmurally more homogeneous fibre stretch at the end-systolic state.*

Author contribution The first author contributed in the following tasks:

- conceptualisation
- methodology
- software
- formal analysis
- writing - original draft
- visualisation

Highlights

- comparison of the pure stress and the stress-strain approach in electromechanically coupled simulation of a rat cardiac cycle
- electrical excitation via the Purkinje fibre network
- ellipsoidal geometry of the rat left ventricle derived from echocardiography
- simulation results are compared with experimental data (end-diastolic volume, end-systolic volume, ejection fraction, wall thickness, myocardial volume)
- stress–strain approach leads to transmurally more homogeneous fibre stretch than the pure stress approach and can capture the Frank-Starling

mechanism

3.3 Conclusion to C1

Combining the results of mechanical testing with experimental data available in the literature (shear tests on healthy myocardium and equibiaxial tests on infarcted tissue), it is shown that the myocardial tissue in rats has orthotropic properties. Further, the stiffness positively correlates with the amount of fibrosis, identified via histological staining of the tissue samples. Based on these findings, a mixture material model, using the amount of fibrosis as a weighting factor, is proposed (objective C1-1). Fitting this model to the experimental data, passive mechanical parameters for healthy and infarcted rat myocardium (objective C1-2) were identified. Subsequently, it is demonstrated that the choice of the passive mechanical parameters significantly influences the whole cardiac cycle. In particular, if an active contraction follows after a passive filling phase, the cardiac performance, measured by the ejection fraction of the left ventricle, significantly varies for different passive material parameters. Further, the electromechanically coupled computational model for the whole cardiac cycle was calibrated with experimental data for rats, partly from the measurements performed by the collaboration partners (via MRI and echocardiography) and partly from the literature (objective C1-2). Two different approaches to model the active cardiac contraction, the pure stress and the stress-strain approaches, were applied and discussed (objective C1-1). In conclusion, the second approach should be preferred if the focus is put on the physiologically motivated stretch-dependence of the active fibre stress development, i.e. Frank-Starling mechanisms (objective C1-3).

4 Support pressure acting on the left ventricle (C2)

4.1 Introduction to C2

To date, mostly, CaADs with extracardiac blood acceleration, bypassing the heart, are in use. However, direct blood contact is disadvantageous in the long-term use of these systems due to the thromboembolic and hemorrhagic hazards [Lima18, Han19]. Alternatively, the insufficient heart muscle can be supported directly via a DCCD. The second research contribution therefore investigates the influence of an unspecific DCCD on the cardiac performance of a weakened rat LV. It is based on the model and parameters obtained in [Mart21b]. Exemplarily, a model for restrictive cardiomyopathy is utilised where the amount of fibrosis allows to consider different disease stages. The DCCD is represented by a support pressure acting on the epicardial surface of the LV without assuming a specific model for it. Experimental approaches allow to support it either only in the systole, only in the diastole or in both phases, systole and diastole, via a positive and negative support pressure acting on the outer wall of the ventricle as illustrated in Figure 4.1. In order to test the influence of such support systems on the cardiac performance, the necessary support pressure in an established cardiac simulation model from C1 is examined. Since the ratio of myocardial fibrosis to the intact myocardium reflects the degree of heart failure, the necessary support pressure up to the restoration of normal cardiac output in rat LV with different amounts of fibrosis is optimised. In [Mart22b], for the first time, the influence of epicardial support in systole and diastole is examined and compared with the influence of a support in systole or diastole alone. The results demonstrate a clear benefit of combined support in systole and diastole.

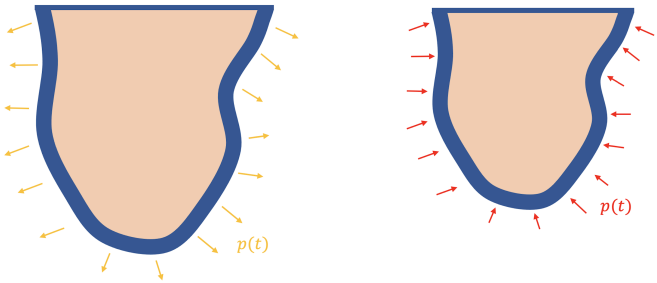

(a) diastole (b) systole

Figure 4.1: Support pressure $p(t)$ acting on the epicardial wall of the left ventricle (negative value during the diastole (a), positive value during the systole (b)).

4.2 Summary of publication within C2

4.2.1 Support Pressure Acting on the Epicardial Surface of a Rat Left Ventricle – A Computational Study

[Mart22a] D. Martonová, D. Holz, D. Brackenhammer, M. Weyand, S. Leyendecker, and M. Alkassar. Support Pressure Acting on the Epicardial Surface of a Rat Left Ventricle – A Computational Study. *Frontiers in Cardiovascular Medicine*, 9:850274, 2022.

Abstract *The present computational study investigates the effects of an epicardial support pressure mimicking a heart support system without direct blood contact. We chose restrictive cardiomyopathy as a model for a diseased heart. By changing one parameter representing the amount of fibrosis, this model allows us to investigate the impairment in a diseased left ventricle, both during diastole and systole. The aim of the study is to determine the temporal course and value of the support pressure that leads to a normalization of the cardiac parameters in diseased hearts. These are quantified via the end-diastolic pressure, end-diastolic volume, end-systolic volume and ejection fraction. First, the amount of fibrosis is increased to model diseased hearts at different stages. Second, we determine the difference in the left ventricular pressure between a healthy and diseased heart during a cardiac cycle and apply the epicardial support as the respective pressure difference. Third, an epicardial support*

pressure is applied in form of a piecewise constant step function. The support is provided only during diastole, only during systole, or during both phases. Finally, the support pressure is adjusted to reach the corresponding parameters in a healthy rat. Parameter normalization is not possible to achieve with solely diastolic or solely systolic support; for the modeled case with 50% fibrosis, the ejection fraction can be increased by 5% with purely diastolic support and 14% with purely systolic support. However, the ejection fraction reaches the value of the modeled healthy left ventricle (65.6%) using a combination of the diastolic and systolic support. The end-diastolic pressure of 13.5 mmHg cannot be decreased with purely systolic support. However, the end-diastolic pressure reaches the value of the modeled healthy left ventricle (7.5 mmHg) with diastolic support as well as with the combination of the diastolic and systolic support. The resulting negative diastolic support pressure is -4.5 mmHg, and the positive systolic support pressure is 90 mmHg. We thereby conclude that ventricular support during both diastole and systole is beneficial for normalizing the left ventricular ejection fraction as well as the end-diastolic pressure, and thus it is a potentially interesting therapy for cardiac insufficiency.

Author contribution

- writing - original draft
- deriving the equations
- modelling and simulation
- post-processing and visualisation of the results

Highlights

- computational model for restrictive cardiomyopathy
- ventricular support during both diastole and systole for normalising the left ventricular EF and EDP
- support pressure as potentially interesting therapy for cardiac insufficiency

4.3 Conclusion to C2

Through modifying the amount of fibrosis, the proposed material law in C1 [Mart21b, Mart21a] was used to model a LV with restrictive cardiomyopathy at different fibrosis stages (objective C2-1). It is investigated how much support

pressure is needed to normalise the EF (positive support pressure during systole) and to lower the EDP (negative support pressure in diastole) and concluded that ventricular support during both, diastole and systole, is beneficial for normalising the left ventricular EF and the EDP (C2-2). In particular, for the amount of fibrosis of 30% and 50%, the support pressure ranges from -0.5kPa to -0.6kPa during the diastole and from 10kPa to 12kPa during the systole (objective C2-3). This early research ansatz has, however, several limitations which are listed at the end of the Section 4 in [Mart22a]. To name an example, only one parameter, the amount of fibrosis, is changed to model a diseased heart. However, in reality, various other pathological conditions like alterations in the heart geometry or in the heart conduction system occur during the remodelling process. Nevertheless, the model opens possibilities for future model development of DCCMs. For example, employing mechano-active materials, such as biocompatible dielectric elastomer actuators [Ponn16] could be an option. They are able to compress and expand in response to a voltage. Hence, their relatively significant (more than 40%) expandability would be advantageous for producing the support pressure required during the diastole [Alka21].

5 S-FEMs towards active cardiac mechanics (C3)

5.1 Introduction to C3

The third research contribution is focused on the numerical solution of the balance equation given in (2.12). As introduced in Chapter 2, besides the classical FEM, various S-FEMs are often used in biomechanical simulations due to their softening effect and relatively low computational cost. Within C3, different S-FEMs, particularly NS-FEM, FS-FEM and FS/NS-FEM, are extended for the simulation of an active cardiac contraction. Firstly, NS-FEM is tested in 2D [Mart21c]. Secondly, NS-FEM, FS-FEM and selective FS/NS-FEM are utilised in an active contraction in a 3D benchmark geometry, i.e. a cube with an assigned fibre direction [Mart23a]. Finally, these methods are applied to a realistic geometry of the rat LV obtained from MRI (not published yet).

5.1.1 Implementation

All S-FEMs were originally implemented into in-house codes by Liu and co-workers. Subsequently, FS-FEM and ES-FEM have been implemented into *code_aster* [Elec89] and Julia [Beza17] by [Nix12, Duon14, Huo21] in a SD-based formulation, and very recently in the element-based formulation [Colo22]. To make the S-FEMs available for a broader engineering community, some S-FEMs were included into the widely used commercial finite element software Abaqus as UELs, namely CS-FEM [Cui18, Kumb20, Bhow18, Guan21] and NS-FEM in 2D for passive [Kshr19] and active mechanics [Mart21c]. We refer to Table 5.1 for an overview of available implementations. In C3, the governing equation (2.12) is solved with Abaqus. Because its element library does not include smoothed finite elements (UELs neither for NS-FEM nor for FS-FEM in 3D are freely available), a UEL providing the stiffness matrix and the residual vector for each SD is developed. This requires a pre-processing step that includes an automatic mesh generation (e.g. with Abaqus). Based on the created tetrahedral mesh, a MATLAB script provides the generation of n_{sd} SDs Ω_k in 3D. In particular, a generation of n_{sd} user elements U_k is

performed such that $\Omega_k \subsetneq U_k$ holds for each k and such that each U_k consists of all nodes of the n_k^e adjacent tetrahedral elements to the face or node k for FS-FEM and NS-FEM, respectively, see Figures 2.3 and 5.1. Note that the U_k's build an overlapping set whereas the Ω_k's build a non-overlapping set. The smoothed deformation gradient $\bar{\mathbf{F}}$ is computed for each SD according to (2.34). To define the material properties, a user subroutine UMAT as a function of the smoothed deformation gradient $\bar{\mathbf{F}}$ is called within the subroutine UEL. It returns the smoothed stress $\bar{\sigma}$ and the smoothed tangent of the constitutive model $\frac{\Delta\bar{\sigma}}{\Delta\bar{\epsilon}}$ such that $\Delta\bar{\sigma}$ and $\Delta\bar{\epsilon}$ are the smoothed stress and strain increments, respectively. The user element stiffness matrix and the residual vector are assembled analogously to the FEM, but integration is performed over the SD $\Omega_k \subsetneq U_k$ rather than over whole user elements as in FEM, see Figure 5.1 for the workflow.

Table 5.1: S-FEMs implementations in different softwares.

software	method	dimension	literature
in-house	CS-FEM	2D,3D	[Liu07]
in-house	NS-FEM	2D,3D	[Liu09a]
in-house	ES-FEM	2D,3D	[Liu09b]
in-house	FS-FEM	2D,3D	[NT09]
in-house	FS/NS-FEM	3D	[Jian14]
code_aster	ES-FEM	2D	[Nix12],[Colo22]
code_aster	FS-FEM	3D	[Duon14], [Colo22]
Julia	FS-FEM	3D	[Huo21]
Abaqus (UEL)	CS-FEM	2D,3D	[Cui18, Kumb20, Bhow18, Guan21]
Abaqus (UEL)	NS-FEM	2D	[Kshr19, Mart21c]
Abaqus (UEL)	NS-FEM	3D	[Mart23a]
Abaqus (UEL)	FS-FEM	3D	[Mart23a]
Abaqus (UEL)	FS/NS-FEM	3D	[Mart23a]

The implementation of the above-mentioned S-FEMs in Abaqus with the material definition and parameters from [Jian14] is verified with their published results in a simulation of a cantilever beam bending (10m x 1m x 1m, applied force $F = 0.5$N) as shown in Figure 5.2. The relative differences in the deflection of the point P in the centre of the free surface are less than 3%, see Table 5.2. This slight deviation may be caused by the fact that not exactly the same tetrahedral mesh could be reconstructed.

Further, to test the large deformation capabilities of the different methods, a torsion test is performed on a cube. Linear FEM, quadratic FEM and the above S-FEMs are compared. It is confirmed that for large deformations, S-FEMs perform softer than linear FEM [Jian14] and are close to the results obtained by quadratic FEM, even though linear shape functions are used. The

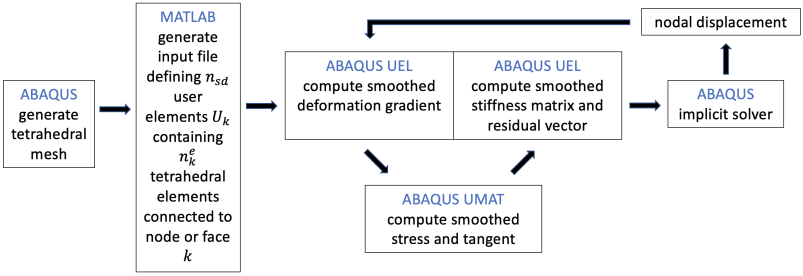

Figure 5.1: Workflow schematically displaying the major steps in the implementation of S-FEMs in Abaqus.

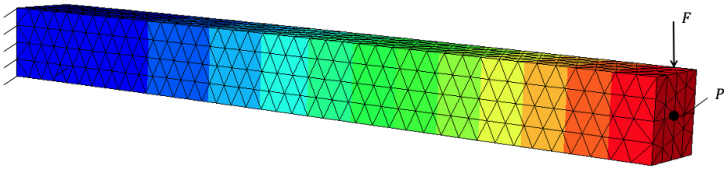

Figure 5.2: Exemplary result (FS/NS-FEM, 1010 nodes) for a beam bending problem.

Table 5.2: Results for deflection of point $\boldsymbol{P}$ computed by different methods. Comparison to literature data.

	implementation in Abaqus		[Jian14]	
method	no. of nodes	deflection (cm)	no. of nodes	deflection (cm)
FEM-H8	1025	8.291	1025	8.291
FEM-C3D10	6470	8.331	6398	8.379
FEM-C3D4	1010	6.642	1006	5.914
NS/FEM	1010	9.326	1006	9.258
FS/NS-FEM	1010	7.827	1006	7.627

simulation results for a torque $M_t = 5000$Nmm applied on an upper square of a cube ($a = 10$mm) with the NH material are displayed in Figure 5.3.

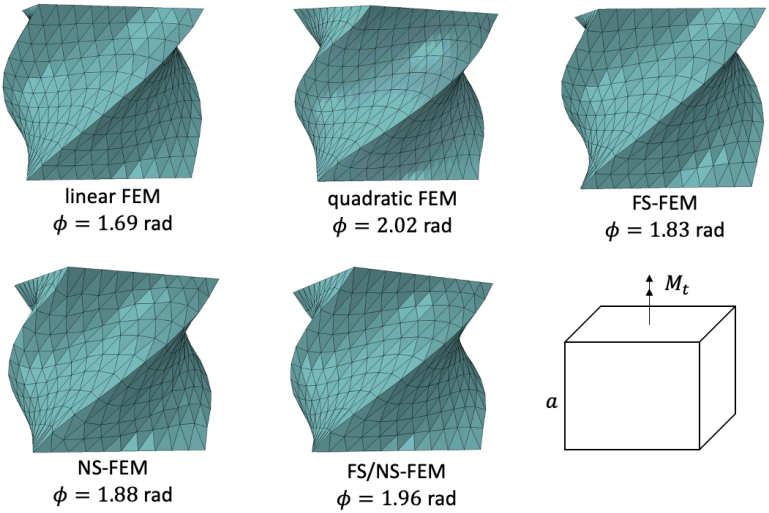

Figure 5.3: Torsion of a cube computed with different numerical methods. The magnitude of the applied torque M_t is 5000Nmm.

5.1.2 Active contraction – numerical examples

Previous examples serve to verify the S-FEMs' implementation and to highlight their already known properties. However, the objective of this work (objective C3-1) is to extend S-FEMs for an active cardiac contraction. This is done through a series of numerical examples, partially published in [Mart21c] and [Mart23a].

2D transversal cut through LV In the numerical example in [Mart21c], an active contraction in the circumferentially aligned fibre direction is induced. By modulating the value of the active tension in (2.14), both healthy and infarcted cases, are simulated. The results computed by FEM and NS-FEM, using different discretisations are compared, see Figure 3 in [Mart21c]. It is shown that using NS-FEM, the volumetric locking phenomenon is not present and even a coarse discretisation (150 degrees of freedom (DOF)) yields almost the same solution as FEM on a much finer mesh (1554 DOF). Based on this initial 2D example, we conclude that S-FEMs are a promising alternative in the modelling of active cardiac mechanics, respectively electromechanics.

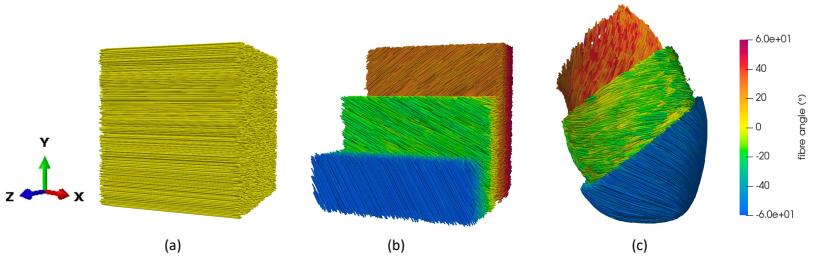

Figure 5.4: Schematic representation of the geometries and fibre orientations considered in the numerical examples. (a) Globally aligned fibre orientation on a cube, (b) fibre orientation from -60° to $+60^\circ$ on a cube, (b) fibre orientation from -60° on the epicardium to $+60^\circ$ on the endocardium of a rat LV, respectively.

3D cube contracting in fibre direction Subsequently, in [Mart23a], the S-FEM approach is extended for 3D geometries using various S-FEMs, namely NS-FEM, FS-FEM, FS/NS-FEM vol (NS-FEM for the volumetric part and active part and FS-FEM for the isochoric part), FS/NS-FEM iso (NS-FEM for the volumetric part and FS-FEM for the isochoric and active part). Table 5.3 summarises the numerical methods and indicates which part of the constitutive model is computed on which domain. The results produced by these S-FEMs are compared with the results obtained by linear FEM discretised with four-node tetrahedral elements (C3D4) and quadratic FEM discretised with ten-node tetrahedral elements (C3D10).

Two simulation scenarios are considered in [Mart23a], a cube with globally aligned fibres, see Figure 5.4(a), and a cube with rotating fibres from -60° to $+60^\circ$ as shown in Figure 5.4(b), mimicking the fibre structure in a rat LV [Miln19, Chen05]. The active contraction is induced in the fibre direction and the tissue is modelled with HO material [Holz09].

3D rat LV contracting in fibre direction To proceed further towards a more realistic cardiac simulation using S-FEMs, a LV derived from the MRI of a rat heart, see Figure 5.4(c), is used as the geometry. Transmurally rotating fibre orientation, from -60° on the epicardium to $+60^\circ$ on the endocardium [Miln19, Chen05], and HO material according [Holz09] are utilised for the

Table 5.3: Summary of numerical methods used in simulations. For each numerical method listed in the first column, the table identifies on which finite element or SD, the passive isochoric Ψ_{iso}, passive volumetric Ψ_{vol} and active $\mathbf{S}_{act}$ parts of the constitutive law are computed.

method \ discretisation	C3D10	C3D4	node-based SD	face-based SD
quadratic FEM	Ψ_{iso} Ψ_{vol} $\mathbf{S}_{act}$			
linear FEM		Ψ_{iso} Ψ_{vol} $\mathbf{S}_{act}$		
NS-FEM			Ψ_{iso} Ψ_{vol} $\mathbf{S}_{act}$	
FS-FEM				Ψ_{iso} Ψ_{vol} $\mathbf{S}_{act}$
FS/NS-FEM vol			Ψ_{vol} $\mathbf{S}_{act}$	Ψ_{iso}
FS/NS-FEM iso			Ψ_{vol}	Ψ_{iso} $\mathbf{S}_{act}$

simulation. The endocardial pressure is increased from zero to 5mmHg in the first simulation step (1ms) to reach the end-diastolic state. For the whole remaining simulation time (180ms), representing a cardiac cycle of the rat heart, see Table 2.1 for the typical heart frequencies, the endocardial pressure is kept constant and an active contraction is included according to (2.14). The base of the LV is fixed for the whole simulation time. End-diastolic volume (EDV), end-systolic volume (ESV) and the resulting EF are compared for the different numerical methods. In Table 5.4 and in Figures 5.6 and 5.5, the simulation results for the realistic LV geometry with the orthotropic HO material are shown. Here, the above findings on the benchmark geometry are confirmed. In particular, it is shown that, due to the volumetric locking, linear FEM underestimates the deformation significantly (EF = 12% with linear FEM versus the reference EF = 28%). While FS-FEM still overestimates and NS-FEM, FS/NS-FEM iso underestimate the stiffness, the selective NS/FS-FEM vol is very close to the reference solution (even if linear shape functions are used in the analysis). It is worth noting that the computational time is higher than for the linear FEM, but it is two orders of magnitude lower than for the reference solution computed on a very fine mesh ($\approx 10^6$ C3D4). NS-FEM produces similar results as FS/NS-FEM iso, but it is computationally more expensive. This is due to the requirement to use very small load increments to ensure the

convergence of Newton's method when solving the balance equations in each load step. The reason may lie in the temporal instability of NS-FEM shown previously [Liu09a, Zhan10, Liu16]. However, FS-FEM has a stabilising effect [NT09] and therefore, in this numerical example, both FS/NS-FEMs perform more efficiently than NS-FEM alone. For quadratic FEM, the simulation breaks down before the end-systolic state is reached. It demonstrates that although quadratic FEM produces very accurate solutions and volumetric locking is not present, for large deformation, it may lead to numerical instabilities due to possibly negative Jacobian determinants [Jian14].

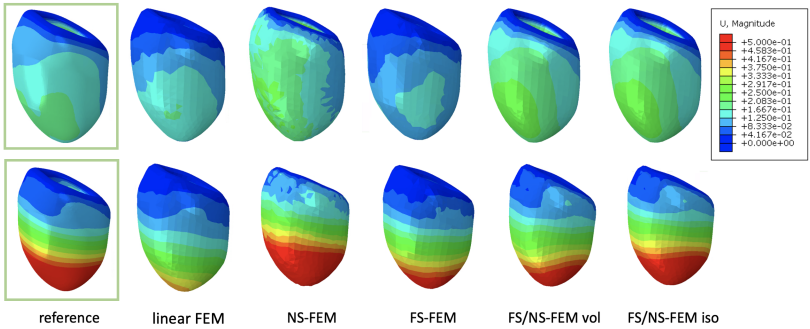

Figure 5.5: Snapshots showing the displacement field for the rat LV at end-diastolic (first line) and end-systolic (second line) states.

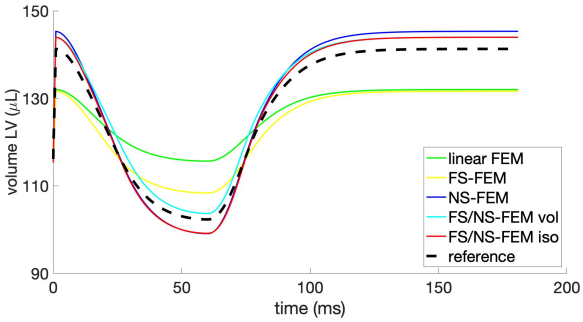

Figure 5.6: Temporal evolution of the left-ventricular volume with HO material. The reference solution is computed for a very fine mesh ($\approx 10^6$ C3D4 elements).

Table 5.4: Results for simulation of rat cardiac cycle using different numerical methods. The computational time is denoted by t.

method	EDV(μL)	ESV (μL)	EF (%)	t (s)
quadratic FEM	142.9	-	-	-
linear FEM	132.0	115.7	12.3	$5.9\cdot 10^2$
NS-FEM	145.3	92.8	36.1	$1.8\cdot 10^4$
FS-FEM	131.6	108.4	17.6	$2.5\cdot 10^3$
FS/NS-FEM vol	144.0	103.7	28.0	$4.7\cdot 10^3$
FS/NS-FEM iso	144.0	99.2	31.1	$5.1\cdot 10^3$
reference	141.3	102.3	27.6	$2.8\cdot 10^5$

5.2 Summary of publications within C3

5.2.1 Towards the simulation of active cardiac mechanics using a smoothed finite element method

[Mart21c] D. Martonová, D. Holz, M. T. Duong, and S. Leyendecker. Towards the simulation of active cardiac mechanics using a smoothed finite element method. *Journal of Biomechanics*, 115:110153, 2021.

Abstract *In the last decades, various computational models have been developed to simulate cardiac electromechanics. The most common numerical tool is the finite element method (FEM). However, this method crucially depends on the mesh quality. For complex geometries such as cardiac structures, it is convenient to use tetrahedral discretisations which can be generated automatically. On the other hand, such automatic meshing with tetrahedrons together with large deformations often lead to elements distortion and volumetric locking. To overcome these difficulties, different smoothed finite element methods (S-FEMs) have been proposed in the recent years. They are known to be volumetric locking free, less sensitive to mesh distortion and so far have been used e.g. in simulation of passive cardiac mechanics. In this work, we extend for the first time node-based S-FEM (NS-FEM) towards active cardiac mechanics. Firstly, the sensitivity to mesh distortion is tested and compared to that of FEM. Secondly, an active contraction in circumferentially aligned fibre direction is modelled in the healthy and the infarcted case. We show, that the proposed method is more robust with respect to mesh distortion and computationally more efficient than standard FEM. Being furthermore free of volumetric locking problems makes S-FEM a promising alternative in modelling of active cardiac mechanics, respectively electromechanics.*

Author contribution The first author contributed in the following tasks:

- conceptualisation
- methodology
- software
- formal analysis
- writing - original draft
- visualisation

Highlights

- extension of NS-FEM in 2D for active cardiac mechanics
- volumetric locking during cardiac contraction is reduced
- implementation of different NS-FEM as user elements in Abaqus

5.2.2 Smoothed finite element methods in simulation of active contraction of myocardial tissue samples

[Mart23a] D. Martonová, D. Holz, M. T. Duong, and S. Leyendecker. Smoothed finite element methods in simulation of active contraction of myocardial tissue samples. *Journal of Biomechanics*, 157:111691, 2023.

Abstract *In modelling and simulation of cardiac mechanics, tetrahedral meshes are often used due to the easy availability of efficient meshing algorithms. This is beneficial in particular when complex geometries such as cardiac structures are considered. The gold standard in simulating the cardiac cycle is to solve the mechanical balance equations with the finite element method (FEM). However, using linear shape functions in the FEM in combination with nearly-incompressible material models is known to produce overly stiff approximations, whereas higher order elements are computationally more expensive. To overcome these problems, smoothed finite element methods (S-FEMs) have been proposed by Liu and co-workers. So far, S-FEMs in 3D have been utilised only in simulations of passive mechanics. In the present work, different S-FEMs are for the first time used for simulation of an active cardiac contraction on three-dimensional myocardial tissue samples. Further, node-based S-FEM (NS-FEM), face-based S-FEM (FS-FEM) and selective FS/NS-FEM are for the first time implemented as user subroutine in the commercial software Abaqus. Our results confirm that all S-FEMs perform softer than linear FEM and volumetric*

locking is reduced. The FS/NS-FEM produces solutions with the relative error in maximum displacement and rotation being less than 5% with respect to the reference solution obtained by the quadratic FEM for all considered mesh sizes, although linear shape functions are used. We therefore conclude that in particular FS/NS-FEM is an efficient and accurate numerical method in the simulation of an active cardiac muscle contraction.

Author contribution The first author contributed in the following tasks:

- conceptualisation
- methodology
- software
- formal analysis
- writing - original draft
- visualisation

Highlights

- extension of S-FEMs for active cardiac mechanics using 3D contractile orthotropic material model
- volumetric locking during cardiac contraction is reduced
- implementation of different S-FEMs as user elements in Abaqus

5.3 Conclusion to C3

In two journal publications, different S-FEMs were extended for the simulation of active cardiac mechanics, both in 2D and 3D. Finally, S-FEMs were used for the simulation of a cardiac cycle of a rat heart (objective C3-1). All S-FEMs were implemented as UELs within the commercial software Abaqus and therefore made available to a broader engineering community (objective C3-2). By comparing the performance of all considered S-FEMs, linear FEM and quadratic FEM among each other, the selective FS/NS-FEMs were identified as the most suitable method for the simulation of an active cardiac contraction using a complex geometry with designed fibre orientation. Considering the realistic FS/NS-FEM vol, where the active part is computed on the node-based SD, produced the most accurate results compared with the reference solution (objective C3-3).

6 Two-state ligand-receptor binding model (C4)

6.1 Introduction to C4

The fourth research contribution covers the work during the doctoral researcher's stay at Queensland University of Technology in Brisbane, Australia (May to August 2022). As the principal expertise of the hosting university lies in bone (re)modelling, the developed ligand-receptor binding model is exemplarily applied to the parathyroid hormone (PTH), mainly influencing bone metabolism. However, the model can be applied to any other GPCR. The work investigates the effects of PTH glandular secretion patterns on bone cellular activity. PTH binds on GPCR referred to as PTH1R. In [Mart23b], a widely accepted [Leff95] two-state ligand-receptor binding model is utilised, see Figure 6.1 for the schematic of the kinetics. It was first proposed by Segel et al. in the study of exact sensory adaptation [Sege86]. It has been shown that PTH1R undergoes multiple conformational changes and becomes activated as it binds to its ligand [Parf02, Gard01]. We refer to the Introduction in [Mart23b] and Section 2.3.2 for more details regarding the two-state receptor model. Solving the following system of ordinary differential equations

Let r_a/r_i and c_a/c_i be active/inactive receptor and active/inactive ligand-receptor-complex concentrations, respectively, being normalised with respect to their sum. Then, solving the following system of ordinal differential equations

$$\begin{bmatrix} \dot{r}_a \\ \dot{c}_a \\ \dot{c}_i \\ \dot{r}_i \end{bmatrix} = \begin{bmatrix} -k_1 - k_r L & k_{-r} & 0 & k_{-1} \\ k_r L & -k_2 - k_{-r} & k_{-2} & 0 \\ 0 & k_2 & -k_{-2} - k_{-d} & k_d L \\ k_1 & 0 & k_{-d} & -k_{-1} - k_d L \end{bmatrix} \begin{bmatrix} r_a \\ c_a \\ c_i \\ r_i \end{bmatrix} \tag{6.1}$$

yields for each ligand concentration L the respective concentrations at the chemical equilibrium. As proposed in [Sege86], via linear combination of these concentrations, cellular activity α and finally a scalar value referred to as cellular responsiveness α_R are computed, see Section 2 in [Mart23b] and [Sege86] for more details. Various PTH secretion patterns corresponding to diseases with altered PTH secretion such as idiopathic osteoporosis, postmenopausal osteoporosis, glucocorticoid-induced osteoporosis, hyperparathyroidism, hypocalcemia

and hypercalcemia are modelled. Further, several constrained optimisation problems are solved in order to either maximise α_R or regain its reference value, see Section 3 in [Mart23b]. On the one hand, an optimal pulsatile pattern for the baseline PTH secretion is derived for the above-named diseases, see (20) and (21) in [Mart23b]. On the other hand, an optimal external dose of PTH (via subcutaneous injection) is determined by optimisation of the objective function given in (22) in [Mart23b].

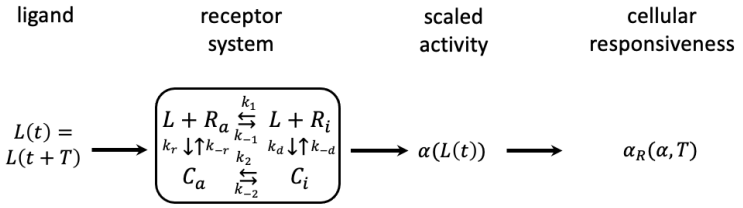

Figure 6.1: Schematic representation of the two-state receptor model representing the binding of a ligand to its receptor. Reproduced and edited based on [Li89].

6.2 Summary of publications within C4

6.2.1 Effects of PTH glandular and external dosing patterns on bone cell activity using a two-state receptor model – Implications for bone disease progression and treatment

[Mart23b] D. Martonová, M. Lavaill, M. R. Forwood, A. Robling, D. M. L. Cooper, S. Leyendecker and P. Pivonka. Effects of PTH glandular and external dosing patterns on bone cell activity using a two-state receptor model–Implications for bone disease progression and treatment. *PLOS ONE*, 2023.

Abstract *Temporal aspects of ligand specificity have been shown to play a significant role in the case of pulsatile hormone secretion, as exemplified by parathyroid hormone (PTH) binding to its receptor (PTH1R), a G-protein-coupled receptor expressed on surfaces of osteoblasts and osteocytes. The latter binding reaction regulates intracellular signalling and subsequently modulates*

skeletal homeostasis via bone remodelling. PTH glandular secretion patterns dictate bone cellular activity. In healthy humans, 70% of PTH is secreted in a tonic fashion, whereas 30% is secreted in low-amplitude and high-frequency bursts occurring every 10– 20 min, superimposed on the tonic secretion. Changes in the PTH secretion patterns have been associated with various bone diseases. In this paper, we analyse PTH glandular secretion patterns for healthy and pathological states and their link to bone cellular responsiveness (α_R). We utilise a two-state receptor ligand binding model of PTH to PTH1R together with a cellular activity function which is able to distinguish various aspects of the stimulation signal including peak dose, time of ligand exposure, and exposure period. Formulating and solving several constrained optimisation problems, we investigate the potential of pharmacological manipulation of the diseased glandular secretion and via clinical approved external PTH injections to restore healthy bone cellular responsiveness. Based on the mean experimentally reported data, our simulation results indicate cellular responsiveness in healthy subjects is sensitive to the tonic baseline stimulus and it is 28% of the computed maximum responsiveness. Simulation results for pathological cases of glucocorticoid- induced osteoporosis, hyperparathyroidism, initial and steady state hypocalcemia clamp tests indicate α_R values significantly larger than the healthy baseline (1.7, 2.2, 4.9 and 1.9-times, respectively). Manipulation of the pulsatile glandular secretion pattern, while keeping the mean PTH concentration constant, allowed restoration of healthy baseline values from these catabolic bone diseases. Conversely, PTH glandular diseases that led to maximum bone cellular responsiveness below the healthy baseline value can't be restored to baseline via glandular manipulation. However, external PTH injections allowed restoration of these latter cases.

Author contribution The first author contributed in the following tasks:

- conceptualisation
- methodology
- software
- writing - original draft
- visualisation

Highlights

- two-state receptor model for PTH and PTH1R for healthy and various diseased cases

- optimisation of the pulsatile glandular secretion pattern to restore healthy baseline values of bone cellular responsiveness
- optimisation of external PTH injection to restore healthy baseline values of bone cellular responsiveness

6.3 Conclusion to C4

In C4, a novel two-state receptor binding model was developed and numerically solved in order to investigate the differences between healthy and pathological secretion patterns and their effects on bone cellular responsiveness. The potential of (pharmacological) manipulation of pathological glandular secretion patterns back to its normal baseline bone cellular responsiveness was explored. Further, the effects of (external) once-daily PTH injections on bone cellular responsiveness were investigated (objective C4-2). For this purpose, a variety of constrained optimisation problems were solved (objective C4-3). Based on the numerical simulations, it is found that bone cellular responsiveness in healthy subjects is sensitive to the tonic baseline stimulus and greatly varies between healthy and pathological cases. Most catabolic bone diseases with the cellular responsiveness being below the reference value could be restored back to this value by manipulating the pulsatile component of glandular secretion of the pathological gland, see Table 3 in [Mart23b]. Also, external once daily PTH injections could restore the pathological cases back to normal if an optimal dose is given to the patient, see Table 4 in [Mart23b].

7 Fibre orientation in myocardium (co-authorship)

The last research part, to which the doctoral researcher contributed as a co-author, covers the work regarding the interpolation of the fibre orientation in cardiac structures [Holz22, Holz23]. In [Holz22], a finite element-based discontinuous Galerkin approach is developed to accurately determine the transmural depth on an unstructured tetrahedral mesh. This eventually allows an assignment of the fibre, sheet and sheet-normal orientations in cardiac structures. Hence, a novel LDRBM is proposed. In the subsequent work [Holz23], this method and two previously established LDRBMs [Baye12, Wong14] are utilised in the simulation of a cardiac cycle. It is investigated how these approaches influence the local myofibre orientation, the local (active fibre stress, fibre strain) and global (EF, peak pressure, apex shortening, myocardial volume reduction, fractional wall thickening) characteristics in a human heart. For more details, the reader is referred to the original publications as they are not the core part of the doctoral thesis.

7.1 Summary of publications

7.1.1 A Transmural Path Model Improves the Definition of the Orthotropic Tissue Structure in Heart Simulations

[Holz22] D. Holz, M. T. Duong, D. Martonová, M. Alkassar, and S. Leyendecker. A Transmural Path Model Improves the Definition of the Orthotropic Tissue Structure in Heart Simulations. *Journal of Biomechanical Engineering*, 144(3):031002, 2022.

Abstract *In the past decades, the structure of the heart, human as well as other species, has been explored in a detailed way, e.g., via histological studies or diffusion tensor magnetic resonance imaging. Nevertheless, the assignment of the characteristic orthotropic structure in a patient-specific finite element model remains a challenging task. Various types of rule-based models, which define the local fiber and sheet orientation depending on the transmural depth,*

have been developed. However, the correct assessment of the transmural depth is not trivial. Its accuracy has a substantial influence on the overall mechanical and electrical properties in rule-based models. The main purpose of this study is the development of a finite element-based approach to accurately determine the transmural depth on a general unstructured grid. Instead of directly using the solution of the Laplace problem as the transmural depth, we make use of a well-established model for the assessment of the transmural thickness. It is based on two hyperbolic first-order partial differential equations for the definition of a transmural path, whereby the transmural thickness is defined as the arc length of this path. Subsequently, the transmural depth is determined based on the position on the transmural path. Originally, the partial differential equations were solved via finite differences on structured grids. In order to circumvent the need of two grids and mapping between the structured (to determine the transmural depth) and unstructured (electromechanical heart simulation) grids, we solve the equations directly on the same unstructured tetrahedral mesh. We propose a finite-element based discontinuous Galerkin approach. Based on the accurate transmural depth, we assign the local material orientation of the orthotropic tissue structure in a usual fashion. We show that this approach leads to a more accurate definition of the transmural depth. Furthermore, for the left ventricle, we propose functions for the transmural fiber and sheet orientation by fitting them to literature-based diffusion tensor magnetic resonance imaging data. The proposed functions provide a distinct improvement compared to existing rules from the literature.

Author contribution The third author contributed in the following tasks:

- writing review and editing

Highlights

- finite-element based discontinuous Galerkin approach to compute transmural depth in a left ventricle
- assignment of the local material orientation of the orthotropic tissue structure
- improved definition of the orthotropic tissue structure in finite element models

7.1.2 Transmural fibre orientations based on Laplace-Dirichlet-Rule-Based-Methods and their influence on human heart simulations

[Holz23] D. Holz, D. Martonová, E. Schaller, M. T. Duong, M. Alkassar, M. Weyand and S. Leyendecker. Transmural fibre orientations based on Laplace-Dirichlet-Rule-Based-Methods and their influence on human heart simulations. *Journal of Biomechanics*, p. 111643, 2023.

Abstract *Numerous approaches to compute the orthotropic tissue structure in computational heart models have been developed in the past decades. In this study, we investigate to what extent the different approaches influence the local orthotropic tissue structure and thus the electromechanical behaviour of the subsequent cardiac simulation. It is well known that the orthotropic tissue structure decisively influences the mechanical and electrical properties. In detail, we are utilising three Laplace-Dirichlet-Rule-Based-Methods and compare: (i) the local myofibre orientation; (ii) important global characteristics (ejection fraction, peak pressure, apex shortening, myocardial volume reduction, fractional wall thickening); (iii) local characteristics (active fibre stress, fibre strain). We observe that the orthotropic tissue structures for the three LDRBMs show significant differences in the local myofibre orientation. The global characteristics myocardial volume reduction and peak pressure are rather insensitive to a change in local myofibre orientation, while the ejection fraction is moderately influenced by the different LDRBMs. Moreover, the apical shortening and fractional wall thickening exhibit a sensitive behaviour to a change in the local myofibre orientation. The highest sensitivity can be observed for the local characteristics.*

Author contribution The second author contributed in the following tasks:

- writing review and editing
- software
- methodology

Highlights

- comparison of three LDRBMs in simulation of the human heart cycle
- significant differences in local myofibre orientation when different LDRBMs are utilised
- local characteristics (active fibre stress, fibre strain) show the highest sensitivity with respect to the choice of LDRBM

8 Summary and prospect

Around thirty years ago, the first and simplest mathematical models of the heart using simplified cylindrical geometries were developed [Gucc91, Rodr94]. To date, numerous more advanced models are in use, ranging from generic geometry models to personalised full heart models including different specific ingredients such as fibre-reinforced microstructure, Purkinje fibre network, fluid-structure interaction, etc. However, despite this rapid development in the last three decades, cardiac modelling and simulations are still the subject of intensive research. In this doctoral thesis, the focus was put on the development of a novel computational model of a rat heart which can eventually help in further development of CaADs, particularly DCCDs.

The following achievements summarise the research contributions obtained by the present doctoral thesis:

- Based on the experimental data and data available in the literature, passive material properties of healthy and infarcted rat myocardium were characterised. A model for the modified Holzapfel-Ogden strain energy function was proposed. The infarcted tissue is modelled as a mixture of the intact orthotropic myocardium and transversely isotropic collagenous scar formation. The amount of fibrosis serves as a weighting factor. The fitting results confirm that the proposed model can capture the behaviour of the healthy and infarcted tissue.

- A set of passive material parameters were derived. It was further used for simulations of the rat heart cardiac cycle in a healthy and an infarcted case.

- Based on the measurements via echocardiography, three different generic ellipsoidal 3D models of the rat LVs were constructed and used as input for simulations of the rat cardiac cycle.

- In a fully electromechanically coupled simulation of the rat cardiac cycle including excitation via the PFN and pressure boundary condition via the Windkessel model, two different modelling approaches (pure stress and stress-strain), were compared regarding stress and fibre stretch

distribution in the computational domain, i.e. left ventricle.

- Based on a simple model, depending on the amount of fibrosis, an initial quantitative estimate for the needed support pressure at different stages of left-ventricular fibrosis was computed. In particular, to regain the normal physiological values of ejection fraction and end-diastolic pressure, a negative support pressure during the diastole and a positive support pressure during the systole were identified as optimal pressures.

- Besides the numerical solution with the standard FEM, different S-FEMs are for the first time adapted to simulate an active cardiac contraction. It was shown that all S-FEMs are able to eliminate the volumetric locking phenomenon being present in linear FEM, and based on the performed numerical examples, the FS/NS-FEM vol was identified as the most accurate S-FEM.

- A two-state ligand-receptor binding model of a GPCR and its ligand were utilised and numerically solved for a given ligand concentration. Together with a cellular activity function, it is able to distinguish various aspects of the stimulation signal, including peak dose, time of ligand exposure, and exposure period. Formulating and solving several constrained optimisation problems, the potential of pharmacological manipulation of the diseased glandular secretion and via external ligand administration to restore a reference cellular responsiveness was investigated. Exemplarily, PTH and its receptor PTH1R were considered, however, an application to a different GPCR and its corresponding ligand is straightforward.

The above summarised achievements contribute to develop an innovative more precise and robust computational simulation of the rat heart cycle under healthy and pathological conditions. However, there are still some open points and future challenges of scientific interests which can be investigated.

Firstly, in [Mart22a], a simple computational model determining the needed ventricular support pressure is presented. This ansatz can be further developed under different aspects. On the one hand, instead of exemplarily analysing the restrictive cardiomyopathy, different CVDs can be modelled and one can investigate whether and how an applied support pressure would improve the cardiac function. On the other hand, so far, it is not modelled how the proposed support pressure is generated. One possibility would be to implant a mechano-active membrane around the heart. This can for example be made of dielastic elastomere actuators which are able to expand and thus generate a negative pressure, as well as contract and thus generate a positive pressure on the outer heart wall. The future modelling and simulation challenge includes a

coupling of both, a model for the heart as well as a model for a DCCD in order to obtain a clinically more relevant simulation and eventually to estimate the appropriate parameters for a particular DCCD.

Secondly, in the future, the application of S-FEMs in the simulation of a realistic cardiac cycle should be further investigated on a more complex model including electromechanical coupling [Gökt10], the Windkessel model imitating the haemodynamics of the fluid flow [Mart22b], more realistic fibre architecture [Holz22, Holz23] as well as interaction with other cardiac structures such as atrium and right ventricle.

Thirdly, [Mart23b], the two-state ligand-receptor model is exemplarily utilised for PTH and its receptor PTH1R, belonging to the family of the GPCRs. However, the model can be easily transferred to a GPCR influencing the cardiac physiology and the resulting cardiac cell responsiveness can be input as a parameter for the simulation of the cardiac cycle. One possible example would be the investigation of the hormone adrenaline binding to β-receptors which are predominant GPCR subtypes in mammals. On the one hand, their stimulation during a fight-or-flight scenario is the most effective way to control cardiac output. On the other hand, a prolonged stimulation is crucial for both physiological and pathological cardiac remodelling [Woo12, Wang18]. Further, in analogy to the optimisation of the dose PTH injection in [Mart23b], the dose of commonly used drugs known as β-blockers can be investigated and optimised via such a two-state ligand-receptor model.

References

[AB18] A. Ahmad Bakir, A. Al Abed, M. C. Stevens, N. H. Lovell, and S. Dokos. A Multiphysics Biventricular Cardiac Model: Simulations With a Left-Ventricular Assist Device. *Frontiers in Physiology*, 9, 2018.

[Ahma18] F. Ahmad, R. Prabhu, J. Liao, S. Soe, M. D. Jones, J. Miller, P. Berthelson, D. Enge, K. M. Copeland, S. Shaabeth, et al. Biomechanical properties and microstructure of neonatal porcine ventricles. *Journal of the Mechanical Behavior of Biomedical Materials*, 88:18–28, 2018.

[Alie96] R. R. Aliev and A. V. Panfilov. A simple two-variable model of cardiac excitation. *Chaos, Solitons & Fractals*, 7(3):293–301, 1996.

[Alka21] M. Alkassar. *Circulatory Assistance Device*. European patent No. EP3503938 B1. European Patent Office, 2021.

[Ande04] R. Anderson, R. Razavi, and A. Taylor. Cardiac anatomy revisited. *Journal of Anatomy*, 205(3):159–177, 2004.

[Artr99] J. H. Artrip, G.-H. Yi, H. R. Levin, D. Burkhoff, and J. Wang. Physiological and Hemodynamic Evaluation of Nonuniform Direct Cardiac Compression. *Circulation*, 100(suppl_2):II–236, 1999.

[Bail14] B. Baillargeon, N. Rebelo, D. D. Fox, R. L. Taylor, and E. Kuhl. The Living Heart Project: A robust and integrative simulator for human heart function. *European Journal of Mechanics - A/Solids*, 48:38–47, 2014.

[Bail15] B. Baillargeon, I. Costa, J. R. Leach, L. C. Lee, M. Genet, A. Toutain, J. F. Wenk, M. K. Rausch, N. Rebelo, G. Acevedo-Bolton, et al. Human cardiac function simulator for the optimal design of a novel annuloplasty ring with a sub-valvular element for correction of ischemic mitral regurgitation. *Cardiovascular engineering and technology*, 6(2):105–116, 2015.

[Bath06] K.-J. Bathe. *Finite Element Procedures*. Klaus-Jurgen Bathe, 2006.

[Baye12] J. D. Bayer, R. C. Blake, G. Plank, and N. A. Trayanova. A Novel Rule-Based Algorithm for Assigning Myocardial Fiber Orientation to Computational Heart Models. *Annals of Biomedical Engineering*, 40(10):2243–2254, 2012.

[Bely13] T. Belytschko, W. K. Liu, B. Moran, and K. Elkhodary. *Nonlinear Finite Elements for Continua and Structures*. John Wiley & Sons, 2013.

[Berb15] E. Berberoglu and S. Göktepe. Computational Modeling of Myocardial Infarction. *Procedia IUTAM*, 12:52–61, 2015.

[Beza17] J. Bezanson, A. Edelman, S. Karpinski, and V. B. Shah. Julia: A Fresh Approach to Numerical Computing. *SIAM Review*, 59(1):65–98, 2017.

[Bhow18] S. Bhowmick and G.-R. Liu. Three Dimensional CS-FEM Phase-Field Modeling Technique for Brittle Fracture in Elastic Solids. *Applied Sciences*, 8(12):2488, 2018.

[Boyl19] P. M. Boyle, T. Zghaib, S. Zahid, R. L. Ali, D. Deng, W. H. Franceschi, J. B. Hakim, M. J. Murphy, A. Prakosa, S. L. Zimmerman, et al. Computationally guided personalized targeted ablation of persistent atrial fibrillation. *Nature Biomedical Engineering*, 3(11):870–879, 2019.

[Chen05] J. Chen, W. Liu, H. Zhang, L. Lacy, X. Yang, S.-K. Song, S. A. Wickline, and X. Yu. Regional ventricular wall thickening reflects changes in cardiac fiber and sheet structure during contraction: Quantification with diffusion tensor MRI. *American Journal of Physiology-Heart and Circulatory Physiology*, 289(5):H1898–H1907, 2005.

[Clar63] E. Clarke. Aristotelian concepts of the form and function of the brain. *Bulletin of the History of Medicine*, 37:1–14, 1963.

[Colo22] D. Colombo, S. Drira, R. Frotscher, and M. Staat. An element-based formulation for ES-FEM and FS-FEM models for implementation in standard solid mechanics finite element codes for 2D and 3D static analysis. *International Journal for Numerical Methods in Engineering*, p. nme.7126, 2022.

[Conn00] A. R. Conn, N. I. M. Gould, and P. L. Toint. *Trust Region Methods*. Society for Industrial and Applied Mathematics, 2000.

[Cui18] X. Cui, X. Han, D. Shuyong, and G. Liu. An ABAQUS Implementation of the Cell-based Smoothed Finite Element Method (CS-FEM). *International Journal of Computational Methods*, 17, 2018.

[DO16] B. L. De Oliveira and J. Sundnes. Comparison of tetrahedral and hexahedral meshes for finite element simulation of cardiac electro-mechanics. In *ECCOMAS Congress 2016*, pp. 164–177. Institute of Structural Analysis and Antiseismic Research School of Civil Engineering National Technical University of Athens (NTUA) Greece, Crete Island, Greece, 2016.

[Doko02] S. Dokos, B. H. Smaill, A. A. Young, and I. J. LeGrice. Shear properties of passive ventricular myocardium. *American Journal of Physiology. Heart and Circulatory Physiology*, 283(6):H2650–2659, 2002.

[Duon14] M. T. Duong and M. Staat. A face-based smoothed finite element method for hyperelastic models and tissue growth. *11th World Congress on Computational Mechanics*, 2014.

[Duon15] M. T. Duong, M. Staat, and H. Nguyen-Nhu. Modeling and simulation of a growing mass by the Smoothed Finite Element Method (SFEM). *3rd ECCOMAS Young Investigators Conference*, 2015.

[Duon19] M. T. Duong, D. Holz, M. Alkassar, S. Dittrich, and S. Leyendecker. Interaction of the Mechano-Electrical Feedback With Passive Mechanical Models on a 3D Rat Left Ventricle: A Computational Study. *Frontiers in Physiology*, 10:1041, 2019.

[Elec89] Electricite de France. Finite element code_aster, Analysis of Structures and Thermomechanics for Studies and Research. Open source on www.code-aster.org, 1989.

[Gard01] T. J. Gardella and H. Jüppner. Molecular properties of the PTH/PTHrP receptor. *Trends in endocrinology and metabolism: TEM*, 12(5):210–217, 2001.

[Gökt10] S. Göktepe and E. Kuhl. Electromechanics of the heart: A unified approach to the strongly coupled excitation–contraction problem. *Computational Mechanics*, 45(2-3):227–243, 2010.

[Gökt14] S. Göktepe, A. Menzel, and E. Kuhl. The Generalized Hill Model: A Kinematic Approach Towards Active Muscle Contraction. *Journal of the mechanics and physics of solids*, 72:20–39, 2014.

[Gonz08] O. Gonzalez and A. M. Stuart. *A First Course in Continuum Mechanics*. Cambridge University Press, Cambridge, 1st edition edn., 2008.

[Graw12] J. Graw, B. Alberts, D. Bray, K. Hopkin, A. D. Johnson, J. Lewis, M. Raff, K. Roberts, and P. Walter. *Lehrbuch der Molekularen Zellbiologie*. Wiley-Blackwell, Weinheim, 4. vollständig überarbeitete edition edn., 2012.

[Guan21] W. Guan, S. Bhowmick, G. Gao, and G.-R. Liu. A phase-field modelling for 3D fracture in elasto-plastic solids based on the cell-based smoothed finite element method. *Engineering Fracture Mechanics*, 254:107920, 2021.

[Gucc91] J. M. Guccione, A. D. McCulloch, and L. K. Waldman. Passive material properties of intact ventricular myocardium determined from a cylindrical model. *Journal of Biomechanical Engineering*, 113(1):42–55, 1991.

[Gucc93] J. M. Guccione, L. K. Waldman, and A. D. McCulloch. Mechanics of Active Contraction in Cardiac Muscle: Part II—Cylindrical Models of the Systolic Left Ventricle. *Journal of Biomechanical Engineering*, 115(1):82–90, 1993.

[Gurt81] M. E. Gurtin. *An Introduction to Continuum Mechanics*. Academic Press, New York, 1 edn., 1981.

[Han19] J. Han and D. R. Trumble. Cardiac Assist Devices: Early Concepts, Current Technologies, and Future Innovations. *Bioengineering*, 6(1):18, 2019.

[Haug18] M. Haug, B. Reischl, G. Prölß, C. Pollmann, T. Buckert, C. Keidel, S. Schürmann, M. Hock, S. Rupitsch, M. Heckel, et al. The MyoRobot: A novel automated biomechatronics system to assess voltage/Ca2+ biosensors and active/passive biomechanics in muscle and biomaterials. *Biosensors and Bioelectronics*, 102:589–599, 2018.

[Haug19] M. Haug. MyoRobot 2.0_ An advanced biomechatronics platform for automated, environmentally controlled skeletal muscle single

fiber biomechanics assessment employing inbuilt real-time optical imaging. *Biosensors and Bioelectronics*, p. 10, 2019.

[Hirs19] M. Hirschvogel, L. Jagschies, A. Maier, S. M. Wildhirt, and M. W. Gee. An in silico twin for epicardial augmentation of the failing heart. *International Journal for Numerical Methods in Biomedical Engineering*, 35(10):e3233, 2019.

[Holz00] G. A. Holzapfel. *Nonlinear Solid Mechanics, A Continuum Approach for Engineering*. John Wiley & Sons, Chichester, 2000.

[Holz09] G. A. Holzapfel and R. W. Ogden. Constitutive modelling of passive myocardium: A structurally based framework for material characterization. *Philosophical Transactions of the Royal Society A: Mathematical, Physical and Engineering Sciences*, 367(1902):3445–3475, 2009.

[Holz22] D. Holz, M. T. Du'o'ng, D. Martonová, M. Alkassar, and S. Leyendecker. A Transmural Path Model Improves the Definition of the Orthotropic Tissue Structure in Heart Simulations. *Journal of Biomechanical Engineering*, 144(3):031002, 2022.

[Holz23] D. Holz, D. Martonová, E. Schaller, M. T. Duong, M. Alkassar, M. Weyand, and S. Leyendecker. Transmural fibre orientations based on Laplace-Dirichlet-Rule-Based-Methods and their influence on human heart simulations. *Journal of Biomechanics*, p. 111643, 2023.

[Hord19] E. C. Hord, C. M. Bolch, E. Tuzun, W. E. Cohn, B. Leschinsky, and J. C. Criscione. Evaluation of the CorInnova Heart Assist Device in an Acute Heart Failure Model. *Journal of Cardiovascular Translational Research*, 12(2):155–163, 2019.

[Hugh00] T. J. R. Hughes. *The Finite Element Method: Linear Static and Dynamic Finite Element Analysis*. Dover Publications, New York, 2000.

[Huo21] Z. Huo, G. Mei, and N. Xu. juSFEM: A Julia-based open-source package of parallel Smoothed Finite Element Method (S-FEM) for elastic problems. *Computers & Mathematics with Applications*, 81:459–477, 2021.

[Jags18] L. Jagschies, M. Hirschvogel, J. Matallo, A. Maier, K. Mild, H. Brun-

ner, R. Hinkel, M. W. Gee, P. Radermacher, S. M. Wildhirt, et al. Individualized Biventricular Epicardial Augmentation Technology in a Drug-Induced Porcine Failing Heart Model. *ASAIO Journal*, 64(4):480–488, 2018.

[Jegg06] D. Jegger, X. Jeanrenaud, M. Nasratullah, P.-G. Chassot, A. Mallik, H. Tevaearai, L. K. von Segesser, P. Segers, and N. Stergiopulos. Noninvasive Doppler-derived myocardial performance index in rats with myocardial infarction: Validation and correlation by conductance catheter. *American Journal of Physiology-Heart and Circulatory Physiology*, 290(4):H1540–H1548, 2006.

[Jian14] C. Jiang, Z.-Q. Zhang, X. Han, and G.-R. Liu. Selective smoothed finite element methods for extremely large deformation of anisotropic incompressible bio-tissues. *International Journal for Numerical Methods in Engineering*, 99(8):587–610, 2014.

[Jian15a] C. Jiang, G.-R. Liu, X. Han, Z.-Q. Zhang, and W. Zeng. A smoothed finite element method for analysis of anisotropic large deformation of passive rabbit ventricles in diastole. *International Journal for Numerical Methods in Biomedical Engineering*, 31(1):e02697, 2015.

[Jian15b] C. Jiang, Z.-Q. Zhang, G. Liu, X. Han, and W. Zeng. An edge-based/node-based selective smoothed finite element method using tetrahedrons for cardiovascular tissues. *Engineering Analysis with Boundary Elements*, 59:62–77, 2015.

[Kada19] C. Kadapa. Novel quadratic Bézier triangular and tetrahedral elements using existing mesh generators: Applications to linear nearly incompressible elastostatics and implicit and explicit elastodynamics. *International Journal for Numerical Methods in Engineering*, 117(5):543–573, 2019.

[Katz10] A. M. Katz. *Physiology of the Heart*. Lippincott Williams & Wilkins, 2010.

[Klab11] R. Klabunde. *Cardiovascular Physiology Concepts*. Lippincott Williams & Wilkins, 2011.

[Kshr19] S. Kshrisagar, A. Francis, J. J. Yee, S. Natarajan, and C. K. Lee. Implementing the Node Based Smoothed Finite Element Method as User Element in Abaqus for Linear and Nonlinear Elasticity. *Computers, Materials & Continua*, 61(2):481–502, 2019.

[Kumb20] P. Y. Kumbhar, A. Francis, N. Swaminathan, R. K. Annabattula, and S. Natarajan. Development of User Element Routine (UEL) for Cell-Based Smoothed Finite Element Method (CSFEM) in Abaqus. *International Journal of Computational Methods*, 17(02):1850128, 2020.

[Laga98] J. C. Lagarias, J. A. Reeds, M. H. Wright, and P. E. Wright. Convergence Properties of the Nelder–Mead Simplex Method in Low Dimensions. *SIAM Journal on Optimization*, 9(1):112–147, 1998.

[Lang22] M. Lange, E. Kwan, D. J. Dosdall, R. S. MacLeod, T. J. Bunch, and R. Ranjan. Case report: Personalized computational model guided ablation for left atrial flutter. *Frontiers in Cardiovascular Medicine*, 9:893752, 2022.

[Lauf96] D. A. Lauffenburger and J. Linderman. *Receptors: Models for Binding, Trafficking, and Signaling*. Oxford University Press, New York, NY, revised edition edn., 1996.

[Leff95] P. Leff. The two-state model of receptor activation. *Trends in Pharmacological Sciences*, 16(3):89–97, 1995.

[Li89] Y. Li and A. Goldbeter. Frequency specificity in intercellular communication. Influence of patterns of periodic signaling on target cell responsiveness. *Biophysical Journal*, 55(1):125–145, 1989.

[Lima18] B. Lima, A. Bansal, J. Abraham, J. D. Rich, S. S. Lee, B. Soleimani, J. N. Katz, A. Kilic, J. S. Young, C. B. Patel, et al. Controversies and Challenges of Ventricular Assist Device Therapy. *The American Journal of Cardiology*, 121(10):1219–1224, 2018.

[Lin98] D. H. S. Lin and F. C. P. Yin. A Multiaxial Constitutive Law for Mammalian Left Ventricular Myocardium in Steady-State Barium Contracture or Tetanus. *Journal of Biomechanical Engineering*, 120(4):504–517, 1998.

[Liu07] G. R. Liu, K. Y. Dai, and T. T. Nguyen. A Smoothed Finite Element Method for Mechanics Problems. *Computational Mechanics*, 39(6):859–877, 2007.

[Liu09a] G. Liu, T. Nguyen-Thoi, H. Nguyen-Xuan, and K. Lam. A node-based smoothed finite element method (NS-FEM) for upper bound

solutions to solid mechanics problems. *Computers & Structures*, 87(1-2):14–26, 2009.

[Liu09b] G. R. Liu, T. Nguyen-Thoi, and K. Y. Lam. An edge-based smoothed finite element method (ES-FEM) for static, free and forced vibration analyses of solids. *Journal of Sound Vibration*, 320:1100–1130, 2009.

[Liu16] G. R. Liu and N. T. Trung. *Smoothed Finite Element Methods*. CRC Press, 1st edition edn., 2016.

[Liu19] G.-R. Liu. The smoothed finite element method (S-FEM): A framework for the design of numerical models for desired solutions. *Frontiers of Structural and Civil Engineering*, 13(2):456–477, 2019.

[Lope15] A. Lopez-Perez, R. Sebastian, and J. M. Ferrero. Three-dimensional cardiac computational modelling: Methods, features and applications. *BioMedical Engineering OnLine*, 14(1):35, 2015.

[Lowe91] J. E. Lowe, M. P. Anstadt, P. Van Trigt, P. K. Smith, P. J. Hendry, M. D. Plunkett, and G. L. Anstadt. First successful bridge to cardiac transplantation using direct mechanical ventricular actuation. *The Annals of Thoracic Surgery*, 52(6):1237–1245, 1991.

[Mart21a] D. Martonová, M. Alkassar, J. Seufert, D. Holz, M. Tuan Duong, B. Reischl, O. Friedrich, and S. Leyendecker. Influence of passive mechanical properties in healthy and infarcted rat myocardium on the cardiac cycle. *PAMM*, 21(1):e202100054, 2021.

[Mart21b] D. Martonová, M. Alkassar, J. Seufert, D. Holz, M. T. Duong, B. Reischl, O. Friedrich, and S. Leyendecker. Passive mechanical properties in healthy and infarcted rat left ventricle characterised via a mixture model. *Journal of the Mechanical Behavior of Biomedical Materials*, 119:104430, 2021.

[Mart21c] D. Martonová, D. Holz, M. T. Duong, and S. Leyendecker. Towards the simulation of active cardiac mechanics using a smoothed finite element method. *Journal of Biomechanics*, 115:110153, 2021.

[Mart22a] D. Martonová, D. Holz, D. Brackenhammer, M. Weyand, S. Leyendecker, and M. Alkassar. Support Pressure Acting on the Epicardial Surface of a Rat Left Ventricle – A Computational Study. *Frontiers in Cardiovascular Medicine*, 9:850274, 2022.

[Mart22b] D. Martonová, D. Holz, J. Seufert, M. T. Duong, M. Alkassar, and S. Leyendecker. Comparison of stress and stress–strain approaches for the active contraction in a rat cardiac cycle model. *Journal of Biomechanics*, 134:110980, 2022.

[Mart23a] D. Martonová, D. Holz, M. T. Duong, and S. Leyendecker. Smoothed finite element methods in simulation of active contraction of myocardial tissue samples. *Journal of Biomechanics*, 157:111691, 2023.

[Mart23b] D. Martonová, M. Lavaill, M. R. Forwood, A. Robling, D. M. L. Cooper, S. Leyendecker, and P. Pivonka. Effects of PTH glandular and external dosing patterns on bone cell activity using a two-state receptor model—Implications for bone disease progression and treatment. *PLOS ONE*, 2023.

[McCo13] M. McCormick, D. A. Nordsletten, D. Kay, and N. P. Smith. Simulating left ventricular fluid–solid mechanics through the cardiac cycle under LVAD support. *Journal of Computational Physics*, 244:80–96, 2013.

[Mila14] N. Milani-Nejad and P. M. L. Janssen. Small and large animal models in cardiac contraction research: Advantages and disadvantages. *Pharmacology & Therapeutics*, 141(3):235–249, 2014.

[Miln19] M. L. Milne, B. M. Schick, T. Alkhazal, and C. S. Chung. Myocardial Fiber Mapping of Rat Hearts Using Apparent Backscatter, with Histological Validation. *Ultrasound in medicine & biology*, 45(8):2075–2085, 2019.

[Neld65] J. A. Nelder and R. Mead. A Simplex Method for Function Minimization. *The Computer Journal*, 7(4):308–313, 1965.

[Nguy07] T. T. Nguyen, G. R. Liu, K. Y. Dai, and K. Y. Lam. Selective Smoothed Finite Element Method. *Tsinghua Science & Technology*, 12(5):497–508, 2007.

[Nied19] S. A. Niederer, J. Lumens, and N. A. Trayanova. Computational models in cardiology. *Nature reviews. Cardiology*, 16(2):100–111, 2019.

[Nix12] Y. Nix, R. Frotscher, and M. Staat. Implementation of the edge-based smoothed extended finite element method. *Proceedings Euro-*

pean Congress on Computational Methods in Applied Sciences and Engineering, 2012.

[Nouj04] S. F. Noujaim, E. Lucca, V. Muñoz, D. Persaud, O. Berenfeld, F. L. Meijler, and J. Jalife. From Mouse to Whale. *Circulation*, 110(18):2802–2808, 2004.

[NT09] T. Nguyen-Thoi, G. R. Liu, K. Y. Lam, and G. Y. Zhang. A face-based smoothed finite element method (FS-FEM) for 3D linear and geometrically non-linear solid mechanics problems using 4-node tetrahedral elements. *International Journal for Numerical Methods in Engineering*, 78(3):324–353, 2009.

[O'Ha22] R. P. O'Hara, A. Prakosa, E. Binka, A. Lacy, and N. A. Trayanova. Arrhythmia in hypertrophic cardiomyopathy: Risk prediction using contrast enhanced MRI, T1 mapping, and personalized virtual heart technology. *Journal of Electrocardiology*, 74:122–127, 2022.

[Øste10] G. Østergaard, H. N. Hansen, and J. L. Ottesen. Handbook of Laboratory Animal Science, Volume I: Essential Principles and Practices. https://www.routledge.com/Handbook-of-Laboratory-Animal-Science-Volume-I-Essential-Principles-and/Hau-Schapiro/p/book/9781420084559, 2010.

[Oz02] M. C. Oz, J. H. Artrip, and D. Burkhoff. Direct cardiac compression devices. *The Journal of Heart and Lung Transplantation*, 21(10):1049–1055, 2002.

[Parf02] A. M. Parfitt. Parathyroid Hormone and Periosteal Bone Expansion. *Journal of Bone and Mineral Research*, 17(10):1741–1743, 2002.

[Peir21] M. Peirlinck, F. S. Costabal, J. Yao, J. M. Guccione, S. Tripathy, Y. Wang, D. Ozturk, P. Segars, T. M. Morrison, S. Levine, et al. Precision medicine in human heart modeling: Perspectives, challenges, and opportunities. *Biomechanics and Modeling in Mechanobiology*, 20(3):803–831, 2021.

[Pfal19] M. R. Pfaller, J. M. Hörmann, M. Weigl, A. Nagler, R. Chabiniok, C. Bertoglio, and W. A. Wall. The importance of the pericardium for cardiac biomechanics: From physiology to computational modeling. *Biomechanics and Modeling in Mechanobiology*, 18(2):503–529, 2019.

[Ponn16] J. K. Ponniah, H. Chen, O. Adetiba, R. Verduzco, and J. G. Jacot. Mechanoactive materials in cardiac science. *Journal of Materials Chemistry B*, 4(46):7350–7362, 2016.

[Roch17] E. T. Roche, M. A. Horvath, I. Wamala, A. Alazmani, S.-E. Song, W. Whyte, Z. Machaidze, C. J. Payne, J. C. Weaver, G. Fishbein, et al. Soft robotic sleeve supports heart function. *Science Translational Medicine*, 9(373):eaaf3925, 2017.

[Rodr94] E. K. Rodriguez, A. Hoger, and A. D. McCulloch. Stress-dependent finite growth in soft elastic tissues. *Journal of Biomechanics*, 27(4):455–467, 1994.

[Ross14] S. Rossi, T. Lassila, R. Ruiz-Baier, A. Sequeira, and A. Quarteroni. Thermodynamically consistent orthotropic activation model capturing ventricular systolic wall thickening in cardiac electromechanics. *European Journal of Mechanics - A/Solids*, 48:129–142, 2014.

[Sáez16] P. Sáez and E. Kuhl. Computational modeling of acute myocardial infarction. *Computer methods in biomechanics and biomedical engineering*, 19(10):1107–1115, 2016.

[SC16] F. Sahli Costabal, D. E. Hurtado, and E. Kuhl. Generating Purkinje networks in the human heart. *Journal of Biomechanics*, 49(12):2455–2465, 2016.

[SC18] F. Sahli Costabal, J. Yao, and E. Kuhl. Predicting the cardiac toxicity of drugs using a novel multiscale exposure–response simulator. *Computer Methods in Biomechanics and Biomedical Engineering*, 21(3):232–246, 2018.

[Sege86] L. A. Segel, A. Goldbeter, P. N. Devreotes, and B. E. Knox. A mechanism for exact sensory adaptation based on receptor modification. *Journal of Theoretical Biology*, 120(2):151–179, 1986.

[Serm06] M. Sermesant, H. Delingette, and N. Ayache. An electromechanical model of the heart for image analysis and simulation. *IEEE Transactions on Medical Imaging*, 25(5):612–625, 2006.

[Somm15] G. Sommer, A. J. Schriefl, M. Andrä, M. Sacherer, C. Viertler, H. Wolinski, and G. A. Holzapfel. Biomechanical properties and microstructure of human ventricular myocardium. *Acta Biomaterialia*, 24:172–192, 2015.

[Tike22] O. Z. Tikenoğulları, F. S. Costabal, J. Yao, A. Marsden, and E. Kuhl. How viscous is the beating heart? Insights from a computational study. *Computational Mechanics*, 70(3):565–579, 2022.

[Tray17] N. A. Trayanova, F. Pashakhanloo, K. C. Wu, and H. R. Halperin. Imaging-Based Simulations for Predicting Sudden Death and Guiding VT Ablation. *Circulation. Arrhythmia and electrophysiology*, 10(7), 2017.

[Treu17] P. M. Treuting, S. M. Dintzis, and K. S. Montine. *Comparative Anatomy and Histology: A Mouse, Rat, and Human Atlas*. Elsevier Science, 2017.

[Wang18] J. Wang, C. Gareri, and H. A. Rockman. G-Protein–Coupled Receptors in Heart Disease. *Circulation Research*, 123(6):716–735, 2018.

[Weis96] J. A. Weiss, B. N. Makerc, and S. Govindjee. Finite element implementation of incompressible, transversely isotropic hyperelasticity. *Comput. Methods Appl. Mech. Engrg.*, 135(1-2):107–128, 1996.

[WHO20] WHO. Global health estimates 2019: Disease burden by Cause, Age, Sex, by Country and by Region, 2000-2019. https://www.who.int/data/gho/data/themes/mortality-and-global-health-estimates, 2020.

[Wilk17] E. Wilkins, L. Wilson, K. Wickramasinghe, P. Bhatnagar, J. Leal, R. Luengo-Fernandez, R. Burns, M. Rayner, and N. Townsend. European cardiovascular disease statistics 2017. *Brussels: European Heart Network*, 2017.

[Wong14] J. Wong and E. Kuhl. Generating fibre orientation maps in human heart models using Poisson interpolation. *Computer methods in biomechanics and biomedical engineering*, 17(11):1217–1226, 2014.

[Woo12] A. Y. H. Woo and R.-p. Xiao. β-Adrenergic receptor subtype signaling in heart: From bench to bedside. *Acta Pharmacologica Sinica*, 33(3):335–341, 2012.

[Wrig01] P. Wriggers. *Nichtlineare Finite-Element-Methoden*. Springer, Berlin, Heidelberg, 2001.

[Wu20] S.-W. Wu, C. Jiang, C. Jiang, and G.-R. Liu. A selective smoothed

finite element method with visco-hyperelastic constitutive model for analysis of biomechanical responses of brain tissues. *International Journal for Numerical Methods in Engineering*, 121(22):5123–5149, 2020.

[Wu23] S.-W. Wu, D.-T. Wan, C. Jiang, X. Liu, K. Liu, and G. R. Liu. A finite strain model for multi-material, multi-component biomechanical analysis with total Lagrangian smoothed finite element method. *International Journal of Mechanical Sciences*, 243:108017, 2023.

[Wu23a] S.-W. Wu, G. R. Liu, C. Jiang, X. Liu, K. Liu, D.-T. Wan, J.-H. Yue. Arbitrary polygon mesh for elastic and elastoplastic analysis of solids using smoothed finite element method. *Computer Methods in Applied Mechanics and Engineering*, 405:115874, 2023.

[Yama22] C. Yamamoto and N. A. Trayanova. Atrial fibrillation: Insights from animal models, computational modeling, and clinical studies. *eBioMedicine*, 85:104310, 2022.

[Yan22] X. Yan, D. Wan, D. Hu, X. Han, and G. R. Liu. A selective smoothed finite element method for 3D explicit dynamic analysis of the human annulus fibrosus with modified composite-based constitutive model. *Engineering Analysis with Boundary Elements*, 134:49–65, 2022.

[Yao12] J. Yao, G. R. Liu, D. A. Narmoneva, R. B. Hinton, and Z.-Q. Zhang. Immersed smoothed finite element method for fluid-structure interaction simulation of aortic valves. *Comput Mech*, 50(6):789–804, 2012.

[Zeng18] W. Zeng and G. R. Liu. Smoothed Finite Element Methods (S-FEM): An Overview and Recent Developments. *Archives of Computational Methods in Engineering*, 25(2):397–435, 2018.

[Zhan10] Z.-Q. Zhang and G. R. Liu. Temporal stabilization of the node-based smoothed finite element method and solution bound of linear elastostatics and vibration problems. *Computational Mechanics*, 46(2):229–246, 2010.

A Appendix

journal of the mechanical behavior of biomedical materials 119 (2021) 104430

Contents lists available at ScienceDirect

Journal of the Mechanical Behavior of Biomedical Materials

journal homepage: www.elsevier.com/locate/jmbbm

Research paper

Passive mechanical properties in healthy and infarcted rat left ventricle characterised via a mixture model

Denisa Martonová [a,*], Muhannad Alkassar [b], Julia Seufert [b], David Holz [a], Minh Tuấn Dương [a,d], Barbara Reischl [c], Oliver Friedrich [c], Sigrid Leyendecker [a]

[a] Friedrich-Alexander-Universität Erlangen-Nürnberg, Institute of Applied Dynamics, Immerwahrstraße 1, 91058 Erlangen, Germany
[b] Friedrich-Alexander-Universität Erlangen-Nürnberg, Pediatric Cardiology, Loschgestraße 15, 91054 Erlangen, Germany
[c] Friedrich-Alexander-Universität Erlangen-Nürnberg, Institute of Medical Biotechnology, Paul-Gordan-Str. 3, 91052 Erlangen, Germany
[d] School of Mechanical Engineering, Hanoi University of Science and Technology, 1 DaiCoViet Road, Hanoi, Vietnam

ARTICLE INFO

Keywords:
Rat left ventricle
Myocardial infarction
Fibrosis
Passive mechanics
Incompressibility
Holzapfel-Ogden strain energy
Parameter fitting

ABSTRACT

During the cardiac cycle, electrical excitation is coupled with mechanical response of the myocardium. Besides the active contraction, passive mechanics plays an important role, and its behaviour differs in healthy and diseased hearts as well as among different animal species. The aim of this study is the characterisation of passive mechanical properties in healthy and infarcted rat myocardium by means of mechanical testing and subsequent parameter fitting. Elasticity assessments via uniaxial extension tests are performed on healthy and infarcted tissue samples from left ventricular rat myocardium. In order to fully characterise the orthotropic cardiac tissue, our experimental data are combined with other previously published tests in rats – shear tests on healthy myocardium and equibiaxial tests on infarcted tissue. In a first step, we calibrate the Holzapfel-Ogden strain energy function in the healthy case. Sa far, this orthotropic constitutive law for the passive myocardium has been fitted to experimental data in several species, however there is a lack of an appropriate parameter set for the rat. With our determined parameters, a finite element simulation of the end-diastolic filling is performed. In a second step, we propose a model for the infarcted tissue. It is represented as a mixture of intact myocardium and a transversely isotropic scar structure. In our mechanical experiments, the tissue after myocardial infarction shows significantly stiffer behaviour than in the healthy case, and the stiffness correlates with the amount of fibrosis. A similar relationship is observed in the computational simulation of the end-diastolic filling. We conclude that our new proposed material model can capture the behaviour of two kinds of tissues – healthy and infarcted rat myocardium, and its calibration with the fitted parameters represents the experimental data well.

1. Introduction

Cardiovascular diseases remain the leading cause of death, e.g. 30% in the US and 45% in Europe (Wilkins et al., 2017). To understand the normal and pathological physiology in cardiomyopathy, laboratory rats are widely used as experimental animals. Supporting the animal testing, mathematical models and computational simulations can complement these investigations and eventually lead to better diagnostics, therapy and development of medical devices. In the last decades, several constitutive laws for the passive myocardium have been proposed. One of the first models, developed by Demiray (1976), describes myocardium as isotropic hyperelastic material. Later, more realistic, transversely isotropic (Humphrey and Yin, 1987; Guccione et al., 1991; Costa et al., 1996) and orthotropic (Costa et al., 2001; Schmid et al., 2006; Holzapfel and Ogden, 2009), models were introduced. The latter is one of the most frequently used models in the literature (Göktepe et al., 2011; Eriksson et al., 2013; Baillargeon et al., 2014; Gao et al., 2015). It takes the microstructural orthotropy of the myocardium into account and depends on the invariants in fibre, sheet, and sheet-normal directions and eight material parameters $(a, b, a_f, b_f, a_s, b_s, a_{fs}, b_{fs})$ related to the matrix response, response in fibre, sheet direction and fibre-sheet coupling. However, all these models crucially depend on the choice of parameters. Therefore, it is essential to determine appropriate parameters for the constitutive law describing the passive mechanical behaviour.

There are a few studies investigating mechanical properties of myocardium in different species. Dokos et al. (2002) studied porcine

* Corresponding author.
E-mail address: denisa.martonova@fau.de (D. Martonová).

https://doi.org/10.1016/j.jmbbm.2021.104430
Received 7 September 2020; Received in revised form 21 February 2021; Accepted 22 February 2021
Available online 16 March 2021

myocardium by means of biaxial and shear testing. Sommer et al. (2015b) published data from similar biaxial and six shear tests on human myocardium, and recently, Ahmad et al. (2018) performed uniaxial, biaxial and shear tests on neonatal porcine myocardium. These studies provide excellent data to calibrate a species-specific constitutive model for passive mechanical properties. The determination of corresponding material parameters for the Holzapfel-Ogden constitutive law (Holzapfel and Ogden, 2009) is published by Guan et al. (2019). The results yield species- and age-specific parameters. To our best knowledge, there are no studies investigating an orthotropic constitutive model of the rat myocardium.

In addition to healthy cardiac tissue, better understanding of passive mechanics after myocardial infarction (MI) is essential because the heart needs to keep up pump capacity, while the infarcted regions become non-contractile and stiffer. Up to this point, several studies considering infarcted myocardial tissue in different species have been conducted. Biaxial mechanical properties in infarcted sheep hearts have been studied by Gupta et al. (1994), Morita et al. (2011) and Gundiah et al. (2004), whereas Zhang et al. (2010) performed equibiaxial tests on infarcted porcine hearts. The tissue after MI in rats was mechanically tested by Fomovsky and Holmes (2010) and Sirry et al. (2016a). The former noted that the infarcted regions after MI, mostly consisting of the fibrotic scar tissue, are structurally and mechanically isotropic and can be characterised by a simple strain energy function depending only on the first invariant. In contrast to that, Sirry et al. (2016a) observed anisotropy by mechanical testing. As the collagen content is the main determinant of the mechanical properties in the infarcted myocardium in the rat (Fomovsky and Holmes, 2010), a constitutive model taking the collagen fibre dispersion into account is more appropriate when modelling the scar formation after MI.

Although in the last decades, extensive research regarding the passive mechanical behaviour in cardiac tissue has been done, the question remains, what are the adequate passive material parameters for realistic computational rat heart models? These models can support laboratory experiments which are widely performed in rats for several reasons, i.e. availability of rodents, lower breeding costs, shorter pregnancy full term, shorter life cycle and consequently, a quicker clinical manifestation of the MI as well as availability of small animal surgery facilities and diagnostic gears. Such animal models, together with their digital twins, eventually lead to improvements in diagnostics and therapies. Especially the development of medical devices requires a challenging parameter optimisation which is easier to perform in computational simulations prior to the actual animal experiments.

Therefore, in this paper, we investigate the passive mechanical properties of the healthy rat myocardium and 14 ± 2 days after MI. In the experimental part, following the MI induction via ligating the left anterior descending coronary artery (LAD), heart dissection and sectioning, elasticity assessments (EA) via uniaxial extension test both for a control and an infarcted group are performed.

In order to fully characterise the myocardium, a combination of own experimental data from uniaxial extension tests and data from simple shear tests (Dokos et al., 2000) and equibiaxial tests (Sirry et al., 2016b) are used. The reason is that uniaxial testing alone is not sufficient to capture the 3D constitutive behaviour of the anisotropic myocardium, which undergoes complex deformation during the cardiac cycle. Especially shear deformation plays an important role. It has been shown that shearing of myocardial layers contributes to subendocardial wall thickening during the systole (LeGrice et al., 1995) as well as to wall thinning during passive ventricular filling (Spotnitz et al., 1974). Then, the constitutive model is fitted to the experimental data. In a first step, we calibrate the orthotropic Holzapfel-Ogden strain energy function in the healthy case. In a next step, the infarcted tissue is modelled as a mixture of intact myocardium and fibrotic scar tissue. The amount of fibrosis obtained from the histology serves as a weighting factor. The fibre direction is included into the material model using the angular integration approach (AI), firstly introduced by Lanir (1983). With parameters obtained from fitting, we test a finite element (FE) model during the passive end-diastolic filling by applying a pressure boundary condition on the endocardium of the rat left ventricle (LV) model generated from magnetic resonance imaging. The results are compared to the pressure-volume relation obtained with parameters from the literature.

2. Materials and methods

2.1. Experimental setup

2.1.1. Rat heart specimen and myocardial infarction induction

All animal experiments were performed in accordance with the Guide for the Care and Use of Laboratory Animals (National Institutes of Health publication) guidelines. Sprague Dawley rats ($21\text{d} \pm 2\text{d}$) were anaesthetised with isoflurane (5%) and intubated. The rats received positive pressure ventilation (1.5%–2% isoflurane) and the body temperature was controlled with a heating pad. Further, 0.05–0.1 mg/kg buprenorphin was given subcutaneously for analgesia. A heart infarction was established via the fifth intercostal space by a permanent ligation of the left anterior descending artery. Successful ligation was confirmed by instant bleaching of the tissue. The muscles and the wound were sutured (polyethylene, 6-0), and the rat was allowed to wake up. Postoperative analgesia was given in case rats showed signs of pain defined by caretaking guidelines.

2.1.2. Heart dissection and sectioning

At day 14d ($\pm$2d) after MI, the hearts were dissected. For this, the rats received anaesthesia via isoflurane (5%) and analgesia via buprenorphine (0.05–0.1 mg/kg). The hearts were perfused with ice-cold Tyrode's solution (136 mM NaCl, 5.4 mM KCl, 0.33 mM NaH_2PO_4, 1 mM $MgCl_2$-$6H_2O$, 5 mM HEPES, 30 mM 2,3-butanedione monoxime (BDM)) using an injected catheter in the apex of the heart. Afterwards, the hearts were dissected and embedded in 4% low-melting-agarose (Roth; 6351.5; solved in Tyrode's solution) in an upright position and placed on ice. The hearts were sectioned in 300 μm thick slices using a Vt1200S vibratom (Leica). The samples were stored in Tyrode's solution on ice and were constantly shaken to avoid insufficient oxygen supply. The original position of the samples in the heart was listed.

2.1.3. Elasticity assessment via uniaxial extension test

The 300 μm thick slices were further punched at three locations in the LV, see Fig. 1. Two punches were taken from the non-septal area, where the infarcted area is located in the operated rat group, and one sample was taken from the septum. All samples had identical dimensions (circumferential 2.34 mm, radial 1.20 mm, longitudinal 0.30 mm) in order to quantify the cross-sectional area. In preparation for the subsequent measurements, the punched samples were glued on a cut-to-size and holed polymeric printer film (transparencies plain, XEROX, type C) along the both radial sides using a histoacrylic glue (Histoacryl, BBraun) as demonstrated in Fig. 1, blue zoomed box. For the measurement, these holed polymers were mounted through the force transducer (KG-7, MyoTronic, Heidelberg) and the voice-coil (SMAC) of the *MyoRobot* (Haug et al., 2018, 2019) as depicted in Fig. 1. This construction allows a circumferential or radial extension of the specimen. We assumed that the fibre direction varies in the circumferential-longitudinal plane. The clarifications on the fibre direction are given in Section 2.3.2 and Table 1. The *MyoRobot* measurement included four preconditioning cycles (20% time of the main measurement), followed by the main measurement running over 15 min, see Fig. 6 for a representative measurement output. All cycles run with a velocity of 1 μm/s.

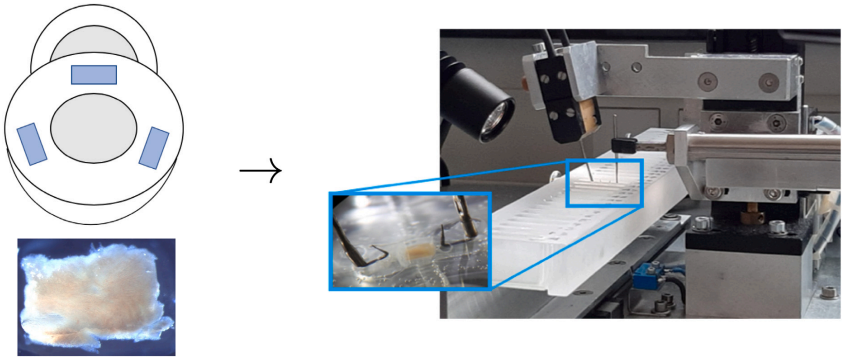

Fig. 1. Experimental setup in the EA via uniaxial extension test. Left: tissue from the middle layer of myocardium (three possible circumferential positions in the LV are schematically shown in the top view). Right: glued sample in *MyoRobot* (Haug et al., 2018, 2019) system.

Table 1
Overview of parameters used for fitting the experimental data from the different mechanical tests: uniaxial extension, shear tests from Dokos et al. (2000) and equibiaxial test from Sirry et al. (2016a).

Mechanical test	fib	$\phi^i_f(\beta)$
Uniaxial extension (muscle)	0	Eq. (22) with $\beta_{min} = -30°$, $\beta_{max} = 30°$
Simple shear (muscle)	0	Eq. (22) with $\beta_{min} = -60°$, $\beta_{max} = 60°$
Uniaxial extension (scar)	0.60	Eq. (23) with $w_1 = 0.37, w_2 = 0.63, \mu_1 = -45.16°, \mu_2 = 36.90°$, $\Sigma_1 = 329.03°, \Sigma_2 = 362.38°$
Equibiaxial extension (scar)	0.47	Eq. (23) with $w_1 = 0.56, w_2 = 0.44, \mu_1 = -46.63°, \mu_2 = 34.83°$, $\Sigma_1 = 209.84°, \Sigma_2 = 446.65°$

Table 2
Summary of subject characteristics in EA via uniaxial extension test (rat group, gender, number of samples, amount of fibrosis). Coding: group m=male, f=female, c=uniaxial extension in circumferential direction, r= uniaxial extension in radial direction. The amount of fibrosis is evaluated for number of samples $n = 6, 9, 23$ in the groups control, sham, infarcted, respectively.

Group	No. of animals	Gender (m/f)	No. of samples (c/r)	Fibrosis in % (mean± SD)
Control	4	2/2	17/7	11.8 ± 5.6
Sham	3	2/1	14/3	1.1 ± 0.7
Infarcted	7	5/2	18/5	60.1 ± 15.9

2.1.4. Histology and quantification of fibrosis

After the mechanical testing, samples were fixed using 4% paraformaldehyde (formaldehyde 35%, Roth, in phosphate-buffered saline (PBS)). They underwent a series of alcohol dehydrations and were embedded in paraffin. The samples were sectioned in 3 μm thick slices and stained in Masson-Goldner-Trichrome (Staining Kit, Roth). The percentage of fibrosis of the samples was quantified using pixel analysis in the image processing program ImageJ. Infarcted tissue (stained blue in Masson-Goldner-Trichrome) was scaled against the overall amount of pixels of the sample. Following the histological analysis, samples from the infarcted group showing less than 35% fibrosis were excluded from the study. Representative images of the intact and infarcted myocardium are shown in Fig. 7.

2.2. Mechanical tests used for parameter fitting

2.2.1. Elasticity assessment via uniaxial extension test – healthy and infarcted myocardium

For this study, we included four animals from the control group (24 tested samples from different regions of myocardium), three from the sham group where surgical intervention without LAD-ligation was performed (17 tested samples) and seven from the infarct group (23 samples with fibrosis $\geq 35\%$). The summary of the subject characteristics for all included samples is given in Table 2.

2.2.2. Elasticity assessment via shear test – healthy myocardium

To calibrate the constitutive model for healthy myocardium, in addition to the EA via uniaxial extension tests, we used the data from shear tests on a rat heart septum published by Dokos et al. (2000).

2.2.3. Elasticity assessment via biaxial test – infarcted myocardium

For the infarcted myocardium, the model was calibrated with the data from our EA via uniaxial extension tests in a combination with the data from equibiaxial tests on a rat LV published by Sirry et al. (2016a,b).

2.3. Constitutive modelling

2.3.1. Deformation resulting from the mechanical tests

In the framework of a standard continuum mechanics (Gurtin, 1981), the macroscopic deformation of each tested sample is described by the map $\boldsymbol{\varphi} : \mathbf{X} \mapsto \boldsymbol{x}$ which maps points from the reference to the deformed configuration. The deformation gradient, mapping line elements from the reference to the deformed configuration, is given by $\mathbf{F}(\mathbf{X}) = \nabla_{\mathbf{X}} \varphi(\mathbf{X})$. We model the tissue as an incompressible hyperelastic material, i.e. $\det\mathbf{F} = 1$ and the Cauchy stress can be computed from the strain energy function $\Psi = \Psi(\mathbf{C})$ as

$$\boldsymbol{\sigma} = 2\mathbf{F}\frac{\partial \Psi}{\partial \mathbf{C}}\mathbf{F}^{\mathrm{T}} - \mathrm{p}\mathbf{I}, \tag{1}$$

where $\mathbf{C} = \mathbf{F}^{\mathrm{T}}\mathbf{F}$ is the right Cauchy-Green tensor, $\mathbf{I}$ the identity tensor and p the hydrostatic pressure. For the incompressible material, the

relation between the applied force and the Cauchy stress is given as

$$\boldsymbol{\sigma} = \mathbf{P}\mathbf{F}^{\mathrm{T}}, \quad \mathbf{P} = \begin{bmatrix} P_{11} & P_{12} & P_{13} \\ P_{21} & P_{22} & P_{23} \\ P_{31} & P_{32} & P_{33} \end{bmatrix} = \begin{bmatrix} \frac{f_{11}}{A_1} & \frac{f_{12}}{A_2} & \frac{f_{13}}{A_3} \\ \frac{f_{21}}{A_1} & \frac{f_{22}}{A_2} & \frac{f_{23}}{A_3} \\ \frac{f_{31}}{A_1} & \frac{f_{32}}{A_2} & \frac{f_{33}}{A_3} \end{bmatrix}, \tag{2}$$

where $\mathbf{P}, f_{ij}, A_j$ denote the first Piola-Kirchhoff stress, the components of the applied forces and the cross-sectional area in the reference configuration, respectively and $i, j \in \{1, 2, 3\}$. A schematic representation of the considered mechanical tests is depicted in Fig. 3. Depending on the loading mode, the deformation gradients and the corresponding components of the Cauchy stress take the following form:

- EA via uniaxial extension test – based on the study Guan et al. (2019) and the assumed HO strain energy function, where the fibres can only bear load if they are elongated, we assume equal deformation in both planes perpendicular to the direction of the applied force and we neglect the shear stress, namely

$$\mathbf{F} = \begin{bmatrix} \lambda_1 & 0 & 0 \\ 0 & \frac{1}{\sqrt{\lambda_1}} & 0 \\ 0 & 0 & \frac{1}{\sqrt{\lambda_1}} \end{bmatrix} \quad \text{and} \quad \sigma_{11} = \lambda_1 \frac{f_{11}}{A_1}, \tag{3}$$

$$\mathbf{F} = \begin{bmatrix} \frac{1}{\sqrt{\lambda_2}} & 0 & 0 \\ 0 & \lambda_2 & 0 \\ 0 & 0 & \frac{1}{\sqrt{\lambda_2}} \end{bmatrix} \quad \text{and} \quad \sigma_{22} = \lambda_2 \frac{f_{22}}{A_2}, \tag{4}$$

  where λ_i are the principal stretches in the circumferential and radial direction, respectively ($i = 1, 2$). The hydrostatic pressure is determined by evaluating the condition $\sigma_{22} = \sigma_{33} = 0$ in the first and $\sigma_{11} = \sigma_{33} = 0$ in the second experiment.
- EA via simple shear test – we use the data published by Dokos et al. (2000). The performed shear tests correspond to shearing in the circumferential-radial plane in circumferential direction (shear 12) and in the radial-longitudinal plane in longitudinal direction (shear 32). The deformation gradients are given by

$$\mathbf{F} = \begin{bmatrix} 1 & \gamma_{12} & 0 \\ 0 & 1 & 0 \\ 0 & 0 & 1 \end{bmatrix} \quad \text{and} \quad \sigma_{12} = \frac{f_{12}}{A_2}, \tag{5}$$

$$\mathbf{F} = \begin{bmatrix} 1 & 0 & 0 \\ 0 & 1 & 0 \\ 0 & \gamma_{32} & 1 \end{bmatrix} \quad \text{and} \quad \sigma_{32} = \frac{f_{32}}{A_2}, \tag{6}$$

  where γ_{ij} is the amount of shear. Note that when assuming fibres to be aligned with the circumferential direction, we can identify the tests with (sf) and (sn) according to the notation in Holzapfel and Ogden (2009).
- EA via biaxial test – for calibration of the model for the infarcted myocardium, we use the data published by Sirry et al. (2016a). The biaxial tests correspond to the extension in circumferential and longitudinal direction. The resulting deformation gradient reads as

$$\mathbf{F} = \begin{bmatrix} \lambda_1 & 0 & 0 \\ 0 & \frac{1}{\lambda_1 \lambda_3} & 0 \\ 0 & 0 & \lambda_3 \end{bmatrix} \quad \text{and} \quad \sigma_{11} = \lambda_1 \frac{f_{11}}{A_1}, \quad \sigma_{33} = \lambda_3 \frac{f_{33}}{A_3}, \tag{7}$$

  The hydrostatic pressure is determined by evaluating the condition $\sigma_{22} = 0$. However, for fibre-reinforced material, a small amount of shear is almost certainly present during the biaxial testing (Freed et al., 2010; Fomovsky and Holmes, 2010). This phenomenon was also observed by Guan et al. (2019) when fitting to the experimental data on neonatal porcine myocardium (Ahmad et al., 2018) and it was identified as a necessary condition to obtain a good fit to the experimental data for human myocardium (Sommer et al., 2015b). If shear is present in the biaxial tests, then $\gamma_{13} \neq 0$ and $\gamma_{31} \neq 0$ and the deformation gradient is

$$\mathbf{F} = \begin{bmatrix} \lambda_1 & 0 & \gamma_{13} \\ 0 & \frac{1}{\lambda_1 \lambda_3 - \gamma_{13}\gamma_{31}} & 0 \\ \gamma_{31} & 0 & \lambda_3 \end{bmatrix} \quad \text{and}$$

$$\sigma_{11} = \lambda_1 P_{11} + \gamma_{13} P_{13} = \lambda_1 \frac{f_{11}}{A_1} + \gamma_{13} \frac{f_{13}}{A_3},$$

$$\sigma_{33} = \lambda_1 P_{33} + \gamma_{31} P_{31} = \lambda_3 \frac{f_{33}}{A_3} + \gamma_{31} \frac{f_{31}}{A_1} \tag{8}$$

  with the notation as above. The applied forces are the sum of the force components (Sommer et al., 2015a), namely:

$$f_1 = f_{11} + f_{13} \quad \text{and} \quad f_3 = f_{33} + f_{31}. \tag{9}$$

The relation between the applied force and the Cauchy stress is then given by

$$\frac{f_1}{A} = (\boldsymbol{\sigma}\mathbf{F}^{-T})_{11} + (\boldsymbol{\sigma}\mathbf{F}^{-T})_{13} \quad \text{and} \quad \frac{f_3}{A} = (\boldsymbol{\sigma}\mathbf{F}^{-T})_{33} + (\boldsymbol{\sigma}\mathbf{F}^{-T})_{31}, \tag{10}$$

where $A = A_1 = A_3$. This condition is fulfilled in biaxial tested samples in Sirry et al. (2016a). Further, we assume the shear to be a linear function of the stretch, see Guan et al. (2019), that is

$$\gamma_{13} = c_1 \frac{\lambda_1 - 1}{\lambda_1^{max} - 1} \quad \text{and} \quad \gamma_{31} = c_2 \frac{\lambda_3 - 1}{\lambda_3^{max} - 1}, \tag{11}$$

where c_1, c_2 and λ_1^{max}, λ_3^{max} are the maximal values of the shear and stretch, respectively. Due to the lack of information on the shear measurements in Sirry et al. (2016a), we assume $c_1 = 0.2$, $c_2 = 0.05$ which is close to the values obtained by Guan et al. (2019) when evaluating the biaxial testing of neonatal porcine ventricular free walls (Ahmad et al., 2018).

2.3.2. Fibre contribution

We assume the myocardium to be orthotropic and the collagenous scar structure transversely isotropic, both incompressible. In the healthy myocardium, the anisotropy is caused by the presence of myofibres organised in the sheet layers, whereas in the infarcted tissue, the myocytes are replaced by a scar structure consisting of collagen fibres (Fomovsky and Holmes, 2010; Talman and Ruskoaho, 2016). Let $\mathbf{f}_0$, $\mathbf{s}_0$ and $\mathbf{n}_0$ denote the fibre, sheet and normal direction in the reference configuration (Holzapfel and Ogden, 2009). The strain energy function can be expressed in terms of invariants of $\mathbf{C}$, namely

$$\Psi = \Psi_{iso}(I_1) + \Psi_{fib}(I_{4_f}) + \nu \Psi_{ortho}(I_{4_s}, I_{8fs}), \tag{12}$$

$$\nu = \begin{cases} 1 & \text{for myocardium} \\ 0 & \text{for scar structure} \end{cases}$$

where $I_1 = \mathrm{tr}(\mathbf{C})$ and $I_{4_f} = \mathrm{tr}(\mathbf{C}\mathbf{f}_0 \otimes \mathbf{f}_0)$, $I_{4s} = \mathrm{tr}(\mathbf{C}\mathbf{s}_0 \otimes \mathbf{s}_0)$, $I_{8fs} = \mathrm{tr}(\mathbf{C}\mathbf{f}_0 \otimes \mathbf{s}_0)$. The Cauchy stress can then be expressed as

$$\boldsymbol{\sigma} = 2\Psi_1 \mathbf{b} + 2\Psi_{4f} \mathbf{f} \otimes \mathbf{f} + \nu \left[2\Psi_{4s} \mathbf{s} \otimes \mathbf{s} + \Psi_{8fs} (\mathbf{f} \otimes \mathbf{s} + \mathbf{s} \otimes \mathbf{f}) \right] - p\mathbf{I}, \tag{13}$$

where $\mathbf{b} = \mathbf{F}\mathbf{F}^{\mathbf{T}}$ is the left Cauchy-Green tensor, $\mathbf{f} = \mathbf{F}\mathbf{f}_0$, $\mathbf{s} = \mathbf{F}\mathbf{s}_0$ is the fibre, sheet direction, respectively, mapped to the deformed configuration. Further $\Psi_i = \frac{\partial \Psi}{\partial I_i}$, $i \in \{1, 4f, 4s, 8fs\}$ represent the derivatives of the strain energy with respect to the invariants.

Due to the fact that the samples from infarcted regions are a mixture of muscle fibres and fibrotic scar tissue (see Fig. 7 and Sirry et al. (2016a)), and since the amount of fibrosis correlates with the tensile modulus described in Section 3.1, we introduce the strain energy function taking the amount of fibrosis $fib \in [0, 1]$ into account:

$$\Psi = (1 - fib)\, \Psi^m + fib\, \Psi^s, \tag{14}$$

where each component can be decomposed according to (12), namely

$$\Psi^i = \Psi^i_{iso}(I^i_1) + \Psi^i_{fib}(I^i_{4f}) + \nu \Psi^m_{ortho}(I^m_{4s}, I^m_{8fs}), \quad \text{for} \quad i \in \{m, s\}. \tag{15}$$

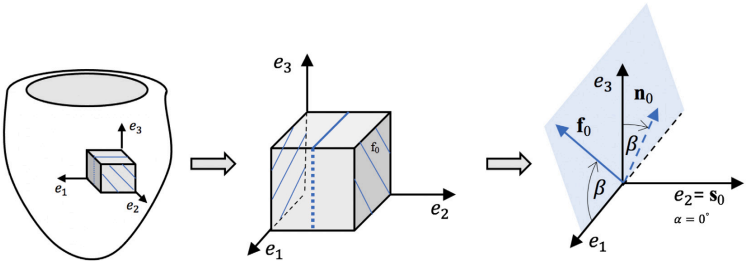

Fig. 2. Schematic representation of the myocardial tissue probe in the reference configuration showing fibre-reinforced structure. The fibre direction $\mathbf{f}_0$ is displayed in the Cartesian coordinates system with the unit basis e_1, e_2, e_3 aligned with the circumferential, radial and longitudinal direction, respectively and in the local coordinate system $\mathbf{f}_0$, $\mathbf{s}_0$, $\mathbf{n}_0$. We assume that the sheet angle is zero. Consequently, $\mathbf{f}_0$ and $\mathbf{n}_0$ rotate in the e_1e_3-plane highlighted in light blue.

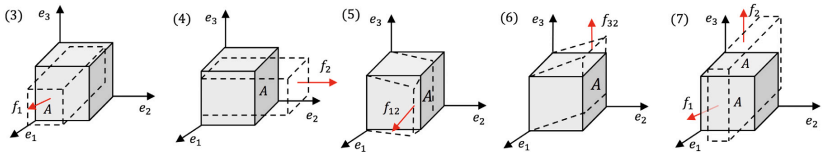

Fig. 3. Schematic representation of the performed mechanical tests. The numbers in the brackets correspond to the equation numbers of loading modes given in Section 2.3.1. Dashed lines represent to the deformed configuration.

The indices m and s represent the quantities associated with the healthy myocardial tissue and the scar structure after MI, respectively. Consequently, the Cauchy stress takes the form

$$\boldsymbol{\sigma} = (1 - fib)\,\boldsymbol{\sigma}^m + fib\,\boldsymbol{\sigma}^s, \tag{16}$$

where each component can be decomposed according to (13), namely

$$\boldsymbol{\sigma}^i = 2\Psi_1^i \mathbf{b} + 2\Psi_4^i \mathbf{f}^i \otimes \mathbf{f}^i + \nu \left[2\Psi_{4s}^m \mathbf{s}^m \otimes \mathbf{s}^m + \Psi_{8fs}^m (\mathbf{f}^m \otimes \mathbf{s}^m + \mathbf{s}^m \otimes \mathbf{f}^m) \right] - p\mathbf{I}. \tag{17}$$

So far, we considered all fibres to have the same direction $\mathbf{f}_0^i$ in the reference configuration. But this is eventually not the case in the considered mechanically tested samples. Therefore, in the following, the presence of multiple fibre directions is considered. Several studies taking fibre dispersion into account have been conducted where two main approaches are widely used, namely angular integration (AI) and a generalised structure tensor (GST). An overview of the previous studies is given in Holzapfel et al. (2015, 2019). In our study, we use the AI approach, firstly introduced by Lanir (1983). The advantage is that AI easily allows the exclusion of individual fibres if they are compressed (Holzapfel et al., 2015), i.e. $\Psi_{fib}^i = 0$ if $I_{4f}^i \leq 1$ (see (24)). We introduce a possible fibre direction in the reference configuration given by spherical coordinates

$$\mathbf{f}_0(\alpha, \beta) = \cos\beta \cos\alpha\, \boldsymbol{e}_1 + \cos\beta \sin\alpha\, \boldsymbol{e}_2 + \sin\beta\, \boldsymbol{e}_3, \tag{18}$$

where $\alpha \in [0, 2\pi]$ and $\beta \in [-\pi/2, \pi/2]$ represent the azimuthal angle (corresponding to the angle with respect to $\boldsymbol{e}_1$) and polar angle (corresponding to the angle with respect to the plane spanned by $\boldsymbol{e}_1$ and $\boldsymbol{e}_2$), respectively. The direction $\boldsymbol{e}_1$ is aligned with the circumferential, $\boldsymbol{e}_2$ with the radial and $\boldsymbol{e}_3$ with the longitudinal direction. The fibre stretch $\lambda^i = \sqrt{I_{4f}^i}$ can be obtained from the transformation of the global deformation gradient to the local fibre coordinates, namely the stretch along a fibre with an angle α and β is given by evaluating the expression $I_{4f}^i = \mathrm{tr}(\mathbf{C}\mathbf{f}_0^i \otimes \mathbf{f}_0^i)$. In the following, we assume the fibre direction to be aligned with the circumferential direction, i.e. $\alpha = 0°$ and only β varies, see Fig. 2. For the healthy myocardium, this assumption is based on the previous studies (Chen et al., 2005; Milne et al., 2019) stating that the sheet angle in rats is close to 0°. In the fibrotic scar tissue of the mid-ventricle MI, the collagen fibres mostly align in circumferential direction (Sirry et al., 2016a) which can also be confirmed by our microscopic images (Fig. 7). With this assumption, we introduce the local coordinate system:

$$\mathbf{f}_0^i = [\cos\beta,\ 0,\ \sin\beta],\ \mathbf{s}_0^m = [0,\ 1,\ 0],\ \mathbf{n}_0^m = [-\sin\beta,\ 0,\ \cos\beta], \tag{19}$$

where the sheet and normal directions are only considered in the healthy muscle. Further, let $\phi_f^i(\beta)$ represent the probability density of the fibre angle β. The Cauchy stress in (17) can be generalised for multiple fibre directions as

$$\boldsymbol{\sigma}^i = 2\Psi_1^i \mathbf{b} + 2 \int_{-\pi/2}^{\pi/2} \phi_f^i(\beta) \Psi_4^i \mathbf{f}^i(\beta) \otimes \mathbf{f}^i(\beta)\, \mathrm{d}\beta \tag{20}$$

$$+ \nu \int_{-\pi/2}^{\pi/2} \phi_f^i(\beta) \left\{ 2\Psi_{4s}^m \mathbf{s}^m \otimes \mathbf{s}^m + \Psi_{8fs}^m (\mathbf{f}^m(\beta) \otimes \mathbf{s}^m + \mathbf{s}^m \otimes \mathbf{f}^m(\beta)) \right\} \mathrm{d}\beta - p\mathbf{I}.$$

The probability density is normalised according to

$$\int_{-\pi/2}^{\pi/2} \phi_f^i(\beta)\, \mathrm{d}\beta = 1. \tag{21}$$

Based on the experimental data, an appropriate function ϕ_f^i has to be designed. In the rat healthy myocardium, the muscle fibres rotate linearly from epicardium to endocardium (Chen et al., 2005; Milne et al., 2019; Teh et al., 2016), therefore we set β to be uniformly distributed, i.e.

$$\phi_f^m(\beta) = \begin{cases} \frac{1}{\beta_{max} - \beta_{min}} & \text{if} \quad \beta \in [\beta_{min}, \beta_{max}], \\ 0 & \text{else,} \end{cases} \tag{22}$$

where β_{min} is the minimal and β_{max} the maximal fibre angles in the probe. If the thickness of the probe equals the ventricular wall thickness, we assume $\beta_{min} = -60°$ and $\beta_{max} = 60°$. In the uniaxial tests, we set $\beta_{min} = -30°$ and $\beta_{max} = 30°$. This assumption is based on the radial dimension of the probe punched from the middle ventricular region (1.2 mm), which accounts for approximately 50% of the full ventricular wall thickness, see Fig. 1.

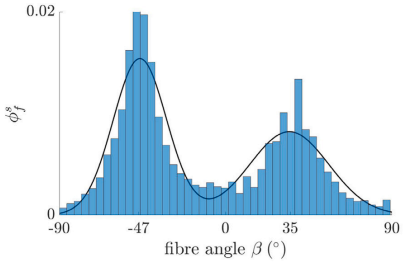

(a) Section S1-S10, fitted parameters: $w_1 = 0.56$, $w_2 = 0.44$, $\mu_1 = -46.63°, \mu_2 = 34.83°$ °, $\Sigma_1 = 209.84°$, $\Sigma_2 = 446.65°$.

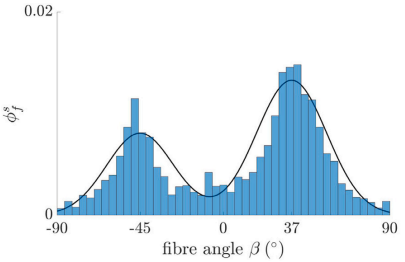

(b) Section S4-S7, fitted parameters: $w_1 = 0.37$, $w_2 = 0.63$, $\mu_1 = -45.16°, \mu_2 = 36.90°$ °, $\Sigma_1 = 329.03°$, $\Sigma_2 = 362.38°$.

Fig. 4. Probability density $\phi_f^s(\beta) = \sum_{i=1}^{2} w_i \mathcal{N}(\mu_i, \Sigma_i)$ plotted against fibre angle β. The histogram data are extracted from Sirry et al. (2016b) (rat group 14 days after MI) for transmural sections S1-S10 and S4-S7 used for fitting of biaxial and uniaxial tests, respectively.

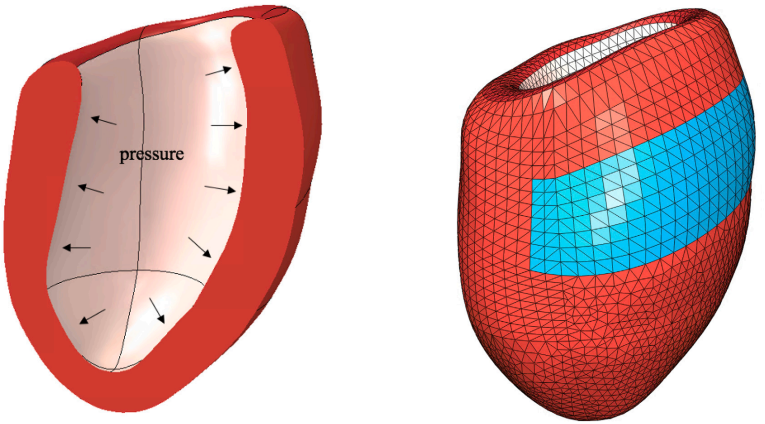

Fig. 5. Left: NURBS model of rat LV reconstructed from MRI. Pressure boundary condition on the inner ventricular surface displayed in rose is applied – the pressure is linearly increased from 0 to 5 mmHg in the healthy case and from 0 to 20 mmHg in the infarcted case. Right: tetrahedral mesh model of rat LV (53 905 FEs). The highlighted blue FEs correspond to the infarcted scar tissue. The remaining red and rose FEs represent the intact myocardium.

The distribution of collagen fibres in the fibrotic scar of the infarcted tissue is modelled with a mixture of the normal distributions, namely

$$\phi_f^s(\beta) = \sum_{j=1}^{n} w_j \mathcal{N}(\mu_j, \Sigma_j), \tag{23}$$

where w_j are weights, $n = 2$ and $\mathcal{N}(\mu_j, \Sigma_j)$ is the probability density function of the normal distribution with mean μ_j and standard deviation Σ_j. The model is calibrated with the experimental data in the group 14 days after MI given in Sirry et al. (2016b) using the function *fitgmdist* from MATLAB, see Fig. 4. For the biaxial tests, we consider the fibre angle distribution over the whole transmural depth (section S1-S10 in Sirry et al. (2016a)). For the uniaxial tests, we assume the same collagen fibre distribution, however, taking into account that the samples are punched from the middle ventricular region, only the sections S4-S7 are considered.

2.4. Parameter fitting

We consider anisotropic exponential strain energy functions depending on the invariants I_1^i, I_{4f}^i, and additionally I_{4s}^m and I_{8fs}^m for the myocardium (Holzapfel and Ogden, 2009). The terms in (15) take the following form

$$\begin{aligned}
\Psi_{iso}^i &= \frac{a^i}{2b^i} \exp\left[b^i (I_1^i - 3)\right], \\
\Psi_{fib}^i &= \frac{a_f^i}{2b_f^i} \left(\exp\left[b_f^i (\max(I_{4f}^i, 1) - 1)^2\right] - 1\right) \\
\Psi_{ortho}^m &= \frac{a_s^m}{2b_s^m} \left(\exp\left[b_s^m (\max(I_{4s}^m, 1) - 1)^2\right] - 1\right) \\
&\quad + \frac{a_{fs}^m}{2b_{fs}^m} \left(\exp\left[b_{fs}^m (I_{8fs}^m)^2 - 1\right]\right).
\end{aligned} \tag{24}$$

Let $\boldsymbol{\mu}^s = \{a^s, b^s, a_f^s, b_f^s\}$ and $\boldsymbol{\mu}^m = \{a^m, b^m, a_f^m, b_f^m, a_s^m, b_s^m, a_{fs}^m, b_{fs}^m\}$ denote the material parameters, which are estimated with a nonlinear least

square minimisation function (*lsqcurvefit* from MATLAB) using the objective functions given in (26) and (28). Due to the presence of the maximum operator, the fibres and sheets do not contribute to the strain energy if they are under compression. The goodness of the fit is evaluated by the widely used coefficient of determination R^2 given as

$$R^2 = 1 - \frac{S_{err}}{S_{tot}}, \tag{25}$$

where S_{err} respectively S_{tot} are the sums of squares of the differences between the stress predicted from the model and experimental data respectively between the mean of experimental data and the experimental data (Budday et al., 2017; Holzapfel et al., 2019).

In a first step, we calibrate the model with the average experimental data for a healthy myocardium such that we set $fib = 0$ in (14). Details are given in Section 2.4.1. In a second step, the material model for the infarcted myocardium is fitted to the experimental data, while the parameters obtained in the first step are kept constant and the muscle contribution is, according to (14), reduced to $(1 - fib)$. Details are given in Section 2.4.2. In both steps, we firstly fit each loading mode separately. Then, in the healthy and infarcted case, simultaneous fitting of all considered loading modes is performed in order to obtain two parameter sets (one for the healthy muscle, one for the scar tissue) which fit the best to all experiments. An overview of parameters used by fitting is given in Table 1.

2.4.1. Healthy myocardium

To characterise the healthy rat myocardium, we calibrate the constitutive model with the average experimental data from uniaxial extension tests described in Section 2.1. As the control and sham groups did not show any significant difference in the stress-strain-relations, the influence on biomechanics from the operative practice is excluded and the average is built from both groups. We define a new group "healthy" consisting of the control and the sham group. In addition to our uniaxial data, we include the shear experiments published by Dokos et al. (2000). The shearing was performed in the circumferential-radial plane in circumferential direction (see (5)) and in longitudinal-radial plane in longitudinal direction (see (6)), the sample dimension is $5 \times 5 \times 2.2$ mm (circumferential, longitudinal, radial). In order to identify suitable material parameters, we solve the minimisation problem

$$\min_{\boldsymbol{\mu^m}} J^m(\boldsymbol{\mu^m}) := \min_{\boldsymbol{\mu^m}} \sum_{(ij)\in\boldsymbol{\gamma}} \sum_{k=1}^{N^{exp}_{(ij)}} (\sigma^m_{ij}(\boldsymbol{\mu^m}) - \bar{\sigma}^k_{ij})^2, \tag{26}$$

where $\boldsymbol{\gamma} := \{11, 22\}$ and $\boldsymbol{\gamma} := \{12, 23\}$ are the directions in the uniaxial and shear tests, respectively and $\boldsymbol{\gamma} := \{11, 22, 12, 23\}$ are the directions by the simultaneous fitting of all loading modes, $N^{exp}_{(ij)}$ the number of considered experimental data, $\boldsymbol{\mu}^m$ the set of material parameters in (24), $\bar{\sigma}^k_{ij}$ and $\sigma^m_{ij}(\boldsymbol{\mu^m})$ the experimentally determined and model predicted Cauchy stresses, respectively. For each combination of the loading modes, we start with the calibration of the 8-parameter orthotropic model, i.e. $\nu = 1$ in (12). To obtain the simplest strain energy function that fits to the test data, we perform the Akaike information criterion (AIC)-based model reduction (Burnham and Anderson, 2002; Guan et al., 2019; Schmid et al., 2006). Briefly, we successively drop off single invariants (i.e. the corresponding material parameters are set to zero) if their exclusion influences the value $\mathrm{AIC} = N^{exp} \ln((1/N^{exp}) J^m(\boldsymbol{\mu^m})) + 2K$ only minimally. K is the number of model parameters and $N^{exp} = \sum_{(ij)\in\boldsymbol{\gamma}} N^{exp}_{(ij)}$. We note that the lowest AIC value corresponds to the best model with respect to the model complexity and the goodness of the fit. The invariant is dropped off if

$$\gamma = \frac{\mathrm{AIC}_{reduced}}{\mathrm{AIC}_{HO}} \geq 0.95, \tag{27}$$

where $\mathrm{AIC}_{reduced}$ and AIC_{HO} are the reduced model and the original 8-parameter HO model, respectively. For the full algorithm we refer to the study Guan et al. (2019).

2.4.2. Infarcted myocardium

To calibrate the constitutive model for the infarcted myocardium, we consider the average experimental data from Section 2.1 for the infarct group with the amount of fibrosis $fib \geq 35\%$ and the data from equibiaxial testing for the group 14 days after MI published by Sirry et al. (2016a). The minimisation problem is given by

$$\min_{\boldsymbol{\mu^s}} J^s(\boldsymbol{\mu^m}) := \min_{\boldsymbol{\mu^s}} \sum_{(ij)\in\boldsymbol{\gamma}} \sum_{k=1}^{N^{exp}_{(ij)}} \left[(1 - fib_{ij})\, \sigma^m_{ij}(\boldsymbol{\mu^m}) + fib_{ij}\, \sigma^s_{ij}(\boldsymbol{\mu^s}) - \bar{\sigma}^k_{ij}\right]^2, \tag{28}$$

where $\boldsymbol{\gamma} := \{11, 22\}$ are the directions in the uniaxial extension tests, $\boldsymbol{\gamma} := \{11, 33\}$ in the equibiaxial tests and $\boldsymbol{\gamma} := \{11, 22, 11, 33\}$ by the simultaneous fitting. The parameter fib_{ij} is given by the average amount of fibrosis in the samples considered in this loading mode, namely $fib_{11} = fib_{22} = 0.60$ and $fib_{11} = fib_{33} = 0.47$ (Sirry et al., 2016a) in the uniaxial and equibiaxial test, respectively.

2.4.3. Passive end-diastolic filling

Similar to Guan et al. (2019), the model behaviour during the passive end-diastolic filling is tested by applying a pressure boundary condition to the endocardium of the LV (Fig. 5). The FE model based on the geometry from magnetic resonance imaging (MRI) from a rat is used for all simulations in order to compare the influence of the species-specific parameters on the pressure-volume relation. For further details see Duong et al. (2019). We investigate the differences between the former passive material parameters used in the study Duong et al. (2019) for a rat LV, the models based on the general Holzapfel-Ogden strain energy function (Holzapfel and Ogden, 2009) in different species (neonatal porcine, adult porcine, human) calibrated with the material parameters identified by Guan et al. (2019) and our model with the new parameters for the healthy myocardium.

In order to simulate the pressure-volume relation in the tissue after MI, we model a connected part of the LV as a fibrotic scar ($fib = 1$) and the remaining part as intact myocardium ($fib = 0$), see Fig. 5. The percentage of scar with respect to the whole LV represents the infarct size. It is modulated by setting $fib = 1$ for a varying amount of FE in the domain (25%, 50%, 75% and 100%). In the healthy case, the pressure is linearly increased from 0 to 5 mmHg which is close to the left ventricular end-diastolic pressure (LVEDP) in healthy rats (Azevedo et al., 2012; Fletcher et al., 1981; Saraiva et al., 2007). For the infarcted case, the pressure is increased from 0 to 20 mmHg. The reason is that in the rats after MI, the LVEDP is increased (Azevedo et al., 2012; Fletcher et al., 1981; Jegger et al., 2006; Saraiva et al., 2007). However, its value varies among the studies (6 mmHg to 33 mmHg) and it is dependent on the infarction size. The simulation is performed with the software Abaqus and we implemented a new user subroutine UMAT for the modified HO strain energy. Furthermore, a rule-based fibre direction (Wong and Kuhl, 2014) with linearly rotating fibres from $\beta_{max} = +60°$ on the epicardium to $\beta_{min} = -60°$ on the endocardium is implemented. The fibre angle is given with respect to the coordinate system depicted in Fig. 2.

2.5. Statistical analysis

The statistical analysis is performed using the Statistics Toolbox in MATLAB and a p-value lower than 0.05 is considered to be significant. The elastic material properties in the uniaxial tests are examined by comparison of the tensile moduli computed from the slope in the steep region of the uniaxial stress-strain curves of individual samples, namely $E_i = \frac{\sigma_{ii}(\epsilon^2_{ii}) - \sigma_{ii}(\epsilon^1_{ii})}{\epsilon^2_{ii} - \epsilon^1_{ii}}$, $i \in \{1, 2\}$. $\epsilon_{11}, \epsilon_{22}$ represent the strain in circumferential and radial direction, respectively and $\epsilon^1_{11} = 0.2$, $\epsilon^2_{11} = 0.35$, $\epsilon^1_{22} = 0.35$, $\epsilon^2_{22} = 0.5$. See Fig. 6 for representative curves. Pairwise t-tests (*ttest2*) are performed for the comparison of means in the following groups: control versus sham; healthy (control and sham) versus infarcted. The linear dependency of tensile moduli on

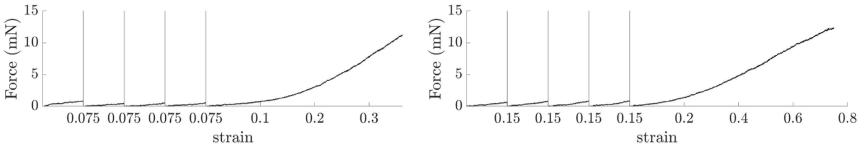

Fig. 6. Representative measurement outputs for EA via uniaxial extension test in circumferential (a) and radial (b) direction with four preconditioning cycles and one main cycle at constant velocity 1 μm/s. Strain values are given with respect to the corresponding cycle. The ends of the preconditioning cycles are marked with vertical lines.

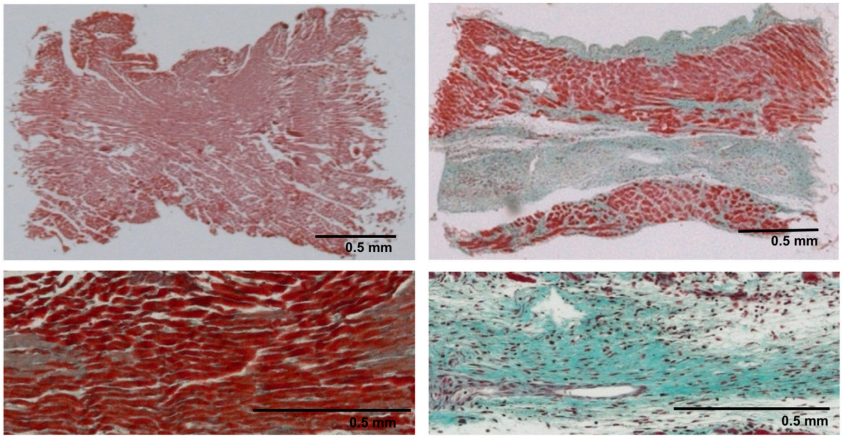

Fig. 7. Masson-Goldner-Trichome staining images of healthy (left) and infarcted (right) rat myocardium at × 2.5 (upper) and × 10 (lower) magnification demonstrating circumferentially aligned fibres. Fibrotic tissue is stained in blue and myocytes in red.

the amount of fibrosis is examined by linear regression (*fitlm*). The normality of the data is confirmed by the Lilliefors test (*lillietest*). We emphasise that the tensile moduli are computed in order to compare differences between different groups and not to determine meaningful material parameters for computational simulation.

3. Results

Table 2 summarises the subject characteristics included in this study. Fig. 6 shows representative force-strain curves of four preconditioning cycles followed by the main measurement in the uniaxial extension tests.

3.1. Healthy vs. infarcted tissue

Representative histology images of healthy and infarcted samples are depicted in Fig. 7. In the EA via uniaxial extension tests, we observe the following differences: Firstly, tensile moduli are significantly different in the healthy and infarcted samples in circumferential and radial direction. Secondly, the circumferential and radial tensile moduli differ significantly in both groups, healthy and infarcted. The group comparison is depicted in Fig. 8 left. The relationship between the amount of fibrosis and tensile moduli in the infarcted samples is modelled with the linear regression shown in Fig. 8 right. The model indicates significant positive correlation ($R^2 = 0.778,\ p < 0.001$) when the circumferential tensile modulus is considered.

3.2. Parameter fitting

3.2.1. Healthy myocardium

Table 3 and Fig. 10 show the results by fitting the strain energy function $\Psi^m = \Psi^m_{iso} + \Psi^m_{fib} + \nu\Psi^m_{ortho}$ to the experimental data from uniaxial tests described in Section 2.1 and shear tests from Dokos et al. (2000). The influence of the invariants on the fitting results is depicted in Fig. 9. By simultaneous fitting, we achieve a good result ($R^2 = 0.998$) when in addition to the invariants I^m_1 and I^m_{4f} at least the coupling invariant I^m_{8fs} is included in (24), see Fig. 10c. The necessity of I_{4f} is based on the included uniaxial tests, whereas I_{8fs} is essential if shear tests are used for the model calibration. With the obtained parameters and reduced strain energy function, we demonstrate six shear experiments according to Holzapfel and Ogden (2009) . The resulting predictive stress-strain curves are depicted in Fig. 11.

3.2.2. Infarcted myocardium

Table 4 and Fig. 12 show the results by fitting the strain energy function $\Psi = \Psi^m + \Psi^s_{iso} + \Psi^s_{fib}$ to the experimental data from uniaxial tests described in Section 2.1 and equibiaxial tests from Sirry et al. (2016a). We clearly observe anisotropic mechanical behaviour during the uniaxial extension tests which is in agreement with findings in Sirry et al. (2016a). They also found that the collagen fibres in mid-ventricle infarcts align mostly in the circumferential direction leading to higher stress in this direction. When calibrating the equibiaxial test, we only achieved good fitting result ($R^2 = 0.999$) if also shear deformation

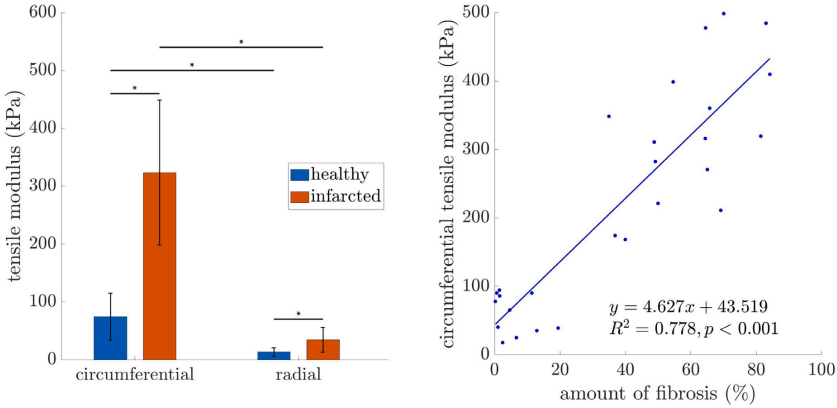

Fig. 8. Left: Circumferential and radial tensile moduli in healthy and infarcted group (mean ± SD). Significantly different pairs are annotated with asterisks (*). Tensile moduli are calculated from the slope of the steep region of the uniaxial stress-strain curves of individual samples. Right: fitted regression line of amount of fibrosis and circumferential tensile modulus.

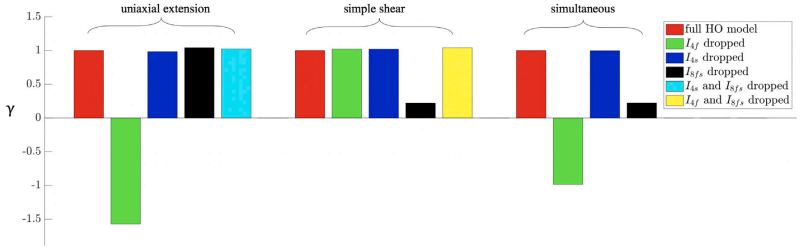

Fig. 9. AIC model reduction for the HO strain energy function.

Table 3
Constitutive parameters obtained from calibrating the strain energy $\Psi^m = \Psi^m_{iso} + \Psi^m_{fib} + \nu\Psi^m_{ortho}$ for the uniaxial extension and simple shear tests. Coding: 0* – parameter is excluded from the strain energy function, based on the AIC-model reduction, see Section 2.4.1.

	a^m (kPa)	b^m (–)	a^m_f (kPa)	b^m_f (–)	a^m_s (kPa)	b^m_s (–)	a^m_{fs} (kPa)	b^m_{fs} (–)	R^2	AIC
1. Uniaxial extension	1.726	1.180	7.048	0.001	0*	0*	0*	0*	0.998	−99.628
2. Simple shear	1.566	1.523	0*	0*	0*	0*	1.463	9.153	0.994	−198.540
3. Simultaneous	1.665	1.237	7.822	0.008	0*	0*	1.342	9.178	0.998	−253.588

Table 4
Constitutive parameters obtained from calibrating the strain energy $\Psi = \Psi^m + \Psi^s_{iso} + \Psi^s_{fib}$ for the uniaxial extension and equibiaxial tests. The material parameters for Ψ^m are according to case 3. in Table 3.

	a^s (kPa)	b^s (–)	a^s_f (kPa)	b^s_f (–)	R^2
1. Uniaxial extension	14.208	0.703	120.382	0.420	0.994
2. Equibiaxial extension (no shear)	0.439	19.552	64.623	0.001	0.907
3. Equibiaxial extension (with shear)	7.330	5.764	2.538	2.725	0.999
4. Simultaneous (no shear)	11.584	0.685	86.059	0.837	0.974
5. Simultaneous (with shear)	16.591	0.180	50.717	1.891	0.877

according to (8) is included. However, combining the biaxial test with uniaxial tests, the simultaneous fit is better for shear-free deformation.

3.3. End-diastolic filling of rat left ventricle

Firstly, applying a pressure boundary condition on the inner wall of the LV up to the physiological range of LVEDP, we observe different pressure-volume relations when different species- and age-specific parameter sets are used (Fig. 13). This result highlights the importance of adequate estimation of species-specific material parameters, especially when a realistic small dimensional rat heart geometry is considered. The curves obtained with our new parameters and parameters for a neonatal porcine heart show nearly identical shape. Compared to our previous parameters for a rat (Duong et al., 2019), the LV tissue is

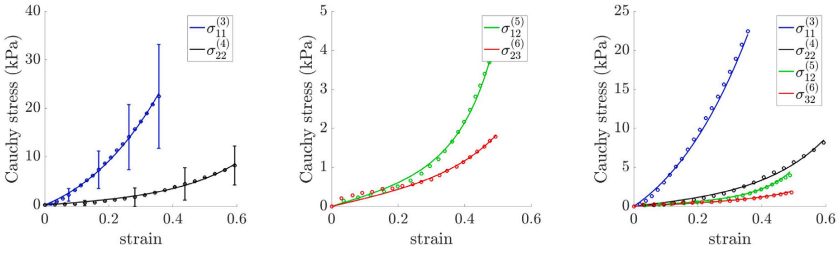

(a) 1. **(b)** 2. **(c)** 3.

Fig. 10. Stress-strain plots with strain energy $\Psi^m = \Psi^m_{iso} + \Psi^m_{flb} + \nu\Psi^m_{ortho}$. Experimental data are marked with dots and model derived data with solid lines. The superscripts in the Cauchy stress components refer to the equation numbers of loading modes given in Section 2.3.1. The numbers in the subfigures correspond to the combination of the loading modes and set of fitted parameters given in Table 3. Error bars describe the standard deviation in the uniaxial tests.
Source: The data for the shear tests are extracted from Dokos et al. (2000).

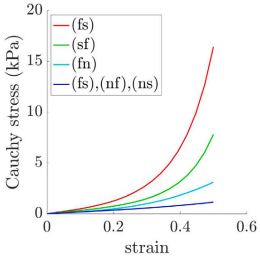

Fig. 11. Predictive stress-strain curves for simple shear test for six loading modes with respect to the local coordinate system $\mathbf{f}_0, \mathbf{s}_0, \mathbf{n}_0$. The shearing modes $(\cdot)$ correspond to the notation in the original work (Holzapfel and Ogden, 2009).

slightly weaker with the new set of parameters. However, the difference in the end-diastolic volume (EDV) is only approximately 2 μL. Therefore, the previous parameter approximation based on the fitting of the shear tests in porcine heart using the scaling factor 0.5 turns out to be almost accurate, when modelling the end-diastolic filling phase in the healthy rat LV. The largest difference in pressure-volume relations is observed by the parameters based on the mechanical tests in human and porcine myocardium.

Secondly, we can confirm a stiffer behaviour in the infarcted myocardium (Fig. 13b). When considering the LVEDP at the volume 131 μL, corresponding to the EDV in the healthy case by LVEDP = 5 mmHg, the infarction size correlates with the increase in the LVEDP. Similar behaviour was observed in an experimental study of Fletcher et al. (1981).

4. Discussion

The focus of the present work is put on the identification of the passive material parameters in the healthy and infarcted rat LV by means of mechanical testing and subsequent parameter fitting. We observed that the infarcted tissue is stiffer in both directions. The reason is that after MI, the myocardium is being replaced by healing scar formation mostly consisting of stiff collagen fibres (Fomovsky and Holmes, 2010; Talman and Ruskoaho, 2016). The different tensile moduli in circumferential and radial directions indicate an anisotropic behaviour both in healthy and infarcted samples. This anisotropy in infarcted samples is in agreement with the findings in Sirry et al. (2016a) but disagrees with Fomovsky and Holmes (2010) who observed that healing infarcts in the rat were mechanically and structurally isotropic. Possible reasons for this discrepancy have been extensively discussed in Sirry et al. (2016a). We note that in these studies, the differences are based on the mechanical testing in circumferential and longitudinal direction, whereas in our study the circumferential and radial directions are tested. The weaker radial direction indicates that the stiff collagen and muscle fibres are mostly aligned circumferentially. This observation also supports our assumption $\alpha = 0°$ for the parameter fitting. The orthotropy in the healthy myocardium in different species was confirmed by various studies (Sommer et al., 2015b; Dokos et al., 2002; Ahmad et al., 2018). Assuming the constant zero sheet angle, the radial extension corresponds to the extension in the sheet direction. This is, based on the fitted parameters in Guan et al. (2019), weaker than the fibre direction in all previous studies mentioned above and agrees with our findings.

Furthermore, a weak exponential behaviour in the fibre direction resulting from the experimental stress-strain relation in the uniaxial extension test is observed. Therefore, the material parameter b_f takes values close to zero if uniaxial tests are included. In contrast to that, b_f reaches approximately the value 15 in the original work introducing the orthotropic strain energy function (Holzapfel and Ogden, 2009) which is calibrated with the shear experiments in a pig. However, the parameter values and the model including four invariants (I_1, I_{4f}, I_{4s} I_{8fs}) are based on the simple shear data from Dokos et al. (2002) and cannot represent all responses of the myocardium. Especially, the parameters show differences if different loading modes are fitted (Guan et al., 2019). The latter study also indicates that if uniaxial extension tests are included, the isotropic response and the response in the fibre direction show a relatively weak exponential growth ($b = 0.484$ kPa and $b_f = 1.25$), whereas if only shear experiments are included, these parameters take higher values. Comparing the parameters used in the study of Duong et al. (2019) obtained by fitting the experimental data provided by Dokos et al. (2002) with the scaling factor 0.5 and results in this study, we observe similar differences, namely the stress-strain curves in the shear testing have stronger exponential growth than in the uniaxial testing.

In Fig. 11, all six shearing modes with respect to the local coordinate system $\mathbf{f}_0, \mathbf{s}_0, \mathbf{n}_0$, introduced by Holzapfel and Ogden (2009) and depicted in Fig. 2 right, are demonstrated with the obtained parameters. Due to the reduced model, the stress-strain curves for the shearing modes (fs),(nf),(ns) overlap. But, this tendency is close to the experimental curves for porcine (Dokos et al., 2002) and human hearts (Sommer et al., 2015b). The stiffest response is in the (fs) mode, corresponding to the shearing in the fibre-sheet plane in the sheet direction, which is also in agreement with the experimental studies

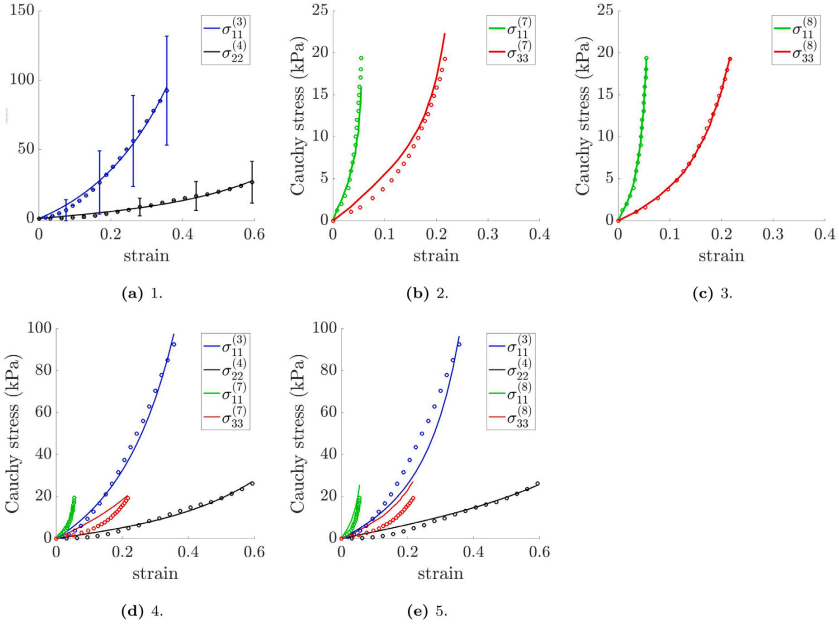

(a) 1. **(b)** 2. **(c)** 3.

(d) 4. **(e)** 5.

Fig. 12. Stress-strain plots with strain energy $\Psi = \Psi^m + \Psi^s_{iso} + \Psi^s_{fib}$. Experimental data are marked with dots and model derived data with solid lines. The superscripts in the Cauchy stress components refer to the equation numbers of loading modes given in Section 2.3.1. The numbers in the subfigures correspond to the combination of the loading modes and set of fitted parameters given in Table 4. Error bars describe the standard deviation in the uniaxial tests.
Source: The data for the biaxial tests are extracted from Sirry et al. (2016a).

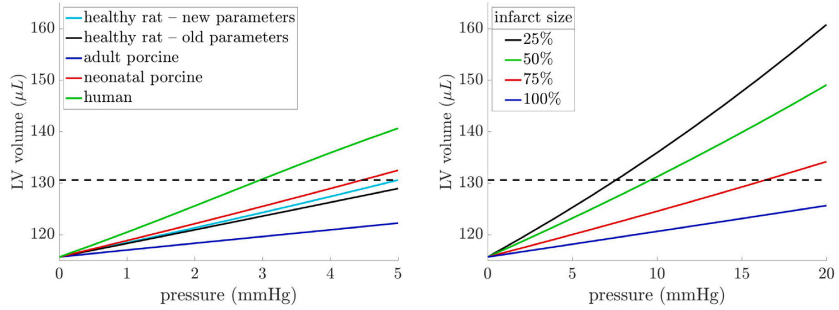

(a) Pressure-volume relation in end-diastolic filling using our new parameters and parameters obtained in Guan et al. (2019) for different species.

(b) Pressure-volume relation in end-diastolic filling with different infarct sizes. The infarct size corresponds to the percentage of the finite elements with the strain energy $\Psi = \Psi^s_{iso} + \Psi^s_{fib}$.

Fig. 13. Comparison of different passive material models in the FE model of the healthy and infarcted rat LV during the end-diastolic filling. The dashed lines represent the EDV obtained with the new parameters for the healthy case.

above. However, compared to these studies, our predictive curve for the (fn) mode is quite flat. On the other hand, due to the lack of experimental data for the rat myocardium, it is not possible to validate this prediction and therefore, an experimental validation should be done in the future.

The fitting results for the infarcted samples demonstrate that the cardiac tissue after MI, consisting of the intact myocardium and scar tissue, can be modelled with the additive decomposition of the strain energy function scaled by the amount of fibrosis, as proposed in (14). The intact myocardium is modelled with an orthotropic Holzapfel-Ogden constitutive law, whereas the scar can be described by the transversely isotropic model. This is also in agreement with the pathophysiological processes after MI: The lack of oxygen induces cardiomyocytes' death which leads to the activation of the fibroblasts and reparative scar formation (Talman and Ruskoaho, 2016). Consequently, the tissue becomes stiffer in the infarcted region. This can be also seen in the increase in the material parameters, both for the isotropic matrix and for the fibres, if the healthy and infarcted tissue is compared, see Tables 3 and 4. The same correlation is observed in the FE simulation, i.e. the bigger the infarcted domain ($fib = 1$) is assigned in the model, the flatter is the pressure-volume curve. However, after MI, the increase in ventricular stiffness is counteracted by the radial ventricular wall thinning, dilation of scar tissue and remodelling (Pfeffer et al., 1991; Stefanon et al., 2013; Sutton Martin and Norman, 2000). This leads to a change in the geometry and especially in the EDV. Therefore, any quantitative comparison is not meaningful and requires more experimental data regarding haemodynamics and geometry.

In the FE simulation of the passive end-diastolic filling, a nearly linear pressure-volume relation for all set of parameters is observed. The reason is that the applied pressure is in the physiological range of LVEDP. At this pressure (5 mmHg for the healthy myocardium), even a strain energy function calibrated with the parameters based on the mechanical properties in porcine and human hearts do not show the exponential growth. The same nearly linear shape was demonstrated in the study Guan et al. (2019) and can be observed in the experimental pressure-volume loops for rats, e.g. in Pacher et al. (2004), Shioura et al. (2007).

5. Conclusion, limitations and future work

In our work, we performed uniaxial extension tests on the healthy and infarcted rat LV. In both cases, we observe anisotropic mechanical properties. The tissue samples after MI are recognised to be significantly stiffer both in circumferential and radial direction. Furthermore, we observe a strong positive linear correlation between the circumferential tensile modulus and the amount of fibrosis.

Subsequently, based on our uniaxial experiments and other mechanical tests from the literature, we propose a model for the modified Holzapfel-Ogden strain energy function. Here, the infarcted tissue is modelled as a mixture of the intact orthotropic myocardium and transversely isotropic collagenous scar formation. The amount of fibrosis fib serves as a weighting factor. The fitting results confirm that the proposed model can capture the behaviour of the healthy and infarcted tissue. This mixture model has two main advantages: Firstly, it can be calibrated with the measurements on tissue samples consisting of the fibrotic scar and healthy muscle together with the known amount of fibrosis ($0 \leq fib \leq 1$). Secondly, the weighting factor allows us to model a healthy myocardium, an infarction zone consisting of the dense fibrotic scar and a transmission zone by setting $fib = 0$, $fib = 1$, $0 < fib < 1$, respectively. With the later approach, especially the infarct border zone can be modelled in analogy to the previous studies (Berberoğlu and Göktepe, 2015; Leong et al., 2019) where the ventricular stiffness was smoothly scaled between the healthy and infarction zone.

To approach a more physiological computational model, the following enhancements are suggested. The assumption on the collagen fibre direction in the uniaxial tests is based on the study Sirry et al. (2016a) and on the observed external texture in the microscopic images. Fibre dispersion measurements on our own samples, e.g. via second harmonic generation microscopy, would increase the modelling accuracy and are subject of an ongoing study. To fully characterise the orthotropic myocardium, more loading modes, especially shear tests in the remaining four directions, should be considered.

Despite the passive mechanical testing, electrophysiological experiments are planned to obtain realistic parameters for fully electromechanically coupled simulations of the rat cardiac cycle in a healthy and diseased case.

CRediT authorship contribution statement

Denisa Martonová: Conceptualisation, Methodology, Software, Formal analysis, Writing - original draft, Visualisation. **Muhannad Alkassar:** Conceptualisation, Methodology, Resources, Writing - review & editing, Project administration, Funding acquisition. **Julia Seufert:** Methodology, Writing - review & editing. **David Holz:** Software, Methodology, Writing - review & editing. **Minh Tuấn Dương:** Software, Methodology, Writing - review & editing. **Barbara Reischl:** Methodology, Writing - review & editing. **Oliver Friedrich:** Methodology, Investigation, Supervision, Resources, Writing - review & editing. **Sigrid Leyendecker:** Conceptualisation, Methodology, Writing - review & editing, Supervision, Funding acquisition.

Declaration of competing interest

The authors declare that they have no known competing financial interests or personal relationships that could have appeared to influence the work reported in this paper.

Acknowledgement

The authors thank the Klaus Tschira Stiftung, Germany grant 00.289.2016 for funding support.

References

Ahmad, F., Prabhu, R., Liao, J., Soe, S., Jones, M.D., Miller, J., Berthelson, P., Enge, D., Copeland, K.M., Shaabeth, S., Johnston, R., Maconochie, I., Theobald, P.S., 2018. Biomechanical properties and microstructure of neonatal porcine ventricles. J. Mech. Behav. Biomed. Mater. 88, 18–28.

Azevedo, P.S., Polegato, B.F., Minicucci, M.F., Pio, S.M., Silva, I.A., Santos, P.P., Okoshi, K., Paiva, S.A.R., Zornoff, L.A.M., 2012. Early echocardiographic predictors of increased left ventricular end-diastolic pressure three months after myocardial infarction in rats. Med. Sci. Monitor Int. Med. J. Exp. Clin. Res. 18 (7), BR253–BR258.

Baillargeon, B., Rebelo, N., Fox, D.D., Taylor, R.L., Kuhl, E., 2014. The living heart project: A robust and integrative simulator for human heart function. Eur. J. Mech. A Solids 48, 38–47.

Berberoğlu, E., Göktepe, S., 2015. Computational modeling of myocardial infarction. Proc. IUTAM 12, 52–61.

Budday, S., Sommer, G., Birkl, C., Langkammer, C., Haybaeck, J., Kohnert, J., Bauer, M., Paulsen, F., Steinmann, P., Kuhl, E., Holzapfel, G., 2017. Mechanical characterization of human brain tissue. Acta Biomater. 48, 319–340.

Burnham, K.P., Anderson, D.R., 2002. Model Selection and Multimodel Inference: A Practical Information-Theoretic Approach, second ed. Springer-Verlag, New York.

Chen, J., Liu, W., Zhang, H., Lacy, L., Yang, X., Song, S.-K., Wickline, S.A., Yu, X., 2005. Regional ventricular wall thickening reflects changes in cardiac fiber and sheet structure during contraction: Quantification with diffusion tensor MRI. Amer. J. Physiol. Heart Circul. Physiol. 289 (5), H1898–H1907.

Costa, K.D., Holmes, J.W., Mcculloch, A.D., 2001. Modelling cardiac mechanical properties in three dimensions. In: Kohl, P., Noble, D., Hunter, P.J. (Eds.), Phil. Trans. R. Soc. A 359 (1783), 1233–1250.

Costa, K.D., Hunter, P.J., Wayne, J.S., Waldman, L.K., Guccione, J.M., McCulloch, A.D., 1996. A three-dimensional finite element method for large elastic deformations of ventricular myocardium: II–Prolate spheroidal coordinates. J. Biomech. Eng. 118 (4), 464–472.

Demiray, H., 1976. Stresses in ventricular wall. J. Appl. Mech. 43 (2), 194–197.

Dokos, S., LeGrice, I.J., Smaill, B.H., Kar, J., Young, A.A., 2000. A triaxial-measurement shear-test device for soft biological tissues. J. Biomech. Eng. 122 (5), 471.

Dokos, S., Smaill, B.H., Young, A.A., LeGrice, I.J., 2002. Shear properties of passive ventricular myocardium. Amer. J. Physiol. Heart Circul. Physiol. 283 (6), H2650–2659.

Duong, M.T., Holz, D., Alkassar, M., Dittrich, S., Leyendecker, S., 2019. Interaction of the mechano-electrical feedback with passive mechanical models on a 3D rat left ventricle: a computational study. Front. Physiol. 10, 1041.

Eriksson, T.S.E., Prassl, A.J., Plank, G., Holzapfel, G.A., 2013. Modeling the dispersion in electromechanically coupled myocardium. Int. J. Numer. Methods Biomed. Eng. 29 (11), 1267–1284.

Fletcher, P.J., Pfeffer, J.M., Pfeffer, M.A., Braunwald, E., 1981. Left ventricular diastolic pressure-volume relations in rats with healed myocardial infarction. effects on systolic function.. Circ. Res. 49 (3), 618–626.

Fomovsky, G.M., Holmes, J.W., 2010. Evolution of scar structure, mechanics, and ventricular function after myocardial infarction in the rat. Amer. J. Physiol. Heart Circul. Physiol. 298 (1), H221–H228.

Freed, A.D., Einstein, D.R., Sacks, M.S., 2010. Hypoelastic soft tissues. Acta Mech. 213 (1–2), 205–222.

Gao, H., Li, W.G., Cai, L., Berry, C., Luo, X.Y., 2015. Parameter estimation in a holzapfel–ogden law for healthy myocardium. J. Eng. Math. 95 (1), 231–248.

Göktepe, S., Acharya, S.N.S., Wong, J., Kuhl, E., 2011. Computational modeling of passive myocardium. Int. J. Numer. Methods Biomed. Eng. 27 (1), 1–12.

Guan, D., Ahmad, F., Theobald, P., Soe, S., Luo, X., Gao, H., 2019. On the AIC-based model reduction for the general Holzapfel–Ogden myocardial constitutive law. Biomech. Model. Mechanobiol. 18 (4), 1213–1232.

Guccione, J.M., McCulloch, A.D., Waldman, L.K., 1991. Passive material properties of intact ventricular myocardium determined from a cylindrical model. J. Biomech. Eng. 113 (1), 42–55.

Gundiah, N., Chang, D., Zhang, P., Ratcliffe, M., Pruitt, L., 2004. Role of Elastin and Collagen in the Passive Mechanics of the Circulatory System (Ph. D. thesis). University of California.

Gupta, K.B., Ratcliffe, M.B., Fallert, M.A., Edmunds, L.H., Bogen, D.K., 1994. Changes in passive mechanical stiffness of myocardial tissue with aneurysm formation. Circulation 89 (5), 2315–2326.

Gurtin, M.E., 1981. An Introduction to Continuum Mechanics, First edn. Academic Press, New York.

Haug, M., Meyer, C., Reischl, B., Prölß, G., Nübler, S., Schürmann, S., Schneidereit, D., Heckel, M., Pöschel, T., Rupitsch, S., Friedrich, O., 2019. MyoRobot 2.0: An advanced biomechatronics platform for automated, environmentally controlled skeletal muscle single fiber biomechanics assessment employing inbuilt real-time optical imaging. Biosens. Bioelectron. 138, 111284.

Haug, M., Reischl, B., Prölß, G., Pollmann, C., Buckert, T., Keidel, C., Schürmann, S., Hock, M., Rupitsch, S., Heckel, M., Pöschel, T., Scheibel, T., Haynl, C., Kiriaev, L., Head, S., Friedrich, O., 2018. The MyoRobot: A novel automated biomechatronics system to assess voltage/Ca2+ biosensors and active/passive biomechanics in muscle and biomaterials. Biosens. Bioelectron. 102, 589–599.

Holzapfel, G.A., Niestrawska, J.A., Ogden, R.W., Reinisch, A.J., Schriefl, A.J., 2015. Modelling non-symmetric collagen fibre dispersion in arterial walls. J. R. Soc. Interface 12 (106), 20150188.

Holzapfel, G.A., Ogden, R.W., 2009. Constitutive modelling of passive myocardium: A structurally based framework for material characterization. Phil. Trans. R. Soc. A 367 (1902), 3445–3475.

Holzapfel, G.A., Ogden, R.W., Sherifova, S., 2019. On fibre dispersion modelling of soft biological tissues: A review. Proc. R. Soc. A: Math. Phys. Eng. Sci. 475 (2224), 20180736.

Humphrey, J.D., Yin, F.C., 1987. On constitutive relations and finite deformations of passive cardiac tissue: I. A pseudostrain-energy function. J. Biomech. Eng. 109 (4), 298–304.

Jegger, D., Jeanrenaud, X., Nasratullah, M., Chassot, P.-G., Mallik, A., Tevaearai, H., von Segesser, L.K., Segers, P., Stergiopulos, N., 2006. Noninvasive doppler-derived myocardial performance index in rats with myocardial infarction: Validation and correlation by conductance catheter. Amer. J. Physiol. Heart Circul. Physiol. 290 (4), H1540–H1548.

Lanir, Y., 1983. Constitutive equations for fibrous connective tissues. J. Biomech. 16 (1), 1–12.

LeGrice, I.J., Takayama, Y., Covell, J.W., 1995. Transverse shear along myocardial cleavage planes provides a mechanism for normal systolic wall thickening. Circ. Res. 77 (1), 182–193.

Leong, C.O., Leong, C.-N., Abed, A.A., Bakir, A.A., Liew, Y.M., Dokos, S., Lim, E., 2019. Computational modelling of the effect of infarct stiffness on regional myocardial mechanics. In: 2019 41st Annual International Conference of the IEEE Engineering in Medicine and Biology Society (EMBC). pp. 6952–6955.

Milne, M.L., Schick, B.M., Alkhazal, T., Chung, C.S., 2019. Myocardial fiber mapping of rat hearts using apparent backscatter, with histological validation. Ultrasound Med. Biol. 45 (8), 2075–2085.

Morita, M., Eckert, C.E., Matsuzaki, K., Noma, M., Ryan, L.P., Burdick, J.A., Jackson, B.M., Gorman, J.H., Sacks, M.S., Gorman, R.C., 2011. Modification of infarct material properties limits adverse ventricular remodeling. Ann. Thoracic Surg. 92 (2), 617–624.

Pacher, P., Mabley, J.G., Liaudet, L., Evgenov, O.V., Marton, A., Haskó, G., Kollai, M., Szabó, C., 2004. Left ventricular pressure-volume relationship in a rat model of advanced aging-associated heart failure. Amer. J. Physiol. Heart Circul. Physiol. 287 (5), H2132–H2137.

Pfeffer, J.M., Pfeffer, M.A., Fletcher, P.J., Braunwald, E., 1991. Progressive ventricular remodeling in rat with myocardial infarction. Amer. J. Physiol. Heart Circul. Physiol. 260 (5), H1406–H1414.

Saraiva, R., Kanashiro-Takeuchi, R., Antonio, E., Campos, O., Tucci, P., Moisés, V., 2007. Rats with high left ventricular end-diastolic pressure can be identified by Doppler echocardiography one week after myocardial infarction. Braz. J. Med. Biol. Res. 40 (11), 1557–1565.

Schmid, H., Nash, M.P., Young, A.A., Hunter, P.J., 2006. Myocardial material parameter estimation—a comparative study for simple shear. J. Biomech. Eng. 128 (5), 742–750.

Shioura, K.M., Geenen, D.L., Goldspink, P.H., 2007. Assessment of cardiac function with the pressure-volume conductance system following myocardial infarction in mice. Amer. J. Physiol. Heart Circul. Physiol. 293 (5), H2870–H2877.

Sirry, M.S., Butler, J.R., Patnaik, S.S., Brazile, B., Bertucci, R., Claude, A., McLaughlin, R., Davies, N.H., Liao, J., Franz, T., 2016a. Characterisation of the mechanical properties of infarcted myocardium in the rat under biaxial tension and uniaxial compression. J. Mech. Behav. Biomed. Mater. 63, 252–264.

Sirry, M.S., Butler, J.R., Patnaik, S.S., Brazile, B., Bertucci, R., Claude, A., McLaughlin, R., Davies, N.H., Liao, J., Franz, T., 2016b. Infarcted rat myocardium: data from biaxial tensile and uniaxial compressive testing and analysis of collagen fibre orientation. Data Brief 8, 1338–1343.

Sommer, G., Haspinger, D.C., Andrä, M., Sacherer, M., Viertler, C., Regitnig, P., Holzapfel, G.A., 2015a. Quantification of shear deformations and corresponding stresses in the biaxially tested human myocardium. Ann. Biomed. Eng. 43 (10), 2334–2348.

Sommer, G., Schriefl, A.J., Andrä, M., Sacherer, M., Viertler, C., Wolinski, H., Holzapfel, G.A., 2015b. Biomechanical properties and microstructure of human ventricular myocardium. Acta Biomater. 24, 172–192.

Spotnitz, H.M., Spotnitz, W.D., Cottrell, T.S., Spiro, D., Sonnenblick, E.H., 1974. Cellular basis for volume related wall thickness changes in the rat left ventricle. J. Mol. Cell. Cardiol. 6 (4), 317–331.

Stefanon, I., Valero-Muñoz, M., Fernandes, A.A., Ribeiro, Jr., R.F., Rodríguez, C., Miana, M., Martínez-González, J., Spalenza, J.S., Lahera, V., Vassallo, P.F., Cachofeiro, V., 2013. Left and right ventricle late remodeling following myocardial infarction in rats. Plos One 8 (5), e64986.

Sutton Martin, G.S.J., Norman, S., 2000. Left ventricular remodeling after myocardial infarction. Circulation 101 (25), 2981–2988.

Talman, V., Ruskoaho, H., 2016. Cardiac fibrosis in myocardial infarction—from repair and remodeling to regeneration. Cell Tissue Res. 365 (3), 563–581.

Teh, I., McClymont, D., Burton, R.A.B., Maguire, M.L., Whittington, H.J., Lygate, C.A., Kohl, P., Schneider, J.E., 2016. Resolving fine cardiac structures in rats with high-resolution diffusion tensor imaging. Sci. Rep. 6 (1), 30573.

Wilkins, E., Wilson, L., Wickramasinghe, K., Bhatnagar, P., Leal, J., Luengo-Fernandez, R., Burns, R., Rayner, M., Townsend, N., 2017. European Cardiovascular disease statistics 2017. Brussels: Eur. Heart Netw..

Wong, J., Kuhl, E., 2014. Generating fibre orientation maps in human heart models using Poisson interpolation. Comput. Methods Biomech. Biomed. Eng. 17 (11), 1217–1226.

Zhang, S., Crow, J.A., Yang, X., Chen, J., Borazjani, A., Mullins, K.B., Chen, W., Cooper, R.C., McLaughlin, R.M., Liao, J., 2010. The correlation of 3D DT-MRI fiber disruption with structural and mechanical degeneration in porcine myocardium. Ann. Biomed. Eng. 38 (10), 3084–3095.

Received: 14 June 2021 | Accepted: 23 September 2021

DOI: 10.1002/pamm.202100054

Influence of passive mechanical properties in healthy and infarcted rat myocardium on the cardiac cycle

Denisa Martonová[1,*], Muhannad Alkassar[2], Julia Seufert[2], David Holz[1], Minh Tuan Duong[1], Barbara Reischl[3], Oliver Friedrich[3], and **Sigrid Leyendecker[1]**

[1] Friedrich-Alexander-Universität Erlangen-Nürnberg, Institute of Applied Dynamics, Immerwahrstr. 1, D-91058 Erlangen
[2] Friedrich-Alexander-Universität Erlangen-Nürnberg, Pediatric Cardiology, Loschgestr. 15, D-91054 Erlangen
[3] Friedrich-Alexander-Universität Erlangen-Nürnberg, Institute of Medical Biotechnology, Paul-Gordan-Str. 3, D-91052 Erlangen

Passive mechanics plays an important role during the electromechanically coupled cardiac cycle and its behaviour strongly changes after myocardial infarction. In the present work, the cardiac tissue is modelled as a mixture of an active orthotropic intact myocardium and a passive transversely isotropic fibrotic scar structure. We apply the constitutive model on the fully electromechanically coupled simulation of a cardiac cycle using a generic geometry of a rat left ventricle. Finally, the ejection fractions for various parameter sets based on the fitting to experimental data in different animal species as well as for a varying amount of fibrosis are compared. We show that both, the choice of species-specific passive material parameters and the amount of fibrosis, have a significant influence on the cardiac performance measured by the ejection fraction of the left ventricle.

1 Modelling and numerical examples

Based on our previous experimental and modelling works [1, 6], we model the healthy and infarcted cardiac tissue as a mixture of the intact myocardium and fibrotic scar structure. Corresponding to the infarct size, the amount of fibrosis fib, serves as a scaling factor. Therefore, as proposed in [6], the passive strain energy function is decoupled in the form $\Psi = fib\,\Psi^s + (1 - fib)\,\Psi^m$, where the scar structure is modelled as a transversely isotropic material and the intact myocardium as an orthotropic material according to [4]. In particular, by setting $fib = 0$, the intact cardiac tissue is modelled. In the present work, the active contraction for the intact myocardium is modelled following the approach from our previous work [1], which is based on [2]. It is as well scaled by the amount of fibrosis and the second Piola Kirchhoff tensor (PK2) reads as

$$\mathbf{S} = fib\,\mathbf{S}^s_{pas} + (1 - fib)(\,\mathbf{S}^m_{pas} + \mathbf{S}^m_{act}), \tag{1}$$

where the superscripts s and m correspond to the scar and intact myocardium and the subscripts pas and act to the passive and active parts of the PK2, respectively. For the electromechanically coupled problem, two governing equations together with the appropriate initial and boundary conditions have to be fulfilled, namely the balance of linear momentum

$$\boldsymbol{0} = \mathrm{Div}[\mathbf{F} \cdot \mathbf{S}] + \mathbf{F}^{\varphi} \text{ in } \Omega_0, \tag{2}$$

with the deformation gradient $\mathbf{F}$ and the external body force $\mathbf{F}^{\varphi}$, and the differential equation describing the spatio-temporal evolution of the transmembrane potential (TP) Φ

$$\dot{\Phi} = \mathrm{Div}[\boldsymbol{Q}] + F^{\Phi} \text{ in } \Omega_0, \tag{3}$$

where F^{Φ} is the non-linear current for the electrical excitation and $\boldsymbol{Q} = \mathbf{D} \cdot \nabla\Phi$ is the flux with the anisotropic conductivity tensor $\mathbf{D}$. For more detail, we refer to [1, 2]. In addition to the last works [1, 2], a pressure boundary condition on the endocardium, represented via the three-element Windkessel model, is included. Here, the parameters are adjusted such that the end-systolic pressure in the left ventricle (LV) reaches a physiological value for rats (12 kPa) [5].
The model is applied on the generic ellipsoidal rat LV displayed in Figure 1, right. Firstly, different passive material parameter sets from [3], [1] and [6] are used for the healthy LV ($fib = 0$). These parameters are obtained via fitting the model to the experimental data for different animal species. Secondly, the model is calibrated with the passive material parameters for healthy and infarcted myocardium from [6] and the amount of fibrosis is varying from 0% to 60% in order to compare the cardiac performance represented by the ejection fraction (EF) in the infarcted rat LV at different infarction stages.

2 Results

The EFs for different passive parameter sets are shown in Figure 1, left. We clearly see that by keeping all other model parameters constant, the choice of the parameter set for the passive mechanics strongly influences the whole cardiac cycle,

* Corresponding author: e-mail denisa.martonova@fau.de, phone +49 9131 85-61013

not only the passive diastolic filling as already demonstrated in [6]. Further, the EF with the new parameters obtained in [6] is close to the physiological value for rats (60%) reported in [5]. Figure 2 illustrates that the EF decreases with an increasing amount of fibrosis. Firstly, the LV becomes stiffer resulting in a smaller end-diastolic volume and secondly, the reduction in the contractility leads to a lower ventricular pressure, a larger end-systolic volume and eventually a decreased EF. Assuming an infarct size of 40%, the EF reaches 33%. This result is in agreement with the experimentally measured EF of 36±17% for the infarct size of 31±6% [5].

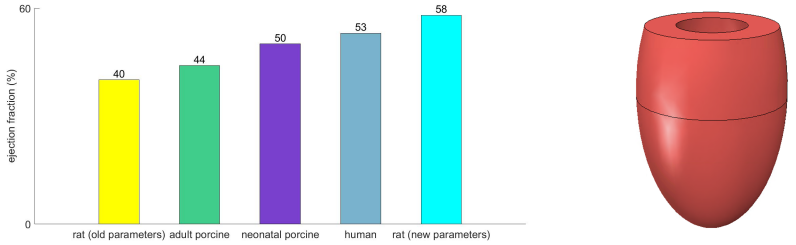

Fig. 1: Left: Ejection fractions of a rat LV for parameter sets from [1, 3, 6] for different species. Right: Generic ellipsoidal model of the rat LV based on data from echocardiography.

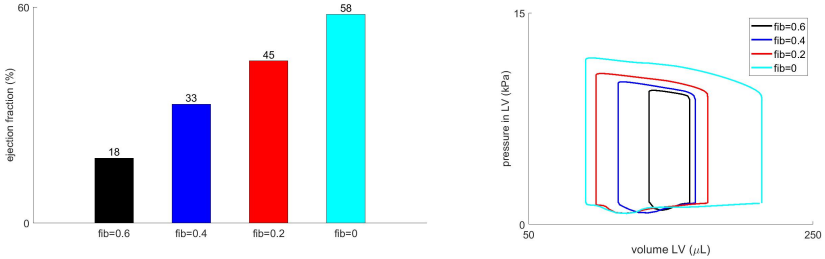

Fig. 2: Left: Ejection fractions of a rat LV for different amount of fibrosis. Right: Pressure-volume loops for different amounts of fibrosis.

3 Conclusion

In this work, a material model for the healthy and infarcted rat myocardium was proposed and utilised in a finite element simulation of the rat cardiac cycle. We show that using our previously fitted passive material parameter set for rats, a physiological EF is reached. Further, the proposed model can be used for a simulation of a rat cardiac cycle at different infarction stages.

Acknowledgements This work is funded by the Klaus Tschira Stiftung grant 00.289.2016. Open access funding enabled and organized by Projekt DEAL.

References

[1] M. T. Duong, D. Holz, M. Alkassar, S. Dittrich and S. Leyendecker. Front. Physiol. **10**, 1041 (2019).
[2] S. Göktepe, E. Kuhl. Comp. Mech. **45**, 227–243 (2010).
[3] D. Guan, F. Ahmad, P. Theobald, S. Soe, G. Hao. Biomech Model Mechanobiol. **18**, 1213-1232 (2019).
[4] G.A. Holzapfel, and R.W. Ogden. Phil. Trans. R. Soc. A. **367**, 3445–3475 (2009).
[5] D. Jegger, A. S. Mallik, M. Nasratullah, X. Jeanrenaud, R. Silva. J. Appl. Physiol. **102**, 1123–1129 (2007).
[6] D. Martonová, M. Alkassar, J. Seufert, D. Holz, M. T. Duong, B. Reischl, O. Friedrich and S. Leyendecker. J. Mech. Behav. Biomed. Mater. **119**, 104430 (2021).

Journal of Biomechanics 134 (2022) 110980

Contents lists available at ScienceDirect

Journal of Biomechanics

journal homepage: www.elsevier.com/locate/jbiomech

Comparison of stress and stress–strain approaches for the active contraction in a rat cardiac cycle model

Denisa Martonová [a,*], David Holz [a], Julia Seufert [b], Minh Tuan Duong [a,c], Muhannad Alkassar [b], Sigrid Leyendecker [a]

[a] Friedrich-Alexander-Universität Erlangen-Nürnberg, Institute of Applied Dynamics, Immerwahrstraße 1, 91058 Erlangen, Germany
[b] Universitätsklinikum Erlangen, Department of Cardiac Surgery, Krankenhausstraße 12, 91054 Erlangen, Germany
[c] School of Mechanical Engineering, Hanoi University of Science and Technology, 1 DaiCoViet Road, Hanoi, Viet Nam

ARTICLE INFO

Keywords:
Cardiac cycle
Rat left ventricle
Cardiac electromechanics
Active stress
Finite element method

ABSTRACT

In the last decades, different strategies to model the active electromechanically coupled behaviour of the cardiac tissue were proposed in order to simulate electromechanics of the heart under healthy and pathological conditions. The main objective of this work is to compare two approaches for modelling the active contraction during the electromechanically coupled rat cardiac cycle —- the stress and the stress–strain approach. Firstly, a cylindrical benchmark is considered and secondly, for a generic model of a rat left ventricle, a simulation including the Windkessel model, excitation via Purkinje fibre network and mechano-electrical feedback is performed. The model is calibrated with experimental data for rats, partly from own measurements via cardiac ultrasound, partly from the literature. Further, possibilities to reach higher ejection fractions are discussed and considered for an exemplary rat left ventricle.

Within each approach, we observe regionally different active stresses and fibre stretches. Moreover, the transmural active stress and fibre stretch distribution is influenced by the pressure load on the endocardial surface. The active stress approach is not sensitive to the fibre stretch and transmurally varying fibre stretch in the left ventricular domain is observed. The active stress–strain approach leads to transmurally more homogeneous fibre stretch at the end-systolic state.

1. Introduction

Recently, modelling and simulation of cardiac electromechanics became a powerful tool in order to better understand, diagnose and treat various diseases (Lopez-Perez et al., 2015; Niederer et al., 2019; Peirlinck et al., 2021). Different approaches to model the active electromechanically coupled behaviour of the cardiac tissue were proposed and used in simulations. However, two main groups can be defined — pure stress and pure strain approach. The first one is based on the additive decomposition of the stress tensor into a passive and active part (Göktepe and Kuhl, 2010; Eriksson et al., 2013; Sack et al., 2018), whereas the basis for the second one is a multiplicative decomposition of the deformation gradient into an active and elastic part (Ambrosi et al., 2011). Both approaches were compared regarding physiological correctness, mathematical stability and numerical complexity in Ambrosi et al. (2011), Ambrosi and Pezzuto (2012) and Goriely (2018).

While most computational studies investigate human heart models, in the present study, a computational model of a rat left ventricle (LV) is considered. The main reasons are: Firstly, thanks to many available experimental data for rats, the simulations can be easily validated and secondly computational simulations can reduce the number of laboratory experiments which are widely performed in rodents. For example, the development of cardiac assist devices requires a demanding parameter optimisation prior to the actual animal experiments.

Based on the experiments, the passive mechanical properties of the rat LV were characterised in our recent work (Martonová et al., 2021a). In the present work, for the modelling of an active contraction, the phenomenologically motivated additive decomposition of the total stress is considered. One of its major advantages is the possibility of the model calibration with experimental data obtained for the passive mechanical part and purely electrical part separately (Göktepe et al., 2014). However, besides the pure stress approach described above, Göktepe et al. (2014) proposed a combination of the stress and strain approach, so-called stress–strain approach. To the authors best knowledge, it was, so far, not applied in any other than the original work. We are going to make this step and utilise the stress and the stress–strain

* Corresponding author.
E-mail address: denisa.martonova@fau.de (D. Martonová).

https://doi.org/10.1016/j.jbiomech.2022.110980
Accepted 24 January 2022
Available online 8 February 2022

approach by using our own and previously published experimental data for rats and calibrate the passive and active part of the constitutive laws. Furthermore, compared to the original works (Göktepe S. Abilez et al., 2010; Göktepe et al., 2014), other essential model features such as excitation via Purkinje fibre network (PFN), Windkessel model and mechano-electrical feedback (MEF) are included into the model. The results are then compared with regard to the experimental data obtained from the ultrasound (US) as well as the distribution of the active stress and fibre stretch in the domain. The focus is put on the end-systolic state as this has a significant influence on the ejection fraction (EF) being one of the most important physiological measures of the heart (Kosaraju et al., 2021).

The main objective of this work is to compare the two known approaches in modelling of the active contraction during the rat cardiac cycle. The models are firstly applied on a cylindrical benchmark and subsequently, a simulation of the rat cardiac cycle is performed. Further, two possibilities to reach high EF are discussed and applied on an exemplary rat LV.

2. Methods

2.1. Modelling

2.1.1. Governing equations

Two field equations governing the state of the material point $\boldsymbol{X} \in \Omega_0$ at time t, $t \in [t_0, t_f]$ (t_0 and t_f are the initial and final time, respectively), can be formulated. The mechanical field equation is the balance of linear momentum together with the boundary conditions (BCs) on the boundaries Γ_φ and Γ_T

$$\mathbf{0} = \mathrm{Div}[\mathbf{F} \cdot \mathbf{S}] + \boldsymbol{F}^{\varphi} \quad \text{in } \Omega_0, \tag{1}$$

$$\boldsymbol{\varphi}(\boldsymbol{X}, t) = \bar{\boldsymbol{\varphi}} \text{ in } \Gamma_\varphi, \quad \boldsymbol{T}(\boldsymbol{X}, t) = \bar{\boldsymbol{T}} \quad \text{in } \Gamma_T, \tag{2}$$

where $\mathbf{F}$ is the deformation gradient, $\mathbf{S}$ is the second Piola–Kirchhoff stress tensor (PK2), $\boldsymbol{F}^{\varphi}$ is the external mechanical body force, $\boldsymbol{\varphi}$ is the displacement and $\boldsymbol{T}$ the surface traction vector. The prescribed values on the boundaries are marked with bars. The differential equation describing the spatio-temporal evolution of the transmembrane potential (TP) $\boldsymbol{\Phi}$ with the BCs on the boundaries Γ_Φ and Γ_Q is

$$\dot{\boldsymbol{\Phi}} = \mathrm{Div}[\boldsymbol{Q}] + F^{\boldsymbol{\Phi}} \quad \text{in } \Omega_0, \tag{3}$$

$$\boldsymbol{\Phi}(\boldsymbol{X}, t) = \bar{\boldsymbol{\Phi}} \quad \text{in } \Gamma_\Phi, \quad \boldsymbol{Q}(\boldsymbol{X}, t) \cdot \boldsymbol{N} = \bar{Q} \quad \text{in } \Gamma_Q, \tag{4}$$

where $F^{\boldsymbol{\Phi}}$ is the non-linear current for the electrical excitation, $\dot{\boldsymbol{\Phi}}$ denotes the material time derivative of the TP, the flux is $\boldsymbol{Q} = \mathbf{D} \cdot \nabla \boldsymbol{\Phi}$ with the anisotropic conductivity tensor $\mathbf{D} = d_{iso}\mathbf{I} + d_{ani}\boldsymbol{f}_0 \otimes \boldsymbol{f}_0$, where $\boldsymbol{f}_0$ is the reference fibre orientation (Göktepe and Kuhl, 2010). $\boldsymbol{N}$ is the unit normal vector pointing outwards of surface Γ_Q. For a more detailed description and visualisation of the BCs, we refer to our previous work (Duong et al., 2019). In the later numerical examples, additionally, the Windkessel model and PFN described in Section 2.3.2 serve as mechanical and electrical BCs, respectively.

2.1.2. Mechanical constitutive model

In both considered models, the total stress is additively decomposed into the passive part $\mathbf{S}^{pas}$ and the active part $\mathbf{S}^{act}$, namely

$$\mathbf{S} = \mathbf{S}^{pas} + \mathbf{S}^{act}. \tag{5}$$

2.1.2.1. Passive mechanics. For the passive mechanical part, the orthotropic Holzapfel–Ogden strain energy function Ψ (Holzapfel and Ogden, 2009) is utilised. It is calibrated with the parameters for healthy rats obtained in Martonová et al. (2021a). The implementation accounting for the near-incompressibility is described in Duong et al. (2019). The passive PK2 is obtained as

$$\mathbf{S}^{pas}(\mathbf{C}) = 2\frac{\partial \Psi}{\partial \mathbf{C}}, \tag{6}$$

where $\mathbf{C}$ the right Cauchy stress tensor.

2.1.2.2. Active mechanics — stress approach (A1). This widely used approach is purely based on the additive decomposition of the total stress. The model and in particular the electromechanical coupling is described in Göktepe and Kuhl (2010) and applied e.g. in our previous work (Duong et al., 2019). Briefly, for the active part of the PK2 and Cauchy stress (CS), the following equations hold:

$$\begin{aligned}\mathbf{S}^{act} &= \mathbf{S}^{act}(\boldsymbol{f}_0, \boldsymbol{n}_0, \boldsymbol{\Phi}) \\ &= T^{act}(\boldsymbol{\Phi})(\boldsymbol{f}_0 \otimes \boldsymbol{f}_0 + \nu \boldsymbol{n}_0 \otimes \boldsymbol{n}_0),\end{aligned} \tag{7}$$

$$\begin{aligned}\boldsymbol{\sigma}^{act} &= \boldsymbol{\sigma}^{act}(\boldsymbol{f}, \boldsymbol{n}, \boldsymbol{\Phi}) \\ &= (\det \mathbf{F})^{-1} T^{act}(\boldsymbol{\Phi})(\boldsymbol{f} \otimes \boldsymbol{f} + \nu \boldsymbol{n} \otimes \boldsymbol{n}).\end{aligned} \tag{8}$$

The evolution equation for the active muscle tension T^{act} reads

$$\dot{T}^{act} = \epsilon(\boldsymbol{\Phi}) \left[k_T \left(\boldsymbol{\Phi} - \boldsymbol{\Phi}_r \right) - T^{act} \right], \tag{9}$$

where k_T specifies the maximal value of T^{act}, $\boldsymbol{\Phi}_r$ is the resting potential, $\boldsymbol{f}_0$, $\boldsymbol{n}_0$ are the fibre and sheet-normal directions in the reference configuration, respectively and $\boldsymbol{f} = \mathbf{F}\boldsymbol{f}_0$, $\boldsymbol{n} = \mathbf{F}\boldsymbol{n}_0$ are their push-forwards into the deformed configuration. The switch function $\epsilon(\boldsymbol{\Phi})$ takes the form

$$\epsilon(\boldsymbol{\Phi}) = \epsilon_0 + \left(\epsilon_\infty - \epsilon_0 \right) \exp\left[-\exp\left(-\xi \left(\boldsymbol{\Phi} - \tilde{\boldsymbol{\Phi}} \right) \right) \right]. \tag{10}$$

The special behaviour can be adjusted by the parameters ϵ_0, ϵ_∞ and ξ. We note that, in contrast to the original work (Göktepe and Kuhl, 2010), in order to achieve a temporal delay between the peak of TP and the peak of the active stress, the inequality $\epsilon_0 > \epsilon_\infty$ should hold (Eriksson et al., 2013). Based on the experimental evidence (Lin and Yin, 1998), in addition to the contraction in the fibre direction, a reduced active stress along the cross-fibre direction is added and scaled by ν in (8).

2.1.2.3. Active mechanics — stress–strain approach (A2). In addition to the additive decomposition of the total stress in (5), the total deformation gradient is multiplicatively decomposed as

$$\mathbf{F} = \mathbf{F}^e \mathbf{F}^a, \tag{11}$$

where $\mathbf{F}^a$ is the active part mapping the line elements from the reference into an intermediate configuration and $\mathbf{F}^e$ is the elastic part mapping the line elements from the intermediate into a deformed configuration. We follow the model proposed in Göktepe et al. (2014). As introduced in Section 2.1.2.2, a reduced contraction in cross-fibre direction is added. The following equations describe the evolution of the active stress depending on the multiplicatively decomposed deformation gradient:

$$\begin{aligned}\mathbf{S}^{act} &= \mathbf{S}^{act}\left(\boldsymbol{f}_0, \boldsymbol{n}_0, \mathbf{F}^a \right) \\ &= 2 \sum_{i \in \{f,n\}} \left[\nu_i (I^e_{4i} - 1) \mathbf{F}^{-a} \check{\mathbf{M}}^e_i (\mathbf{F}^a) \mathbf{F}^{-a^T} \right],\end{aligned} \tag{12}$$

$$\begin{aligned}\boldsymbol{\sigma}^{act} &= \boldsymbol{\sigma}^{act}\left(\boldsymbol{f}_0, \boldsymbol{n}_0, \mathbf{F}^a, \mathbf{F}^e \right) \\ &= 2(\det \mathbf{F})^{-1} \sum_{i \in \{f,n\}} \left[\nu_i (I^e_{4i} - 1) \mathbf{F}^e \check{\mathbf{M}}^e_i (\mathbf{F}^a) \mathbf{F}^{e^T} \right],\end{aligned} \tag{13}$$

where I_{4f} and I_{4n} are the fourth invariants in the fibre and sheet-normal directions (Holzapfel and Ogden, 2009), respectively. See Appendix B and the original work (Göktepe et al., 2014) for more details.

2.1.3. Constitutive model of the electrophysiology

The nonlinear current source term $F^{\boldsymbol{\Phi}}$ controlling the TP is additively split into two parts as

$$F^{\boldsymbol{\Phi}} = F^{\boldsymbol{\Phi}}_e + F^{\boldsymbol{\Phi}}_m, \tag{14}$$

where $F^{\boldsymbol{\Phi}}_e$ represents the pure electrical part and $F^{\boldsymbol{\Phi}}_m$ is the source term accounting for the MEF. As the main focus of this work is put on the active mechanics, we restrict our attention to the simple phenomenological model that qualitatively represents the propagation of the electric signal. In particular, for the purely electrical term $F^{\boldsymbol{\Phi}}_e$, the

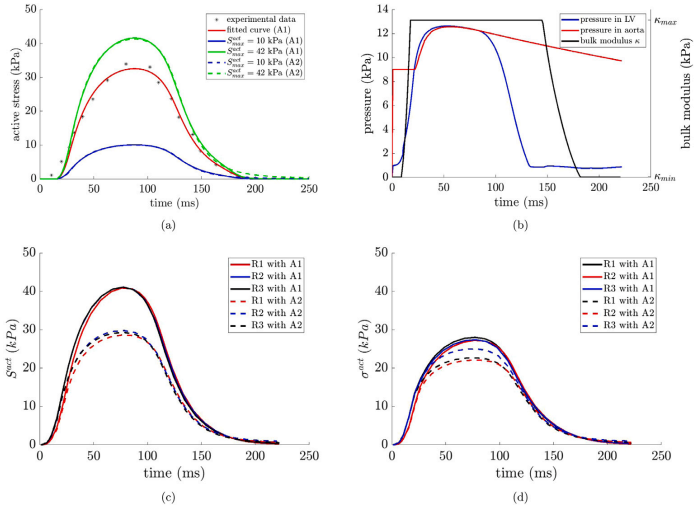

Fig. 1. (a) Temporal evolution of the active stress fitted to the experimental data for the isometric contraction (*) from Nishimura et al. (2004). The fitted curve is drawn in red and the scaled curves in green and blue colour. The curves generated by the model approach A1 and A2 are displayed in solid lines and dashed lines, respectively. (b) Temporal evolution of the pressure in the LV, aorta and the bulk modulus κ during the electromechanically coupled cardiac cycle. For the fitted value of κ_{min}, we refer to Table 1, last column. (c) and (d) Temporal evolution of averaged active stress ((c) PK2, (d) CS) in the fibre direction for three models of the rat LV (R1–R3). The average is computed over all finite elements in the domain. (For interpretation of the references to colour in this figure legend, the reader is referred to the web version of this article.)

model by Aliev and Panfilov (1996) is utilised. We refer to Appendix C for more details. Many computational studies (Baillargeon et al., 2015; Göktepe et al., 2011, 2014; Dal et al., 2013) omit MEF in the model as it requires the solution of a strongly coupled electromechanical problem with high computational costs. However, it is an important feature and should be included (Keldermann et al., 2007; Duong et al., 2019). Therefore, the present work accounts for the MEF. The model is set according to Panfilov et al. (2005) and Keldermann et al. (2007) and more details can be found in Appendix D.

2.2. Experimental data and simulation parameters

All material parameters used in the subsequent simulations are summarised in Table A.3.

2.2.1. Passive mechanical properties

The constitutive model described in Section 2.1.2.1 is calibrated with the experimental data for the rats (Martonová et al., 2021a).

2.2.2. Active electrical and mechanical properties

Due to an increased heart rate in rats compared to humans (Østergaard et al., 2010), the parameter β in (C.4) is scaled. The remaining electrical parameters are according to Göktepe and Kuhl (2010) and Göktepe et al. (2014). For the active contraction, we calibrated both approaches, A1 and A2, with the experimental data for rats presented in Nishimura et al. (2004). The active stress in the isometric contraction is fitted with the *lsqcurvefit* from MATLAB and the maximal tension is further scaled in the following numerical examples, see Fig. 1(a).

2.2.3. Cardiac ultrasound — own data

Three rats (35+/−2 days) underwent cardiac ultrasound (Vevo 3100, Fujifilm Visual Sonics) in the parasternal long axis. Measurements of end-diastolic volume (EDV), end-systolic volume (ESV) and EF of the LV were performed using the Software (VevoLab 5.6.0, Fujifilm Visual Sonics) and an electrocardiogram-gated kilohertz visualisation modus. The left ventricular dimensions depicted in Fig. 2 were measured in ED and ES in order to reconstruct a simplified ellipsoidal geometry as described in Section 2.3.2.1. The experimental data is given in Table 1.

2.3. Numerical examples

2.3.1. Elementary examples — cylinder

Motivated by the work of Goriely (2018), we firstly apply A1 and A2 on a simple cylindrical geometry (inner radius 1 mm, outer radius 2 mm, height 2 mm) depicted in Fig. 3. The fibres are oriented in the circumferential direction and the maximal active stress by the isometric contraction is set to 10 kPa. Three different loading scenarios are considered:

- isometric contraction (S1),
- free contraction in fibre direction, where the longitudinal and circumferential degrees of freedom are fixed (Goriely, 2018) (S2),
- free contraction in fibre direction with a pressure load (10 kPa) on the inner surface of the cylinder in order to investigate the influence of an increased fibre stretch during the contraction (S3).

In all cases, the whole domain is depolarised for 1 ms from the resting potential of −80 mV up to −40 mV in order to fire an action potential and the subsequent contraction.

2.3.2. Electromechanics of the left ventricle

2.3.2.1. Geometry and fibre orientation. In the US measurement in the long axis view, eight distances displayed in Fig. 2 with light orange coloured arrows are measured, both in the end-diastolic and end-systolic state. Assuming a symmetry with respect to the longitudinal z-axis, the points on the endo- and epicardium (x_i^J, z_i^J), $i \in \{1, \dots, 5\}$, $j \in$

Table 1
Experimental data.

Rat	EDV^E (μL)	ESV^E (μL)	EF^E (%)	EDh^E (mm)	ESh^E (mm)	WT^E (%)	a_{ep}/b_{ep} (mm)	a_{en}/b_{en} (mm)	z_0 (mm)	κ_{min} (kPa)
R1	248.8	72.6	70.8	1.52	1.92	25.8	2.51/6.43	4.22/8.05	−3.99	1.4
R2	319.2	74.4	76.5	1.57	2.27	44.6	2.76/8.73	4.68/10.41	−2.76	1.7
R3	218.4	52.1	76.1	1.53	2.14	39.8	2.50/7.76	4.42/9.34	−2.24	1.6
Mean	262.1	66.4	74.5	1.54	2.11	36.7	2.59/7.64	4.44/9.27	−3.00	1.6
SD	42.2	10.1	2.6	0.02	0.14	7.7	0.12/0.94	0.19/0.97	0.74	0.1

EDV end-diastolic volume of LV, ESV end-systolic volume of LV, EF ejection fraction, EDh average end-diastolic wall thickness, ESh average end-systolic wall thickness WT wall thickening. The superscript E refers to the experimentally measured quantities. $a_j b_j$ short and long axis, respectively, of the fitted ellipse to the endocardial ($j = en$) end epicardial ($j = ep$) surface of the rat LV, $z0$ coordinate of the fitted ellipse centred at (x_0, z_0), κ_{min} bulk modulus in (16) such that $|EDV^S/EDV^E - 1| \leq 0.01$ is fulfilled.

Table 2
Simulation results.

Rat	EDV^S (μL)	Approach A1						Approach A2					
		ESV^S (μL)	EF^S (%)	EDh^S (mm)	ESh^S (mm)	WT^S (%)	VL^S (%)	ESV^S (μL)	EF^S (%)	EDh^S (mm)	ESh^S (mm)	WT^S (%)	VL^S (%)
R1	248.7	107.0	56.9	1.51	1.76	16.8	16.3	120.1	51.7	1.51	1.75	15.7	16.2
R2	319.1	140.6	55.9	1.66	1.92	15.4	13.7	163.2	48.8	1.66	1.90	14.5	13.6
R3	219.8	90.0	59.0	1.65	1.96	19.0	12.6	101.7	54.0	1.65	1.92	16.3	12.5
Mean	262.5	113.1	57.1	1.61	1.88	17.1	14.2	128.7	51.3	1.61	1.85	15.4	14.1
SD	51.1	25.6	1.7	0.08	0.11	1.8	1.9	31.2	2.5	0.08	0.09	0.9	1.9
R1[a]	248.7	76.3	69.3	1.51	1.88	24.7	16.8	78.8	68.3	1.51	1.95	28.9	16.7
R1[b]	248.7	85.4	65.7	1.51	1.84	21.6	16.4	81.3	67.3	1.51	1.87	23.6	16.3

Simulation results for the approaches A1 and A2 with maximal active fibre stress in isometric contraction of 42 kPa (Nishimura et al., 2004).
[a]Maximal active fibre stress in isometric contraction 85 kPa (A1), 128 kPa (A2).
[b]Maximal active fibre stress in isometric contraction 42 kPa in A1 and A2, reduced maximal pressure in LV to 4 kPa, VL^S volumetric loss. The superscript S refers to the simulated quantities.

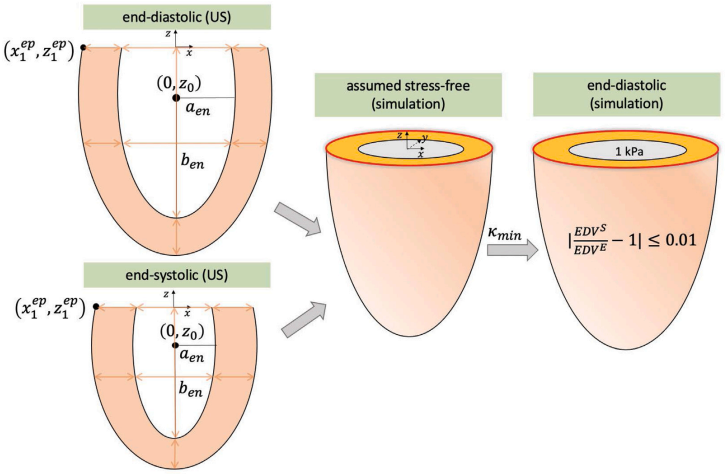

Fig. 2. Schematic workflow for the creation of a generic ellipsoid as an input geometry for the cardiac simulation. From left to right: end-diastolic and end-systolic distances (marked with eight arrows) are measured from the US, (x_1^{ep}, z_1^{ep}) are representative points used for fitting in (15); assumed stress-free configuration is created as described in Section 2.3.2.1; LV is inflated with EDP=1 kPa and the bulk modulus κ_{min} in (16) is optimised such that the experimentally determined EDV^E is reached up to 1%.

$\{en, ep\}$ were fitted to an ellipse centred at $(0, z_0)$ at end-diastole (ED) and end-systole (ES). The optimisation problem is given as

$$\min_{\boldsymbol{\mu}} \sum_{i=1}^{5} \frac{{x_j^i}^2}{a_j^2} + \frac{(z_j^i - z_0)^2}{b_j^2} - 1, \; j \in \{en, ep\} \tag{15}$$

with $\boldsymbol{\mu} = (a_{en}, b_{en}, a_{ep}, b_{ep}, z_0)$, a_j, b_j are the short and long axis for the endo- and epicardial surfaces, respectively. Neglecting the residual stress in the LV (Rodriguez et al., 1994), the stress-free state is reached between ES and ED (Walker et al., 2005; Sermesant and Razavi, 2010). Therefore, for the final input geometry a_j and b_j are linearly scaled between ED and ES in the ratio 6:4, respectively, before the end-diastolic pressure (EDP) of 1 kPa is applied on the endocardial surface.

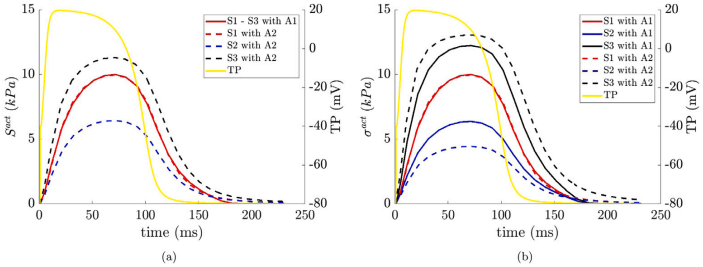

Fig. 3. Temporal evolution of an averaged active stress ((a) PK2, (b) CS) in circumferentially aligned fibre direction and transmembrane potential in the cylindrical example for different scenarios (S1–S3) specified in Section 2.3.1. The curves show the average computed over all finite elements in the domain.

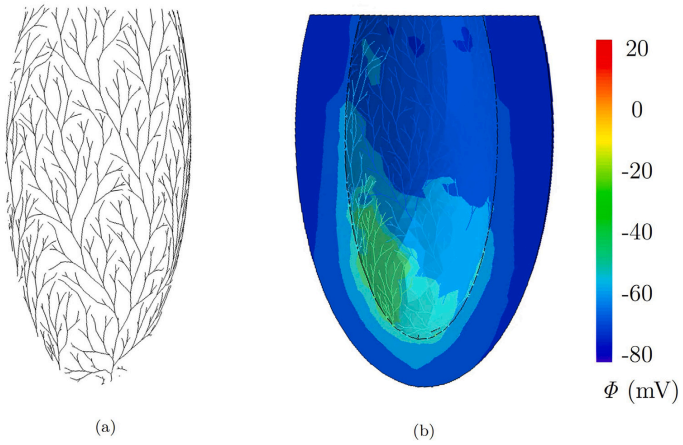

Fig. 4. (a) Purkinje fibre network, (b) transmembrane potential Φ during the activation phase in the purely electrical simulation.

The resulting 3D geometry, i.e. truncated ellipsoid, is obtained by revolving the fitted ellipse and cutting it by the xy-plane being the base of the LV. A schematic workflow for the creation of the simplified geometry is displayed in Fig. 2 and the fitted parameters in (15) are given in Table 1. The domain is meshed with tetrahedral elements with an average element edge length of 0.5 mm. The fibre orientation is implemented according to Wong and Kuhl (2014). The fibre angles are set to +60° on the endocardium and −60° on the epicardium (Milne et al., 2019; Chen et al., 2005).

2.3.2.2. Boundary conditions and solver. The applied mechanical BCs are according to Eriksson et al. (2013). Briefly, the basal surface of the LV (yellow colour in Fig. 2) is fixed in x and y directions and additionally, the z direction is fixed for the outer basal nodes (red colour in Fig. 2). This is in agreement with our experimental measurements where the change in the end-diastolic and end-systolic outer basal radius is only 3.5%± 0.6. Further, a pressure BC representing the Windkessel model specified in Appendix E is applied on the endocardial surface. To induce an electrical excitation, a PFN (Fig. 4(a)) with an increased conductivity d_{purk} is generated on the endocardial surface using a generic algorithm from Sahli Costabal et al. (2016). The endnodes of the created PFN are connected to the surface mesh (endocardial surface) by multi-point-constraints, i.e. for each endnode in the PFN, the closest vertex in the surface mesh is found and it is assigned the same TP as the respective endnode. Firstly, a purely electrical simulation is solved (Fig. 4(b)). The TP at the endocardial nodes during the activation time of 10 ms and the first 25 ms of the beating phase is used as an electrical BC for the subsequent electromechanically coupled simulation which is solved monolithically. For all simulation, the software Abaqus from Simulia inclusive the user subroutines is utilised.

2.3.2.3. Compressibility. As described in the previous works, e.g. Duong et al. (2019) and Göktepe et al. (2014), the near-incompressibility of the cardiac tissue can be enforced by adding a volumetric penalty strain energy function $\Psi_{vol} = \kappa(\det \mathbf{F} - 1)^2$, where κ is the bulk modulus. However, a volumetric change in the myocardium ranging from 5 to 20% has been observed in the experiments in different species. For rats, the average volume loss (VL) in the systolic phase reaches 15% compared to the end-diastolic myocardial volume. The redistribution of the intra- and extra-vascular blood is the main reason of the phenomenon (Avazmohammadi et al., 2020; Bonnemains et al., 2019). Based on this and the results from the inverse fitting of κ in Hassaballah et al. (2013), in the present work, κ changes between its minimal (κ_{min}) and maximal (κ_{max}) value depending on the active

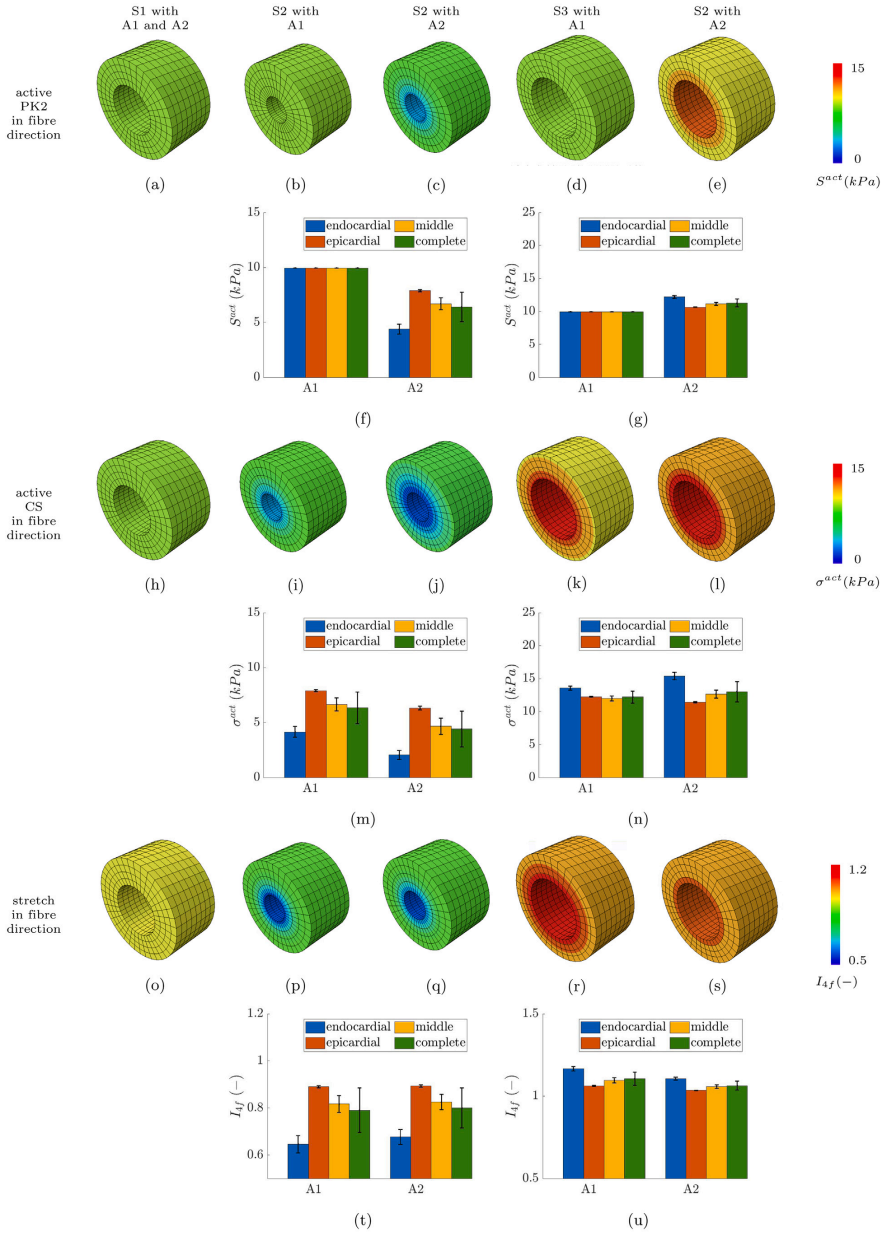

Fig. 5. Regional differences in the active stress and stretch in fibre direction. Contour plots of the active PK2/active CS/stretch in fibre direction at maximal contraction: (a)/(h)/(o) S1 with A1 and A2, (b)/(i)/(p) S2 with A1, (c)/(j)/(q) S2 with A2, (d)/(k)/(r) S3 with A1, (e)/(l)/(s) S3 with A2. Bar plots for the average active PK2/active CS/stretch in fibre direction: (f)/(m)/(t) S2 with A1 and A2, (g)/(n)/(u) S3 with A1 and A2. The error bars represent to the standard deviation.

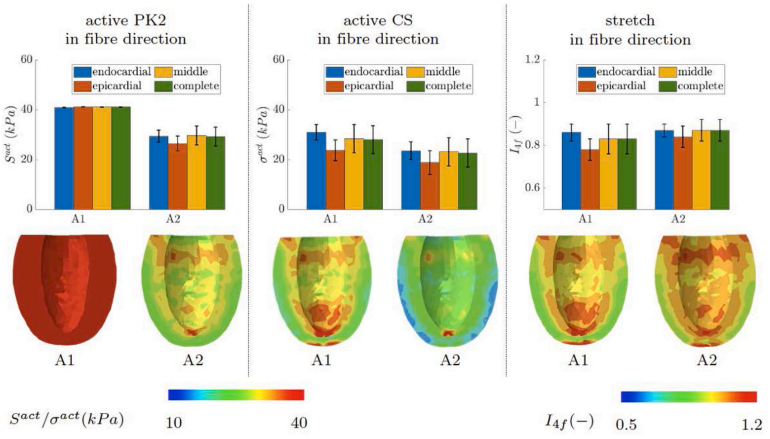

Fig. 6. Model with maximal isometric tension 42 kPa for A1 and A2 and the physiological maximal end-systolic pressure of 12 kPa: regional differences in the active stress and fibre stretch represented by the fourth invariant I_{4f}. First row: bar plots for the average active PK2, CS and stretch in the fibre direction for A1 and A2, respectively. Second row: contour plots at the maximal ventricular contraction for the average active PK2, CS, fibre stretch for A1 and A2, respectively.

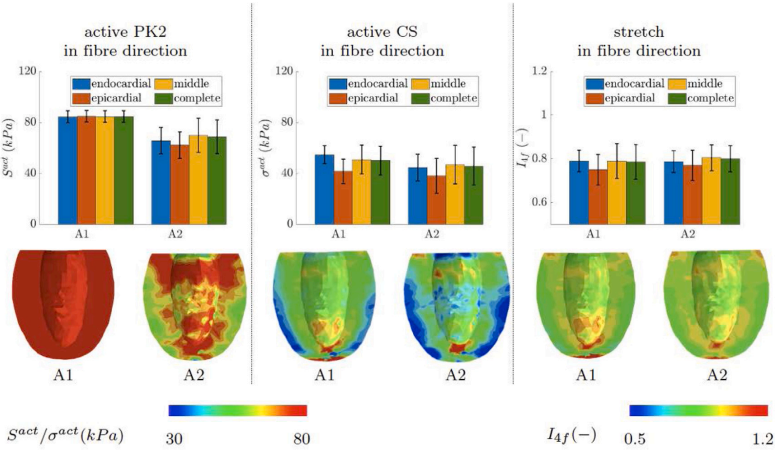

Fig. 7. M1 (model with maximal isometric tension 85 kPa for A1 and 128 kPa for A2 and the physiological maximal end-systolic pressure of 12 kPa): regional differences in the active stress and stretch represented by the fourth invariant I_{4f} in fibre direction. First row: bar plots for the average active PK2, CS and stretch in the fibre direction for A1 and A2, respectively. Second row: contour plots at the maximal ventricular contraction for the average active PK2, CS, fibre stretch for A1 and A2, respectively.

current (S^{act}) and maximal (S^{act}_{max}) active PK2 in fibre direction as:

$$\kappa = \begin{cases} \kappa_{min} & \text{during the end-diastolic filling,} \\ \kappa_{min} + k\frac{S^{act}}{S^{act}_{max}} & \text{if } \kappa < \kappa_{max}, \\ \kappa_{max} & \text{otherwise,} \end{cases} \tag{16}$$

where the constant k governs the rapid change in κ observed in Hassaballah et al. (2013). Furthermore, κ_{min} is optimised such that the end-diastolic volume in the model EDV^S does not differ from the measured end-diastolic volume EDV^E more than 1% as depicted in Fig. 2. The temporal evolution of κ is shown in Fig. 1(b).

3. Results and discussion

3.1. Experimental work

The experimental data is given in Table 1. The average EF of 74.5% is close to the reported one in Pacher et al. (2004) for young rats which we are using in this study. High EFs are typical for young specimen and slightly decrease in adult rats (Pacher et al., 2004; Faber et al., 2006; Jegger et al., 2006). Modelling of such large deformations remains challenging and some specific assumptions have to be made as discussed later.

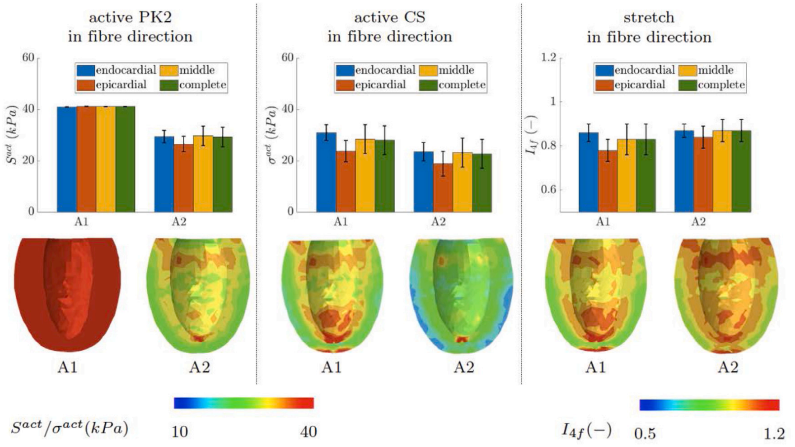

Fig. 8. M2 (model with maximal isometric tension 42 kPa for A1 and A2 and the reduced maximal end-systolic pressure of 4 kPa): regional differences in the active stress and fibre stretch represented by the fourth invariant I_{4f}. First row: bar plots for the average active PK2, CS and stretch in the fibre direction for A1 and A2, respectively. Second row: contour plots at the maximal ventricular contraction for the average active PK2, CS, fibre stretch for A1 and A2, respectively.

3.2. Example — cylinder

Fig. 3 shows the temporal evolution of the fitted active PK2 and CS depending on the TP. The modelled active stresses in the fibre direction during the isometric contraction (S1) in both approaches are indistinguishable with the eye as the model parameters were fitted to an isometric contraction. In Fig. 5, the contour and bar plots of the active PK2, CS and the stretch in circumferentially aligned fibre direction at the maximal contraction (t = 75 ms) are displayed for loading scenarios S1–S3. Clearly, in contrast to A1, PK2 in A2 is sensitive to the fibre-stretch. In particular, a higher active stress is generated when the fibres are stretched as demonstrated in S3 and the active stress decreases when the fibres are compressed as demonstrated in S2. We note, that after the transformation into the CS, both approaches depend on the actual configuration and the stretch-dependence in A2 becomes more prominent. The regional differences in the stress and stretch distribution are influenced by the pressure load on the inner surface. For the isotonic contraction in S2, the fibre stretch decreases from the outer to the inner surface, whereas in S3, the opposite phenomenon is observed, see barplots in Fig. 5. It is due to an additional load causing an increased fibre stretch on the inner surface. In A2, this increased fibre stretch generates a higher active stress. Such regulatory mechanism is analogous to the Frank–Starling mechanism in cardiology. As a result, the transmural differences in the active fibre stress are increased and in the fibre stretch decreased, see also barplots in Fig. 5. This stress–stretch-regulation is not included in the widely used approach A1.

3.3. Example – LV

Comparison with experimental data

The simulation results for the cardiac cycle described in Section 2.3.2 are presented in Table 2. Fig. 1(c),(d) demonstrates that there are no significant differences in the active stress evolution in the considered models corresponding to R1–R3. Clearly, when using the average experimentally determined maximal isometric active tension of 42 kPa (Nishimura et al., 2004), the EF and wall thickening (WT) are below the experimental data in both approaches. In A2, the EF is lower than in A1 because due to the stretch sensitivity in A2, the active stress is reduced when the fibres are compressed in the systolic phase. This phenomenon was also observed in the previous study (Niederer and Smith, 2007). Two possible remedies are either increasing the maximal active fibre tension above the experimentally reported values (M1) or decreasing the pressure in the LV (M2). Both possibilities were used exemplary for the rat R1. A higher EF could possibly be reached by a recently proposed smoothed finite element technique being known for its softening effects (Liu, 2019; Martonová et al., 2021b). However, the application in 3D cardiac electromechanics has yet to be investigated further.

The proposed function for the bulk modulus κ given in (16) leads to an average volumetric loss of 14.2% which is close to the reported value of 15% (Avazmohammadi et al., 2020).

Regional differences in active fibre stress and stretch

As already shown, in the previous numerical example, PK2 in A1 is almost homogeneous in the whole domain. However, in the rat LV, due to an activation via the Purkinje fibre network and MEF, a small variance is present, see Figs. 6(a),7(a),8(a). Figs. 6(c),(h),(i) illustrate that the fibre contraction is most prominent in the epicardial region and decreases transmurally in the endocardial direction. This behaviour is in analogy to the benchmark problem S3 and mirrors the results in Guccione et al. (1993). It leads to the inhomogeneity in CS, epicardial lower than endocardial, for both approaches (A1 and A2), see Figs. 6,7,8(b),(f),(g), and is in agreement with the results in Niederer and Smith (2007). However, looking at Figs. 8(h),(i) and 7(h),(i), we observe significant differences in the distribution of the fibre stretch. Firstly, for both possibilities to increase the EF (M1 and M2), the variance in the fibre stretch is lower in approach A2 (decrease of 25% and 29%, respectively). Secondly, although nearly the same EF is reached in M1 (Fig. 7) and M2 (Fig. 8), the active stress and stretch distribution in the domain is different. In M2, due to the pressure reduction in the LV, the endocardial layers are able to contract more and the fibre stretch is similar to that in the epicardial regions. In the middle layers, the fibres contract less. This behaviour is more prominent for A2. A possible reason is the curvature and fixation of the domain accompanied by the near-incompressibility, as already

observed in our previous work (Duong et al., 2019). On the other hand, in M1, due to a higher pressure in the LV, the smallest contraction is observed in the endocardial region, see Fig. 7.

A higher fibre stretch and eventually active stress in the apical and basal regions are more prominent at the endocardium which was as well observed in Niederer and Smith (2007). The reason for such a difference may be an increased curvature in the apical region and the applied boundary condition in the basal region. However, the contour plots in Figs. 6–8 indicate that the approach A2 is able to slightly reduce the stress and stretch peaks in these regions.

The numerical examples were performed on cylindrical and rat LV geometries. However, the results of this study are transferable to computational models using geometries of human hearts, as the constitutive laws for the active contraction remain unchanged.

4. Conclusion

In the present work, the stress approach (A1) and the stress–strain approach (A2) for modelling the active cardiac contraction are compared. Within each approach, we observe transmurally and longitudinally different active stresses and fibre stretches. With both approaches, the experimentally measured EF can be reached if the maximal active tension or the pressure in the LV are scaled in a proper way. A1 is not sensitive to the fibre stretch, whereas A2 can reproduce the physiological Frank–Starling mechanisms well. Further, A2 leads to a more homogeneous fibre stretch at the end-systolic state. We conclude that the A2 should be preferred in cardiac modelling and simulation if the focus is put on the physiologically motivated stretch-dependence of the active fibre stress development.

CRediT authorship contribution statement

Denisa Martonová: Conceptualization, Methodology, Software, Formal analysis, Writing – original draft, Visualization. **David Holz:** Software, Methodology, Writing – review & editing. **Julia Seufert:** Methodology, Writing – review & editing. **Minh Tuan Duong:** Software, Methodology, Writing – review & editing. **Muhannad Alkassar:** Methodology, Resources, Project administration, Funding acquisition. **Sigrid Leyendecker:** Conceptualization, Methodology, Writing – review & editing, Supervision, Project administration, Funding acquisition.

Declaration of competing interest

The authors declare that they have no known competing financial interests or personal relationships that could have appeared to influence the work reported in this paper.

Acknowledgement

The authors thank the Klaus Tschira Stiftung grant 00.289.2016 for funding support.

Appendix A. Material parameters

See Table A.3.

Appendix B. Specific equation for the stress–strain approach (A2)

$$\tilde{\mathbf{M}}_i^e(\mathbf{F}^a) = \tilde{\boldsymbol{k}}_0 \otimes \tilde{\boldsymbol{k}}_0,\ \tilde{\boldsymbol{k}}_0 = (\mathbf{F}^a \boldsymbol{k}_0)/\|\mathbf{F}^a \boldsymbol{k}_0\|, \tag{B.1}$$

$$\mathbf{F}^a(\lambda^a) = \mathbf{I} + \sum_{i\in\{f,n\}} (\lambda^a(g) - 1)\mathbf{M}_i, \tag{B.2}$$

$$\mathbf{M}_f = \boldsymbol{f}_0 \otimes \boldsymbol{f}_0,\ \mathbf{M}_n = \boldsymbol{n}_0 \otimes \boldsymbol{n}_0, \tag{B.3}$$

$$\lambda^a(g) = \frac{\xi \lambda^a_{max}}{1 + g(c)(\xi(g) - 1)}, \tag{B.4}$$

$$g(c(\phi)) = \frac{1}{2} + \frac{1}{\pi}\arctan(\beta \ln c(\phi)), \tag{B.5}$$

$$\xi = \frac{g(c_0) - 1}{g(c_0) - \lambda^a_{max}}, \tag{B.6}$$

where c is the normalised calcium concentration depending on the normalised TP ϕ and additional parameters k, q. c_0 is the initial calcium concentration at $t = t_0$, λ^a is the active stretch. For a parameter study, we refer to the original work (Göktepe et al., 2014).

Appendix C. Constitutive model for the electrical source term

The phenomenological model (Aliev and Panfilov, 1996) used in the present works reads as

$$F_e^{\Phi}(\boldsymbol{\Phi}, r) = \frac{k_\phi}{k_t} f_e^{\phi}(\phi, r), \tag{C.1}$$

$$f_e^{\phi}(\phi, r) = \phi(\phi - \alpha)(1 - \phi) - r\phi + I, \tag{C.2}$$

where ϕ and $\bar{t}$ are dimensionless TP and time, respectively, obeying the equation

$$\boldsymbol{\Phi} = k_\phi \phi - \delta_\phi, \qquad t = k_t \bar{t}, \tag{C.3}$$

with the additional conversion parameters k_ϕ, δ_ϕ. The parameter α in (C.2) controls the oscillation threshold and I is an external stimulus. The evolution of the recovery variable r is governed by the local ordinary differential equation as

$$\dot{r} = \left[\gamma + \frac{\mu_1 r}{\mu_2 + \boldsymbol{\Phi}}\right][-r - c\boldsymbol{\Phi}(\boldsymbol{\Phi} - \beta - 1)], \tag{C.4}$$

where the variables μ_1, μ_2, β and γ are additional material parameters. β controls the action potential duration and the effective refractory period (Costabal et al., 2017).

Appendix D. Constitutive model for the MEF

MEF can be described by the constitutive equation for the mechanically induced electrical source term F_m^{Φ} as

$$F_m^{\Phi}(\mathbf{C}, \boldsymbol{\Phi}) = \frac{k_\phi}{k_t} f_m^{\phi}(\mathbf{C}, \phi), \tag{D.1}$$

$$f_m^{\phi}(\mathbf{C}, \phi) = \vartheta G_s (\lambda - 1)(\phi_s - \phi) \tag{D.2}$$

where G_s denotes the maximum conductance, ϕ_s is the resting potential at which no deformation can cause any current generation, $\vartheta = 1$ if $I_{4f} > 1$ and $\vartheta = 0$ otherwise, $\lambda = \sqrt{I_{4f}}$ (Panfilov et al., 2005; Keldermann et al., 2007).

Appendix E. Windkessel model

The following steps are defined in order to approximate the three-element-Windkessel model:

1. linear pressure increase starting from $p_{lv} = 0$ kPa to the end-diastolic pressure (EDP) 1 kPa, which is close to the experimental measurements in rats (Pacher et al., 2004; Paterek et al., 2016; Jegger et al., 2007),
2. isovolumetric contraction: p_{lv} increases from EDP up to 9 kPa,

Table A.3
Material parameters used in the numerical examples.

Active stress (A1)	k_T = 0.45/0.94[a]/0.12[c] kPa mV^{-1}, Φ_r = −80 mV, ϵ_0 = 0.1 mV^{-1}, ϵ_∞ = 1.0 mV^{-1}, ν = 0.5, ξ = 1.0 mV^{-1}, $\bar{\Phi}$ = 0 mV
Active stress (A2)	k = 0.59 [–], q = 1.0/0.99[a] [c] [–], β = 0.436/0.427[a]/0.460[c], ν_f = 0.001/0.0015[a]/0.001[c] [–], ν_n = 0.0005/0.00075[b]/0.0[c] [–], λ^a_{max} = 0.049/0.040[a]/0.071[c] [–]
Passive stress	a = 1.665 kPa, b = 1.237 [–], a_f = 7.822 kPa, b_f = 0.008 [–], a_s = 0.0 kPa, b_s = 0.0 [–], a_{fs} = 1.342 kPa, b_{fs} = 9.178 [–], see Table 1 for κ_{min}, κ_{max}=1500 kPa
Conduction	d_{iso} = 0.1 mm^2 ms^{-1}, d_{ani} = 0.9 mm^{2}ms^{-1}, d_{purk} = 100mm^{2}ms^{-1}
Excitation	α = 0.01 [–], β = 0.6 [–], c = 8 [–], γ = 0.002 [–], μ_1 = 0.2 [–], μ_2 = 0.3 [–]
MEF	G_s = 0[c]/10/15[a] [–], ϕ_s = 0.6 [–]
Conversion	k_ϕ = 100 mV, δ_ϕ = 80 mV, k_t = 12.9 ms
Windkessel model	R_p = 15 kPa μL^{-1} ms, R_{v1} =0.067 kPa μL^{-1} ms, R_{v2} = 0.1 kPa μL^{-1} ms, C = 40 μL kPa $^{-1}$ ms^{-1}

[a]Simulation of cardiac cycle with increased maximal active tension.
[b]Simulation of cardiac cycle with decreased pressure in LV.
[c]Simulation of cylindrical benchmark.

3. ejection phase: the pressure in the aorta p_a obeys the two-element Windkessel model

$$\frac{-dV(t)}{dt} = \frac{p_a(t)}{R_p} + C\frac{dp_a(t)}{dt} \tag{E.1}$$

with the LV volume V, the periphery resistances R_p and the capacitance of the aorta C. By adding an additional resistance and assuming that flow between LV and aorta is proportional to the pressure difference in their chambers scaled by the valve resistance R_{v1} (Baillargeon et al., 2014). The pressure in LV is computed as

$$p_{lv}(t) = R_{v1}\frac{-dV(t)}{dt} + p_a(t) \tag{E.2}$$

4. isovolumetric relaxation, if the condition $p_{lv} < p_a$ is satisfied,
5. early diastolic filling phase, if p_{lv} drops under the EDP. In analogy to (E.2), the following equation holds

$$p_{lv}(t) = R_{v2}\frac{-dV(t)}{dt} + EDP, \tag{E.3}$$

where R_{v2} represents the atrioventricular valve resistance.

The specific parameters C, R_{v1}, R_{v2} are provided in Table A.3 and are set such that the experimentally measured ESP of 12 kPa is reached (Faber et al., 2006; Jegger et al., 2007), see Fig. 1(b).

References

Aliev, R.R., Panfilov, A.V., 1996. A simple two-variable model of cardiac excitation. Chaos Solitons Fractals 7, 293–301. http://dx.doi.org/10.1016/0960-0779(95)00089-5.

Ambrosi, D., Arioli, G., Nobile, F., Quarteroni, A., 2011. Electromechanical coupling in cardiac dynamics: The active strain approach. SIAM J. Appl. Math. 71, 605–621. http://dx.doi.org/10.1137/100788379.

Ambrosi, D., Pezzuto, S., 2012. Active stress vs. Active strain in mechanobiology: Constitutive issues. J. Elasticity 107, 199–212. http://dx.doi.org/10.1007/s10659-011-9351-4.

Avazmohammadi, R., Soares, J.S., Li, D.S., Eperjesi, T., Pilla, J., Gorman, R.C., Sacks, M.S., 2020. On the in vivo systolic compressibility of left ventricular free wall myocardium in the normal and infarcted heart. J. Biomech. 107, 109767. http://dx.doi.org/10.1016/j.jbiomech.2020.109767.

Baillargeon, B., Costa, I., Leach, J.R., Lee, L.C., Genet, M., Toutain, A., Wenk, J.F., Rausch, M.K., Rebelo, N., Acevedo-Bolton, G., et al., 2015. Human cardiac function simulator for the optimal design of a novel annuloplasty ring with a sub-valvular element for correction of ischemic mitral regurgitation. Cardiovasc. Eng. Technol. 6, 105–116.

Baillargeon, B., Rebelo, N., Fox, D.D., Taylor, R.L., Kuhl, E., 2014. The living heart project: A robust and integrative simulator for human heart function. Eur. J. Mech. A Solids 48, 38–47. http://dx.doi.org/10.1016/j.euromechsol.2014.04.001.

Bonnemains, L., Guerard, A.S., Soulié, P., Odille, F., Felblinger, J., 2019. Myocardial volume change during cardiac cycle derived from three orthogonal systolic strains: Towards a quality assessment of strains. Acta Radiol. 60, 286–292. http://dx.doi.org/10.1177/0284185118783777.

Chen, J., Liu, W., Zhang, H., Lacy, L., Yang, X., Song, S.K., Wickline, S.A., Yu, X., 2005. Regional ventricular wall thickening reflects changes in cardiac fiber and sheet structure during contraction: Quantification with diffusion tensor MRI. Am. J. Physiol.-Heart Circ. Physiol. 289, H1898–H1907. http://dx.doi.org/10.1152/ajpheart.00041.2005.

Costabal, F.S., Concha, F.A., Hurtado, D.E., Kuhl, E., 2017. The importance of mechano-electrical feedback and inertia in cardiac electromechanics. Comput. Methods Appl. Mech. Engrg. 320, 352–368.

Dal, H., Göktepe, S., Kaliske, M., Kuhl, E., 2013. A fully implicit finite element method for bidomain models of cardiac electromechanics. Comput. Methods Appl. Mech. Engrg. 253, 323–336. http://dx.doi.org/10.1016/j.cma.2012.07.004.

Duong, M.T., Holz, D., Alkassar, M., Dittrich, S., Leyendecker, S., 2019. Interaction of the mechano-electrical feedback with passive mechanical models on a 3D rat left ventricle: A computational study. Front. Physiol. 10 (1041), http://dx.doi.org/10.3389/fphys.2019.01041.

Eriksson, T.S.E., Prassl, A.J., Plank, G., Holzapfel, G.A., 2013. Modeling the dispersion in electromechanically coupled myocardium. Int. J. Numer. Methods Biomed. Eng. 29, 1267–1284. http://dx.doi.org/10.1002/cnm.2575.

Faber, M.J., Dalinghaus, M., Lankhuizen, I.M., Steendijk, P., Hop, W.C., Schoemaker, R.G., Duncker, D.J., Lamers, J.M.J., Helbing, W.A., 2006. Right and left ventricular function after chronic pulmonary artery banding in rats assessed with biventricular pressure-volume loops. Am. J. Physiol.-Heart Circ. Physiol. 291, H1580–H1586. http://dx.doi.org/10.1152/ajpheart.00286.2006.

Göktepe, S., Acharya, S.N.S., Wong, J., Kuhl, E., 2011. Computational modeling of passive myocardium. Int. J. Numer. Methods Biomed. Eng. 27, 1–12. http://dx.doi.org/10.1002/cnm.1402.

Göktepe, S., Kuhl, E., 2010. Electromechanics of the heart: A unified approach to the strongly coupled excitation–contraction problem. Comput. Mech. 45, 227–243. http://dx.doi.org/10.1007/s00466-009-0434-z.

Göktepe, S., Menzel, A., Kuhl, E., 2014. The generalized hill model: A kinematic approach towards active muscle contraction. J. Mech. Phys. Solids 72, 20–39. http://dx.doi.org/10.1016/j.jmps.2014.07.015.

Göktepe S. Abilez, O.J., Parker, K.K., Kuhl, E., 2010. A multiscale model for eccentric and concentric cardiac growth through sarcomerogenesis. J. Theoret. Biol. 265, 433–442. http://dx.doi.org/10.1016/j.jtbi.2010.04.023.

Goriely, A., 2018. Five ways to model active processes in elastic solids: Active forces, active stresses, active strains, active fibers, and active metrics. Mech. Res. Commun. 93, 75–79. http://dx.doi.org/10.1016/j.mechrescom.2017.09.003.

Guccione, J.M., Waldman, L.K., McCulloch, A.D., 1993. Mechanics of active contraction in cardiac muscle: Part II — cylindrical models of the systolic left ventricle. J. Biomech. Eng. 115, 82–90. http://dx.doi.org/10.1115/1.2895474.

Hassaballah, A.I., Hassan, M.A., Mardi, A.N., Hamdi, M., 2013. An inverse finite element method for determining the tissue compressibility of human left ventricular wall during the cardiac cycle. PLoS One 8, e82703. http://dx.doi.org/10.1371/journal.pone.0082703.

Holzapfel, G.A., Ogden, R.W., 2009. Constitutive modelling of passive myocardium: A structurally based framework for material characterization. Phil. Trans. R. Soc. A 367, 3445–3475. http://dx.doi.org/10.1098/rsta.2009.0091.

Jegger, D., Jeanrenaud, X., Nasratullah, M., Chassot, P.G., Mallik, A., Tevaearai, H., von Segesser, L.K., Segers, P., Stergiopulos, N., 2006. Noninvasive Doppler-derived myocardial performance index in rats with myocardial infarction: Validation and correlation by conductance catheter. Am. J. Physiol.-Heart Circ. Physiol. 290, H1540–H1548. http://dx.doi.org/10.1152/ajpheart.00935.2005.

Jegger, D., Mallik, A.S., Nasratullah, M., Jeanrenaud, X., Silva, R.da., Tevaearai, H., von Segesser, L.K., Stergiopulos, N., 2007. The effect of a myocardial infarction on the normalized time-varying elastance curve. J. Appl. Physiol. 102, 1123–1129. http://dx.doi.org/10.1152/japplphysiol.00976.2006.

Keldermann, R.H., Nash, M.P., Panfilov, A.V., 2007. Pacemakers in a reaction–diffusion mechanics system. J. Stat. Phys. 128, 375–392.

Kosaraju, A., Goyal, A., Grigorova, Y., Makaryus, A.N., 2021. Left Ventricular Ejection Fraction. StatPearls StatPearls Publishing, Treasure Island (FL).

Lin, D.H.S., Yin, F.C.P., 1998. A multiaxial constitutive law for mammalian left ventricular myocardium in steady-state barium contracture or tetanus. J. Biomech. Eng. 120, 504–517. http://dx.doi.org/10.1115/1.2798021.

Liu, G.R., 2019. The smoothed finite element method (s-FEM): A framework for the design of numerical models for desired solutions. Front. Struct. Civil Eng. 13, 456–477. http://dx.doi.org/10.1007/s11709-019-0519-5.

Lopez-Perez, A., Sebastian, R., Ferrero, J.M., 2015. Three-dimensional cardiac computational modelling: Methods, features and applications. BioMed. Eng. OnLine 14, 35. http://dx.doi.org/10.1186/s12938-015-0033-5.

Martonová, D., Alkassar, M., Seufert, J., Holz, D., Duong, M.T., Reischl, B., Friedrich, O., Leyendecker, S., 2021a. Passive mechanical properties in healthy and infarcted rat left ventricle characterised via a mixture model. J. Mech. Behav. Biomed. Mater. 119, 104430. http://dx.doi.org/10.1016/j.jmbbm.2021.104430.

Martonová, D., Holz, D., Duong, M.T., Leyendecker, S., 2021b. Towards the simulation of active cardiac mechanics using a smoothed finite element method. J. Biomech. 115, 110153. http://dx.doi.org/10.1016/j.jbiomech.2020.110153.

Milne, M.L., Schick, B.M., Alkhazal, T., Chung, C.S., 2019. Myocardial fiber mapping of rat hearts using apparent backscatter, with histological validation. Ultrasound Med. Biol. 45, 2075–2085. http://dx.doi.org/10.1016/j.ultrasmedbio.2019.05.002.

Niederer, S.A., Campbell, K.S., Campbell, S.G., 2019. A short history of the development of mathematical models of cardiac mechanics. J. Mol. Cell. Cardiol. 127, 11–19. http://dx.doi.org/10.1016/j.yjmcc.2018.11.015.

Niederer, S.A., Smith, N.P., 2007. A mathematical model of the slow force response to stretch in rat ventricular myocytes. Biophys. J. 92, 4030–4044. http://dx.doi.org/10.1529/biophysj.106.095463.

Nishimura, S., Yasuda, Katoh, M., Yamada, K.P., Yamashita, H., Saeki, Y., Sunagawa, K., Nagai, R., Hisada, T., Sugiura, S., 2004. Single cell mechanics of rat cardiomyocytes under isometric, unloaded, and physiologically loaded conditions. Am. J. Physiol.-Heart Circ. Physiol. 287, H196–H202. http://dx.doi.org/10.1152/ajpheart.00948.2003.

Østergaard, G., Hansen, H.N., Ottesen, J.L., 2010. Handbook of Laboratory Animal Science, Volume I: Essential Principles and Practices. https://www.routledge.com/Handbook-of-Laboratory-Animal-Science-Volume-I-Essential-Principles-and/Hau-Schapiro/p/book/9781420084559.

Pacher, P., Mabley, J.G., Liaudet, L., Evgenov, O.V., Marton, A., Haskó, G., Kollai, M., Szabó, C., 2004. Left ventricular pressure-volume relationship in a rat model of advanced aging-associated heart failure. Am. J. Physiol. Heart Circ. Physiol. 287, H2132–H2137. http://dx.doi.org/10.1152/ajpheart.00405.2004.

Panfilov, A.V., Keldermann, R.H., Nash, M.P., 2005. Self-organized pacemakers in a coupled reaction-diffusion-mechanics system. Phys. Rev. Lett. 95, 258104. http://dx.doi.org/10.1103/PhysRevLett.95.258104.

Paterek, A., Kepska, M., Kolodziejczyk, J., Mackiewicz, U., Maczewski, M., 2016. Post-myocardial infarction left ventricular remodelling and function in the rat: Analysis using the pressure-volume loops. Postgrad. Med. J. 7.

Peirlinck, M., Costabal, F.S., Yao, J., Guccione, J.M., Tripathy, S., Wang, Y., Ozturk, D., Segars, P., Morrison, T.M., Levine, S., Kuhl, E., 2021. Precision medicine in human heart modeling: Perspectives, challenges, and opportunities. Biomech. Model. Mechanobiol. 20, 803–831. http://dx.doi.org/10.1007/s10237-021-01421-z.

Rodriguez, E.K., Hoger, A., McCulloch, A.D., 1994. Stress-dependent finite growth in soft elastic tissues. J. Biomech. 27 (4), 455–467.

Sack, K.L., Dabiri, Y., Franz, T., Solomon, S.D., Burkhoff, D., Guccione, J.M., 2018. Investigating the role of interventricular interdependence in development of right heart dysfunction during LVAD support: A patient-specific methods-based. Approach Front. Physiol. 9, http://dx.doi.org/10.3389/fphys.2018.00520.

Sahli Costabal, F., Hurtado, D.E., Kuhl, E., 2016. Generating Purkinje networks in the human heart. J. Biomech. 49, 2455–2465. http://dx.doi.org/10.1016/j.jbiomech.2015.12.025.

Sermesant, M., Razavi, R., 2010. Personalized computational models of the heart for cardiac resynchronization therapy. 16.

Walker, J.C., Ratcliffe, M.B., Zhang, P., Wallace, A.W., Fata, B., Hsu, E.W., Saloner, D., Guccione, J.M., 2005. MRI-based finite-element analysis of left ventricular aneurysm. Am. J. Physiol.-Heart Circ. Physiol. 289, H692–H700. http://dx.doi.org/10.1152/ajpheart.01226.2004.

Wong, J., Kuhl, E., 2014. Generating fibre orientation maps in human heart models using Poisson interpolation. Comput. Methods Biomech. Biomed. Eng. 17, 1217–1226.

frontiers | Frontiers in Cardiovascular Medicine

ORIGINAL RESEARCH
published: 06 July 2022
doi: 10.3389/fcvm.2022.850274

Support Pressure Acting on the Epicardial Surface of a Rat Left Ventricle—A Computational Study

Denisa Martonová[1], David Holz[1], Dorothea Brackenhammer[1], Michael Weyand[2], Sigrid Leyendecker[1] and Muhannad Alkassar[2]*

[1] Institute of Applied Dynamics, Friedrich-Alexander-Universität Erlangen-Nürnberg, Erlangen, Germany, [2] Department of Cardiac Surgery, Friedrich-Alexander-Universität Erlangen-Nürnberg, Erlangen, Germany

The present computational study investigates the effects of an epicardial support pressure mimicking a heart support system without direct blood contact. We chose restrictive cardiomyopathy as a model for a diseased heart. By changing one parameter representing the amount of fibrosis, this model allows us to investigate the impairment in a diseased left ventricle, both during diastole and systole. The aim of the study is to determine the temporal course and value of the support pressure that leads to a normalization of the cardiac parameters in diseased hearts. These are quantified *via* the end-diastolic pressure, end-diastolic volume, end-systolic volume, and ejection fraction. First, the amount of fibrosis is increased to model diseased hearts at different stages. Second, we determine the difference in the left ventricular pressure between a healthy and diseased heart during a cardiac cycle and apply for the epicardial support as the respective pressure difference. Third, an epicardial support pressure is applied in form of a piecewise constant step function. The support is provided only during diastole, only during systole, or during both phases. Finally, the support pressure is adjusted to reach the corresponding parameters in a healthy rat. Parameter normalization is not possible to achieve with solely diastolic or solely systolic support; for the modeled case with 50% fibrosis, the ejection fraction can be increased by 5% with purely diastolic support and 14% with purely systolic support. However, the ejection fraction reaches the value of the modeled healthy left ventricle (65.6%) using a combination of diastolic and systolic support. The end-diastolic pressure of 13.5 mmHg cannot be decreased with purely systolic support. However, the end-diastolic pressure reaches the value of the modeled healthy left ventricle (7.5 mmHg) with diastolic support as well as with the combination of the diastolic and systolic support. The resulting negative diastolic support pressure is −4.5 mmHg, and the positive systolic support pressure is 90 mmHg. We, thereby, conclude that ventricular support during both diastole and systole is beneficial for normalizing the left ventricular ejection fraction and the end-diastolic pressure, and thus it is a potentially interesting therapy for cardiac insufficiency.

Keywords: cardiac assist device, cardiomyopathy, epicardial heart support, left ventricle, support pressure, fibrosis

OPEN ACCESS

Edited by:
Sebastiano A. G. Lava, Centre Hospitalier Universitaire Vaudois (CHUV), Switzerland

Reviewed by:
Ender Ödemiş, Koç University Hospital, Turkey
Michał Mączewski, Medical Centre for Postgraduate Education, Poland

****Correspondence:***
Denisa Martonová
denisa.martonova@fau.de

Specialty section:
This article was submitted to Heart Failure and Transplantation, a section of the journal Frontiers in Cardiovascular Medicine

Received: *07 January 2022*
Accepted: *31 May 2022*
Published: *06 July 2022*

Citation:
Martonová D, Holz D, Brackenhammer D, Weyand M, Leyendecker S and Alkassar M (2022) Support Pressure Acting on the Epicardial Surface of a Rat Left Ventricle—A Computational Study. Front. Cardiovasc. Med. 9:850274. doi: 10.3389/fcvm.2022.850274

1. INTRODUCTION

Cardiovascular diseases remain the leading cause of death worldwide (1). If conservative therapy is inadequate due to the pathological condition of the heart, there are usually only two options remaining to treat this condition: cardiac assist devices or heart transplantation. However, there is a chronic shortage of donors. For example, in Germany, 320 patients received a donor heart in 2020, while the remaining 700 patients were still on the waiting list at the end of that year (2). While heart transplantation is a superior option in terms of survival and functional capacity, significant improvements in the field of cardiac assist devices have resulted in promising solutions that close the gap between availability and demand for donor's hearts. Over the last decades, various types of mechanical pumping systems, known as left ventricular (LV) assist devices, have been developed (3). They are used as an invasive form of therapy to directly support blood circulation. In principle, these systems mostly work to bypass the weakened heart. Such cardiac assist devices can relieve the load on the heart and become either a short- to medium-term bridge to treat cardiac insufficiency until possible transplantation (bridge-to-transplantation) or a permanent solution (destination therapy). Despite the rapid development of new devices and improvements in post-surgery survival and functional capacity nearing those of heart transplantation, there are still many problems to solve, including bleeding, thrombosis, strokes, and infections (3, 4).

For the most part, these problems are caused by the direct contact of blood with the cardiac assist device. Several approaches to avoiding direct blood contact, commonly referred to as direct cardiac compression devices, have been proposed to overcome such difficulties. The first bridge-to-transplantation based on a pneumatic compression cup (5) was followed by several other innovative approaches, e.g., (6–9). Review articles provide a more detailed overview of available direct cardiac compression devices (3, 10). For example, systems from AdjuCor GmbH (8) and CorInnova Inc. (9), currently in the preclinical testing phase, provide support during systole and are minimally invasive implants. The common principle of these devices is that they develop a pressure (force per area) that acts on the epicardial surface. Theoretically, a diseased heart can be thereby supported solely in the diastole, solely in the systole, or in both cardiac phases. However, most direct cardiac compression devices only work during systole. The objective of our computational study is to investigate (1) if an application of support pressure on the LV during both the diastolic and systolic phases is able to normalize the ejection fraction (EF) and left ventricular end-diastolic pressure (EDP) and (2) how much pressure is needed. The current study does not focus on the modeling of a particular cardiac assist device.

In general, the functionality of a direct cardiac compression device is mainly determined by the improvement in the pump function of a diseased heart. In the present study, it is quantified *via* the EF and EDP. However, the influence of a direct cardiac compression device on cardiac performance is not straightforward to compute, due to, e.g., the varying mechanical properties of active biological cardiac tissue that is undergoing complex deformations. The complex orthotropic tissue structure of the healthy myocardium, which can be modeled with different approaches (11–13), plays an important role. Furthermore, the amount of fibrosis in the ventricular wall strongly influences cardiac performance. Over the course of many heart diseases, there is a remodeling process that leads to an increase in fibrosis (14, 15). This is often independent of the triggering disease and can occur after cardiac volumetric pressure loading or ischemia (16). Various studies indicate a correlation between diastolic function and the amount of myocardial fibrosis (17, 18). Regardless of the functional impact of primary cardiomyopathy, the fibrosis progressively limits the diastolic function of the ventricle (19). As long as the condition can be systolically compensated, there is no reduction in the overall myocardial function (heart failure with preserved ejection fraction) (20). However, if the amount of fibrosis exceeds a certain level, the reduction in the diastolic function can no longer be systolically compensated, and the overall myocardial function is reduced (19). It has been shown that ventricular fibrosis inversely correlates with the ejection fraction, both in rats (21) and humans (17). Since the functional impairment resulting from the diastolic dysfunction due to myocardial fibrosis is the terminal stage of most cardiac diseases (17), a better understanding of the role of diastolic function and its relationship with the amount of fibrosis is important. We, therefore, calculated the effects of increasing fibrosis on cardiac function in a computational model of restrictive cardiomyopathy. Studies using postmortem mechanical testing in animal models after myocardial infarction have shown that the fibrosis leads to the stiffening of the cardiac tissue (22–25).

To optimally support a diseased heart *via* a direct cardiac compression device, two main factors play an important role: the time evolution of the force generated by the device and its maximum and minimum values. To date, how these factors influence cardiac function has not been investigated in detail. In this early research study, a computer simulation offers many advantages. First, it saves time compared to experimental testing. Second, there are beneficial synergies between computational modeling and simulation and experimental testing; for example, various parameters can be predicted that cannot be directly measured. Third, modeling and simulation can eventually be used to improve the adaptivity of such a system at a patient-specific level, making it a fundamental instrument in modern and future medicine. So far, a few finite element-based computational models that account for the coupling between a cardiac assist device and the heart have been developed. The existing work presents simulations for the ventricular pumps that are coupled with a univentricular (26) or biventricular heart models (27) *via* a cannula. A computational model for the innovative support system from AdjuCor GmbH is presented in Hirschvogel et al. (28). Recently, Chavanne (29) presented a simulation of a dielectric elastomer actuator-based aortic plaster interacting with a lumped parameter model for the heart.

The present study uses a finite element-based computer simulation. The study models an actively contracting rat LV with different amounts of fibrosis (30) and investigates the influence of direct cardiac compression devices supporting the LV on

cardiac performance during both diastolic and systolic phases. As the current study does not focus on modeling a particular cardiac assist device, for simplicity, the model represents a support pressure acting on the outer surface of the modeled LV, as depicted in **Figure 2A**. During diastole, a negative support pressure is modeled to facilitate the ventricular filling, whereas a positive support pressure in systole is applied to eventually support the blood outflow from the LV. In particular, we investigate whether a support pressure calculated as a difference between the modeled ventricular pressure in a fibrotic and healthy LV would lead to a normalization of cardiac function parameters. Subsequently, the maximum positive systolic and negative diastolic support pressures are optimized such that the EF, EDP, and left ventricular end-diastolic volume (EDV) of a control healthy rat LV are restored. In the present study, a simplified rat LV ventricle is computationally modeled.

2. METHODS

This section describes the computational model of the contraction of a rat LV and the associated numerical experiments.

2.1. Modeling

2.1.1. Balance Equations and Support Pressure Boundary Conditions

The field equation governing the state of the material point $\boldsymbol{X} \in \Omega_0$ at time t, $t \in [t_0, t_f]$ (t_0 and t_f are the initial and final times, respectively) can be formulated. The mechanical field equation is the balance of linear momentum together with the boundary conditions on the boundaries Γ_φ, Γ_1, and Γ_2:

$$0 = \mathrm{Div}[\mathbf{F} \cdot \mathbf{S}] + \boldsymbol{F}^{\varphi} \quad \text{in } \Omega_0, \tag{1}$$

$$\boldsymbol{\varphi}(\boldsymbol{X}, t) = \bar{\boldsymbol{\varphi}} \quad \text{in } \Gamma_\varphi, \qquad \boldsymbol{T}(\boldsymbol{X}, t) = -p_i J \mathbf{F}^{-T} \boldsymbol{N} \quad \text{in } \Gamma_i,\ i \in \{1, 2\} \tag{2}$$

where $\mathbf{F}$ is the deformation gradient with its determinant $J = \det \mathbf{F}$, $\mathbf{S}$ is the second Piola Kirchhoff stress (PK2), $\boldsymbol{F}^{\varphi}$ is the external mechanical body force, $\boldsymbol{\varphi}$ is the displacement with prescribed value $\bar{\boldsymbol{\varphi}}$ on the boundary Γ_φ, $\boldsymbol{T}$ is the surface traction vector in the reference configuration, $\boldsymbol{N}$ is the outer unit normal in the reference configuration and p_i are the prescribed values of the pressures acting on the boundaries Γ_i, $i \in \{1, 2\}$. The pressure p_1 in the LV, obtained from the three-element Windkessel model (representing the interaction between the LV, aorta, and peripheral arteries), serves as a Neumann boundary condition on the endocardial surface Γ_1 whereas the support pressure p_2 serves as a Neumann boundary condition on the epicardial surface Γ_2. The basis of the LV (Γ_φ) is fixed in the longitudinal direction; additionally, the nodes on the outer basis are fixed in all directions (31).

2.1.2. Constitutive Equations

In the present study, the total PK2 is additively decomposed into the passive part $\mathbf{S}_{pas}$ and the active part $\mathbf{S}_{act}$ (31–35), namely

$$\mathbf{S} = \mathbf{S}_{pas} + \mathbf{S}_{act}. \tag{3}$$

Based on Martonová et al. (23), we model the LV as a mixture of the intact myocardium and fibrotic scar structure. The amount of fibrosis, *fib*, serves as a scaling factor. Furthermore, we assume that only the intact muscle tissue is able to contract (30, 36), and therefore the active part of the stress tensor is as well-scaled by the amount of fibrosis. The resulting PK2 reads as

$$\mathbf{S} = fib\, \mathbf{S}^{s}_{pas} + (1 - fib)(\mathbf{S}^{m}_{pas} + \mathbf{S}^{m}_{act}), \tag{4}$$

where the superscripts s and m correspond to the scar and intact myocardium and the subscripts *pas* and *act* to the passive and active parts of the PK2, respectively. In particular, by setting $fib = 0$, only the intact cardiac tissue is modeled. As proposed in Martonová et al. (23) for the passive part, the scar structure is modeled as a transversely isotropic material and the intact myocardium as an orthotropic material, according to Holzapfel and Ogden (37). The active contraction of the intact myocardium is modeled following the simple time-dependent approach from Pfaller et al. (38):

$$\mathbf{S}^{act}(t, \boldsymbol{f}_0, \boldsymbol{n}_0) = T(t)(\boldsymbol{f}_0 \otimes \boldsymbol{f}_0 + \nu \boldsymbol{n}_0 \otimes \boldsymbol{n}_0). \tag{5}$$

The temporal evolution of the active tension T depicted in **Figure 1** is obtained by using the parameters shown in **Table A1**. For the equations describing $T(t)$, we refer to the **Appendix** or the original study (38).

Based on the experimental evidence (39) and our previous study (30), in addition to the contraction in the fiber direction $\boldsymbol{f}_0$, reduced active stress along the cross-fiber direction $\boldsymbol{n}_0$ is added and scaled by ν in Equation (5). We note that the electromechanical coupling is omitted in this study as it would introduce further complexity and variability. However, the model can be coupled with a model for electrical excitation (38). The constitutive model is applied to the generic ellipsoidal rat LV based on the data from echocardiography. For more details regarding the geometry, fiber orientation, compressibility, and the Windkessel model serving as a boundary condition in Equation (1), we refer to previous study (35).

2.1.3. Diastolic Filling

The blood flow I between the left atrium and LV is given as

$$I = \frac{\Delta p}{R_{v1}}, \tag{6}$$

where Δp is the pressure difference between the left atrium and LV, and R_{v1} is the resistance of the atrioventricular valve. The pressure in the atrium p_a is modeled according to the following equation:

$$p_a(t) = \begin{cases} (1 + fib)p_{a1} & \text{if } t \le t_a \\ (1 + fib)(p_{a1} + p_{a2} \sin(t - t_a)) & \text{if } t_a < t \le t_{ed} \\ (1 + fib)p_{a1} & \text{if } t > t_{ed} \end{cases} \tag{7}$$

where p_{a1} and p_{a2} are the minimum and maximum atrial pressures, and t_a, t_{ed} model the onset of the atrial and ventricular

contraction, respectively. The resulting curve is shown in **Figure 1**. We note that the atrial pressure is as well-scaled by the amount of fibrosis, allowing us to model the higher EDP observed in rats with different amounts of fibrosis after myocardial infarction (40). To avoid an unlimited blood inflow from the atrium to the LV, the maximal EDV is restricted to that of the control rat.

2.2. Numerical Experiments

In the following, $p(t)$ defines the support pressure acting on the epicardial surface of the LV. Three numerical experiments are performed.

First, the amount of fibrosis is varied from 0% to 60% in order to compare the cardiac performance represented by the EF in the fibrotic rat LV at different fibrosis stages without a support pressure.

Second, a support pressure is applied in order to increase the diastolic and systolic performance of the diseased LV at different fibrosis stages. The support pressure is computed as a difference between the left ventricular pressure in the control and diseased LV at each time point during the cardiac cycle (**Figure 2B**), namely

$$p(t) = p^0_{LV}(t) - p^{fib}_{LV}(t), \tag{8}$$

where p^0_{LV} is the pressure in the control LV ($fib = 0$), and p^{fib}_{LV} is the left ventricular pressure in a fibrotic LV for different amounts of fibrosis. In these examples, we consider $fib \in \{0.1, 0.3, 0.5\}$.

Third, the support pressure displayed in **Figure 2C** and obeying the following equation is applied on exemplary fibrotic LVs, namely $fib \in \{0.3, 0.5\}$.

$$p(t) = \begin{cases} p_{min} & \text{if } t \le t_{ed} \\ p_{min} + \frac{p_{max}-p_{min}}{t_\Delta}(t - t_{ed}) & \text{if } t_{ed} < t \le t_{ed} + t_\Delta \\ p_{max} & \text{if } t_{ed} + t_\Delta \le t \le t_{es} \\ p_{max} - \frac{p_{max}-p_{min}}{t_\Delta}(t - t_{es}) & \text{if } t_{es} < t \le t_{es} + t_\Delta \\ p_{min} & \text{if } t > t_{es} + t_\Delta \end{cases} \tag{9}$$

As mentioned in the Introduction, three possibilities for supporting a weakened heart can be distinguished: pure diastolic, pure systolic, and combined diastolic and systolic support. For the first possibility, we aim to regain EDP^* and EDV^* of the healthy control LV (within given tolerances tol_1, tol_2). For the second and third possibilities, we additionally aim to nearly reach ESV^* of the healthy control LV. Note that EDP and EDV depend on the value of p_{min} only, i.e., $EDP(p_{min})$, $EDV(p_{min})$, while ESV depends on both values p_{min} and p_{max}, i.e., $ESV(p_{min}, p_{max})$. We started with the determination of the optimal negative support pressure during the diastole $p_{min} = p^*_{min}$ in Equation (9). In a second step, only systolic support is considered, i.e., p_{min} in Equation (9) is set to zero, and the maximal positive support pressure $p_{max} = p^*_{max-sys}$ is determined. In the last step, a combination of diastolic and systolic support is assumed. Therefore, p^*_{min} from the first step is fixed, and the optimal systolic support $p_{max} = p^*_{max}$ is to be found. We note that $p^*_{max-sys} \neq p^*_{max}$ hold in general, as the end-diastolic states are different in both cases. For these three steps, the following algorithm is performed:

1. Diastolic support: Find p^*_{min} so that $|EDV(p^*_{min}) - EDV^*| \le tol_1$ and $|EDP(p^*_{min}) - EDP^*| \le tol_2$ are fulfilled

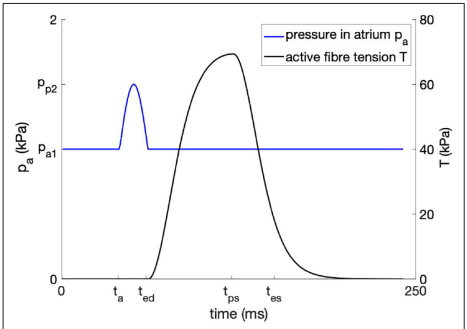

FIGURE 1 | Temporal evolution of the time-dependent atrial pressure and the active fiber tension.

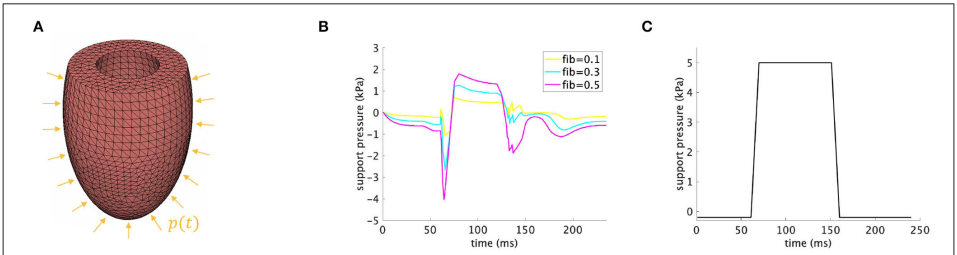

FIGURE 2 | (A) Discretized model of the rat LV with applied support pressure $p(t)$ on the epicardial surface. **(B)** Time-dependent support pressure according to Equation (8) for $fib \in \{0.1, 0.3, 0.5\}$. **(C)** Time-dependent support pressure according to Equation (9).

2. Systolic support: Set $p_{min} = 0$ kPa and find $p^*_{max-sys}$ so that $|ESV(0 \text{ kPa}, p^*_{max-sys}) - ESV^*| \leq tol_1$ is fulfilled
3. Diastolic and systolic support: Set $p_{min} = p^*_{min}$ and find p^*_{max} so that $|ESV(p^*_{min}, p^*_{max}) - ESV^*| \leq tol_1$ is fulfilled

where the optimal support pressure $p^*(t)$ from Equation (9) is determined via the negative diastolic support pressure p^*_{min} and positive systolic support pressures $p^*_{max-sys}, p^*_{max}$, for the purely systolic support and systolic support combined with diastolic support, respectively.

3. RESULTS

Different quantities characterizing the cardiac performance are plotted for all simulations introduced in Section 2.2, including pressure volume loop, EF, EDV, ESV, EDP, and averaged end-diastolic hydrostatic stress over the domain, that is $\sigma_H = \frac{1}{n_{el}} \sum_{i=1}^{n_{el}} \sum_{j=1}^{3} \frac{\sigma^i_{jj}}{3}$, where σ^i_{jj} $(j = 1, 2, 3)$ are the diagonal components of the Cauchy stress in the i-th finite element and $n_{el} = 22846$ is the total number of the tetrahedral finite elements in the computational domain representing the LV; refer to **Figure 2A**. We note that EDP is the fluid pressure inside the cavity of the modeled LV, whereas the end-diastolic hydrostatic stress, computed according to the above formula, depends on the myocardial tissue structure and its volume change during the deformation (41). The latter can be interpreted as a measure of the force that drives fluid out of the myocardium and into the surrounding tissues. Positive hydrostatic stress means that the tissue is under extension and there is an increase in its volume (fluid flows into the myocardium), whereas negative hydrostatic stress implies that the myocardial tissue is compressed (fluid flows out of the myocardium).

3.1. Different Amounts of Fibrosis Without Support

Figure 3 shows the simulation results for scenarios with different amounts of fibrosis without any support pressure. Clearly, by increasing the amount of fibrosis, EF and EDV decrease, whereas ESV and EDP increase. For example, EF and EDP in the healthy model are 65.6% and 1 kPa (7.5 mmHg), respectively. These are close to the experimentally reported values in rats, which are slightly above the normal values in humans (35, 42, 43). By increasing the amount of fibrosis to 30% and 50%, EF reduces to 56.1% and 46.1%, whereas EDP increases to 1.6 kPa (12 mmHg) and 1.8 kPa (13.5 mmHg), respectively; refer to **Figures 3B,E**.

3.2. Support Pressure as the Difference With Respect to the Control Rat (*fib* = 0)

In **Figure 4**, changes in the cardiac function parameters are displayed for the rats with 10%, 30%, and 50% fibrosis in the LV. By applying a support pressure, computed according to Equation (8) and displayed in **Figure 2B**, EF, EDV, EDP, and end-diastolic hydrostatic pressure are at least partially improved, refer to **Figures 4B,C,E,F**, respectively. ESV remains nearly unchanged, refer to **Figure 4D**.

3.3. Constant Minimal and Maximal Support Pressure

Figures 5, **6** illustrate how the stepwise increase in the negative diastolic and positive systolic support pressure influences cardiac performance. The support pressure is increased until the EDP, EDV, and ESV of the control rat are reached up to tolerance. The resulting optimal values of the support pressure are $p^*_{min} = -0.5$ kPa (3.8 mmHg) and $p^*_{max} = 6$ kPa (45 mmHg) for $fib = 0.3$ and $p^*_{min} = -0.6$ kPa (4.5 mmHg), $p^*_{max} = 12$ kPa (90 mmHg) for $fib = 0.5$. For example, for the modeled case with 50% fibrosis in comparison with the control LV, the EF can be increased by 5% with only diastolic support, increased by 14% with only systolic support, and completely reach the value of the modeled control LV (65.6%) with the combination of the diastolic and systolic support. The end-diastolic pressure of 1.8 kPa (13.5 mmHg) cannot be decreased with only systolic support and can completely reach the value of the modeled control LV (7.5 mmHg) with only diastolic support as well as with the combination of the diastolic and systolic support. By increasing the value of the diastolic support, the end-diastolic hydrostatic stress becomes positive. This means that the myocardial tissue is extended and volumetric increase (possibly via a fluid inflow) is present.

4. DISCUSSION

The simulation results show that, with an increased amount of fibrosis, the cardiac performance is reduced; specifically, a reduction in EF is accompanied by increases in ESV and EDP, as shown in **Figures 3B,D,E**. These results mirror the experimental studies in rats after myocardial infarction, where the infarct size was determined as the percentage of the fibrotic scar in the LV (21, 40). As depicted in **Figure 3C**, for an amount of fibrosis of 20%, EDV decreases by 11%. With a further increase in the amount of fibrosis, EDV remains nearly constant due to the combination of the stiffer myocardium and a higher EDP, as shown in **Figure 3E**.

It is worth noting that the alterations in EDP and EDV are caused solely by changes in the passive material properties, whereas the value of ESV is influenced by both the change in the stiffness as well as the reduced maximum active tension, i.e., contractility, which is in Equation (5) scaled by the amount of fibrosis. The absolute value of the hydrostatic stress depicted in **Figure 3F** increases nearly linearly with the amount of fibrosis. Its negative value represents a mechanical compression in the cardiac tissue modeled as a continuum. Theoretically, a high negative hydrostatic stress together with a high EDP might lead to compression and the closure of arterioles supplying the heart and then eventually to an under-perfusion. A more elaborate computational model accounting for the heart perfusion is needed to interpret the results quantitatively.

Considering the support pressure resulting from the difference between the ventricular pressure in a healthy and diseased LV, **Figure 4C** shows that the support pressure is sufficient for reaching the control EDV. We note that the maximum possible EDV was limited to that of the healthy

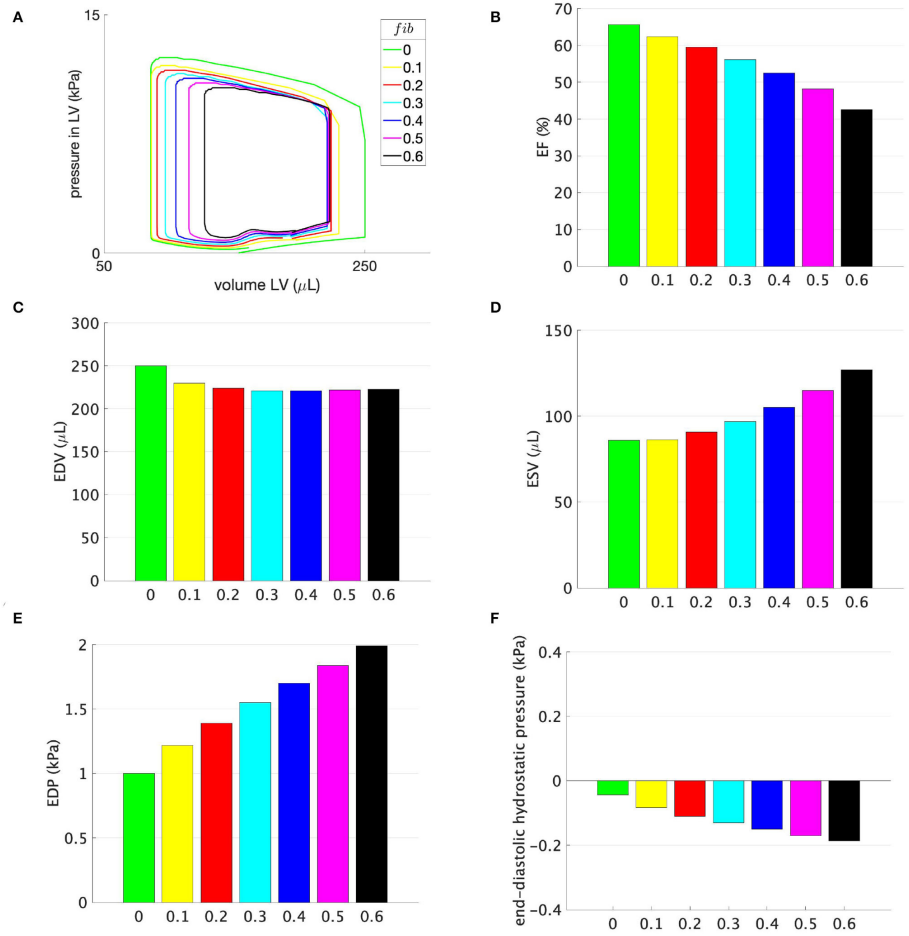

FIGURE 3 | (A) Pressure-volume loops, **(B)** ejection fraction (EF), **(C)** EDV, **(D)** ESV, **(E)** EDP, and **(F)** end-diastolic hydrostatic stress for models with different amounts of fibrosis *fib* displayed on the horizontal axis. No support pressure is applied.

rat. Therefore, even if the negative support pressure is higher than necessary, a normalization of the EDV is accompanied by a reduction in the EDP as depicted in **Figures 4C,E**. Due to the reduction in the EDP and enlargement of the LV, the hydrostatic stress becomes positive for all three fibrosis stages. This means that the tissue is under tension and better perfusion is expected. However, the observed decrease in ESV (**Figure 4D**) is marginal and only sufficient for the case $fib = 0.1$. Therefore, higher systolic support pressure is needed in order to reduce the ESV and eventually increase the EF, which is significantly below that of the control rat for higher amounts of fibrosis. For example, the resulting EFs are 61.1%, 55.2% for $fib = 0.3, 0.5$, respectively, compared to the control rat with EF= 65.6%.

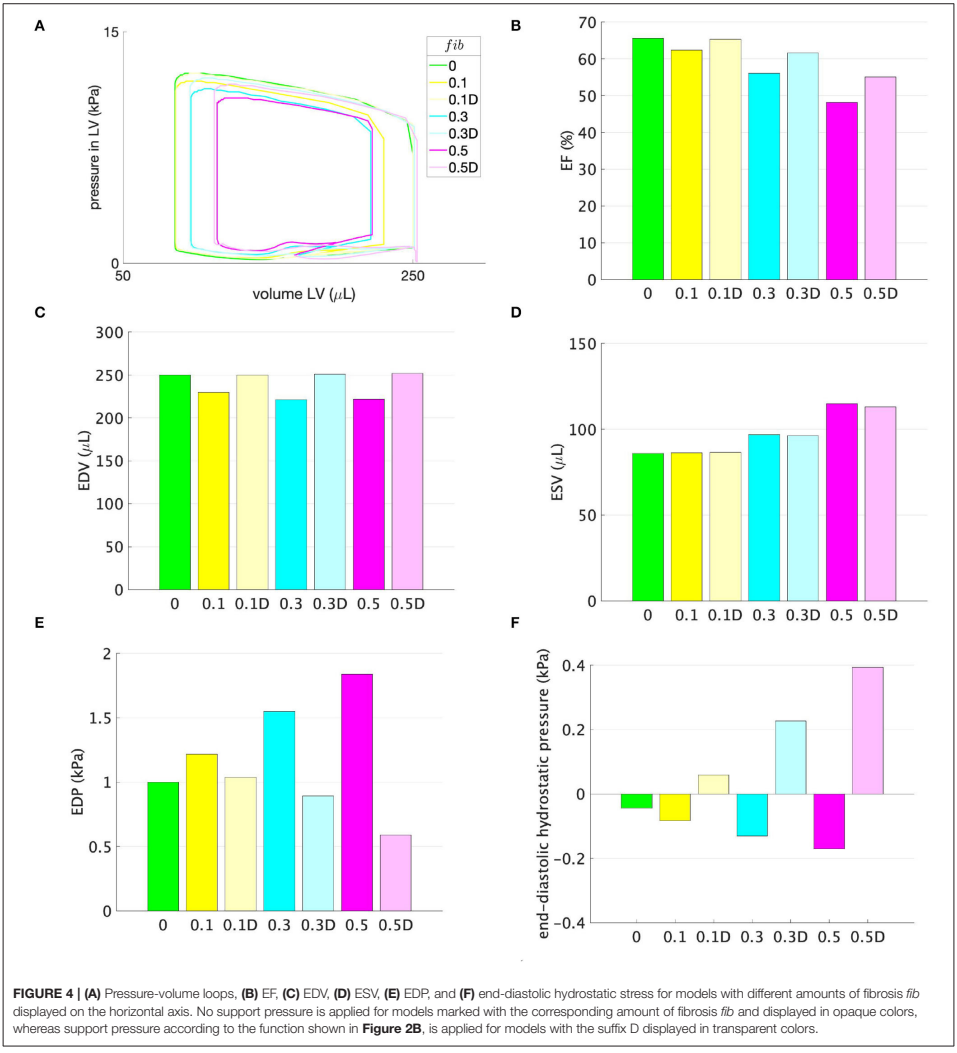

FIGURE 4 | (A) Pressure-volume loops, **(B)** EF, **(C)** EDV, **(D)** ESV, **(E)** EDP, and **(F)** end-diastolic hydrostatic stress for models with different amounts of fibrosis *fib* displayed on the horizontal axis. No support pressure is applied for models marked with the corresponding amount of fibrosis *fib* and displayed in opaque colors, whereas support pressure according to the function shown in **Figure 2B**, is applied for models with the suffix D displayed in transparent colors.

In the numerical test, that applied a constant minimum and maximum support pressure during the diastole and systole, respectively, the algorithm described in Section 2.2 is exemplarily performed for two fibrosis stages, namely $fib = 0.3, 0.5$. We started with supporting only the diastolic phase such that the negative value of the support pressure is increased until the desired EDV and EDP are reached up to a given tolerance. The EF can be increased by approximately 5% for both fibrosis stages, resulting in EF= 60.7%, 53.3% for $fib = 0.3, 0.5$, respectively. Even for the case with 50% fibrotic tissue, a relatively small support pressure of −0.6 kPa (−5.3 mmHg) is sufficient for regaining the desired EDV and EDP. Furthermore, as depicted in **Figure 7**, the compressive hydrostatic stress in the stiff fibrotic myocardium can be reduced and even changed into positive

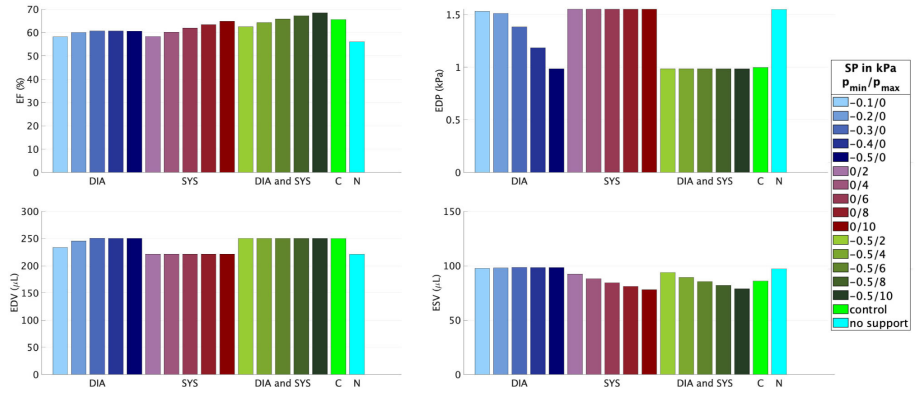

FIGURE 5 | Ejection fraction, EDP, EDV, and ESV for different combinations of the minimal p_{min} and maximal p_{max} values of the support pressure (SP) applied to the epicardial surface of the model with *fib* = 0.3. DIA, diastolic support (blue); SYS, systolic support (red); DIA and SYS, combined support (green); C, control rat LV (light green); N, rat LV with *fib* = 0.3 without any support (blue-green).

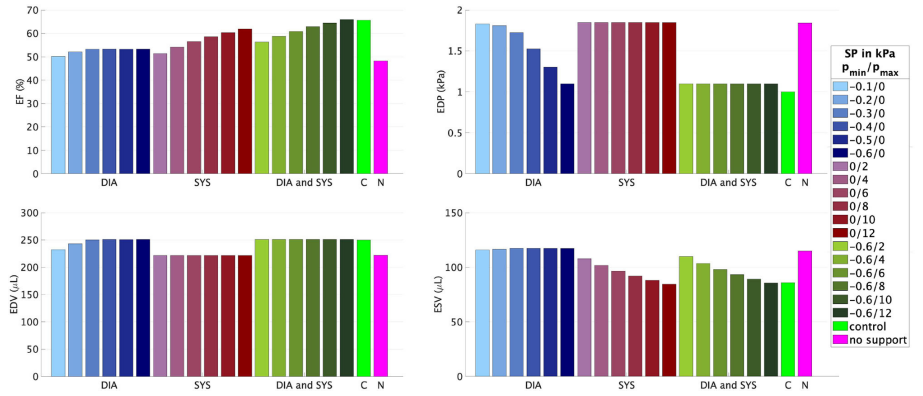

FIGURE 6 | Ejection fraction, EDP, EDV, and ESV for different combinations of the minimal p_{min} and maximal p_{max} values of the support pressure (SP) applied to the epicardial surface of the model with *fib* = 0.5. DIA, diastolic support (blue); SYS, systolic support (red); DIA and SYS, combined support (green); C, control rat LV (light green); N, rat LV with *fib* = 0.5 without any support (pink).

hydrostatic stress. We believe that this phenomenon could improve myocardial perfusion. However, as discussed above, this is currently only speculative and needs to be investigated. When only the systolic phase is supported, significantly higher positive support pressures are needed to normalize the systolic function, 6 kPa (45 mmHg) and 12 kPa (90 mmHg) for *fib* = 0.3, 0.5, respectively. Nevertheless, in this case, the desired EF of the control rat (65.6%) is not reached due to insufficient diastolic filling caused by the stiff fibrotic tissue. When using only the systolic support, a further increase in the support pressure would theoretically lead to the desired EF. However, the EDP would remain elevated, which has been identified as a potential predictor of heart failure (44–46). Whether solely the reduction in EDP would eventually lower

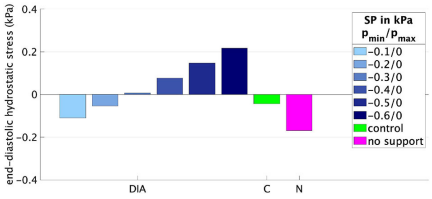

FIGURE 7 | End-diastolic hydrostatic stress for different support pressures (SPs) applied to the rat LV with *fib* = 0.5. DIA, diastolic support; C, control rat LV; N, rat LV with *fib* = 0.5 without any support.

the risk needs to be investigated further. The best option for normalizing EF and EDP turns out to be a combination of both, diastolic and systolic support. As demonstrated in **Figures 5**, **6**, complete normalization of the functional parameters can be reached.

The present study aimed to explore the potential usefulness of diastolic support during the cardiac cycle of a rat LV suffering from restrictive cardiac disease. A simple computational model based on an investigation of mechanical support acting on the outer surface of the LV was chosen. However, there are some limitations and possibilities for future model development. First, the present study investigated the rat heart model and, to date, is not clinically applicable. However, as pointed out in the Introduction, some innovative approaches have investigated possible direct compression assist devices for clinical use in humans. Second, since it is difficult to develop a model that accounts for all influencing factors causing heart insufficiency, we initially chose a model in which we can change both the diastolic and the systolic function of a ventricle by changing one parameter, namely the amount of fibrosis. Besides this, various other factors must be considered in the future to more realistically mimic the remodeling process. These include the effects of geometric changes (in particular those due to ventricular dilatation or hypertrophy), the fact that most failing hearts are rather dilated than restrictive (especially in Paediatrics), the fact that myocardial infarction and ischaemic heart disease are only one among multiple causes of heart failure, the influence of arrhythmias and synchronization, the ever-changing metabolic needs, the fluid status of the patient impacting the preload of the heart, and much more. Third, for a better understanding of the interaction between the heart and a direct cardiac compression device, instead of the prescribed support pressure, a complete direct cardiac compression device should be modeled. Here, one possibility would be to use mechano-active materials, such as biocompatible dielectric elastomer actuators (47) that compress and expand when a voltage is applied. Their relatively large (more than 40%) expandability would be beneficial for generating the support pressure needed during the diastole (48). Fourth, in future development, electromechanical coupling and in particular electromechanical feedback would possibly play a role with respect to the interaction of the heart and the direct cardiac compression device.

5. CONCLUSION

A computational model for different amounts of fibrosis in the rat LV is presented. Based on this model, we investigate how a support pressure acting on the outer surface of the diseased LV influences the cardiac performance quantified via the EF, EDP, and ESV, as well as the hydrostatic stress in the cardiac tissue. We conclude that a negative support pressure during diastole combined with a positive support pressure during systole can normalize the modeled diastolic and systolic function of the rat LV at different fibrosis stages. Although not investigated in this study, it is tempting to assume that the negative diastolic support pressure could potentially improve cardiac perfusion. Furthermore, we adjusted the value of the support pressure so that functional parameters of the healthy rat LV are restored. We conclude that cardiac assist devices without direct blood contact and with a simultaneous diastolic and systolic support functionality present a potentially interesting therapy for heart failure in restrictive LV physiology, as that is resulting from myocardial scars after ischaemic insults.

DATA AVAILABILITY STATEMENT

The raw data supporting the conclusions of this article will be made available by the authors, without undue reservation.

AUTHOR CONTRIBUTIONS

DM mainly contributed to this study concerning the writing of the original manuscript, deriving the equations, modeling, simulation, and post-processing and visualization of the results. DH contributed to the fiber modeling and the revision of the manuscript. DB contributed to initial simulations and post-processing of simulation results. MW contributed to the acquisition of the publication fee support and advice for the medical part. SL and MA contributed to the conception and design of the study and the revision of the manuscript and provided the leadership responsibility for the technical and medical parts, respectively. MA contributed by writing and improving the medical parts of the manuscript. All authors contributed to the article and approved the submitted version.

FUNDING

This study was funded by the Klaus Tschira Stiftung Grant 00.289.2016. The authors acknowledge financial support by Deutsche Forschungsgemeinschaft and Friedrich-Alexander-Universität Erlangen-Nürnberg within the funding programme "Open Access Publication Funding".

REFERENCES

1. WHO. *Global Health Estimates 2019: Disease Burden By Cause, Age, Sex, By Country And By Region, 2000-2019*. (2020). Available online at: https://www.who.int/data/gho/data/themes/mortality-and-global-health-estimates (accessed May 25, 2022).
2. Eurotransplant. *Annual Report 2020*. (2021). Available online at: https://www.eurotransplant.org/statistics/annual-report/ (accessed May 25, 2022).
3. Han J, Trumble DR. Cardiac assist devices: early concepts, current technologies, and future innovations. *Bioengineering*. (2019) 6:18. doi: 10.3390/bioengineering6010018
4. Lima B, Bansal A, Abraham J, Rich JD, Lee SS, Soleimani B, et al. Controversies and challenges of ventricular assist device therapy. *Am J Cardiol*. (2018) 121:1219–24. doi: 10.1016/j.amjcard.2018.01.034
5. Lowe JE, Anstadt MP, Van Trigt P, Smith PK, Hendry PJ, Plunkett MD, et al. First successful bridge to cardiac transplantation using direct mechanical ventricular actuation. *Ann Thorac Surg*. (1991) 52:1237–45. doi: 10.1016/0003-4975(91)90007-D
6. Artrip JH, Yi GH, Levin HR, Burkhoff D, Wang J. Physiological and hemodynamic evaluation of nonuniform direct cardiac compression. *Circulation*. (1999) 100:II236–43. doi: 10.1161/01.CIR.100.suppl_2.II-236
7. Roche ET, Horvath MA, Wamala I, Alazmani A, Song SE, Whyte W, et al. Soft robotic sleeve supports heart function. *Sci Transl Med*. (2017) 9:eaaf3925. doi: 10.1126/scitranslmed.aaf3925
8. Jagschies L, Hirschvogel M, Matallo J, Maier A, Mild K, Brunner H, et al. Individualized biventricular epicardial augmentation technology in a drug-induced porcine failing heart model. *ASAIO J*. (2018) 64:480–8. doi: 10.1097/MAT.0000000000000686
9. Hord EC, Bolch CM, Tuzun E, Cohn WE, Leschinsky B, Criscione JC. Evaluation of the corinnova heart assist device in an acute heart failure model. *J Cardiovasc Transl Res*. (2019) 12:155–63. doi: 10.1007/s12265-018-9854-5
10. Oz MC, Artrip JH, Burkhoff D. Direct cardiac compression devices. *J Heart Lung Transpl*. (2002) 21:1049–55. doi: 10.1016/S1053-2498(02)00482-5
11. Bayer JD, Blake RC, Plank G, Trayanova NA. A novel rule-based algorithm for assigning myocardial fiber orientation to computational heart models. *Ann Biomed Eng*. (2012) 40:2243–54. doi: 10.1007/s10439-012-0593-5
12. Wong J, Kuhl E. Generating fibre orientation maps in human heart models using Poisson interpolation. *Comput Methods Biomech Biomed Eng*. (2014) 17:1217–26. doi: 10.1080/10255842.2012.739167
13. Holz D, Duong MT, Martonová D, Alkassar M, Dittrich S, Leyendecker S. Transmural path model improves definition of orthotropic tissue structure in heart simulation. *J Biomech Eng*. (2022) 144:031002. doi: 10.1115/1.4052219
14. Heusch G, Libby P, Gersh B, Yellon D, Böhm M, Lopaschuk G, et al. Lancet seminar: cardiovascular remodelling in coronary artery disease and heart failure. *Lancet*. (2014) 383:1933–43. doi: 10.1016/S0140-6736(14)60107-0
15. Liu T, Song D, Dong J, Zhu P, Liu J, Liu W, et al. Current understanding of the pathophysiology of myocardial fibrosis and its quantitative assessment in heart failure. *Front Physiol*. (2017) 8:238. doi: 10.3389/fphys.2017.00238
16. Humeres C, Frangogiannis NG. Fibroblasts in the infarcted, remodeling, and failing heart. *JACC. Basic Transl Sci*. (2019) 4:449–467. doi: 10.1016/j.jacbts.2019.02.006
17. Moreo A, Ambrosio G, De Chiara B, Pu M, Tran T, Mauri F, et al. Influence of myocardial fibrosis on left ventricular diastolic function: noninvasive assessment by cardiac magnetic resonance and echo. *Circ Cardiovasc Imaging*. (2009) 2:437–43. doi: 10.1161/CIRCIMAGING.108.838367
18. Zile MR, Baicu CF, S Ikonomidis J, Stroud RE, Nietert PJ, Bradshaw AD, et al. Myocardial stiffness in patients with heart failure and a preserved ejection fraction: contributions of collagen and titin. *Circulation*. (2015) 131:1247–59. doi: 10.1161/CIRCULATIONAHA.114.013215
19. Kane GC, Karon BL, Mahoney DW, Redfield MM, Roger VL, Burnett JC, et al. Progression of left ventricular diastolic dysfunction and risk of heart failure. *JAMA*. (2011) 306:856–63. doi: 10.1001/jama.2011.1201
20. Sweeney M, Corden B, Cook SA. Targeting cardiac fibrosis in heart failure with preserved ejection fraction: mirage or miracle? *EMBO Mol Med*. (2020) 12:e10865. doi: 10.15252/emmm.201910865
21. Fletcher PJ, Pfeffer JM, Pfeffer MA, Braunwald E. Left ventricular diastolic pressure-volume relations in rats with healed myocardial infarction. Effects on systolic function. *Circ Res*. (1981) 49:618–26. doi: 10.1161/01.RES.49.3.618
22. Fomovsky GM, Holmes JW. Evolution of scar structure, mechanics, and ventricular function after myocardial infarction in the rat. *Am J Physiol Heart Circ Physiol*. (2010) 298:H221–8. doi: 10.1152/ajpheart.00495.2009
23. Martonová D, Alkassar M, Seufert J, Holz D, Duong MT, Reischl B, et al. Passive mechanical properties in healthy and infarcted rat left ventricle characterised via a mixture model. *J Mech Behav Biomed Mater*. (2021) 119:104430. doi: 10.1016/j.jmbbm.2021.104430
24. Gupta KB, Ratcliffe MB, Fallert MA, Edmunds LH, Bogen DK. Changes in passive mechanical stiffness of myocardial tissue with aneurysm formation. *Circulation*. (1994) 89:2315–26. doi: 10.1161/01.CIR.89.5.2315
25. Morita M, Eckert CE, Matsuzaki K, Noma M, Ryan LP, Burdick JA, et al. Modification of infarct material properties limits adverse ventricular remodeling. *Ann Thorac Surg*. (2011) 92:617–24. doi: 10.1016/j.athoracsur.2011.04.051
26. McCormick M, Nordsletten DA, Kay D, Smith NP. Simulating left ventricular fluid-solid mechanics through the cardiac cycle under LVAD support. *J Comput Phys*. (2013) 244:80–96. doi: 10.1016/j.jcp.2012.08.008
27. Ahmad Bakir A, Al Abed A, Stevens MC, Lovell NH, Dokos S. A multiphysics biventricular cardiac model: simulations with a left-ventricular assist device. *Front Physiol*. (2018) 9:1259. doi: 10.3389/fphys.2018.01259
28. Hirschvogel M, Jagschies L, Maier A, Wildhirt SM, Gee MW. An *in silico* twin for epicardial augmentation of the failing heart. *IInt J Numer Method Biomed Eng*. (2019) 35:1–23. doi: 10.1002/cnm.3233
29. Chavanne JAJM. Cylindrical dielectric elastomer actuator for cardiac assist device. Ph.D. thesis. Lausanne: Integrated Actuators Laboratory (2019).
30. Martonová D, Alkassar M, Seufert J, Holz D, Tuan Duong M, Reischl B, et al. Influence of passive mechanical properties in healthy and infarcted rat myocardium on the cardiac cycle. *PAMM*. (2021) 21:e202100054. doi: 10.1002/pamm.202100054
31. Eriksson TSE, Prassl AJ, Plank G, Holzapfel GA. Modeling the dispersion in electromechanically coupled myocardium. *Int J Num Methods Biomed Eng*. (2013) 29:1267–84. doi: 10.1002/cnm.2575
32. Göktepe S, Kuhl E. Electromechanics of the heart: a unified approach to the strongly coupled excitation–contraction problem. *Comput Mech*. (2010) 45:227–43. doi: 10.1007/s00466-009-0434-z
33. Sack KL, Dabiri Y, Franz T, Solomon SD, Burkhoff D, Guccione JM. Investigating the role of interventricular interdependence in development of right heart dysfunction during LVAD support: a patient-specific methods-based approach. *Front Physiol*. (2018) 9:524. doi: 10.3389/fphys.2018.00520
34. Duong MT, Holz D, Alkassar M, Dittrich S, Leyendecker S. Interaction of the mechano-electrical feedback with passive mechanical models on a 3D rat left ventricle: a computational study. *Front Physiol*. (2019) 10:1041. doi: 10.3389/fphys.2019.01041
35. Martonová D, Holz D, Seufert J, Duong MT, Alkassar M, Leyendecker S. Comparison of stress and stress-strain approaches for the active contraction in a rat cardiac cycle model. *J Biomech*. (2022) 134:110980. doi: 10.1016/j.jbiomech.2022.110980
36. Berberoğlu E, Göktepe S. Computational modeling of myocardial infarction. *Proc IUTAM*. (2015) 12:52–61. doi: 10.1016/j.piutam.2014.12.007
37. Holzapfel GA, Ogden RW. Constitutive modelling of passive myocardium: a structurally based framework for material characterization. *Philos Trans R Soc A Math Phys Eng Sci*. (2009) 367:3445–75. doi: 10.1098/rsta.2009.0091
38. Pfaller MR, Hörmann JM, Weigl M, Nagler A, Chabiniok R, Bertoglio C, et al. The importance of the pericardium for cardiac biomechanics: from physiology to computational modeling. *Biomech Model Mechanobiol*. (2019) 18:503–29. doi: 10.1007/s10237-018-1098-4
39. Lin DHS, Yin FCP. A multiaxial constitutive law for mammalian left ventricular myocardium in steady-state barium contracture or tetanus. *J Biomech Eng*. (1998) 120:504–17. doi: 10.1115/1.2798021
40. Pfeffer MA, Pfeffer JM, Fishbein MC, Fletcher PJ, Spadaro J, Kloner RA, et al. Myocardial infarct size and ventricular function in rats. *Circ Res*. (1979) 44:503–12. doi: 10.1161/01.RES.44.4.503
41. Gurtin ME. *An Introduction to Continuum Mechanics*. 1st ed. New York, NY: Academic Press (1981).

42. Pacher P, Mabley JG, Liaudet L, Evgenov OV, Marton A, Haskó G, et al. Left ventricular pressure-volume relationship in a rat model of advanced aging-associated heart failure. *Am J Physiol Heart Circ Physiol.* (2004) 287:H2132–7. doi: 10.1152/ajpheart.00405.2004
43. Jegger D, Jeanrenaud X, Nasratullah M, Chassot PG, Mallik A, Tevaearai H, et al. Noninvasive Doppler-derived myocardial performance index in rats with myocardial infarction: validation and correlation by conductance catheter. *Am J Physiol Heart Circ Physiol.* (2006) 290:H1540–8. doi: 10.1152/ajpheart.00935.2005
44. Mielniczuk LM, Lamas GA, Flaker GC, Mitchell G, Smith SC, Gersh BJ, et al. Left ventricular end-diastolic pressure and risk of subsequent heart failure in patients following an acute myocardial infarction. *Congest Heart Fail.* (2007) 13:209–14. doi: 10.1111/j.1527-5299.2007.06624.x
45. Planer D, Mehran R, Witzenbichler B, Guagliumi G, Peruga JZ, Brodie BR, et al. Prognostic utility of left ventricular end-diastolic pressure in patients with ST-segment elevation myocardial infarction undergoing primary percutaneous coronary intervention. *Am J Cardiol.* (2011) 108:1068–74. doi: 10.1016/j.amjcard.2011.06.007
46. Khan AA, Al-Omary MS, Collins NJ, Attia J, Boyle AJ. Natural history and prognostic implications of left ventricular end-diastolic pressure in reperfused ST-segment elevation myocardial infarction: An analysis of the thrombolysis in myocardial infarction (TIMI) II randomized controlled trial. *BMC Cardiovasc Disord.* (2021) 21:243. doi: 10.1186/s12872-021-02046-x
47. Ponniah JK, Chen H, Adetiba O, Verduzco R, Jacot JG. Mechanoactive materials in cardiac science. *J Mater Chem B.* (2016) 4:7350–62. doi: 10.1039/C6TB00069J
48. Alkassar M. *Circulatory Assistance Device*. European patent No. EP3503938 B1. Munich, Germany. European Patent Office (2021).

Conflict of Interest: The authors declare that the research was conducted in the absence of any commercial or financial relationships that could be construed as a potential conflict of interest.

Publisher's Note: All claims expressed in this article are solely those of the authors and do not necessarily represent those of their affiliated organizations, or those of the publisher, the editors and the reviewers. Any product that may be evaluated in this article, or claim that may be made by its manufacturer, is not guaranteed or endorsed by the publisher.

APPENDIX

Simulation Parameters

TABLE A1 | Material parameters used in the numerical examples.

Active stress	t_{ed} = 60 ms, t_{ps} = 120 ms, $\alpha_{min} = -0.1\text{ms}^{-1}$, $\alpha_{max} = 0.1\text{ms}^{-1}$, γ = 25 ms, T_{max}=70 kPa,
Passive stress	a = 1.665 kPa, b = 1.237 (-), a_f = 7.822 kPa, b_f = 0.008 (-), a_s = 0.0 kPa,
	b_s = 0.0 (-), a_{fs} = 1.342 kPa, b_{fs} = 9.178 (-)
Windkessel model	R_p = 15 kPa μL^{-1}ms, R_{v1} =0.1 kPa μL $^{-1}$ms, R_{v2} =0.067 kPa μL^{-1}ms,
	C = 40 μL kPa $^{-1}$ ms^{-1}, t_a = 40 ms
Support pressure	t_{es} = 150 ms, t_Δ = 10 ms, tol_1 = 1 μL, tol_2 = 0.1 kPa

Active Tension

Based on the study by Pfaller et al. (38), the evolution of the active tension T reads as

$$\dot{T}(t) = -|a(t)|T(t) + T_{max}|a(t)|_+$$

with activation function a, the maximum value of the active stress T, and the function $|a(t)|_+ = \max(a(t); 0)$. The activation function $a(t)$ is modeled by

$$a(t) = \alpha_{max} \cdot f(t) + \alpha_{min} \cdot (1 - f(t))$$

with maximum and minimum activation rates α_{max} and α_{min}, respectively, and functions

$$f(t) = S^+(t - t_{ed})\Delta S^-(t - t_{ps}),$$
$$S^\pm(\Delta t) = \frac{1}{2}(1 \pm \tanh(\frac{\Delta t}{\gamma}))$$

with steepness γ and descending and ascending sigmoid functions S^+ and S^-, respectively. The indicator function $f \in (0, 1)$ indicates systole. The times t_{ed} and t_{ps} model the end-diastolic and the peak-systolic times, respectively.

Journal of Biomechanics 115 (2021) 110153

Contents lists available at ScienceDirect

Journal of Biomechanics

journal homepage: www.elsevier.com/locate/jbiomech
www.JBiomech.com

Towards the simulation of active cardiac mechanics using a smoothed finite element method

Denisa Martonová [a,*], David Holz [a], Minh Tuan Duong [a,b], Sigrid Leyendecker [a]

[a] Friedrich-Alexander-Universität Erlangen-Nürnberg, Institute of Applied Dynamics, Immerwahrstraße 1, 91058 Erlangen, Germany
[b] Hanoi University of Science and Technology, School of Mechanical Engineering, 1 Dai Co Viet Road, Ha Noi, Viet Nam

ARTICLE INFO

Article history:
Accepted 23 November 2020

Keywords:
Heart
Left ventricle
Cardiac mechanics
Smoothed finite element method
Mesh distortion

ABSTRACT

In the last decades, various computational models have been developed to simulate cardiac electromechanics. The most common numerical tool is the finite element method (FEM). However, this method crucially depends on the mesh quality. For complex geometries such as cardiac structures, it is convenient to use tetrahedral discretisations which can be generated automatically. On the other hand, such automatic meshing with tetrahedrons together with large deformations often lead to elements distortion and volumetric locking. To overcome these difficulties, different smoothed finite element methods (S-FEMs) have been proposed in the recent years. They are known to be volumetric locking free, less sensitive to mesh distortion and so far have been used e.g. in simulation of passive cardiac mechanics. In this work, we extend for the first time node-based S-FEM (NS-FEM) towards active cardiac mechanics. Firstly, the sensitivity to mesh distortion is tested and compared to that of FEM. Secondly, an active contraction in circumferentially aligned fibre direction is modelled in the healthy and the infarcted case. We show, that the proposed method is more robust with respect to mesh distortion and computationally more efficient than standard FEM. Being furthermore free of volumetric locking problems makes S-FEM a promising alternative in modelling of active cardiac mechanics, respectively electromechanics.

1. Introduction

The finite element method is a standard numerical technique in cardiac simulation, as reported in recent reviews, e.g. Lopez-Perez et al. (2015), Niederer et al. (2019). In the last decades, numerous univentricular (Duong et al., 2019; Eriksson et al., 2013; Guccione et al., 2001; Sermesant et al., 2006), biventricular (Sermesant et al., 2006; Trayanova et al., 2011) and full heart models (Baillargeon et al., 2014; Trayanova, 2011) have been developed to simulate cardiac function, study pathologies (Berberoğlu and Göktepe, 2015; Sáez and Kuhl, 2016; Trayanova et al., Jul. 2017) or to investigate the arrhythmogenic influence of drugs (Sahli Costabal et al., 2018). One aim of the current research going on worldwide in this field is the development of methods for robust and efficient patient-specific virtual heart models. Besides the experimentally derived parameters, such models require a patient-specific geometry, mostly based on magnetic resonance imaging (MRI) data. However, heart geometries can be very complex. Therefore, automatically generated tetrahedral elements (T4) are often used in cardiac simulations (Baillargeon et al., 2014; Rossi et al., 2014; Sermesant et al., 2006). On the other hand, when T4 are considered in combination with a nearly incompressible material and large deformations, which is the case in cardiac (electro) mechanics, the standard FEM has some limitations: T4 are known to behave very stiffly due to the volumetric locking phenomenon which leads to inaccuracies (De Oliveira and Sundnes, 2016; Jiang et al., 2015a). Secondly, for the simulation of large deformations, a high quality mesh is required to avoid element distortion. As an alternative to T4, hexahedral elements can be utilised. These were shown to provide more accurate solutions in cardiac mechanics (De Oliveira and Sundnes, 2016). However, the mesh generation for complex geometries cannot be performed automatically and requires a significant effort. To overcome these challenges, some alternative approaches to classical FEM have been considered in the recent years.

For example, meshless methods (MM) were shown to provide accurate results in cardiac simulations (Lluch et al., 2019; Lluch et al., 2020; Wong et al., 2010). In (Lluch et al., 2019; Lluch et al., 2020), the first fully coupled electromechanical meshless model was described and calibrated with clinical imaging data and pressure measurements. Comparison of the simulation results to the

* Corresponding author.
E-mail address: denisa.martonova@fau.de (D. Martonová).

https://doi.org/10.1016/j.jbiomech.2020.110153
0021-9290/

experimental data showed that the method performs accurately in cardiac mechanics and hemodynamics. However, MM are computationally much more expensive than linear FEM.

Another approach combining some techniques from FEM and MM are smoothed finite elements methods, originally proposed by Liu and co-workers (Liu et al., 2007). They are based on the strain smoothing over a designed smoothing domain (SD). Depending on the SD type, different S-FEM techniques with different properties are distinguished. The main variants are cell-based S-FEM (CS-FEM) (Liu et al., 2007), NS-FEM (Liu et al., 2009b), and edge-based S-FEM (ES-FEM) for both 2D and 3D problems (Liu et al., 2009a) and face-based S-FEM (FS-FEM) for 3D problems (Duong, 2014; Nguyen-Thoi et al., 2009). Additionally, the selective NS-/FS-FEM is proposed for nearly incompressible materials, where NS-FEM is used for the volumetric and FS-FEM for the isochoric part (Jiang et al., 2014). The advantages and applications of S-FEM are summarised in Liu (2019), Zeng and Liu (2018). Briefly, S-FEM models are softer than their FEM counterparts using the same mesh, less sensitive to mesh distortion, able to overcome the volumetric locking problems and working well with triangular and tetrahedral meshes which can be generated automatically.

In the last years, S-FEM has been applied in different fields, e.g. material mechanics, fracture mechanics, structural mechanics of plates and shells, dynamics, acoustics, heat transfer and fluid–structure interactions. A detailed overview is given in Liu (2019), Zeng and Liu (2018).

Recently, biomechanics became another promising field of application for S-FEM for several reasons. On the one hand, because biological materials are often modelled as nearly incompressible. On the other hand, geometries are usually complex and need to be meshed with T4. Further, high accuracy is required to be accompanied with a low computational cost. For nearly incompressible materials undergoing large deformation, the selective S-FEM combining NS-FEM for the volumetric part and FS-FEM for the deviatoric part (NS/FS-FEM) was proposed by Jiang et al. (2014).

Up to date, S-FEM techniques have been implemented in biomechanical simulations for the growth of soft biological tissue (Duong and Staat, 2014; Duong et al., 2015), aortic valve opening (Yao et al., 2012) and passive cardiac mechanics (Jiang et al., 2015a; Jiang et al., 2015b). All studies demonstrated that S-FEM performs highly accurate, is able to overcome volumetric-locking, insensitive to mesh distortion and computationally efficient. Jiang et al. (2015a) concludes that S-FEM is a promising alternative in cardiac simulation. However, so far, S-FEM has only been applied to passive cardiac mechanics (Jiang et al., 2015a). The next logical step is to extend S-FEM to active mechanics and fully coupled electromechanics. In our work, we develop a 2D model for active cardiac mechanics using NS-FEM.

2. Methods

The basic idea of S-FEM is the strain smoothing over a smoothing domain. In particular, the strain field become continuous over the elements boundaries, where it is discontinuous in the linear FEM. Firstly, the domain Ω bounded by Γ is discretised into non-overlapping elements in the same way as in the FEM. Subsequently, it is subdivided into a finite number of non-overlapping SDs Ω_k with boundary Γ_k, i.e. $\Omega = \cup_{k=n_{sd}}\Omega_k$, where n_{sd} is the number of SDs and $\Omega_i \cap \Omega_j = \varnothing$ for $i \neq j$. See Fig. 1 for SDs in 2D for NS-FEM.

Let us consider a geometrically and materially non-linear 2D problem with a triangular mesh. The following concept can be extended to 3D problems (Duong and Staat, 2014; Jiang et al., 2015a; Liu, 2019). Let $\Omega \subseteq \mathbb{R}^2$ and consider the balance equation in the reference configuration:

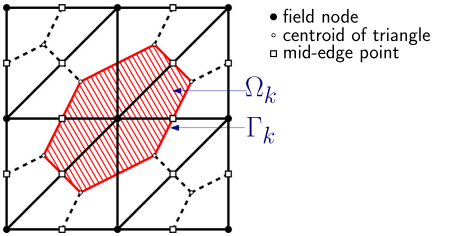

Fig. 1. Smoothing domains in 2D for NS-FEM. In red, the SD Ω_k around the node in the centre of the square is highlighted.

$$\mathrm{Div}\boldsymbol{P} + \boldsymbol{b}_0 = \boldsymbol{0} \tag{1}$$

where $\boldsymbol{P}$ is the first Piola–Kirchhoff stress tensor and $\boldsymbol{b}_0$ the body force. Further, let $\boldsymbol{X}$ be a material point, $\boldsymbol{x}$ a spatial point and $\boldsymbol{I}$ the identity tensor. In FEM, the displacement field $\boldsymbol{u}(\boldsymbol{X}) = \boldsymbol{x}(\boldsymbol{X}) - \boldsymbol{X}$ and deformation gradient $\boldsymbol{F} = \frac{\partial \boldsymbol{x}(\boldsymbol{X})}{\partial \boldsymbol{X}} = \frac{\partial \boldsymbol{u}(\boldsymbol{X})}{\partial \boldsymbol{X}} + \boldsymbol{I}$ are approximated on an element e as

$$\begin{aligned} \boldsymbol{u}^e(\boldsymbol{X}) &= \sum_{\alpha=1}^{nn} N_\alpha(\boldsymbol{X})\boldsymbol{u}_\alpha; \\ F^e_{ij}(\boldsymbol{X}) &= \frac{\partial u^e_i(\boldsymbol{X})}{\partial X_j} + \delta_{ij} = \sum_{\alpha=1}^{nn} \frac{\partial N_\alpha(\boldsymbol{X})}{\partial X_j}(\boldsymbol{u}_\alpha)_i + \delta_{ij}, \end{aligned} \tag{2}$$

where nn is the number of element nodes, $\boldsymbol{u}_\alpha$ the nodal displacement and N_α the nodal shape function. The key idea of S-FEM is gradient smoothing over a SD Ω_k by convolution with a smoothing function Φ_k satisfying at least the property $\int_{\Omega_k}\Phi_k(\boldsymbol{X})\mathrm{d}\Omega = 1$, e.g.

$$\Phi_k(\boldsymbol{X}) = \begin{cases} 1/V_k & \text{if } \boldsymbol{X} \in \Omega_k \\ 0 & \text{else} \end{cases} \quad \text{with } V_k = \int_{\Omega_k} \mathrm{d}\Omega. \tag{3}$$

Assuming linear triangular elements, the smoothed deformation gradient $\bar{\boldsymbol{F}}^k$ is constant for all for $\boldsymbol{X}_k \in \Omega_k$ and takes the form

$$\bar{F}^k_{ij}(\boldsymbol{X}_k) = \int_{\Omega_k} F^e_{ij}(\boldsymbol{X})\Phi_k(\boldsymbol{X})\mathrm{d}\Omega = \frac{1}{V_k}\sum_{e\in n^e_k}\frac{V_e}{3}\frac{\partial u^e_i(\boldsymbol{X})}{\partial X_j} + \delta_{ij} \tag{4}$$

where V_e is the volume (area in 2D) of the element e and n^e_k is the set of elements connected to the node k in NS-FEM. Consequently, the smoothed left Cauchy-Green tensor $\bar{\boldsymbol{C}} = \bar{\boldsymbol{F}}^T\bar{\boldsymbol{F}}$ and the Cauchy stress $\bar{\boldsymbol{\sigma}}$ are computed on a SD. The stiffness matrix is assembled analogously to the FEM, but integration is performed over the SDs rather than over elements.

Towards active cardiac mechanics with S-FEM

In our work, we test the NS-FEM approach on a 2D mechanical problem and we further extend it towards active cardiac mechanics. Recently, Kshrisagar et al. (2019) developed a user element subroutine (UEL) for the NS-FEM in 2D within the commercial software Abaqus. Based on this work, we firstly consider a purely mechanical problem where two concentric circles representing a transversal cut through the left ventricle (LV) with the outer radius $r_o = 5$ mm and inner radius $r_i = 3$ mm are considered. A parabolic-shaped load of -50 mN is applied on the inner boundary over an arc length of 4 mm linearly increasing during the time period of 1s as depicted in Fig. 2. The nodal displacement on the outer circle is fixed. We compare the NS-FEM to FEM with both linear triangular and quadrilateral elements.

Secondly, for the first time, we implement active cardiac mechanics in the framework of S-FEM and test the accuracy of

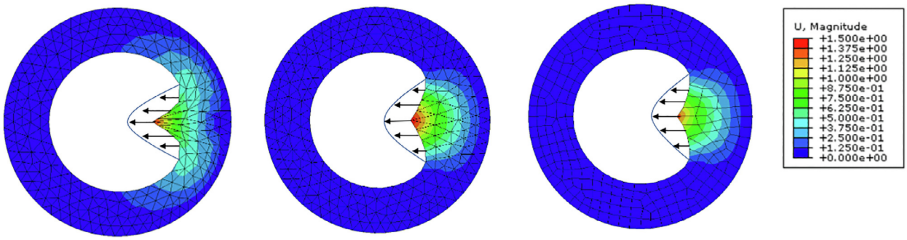

Fig. 2. Parabolic load of −50 mN applied on the inner boundary linearly increasing over the time period of 1s. Final deformed configurations coloured by the displacement. From left to right: NS-FEM with linear triangular elements (simulation completed); FEM with linear triangular elements (aborted at $t = 0.516$ s due to distorted elements); FEM with linear quadrilateral elements (aborted at $t = 0.438$ s due to distorted elements).

the proposed method. The reference solution for our numerical example is obtained using FEM with a very fine mesh (2942 DOF) for the concentric circles described above and depicted in Fig. 3 left. In addition to the smoothed quantities introduced above, reference fibre orientations $\bar{\boldsymbol{f}}_0$ are computed for each SD. Consequently, the deformed fibre orientation is given as $\bar{\boldsymbol{f}} = \bar{\boldsymbol{F}}\bar{\boldsymbol{f}}_0$. For simplicity, the fibres are assumed to be circumferentially aligned in the numerical examples, see Fig. 3a left. We assume an additive decomposition of the smoothed Cauchy stress $\bar{\boldsymbol{\sigma}}$

$$\begin{aligned}\bar{\boldsymbol{\sigma}}(t,\bar{\boldsymbol{F}},\bar{\boldsymbol{f}}) &= \bar{\boldsymbol{\sigma}}_p(\bar{\boldsymbol{F}}) + \bar{\boldsymbol{\sigma}}_a(t,\bar{\boldsymbol{F}},\bar{\boldsymbol{f}}) \\ &= \frac{2}{\det\bar{\boldsymbol{F}}}\,\bar{\boldsymbol{F}}\frac{\partial W(\bar{\boldsymbol{C}})}{\partial \bar{\boldsymbol{C}}}\bar{\boldsymbol{F}}^T + T_a(t,l(\bar{\boldsymbol{C}}))(\bar{\boldsymbol{f}}\otimes\bar{\boldsymbol{f}}),\end{aligned} \tag{5}$$

where W is the Neo-Hookean strain energy function, $\bar{\boldsymbol{\sigma}}_p$ and $\bar{\boldsymbol{\sigma}}_a$ are passive and active smoothed stresses, respectively, and T_a is the active force modelled according to Guccione et al. (1993), Sack et al. (2018). We refer to the Appendix for more details. In the first numerical example, we consider homogenous material representing a transversal cut through a healthy LV. Additionally, myocardial infarction (MI) in the fourth quadrant is modelled by reducing the active force in this region to zero as depicted in Fig. 3(b) left. The active contraction is induced in the circumferentially aligned fibre direction, see (5) and Fig. 3(a) left.

3. Results and discussion

The deformed configurations of the first purely mechanical test are depicted in Fig. 2. It is confirmed that, in contrast to both FEM

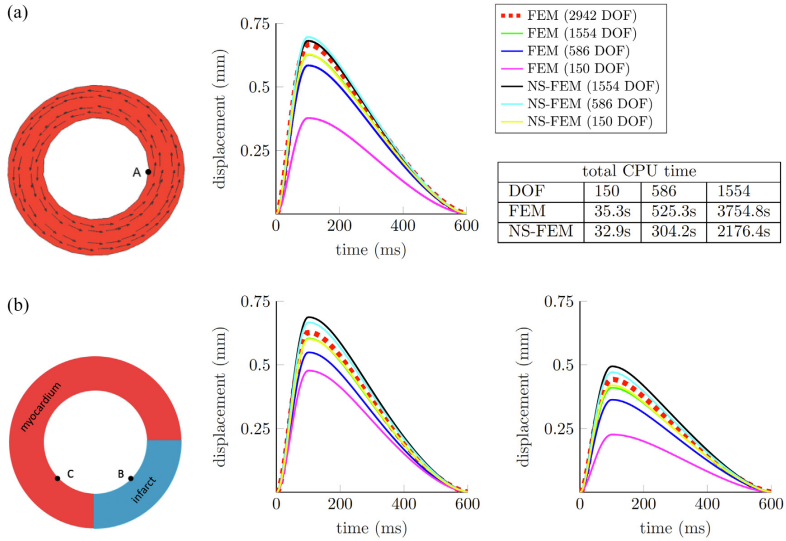

total CPU time			
DOF	150	586	1554
FEM	35.3s	525.3s	3754.8s
NS-FEM	32.9s	304.2s	2176.4s

Fig. 3. Active contraction of a healthy (a) and an infarcted (b) myocardium in 2D. (a) Left to right: undeformed healthy ventricular slice with the circumferentially aligned fibre orientation; displacement of the node A with $T_{max} = 5$ kPa; total CPU time for simulations using FEM and NS-FEM with different DOFs. (b) Left to right: schematic representation of the ventricular slice with MI in the fourth quadrant; displacement of the node C in the healthy region ($T_{max} = 5$ kPa); displacement of the node B in the infarcted region ($T_{max} = 0$ kPa).

examples, the NS-FEM is not sensitive to mesh distortion. The reason is that S-FEMs do not require isoparametric mapping and therefore the Jacobian matrix, which is badly conditioned for distorted elements, has not to be evaluated Liu (2019).

The simulation results shown in Fig. 3 confirm that NS-FEM performs softer than linear FEM for both healthy and infarcted tissue samples. This is in agreement with the known softening effect of NS-FEM presented in previous works (Liu et al., 2009b; Liu, 2019; Zeng and Liu, 2018). We observe that, compared to FEM, NS-FEM is less computationally expensive considering the same number of degrees of freedom (DOF), which is more prominent for fine grids (Fig. 3(a) right). The reason is that the assembly of the global stiffness matrix is performed over the node-based SDs and in the given problem, there are less SDs than elements. Furthermore, even a coarse discretisation (150 DOF) produces close to the same solution as FEM with a much finer mesh (1554 DOF), i.e. yellow and green lines nearly overlap in the plots in Fig. 3. The corresponding central processing unit (CPU) time is more than ten times lower for the NS-FEM approach.

4. Conclusion

In this work, we extend for the first time S-FEM towards the active cardiac mechanics using NS-FEM on a triangular mesh. We observe that the proposed method is more robust against mesh distortion and volumetric locking problem and it is computationally more efficient than FEM with linear triangular elements. Furthermore, it works well with automatically generated triangular meshes and can be extended for 3D problems. We conclude that S-FEM is a promising tool for modelling of 3D cardiac active mechanics and electromechanics using automatically generated tetrahedral meshes.

CRediT authorship contribution statement

Denisa Martonová: Conceptualization, Methodology, Software, Formal analysis, Writing - original draft, Visualization. **David Holz:** Software, Methodology, Writing - review & editing. **Minh Tuan Duong:** Software, Writing - review & editing. **Sigrid Leyendecker:** Conceptualization, Methodology, Supervision, Funding acquisition, Writing - review & editing, Project administration.

Declaration of Competing Interest

The authors report no conflict of interest, financial or otherwise.

Acknowledgement

The authors thank the Klaus Tschira Stiftung grant 00.289.2016 for funding support. We gratefully acknowledge the Pediatric Cardiology at the Friedrich-Alexander-Universität Erlangen-Nürnberg, in particular Dr. rer. nat. Muhannad Alkassar, for the cooperation on the project.

Appendix A

For the passive part, we consider the simple Neo-Hookean strain energy function

$$W = \frac{\lambda}{2}\left(\ln \bar{J}\right)^2 - \mu \ln \bar{J} + \frac{1}{2}\mu\left(\mathrm{tr}\bar{\boldsymbol{C}} - 3\right),$$

where $\bar{J} = \det \bar{\boldsymbol{F}}$ and λ, μ are the material constants. The active part is modelled according to Guccione et al. (1993), Sack et al. (2018) as

$$\bar{\boldsymbol{\sigma}}_a = T_a \bar{\boldsymbol{f}} \otimes \bar{\boldsymbol{f}}).$$

$T_a(t, l(\bar{\boldsymbol{C}}))$ is the time-varying active force and is defined as

$$T_a(t, l(\bar{\boldsymbol{C}})) = T_{max} \frac{Ca_0^2}{Ca_0^2 + ECa_{50}^2(l)} \frac{(1 - \cos(\omega(t,l)))}{2},$$

where

$$ECa_{50}(l) = \frac{Ca_{0max}}{\sqrt{e^{B(l-l_0)} - 1}},$$

$$\omega(t,l) = \begin{cases} \pi \frac{t}{t_0} & \text{if } 0 \leqslant t \leqslant t_0 \\ \pi \frac{t - t_0 + t_r(l)}{t_r(l)} & \text{if } t_0 \leqslant t \leqslant t_0 + t_r(l) \\ 0 & \text{if } t \geqslant t_0 + t_r(l), \end{cases}$$

$$t_r(l) = ml + b,$$

$$l = l_r \sqrt{\bar{\boldsymbol{f}}_0 \cdot \left(\bar{\boldsymbol{C}} \bar{\boldsymbol{f}}_0\right)},$$

and the following parameters: t_0 time to reach the peak tension after the initiation of active tension; Ca_0, Ca_{0max} the peak and maximal peak intracellular calcium concentration, respectively; T_{max} the maximal possible isometric active tension; l, l_r the current and initial sarcomere length, respectively; l_0 the sarcomere length below which no active tension develops; m, b, B govern the slope, length and peak of the active tension, respectively. Parameters used in the numerical examples are: $\lambda = 20$ kPa, $\mu = 0.49$ kPa, $Ca_0 = ECa_{50} = 4.35$ μM, $l_0 = 1.58$ μM, $l_r = 1.85$ μm, $m = 1048.9\ s\ \mu m^{-1}$, $b = -1429$ ms, $B = 4.75\ \mu m^{-1}$.

References

Baillargeon, B., Rebelo, N., Fox, D.D., Taylor, R.L., Kuhl, E., 2014. The Living Heart Project: A robust and integrative simulator for human heart function. Eur. J. Mech. A. Solids 48, 38–47.

Berberoğlu, E., Göktepe, S., 2015. computational modeling of myocardial infarction. Procedia IUTAM 12, 52–61.

De Oliveira, B.L., Sundnes, J., 2016. Comparison of tetrahedral and hexahedral meshes for finite element simulation of cardiac electro-mechanics. In: Proceedings of the VII European Congress on Computational Methods in Applied Sciences and Engineering (ECCOMAS Congress 2016). Institute of Structural Analysis and Antiseismic Research School of Civil Engineering National Technical University of Athens (NTUA) Greece, Crete Island, Greece, pp. 164–177.

Duong, M.T., 2014. Hyperelastic Modeling and Soft-Tissue Growth Integrated with the Smoothed Finite Element Method-SFEM PhD thesis. RWTH Aachen University, Germany.

Duong, M.T., Holz, D., Alkassar, M., Dittrich, S., Leyendecker, S., 2019. Interaction of the mechano-electrical feedback with passive mechanical models on a 3D rat left ventricle: a computational study. Front. Physiol. 10, 1041.

Duong, M.T., Staat, M., 2014. A face-based smoothed finite element method for hyperelastic models and tissue growth. In: 11th World Congress on Computational Methods in Applied Sciences and Engineering (ECCOMAS), p. 12 pages.

Duong, M.T., Staat, M., Nguyen-Nhu, H., 2015. Modeling and simulation of a growing mass by the Smoothed Finite Element Method (SFEM). In: 3rd ECCOMAS Young Investigators Conference, p. 12.

Eriksson, T.S.E., Prassl, A.J., Plank, G., Holzapfel, G.A., 2013. Modeling the dispersion in electromechanically coupled myocardium. Int. J. Num. Methods Biomed. Eng. 29 (11), 1267–1284.

Guccione, J.M., Moonly, S.M., Moustakidis, P., Costa, K.D., Moulton, M.J., Ratcliffe, M. B., Pasque, M.K., 2001. Mechanism underlying mechanical dysfunction in the border zone of left ventricular aneurysm: A finite element model study. Ann. Thoracic Surg. 71 (2), 654–662.

Guccione, J.M., Waldman, L.K., McCulloch, A.D., 1993. Mechanics of active contraction in cardiac muscle: Part II—cylindrical models of the systolic left ventricle. J. Biomech. Eng. 115 (1), 82–90.

Jiang, C., Liu, G.-R., Han, X., Zhang, Z.-Q., Zeng, W., 2015a. A smoothed finite element method for analysis of anisotropic large deformation of passive rabbit ventricles in diastole. Int. J. Num. Methods Biomed. Eng. 31 (1), e02697.

Jiang, C., Zhang, Z.-Q., Han, X., Liu, G.-R., 2014. Selective smoothed finite element methods for extremely large deformation of anisotropic incompressible biotissues. Int. J. Numer. Meth. Eng. 99 (8), 587–610.

Jiang, C., Zhang, Z.-Q., Liu, G., Han, X., Zeng, W., 2015b. An edge-based/node-based selective smoothed finite element method using tetrahedrons for cardiovascular tissues. Eng. Anal. Boundary Elem. 59, 62–77.

Kshrisagar, S., Francis, A., J. Yee, J., Natarajan, S., K. Lee, C., 2019. Implementing the node based smoothed finite element method as user element in Abaqus for linear and nonlinear elasticity. Comput. Mater. Continua 61 (2), 481–502.

Liu, G.-R., 2019. The smoothed finite element method (S-FEM): A framework for the design of numerical models for desired solutions. Front. Struct. Civil Eng. 13 (2), 456–477.
Liu, G.R., Dai, K.Y., Nguyen, T.T., 2007. A smoothed finite element method for mechanics problems. Comput. Mech. 39 (6), 859–877.
Liu, G.R., Nguyen-Thoi, T., Lam, K.Y., 2009a. An edge-based smoothed finite element method (ES-FEM) for static, free and forced vibration analyses of solids. J. Sound Vib. 320, 1100–1130.
Liu, G.R., Nguyen-Thoi, T., Nguyen-Xuan, H., Lam, K.Y., 2009b. A node-based smoothed finite element method (NS-FEM) for upper bound solutions to solid mechanics problems. Comput. Struct. 87 (1–2), 14–26.
Lluch, È., Camara, O., Doste, R., Bijnens, B., De Craene, M., Sermesant, M., Wang, V.Y., Nash, M.P., Morales, H.G., 2020. Calibration of a fully coupled electromechanical meshless computational model of the heart with experimental data. Comput. Methods Appl. Mech. Eng. 364, 112869.
Lluch, È., De Craene, M., Bijnens, B., Sermesant, M., Noailly, J., Camara, O., Morales, H. G., 2019. Breaking the state of the heart: Meshless model for cardiac mechanics. Biomech. Model. Mechanobiol. 18 (6), 1549–1561.
Lopez-Perez, A., Sebastian, R., Ferrero, J.M., 2015. Three-dimensional cardiac computational modelling: Methods, features and applications. BioMed. Eng. OnLine 14 (1), 35.
Nguyen-Thoi, T., Liu, G.R., Lam, K.Y., Zhang, G.Y., 2009. A face-based smoothed finite element method (FS-FEM) for 3D linear and geometrically non-linear solid mechanics problems using 4-node tetrahedral elements. Int. J. Numer. Meth. Eng. 78 (3), 324–353.
Niederer, S.A., Lumens, J., Trayanova, N.A., 2019. Computational models in cardiology. Nat. Rev. Cardiol. 16 (2), 100–111.
Rossi, S., Lassila, T., Ruiz-Baier, R., Sequeira, A., Quarteroni, A., 2014. Thermodynamically consistent orthotropic activation model capturing ventricular systolic wall thickening in cardiac electromechanics. Eur. J. Mech. A. Solids 48, 129–142.
Sack, K.L., Dabiri, Y., Franz, T., Solomon, S.D., Burkhoff, D., Guccione, J.M., 2018. Investigating the Role of Interventricular Interdependence in Development of Right Heart Dysfunction During LVAD Support: A Patient-Specific Methods-Based Approach. Front. Physiol. 9.
Sáez, P., Kuhl, E., 2016. Computational modeling of acute myocardial infarction. Comput. Methods Biomech. Biomed. Eng. 19 (10), 1107–1115.
Sahli Costabal, F., Yao, J., Kuhl, E., 2018. Predicting the cardiac toxicity of drugs using a novel multiscale exposure–response simulator. Comput. Methods Biomech. Biomed. Eng. 21 (3), 232–246.
Sermesant, M., Delingette, H., Ayache, N., 2006. An electromechanical model of the heart for image analysis and simulation. IEEE Trans. Med. Imaging 25 (5), 612–625.
Trayanova, N.A., 2011. Whole-heart modeling: Applications to cardiac electrophysiology and electromechanics. Circ. Res. 108 (1), 113–128.
Trayanova, N.A., Jason, C., Gurev, V., 2011. Electromechanical models of the ventricles. Am. J. Physiol. Heart Circul. Physiol. 301 (2), H279–H286.
Trayanova, N.A., Pashakhanloo, F., Wu, K.C., Halperin, H.R., Jul. 2017. Imaging-Based Simulations for Predicting Sudden Death and Guiding VT Ablation. Circul. Arrhythmia Electrophysiol. 10 (7).
Wong, K.C., Wang, L., Zhang, H., Liu, H., Shi, P., 2010. Meshfree implementation of individualized active cardiac dynamics. Comput. Med. Imaging Graph. 34 (1), 91–103.
Yao, J., Liu, G.R., Narmoneva, D.A., Hinton, R.B., Zhang, Z.-Q., 2012. Immersed smoothed finite element method for fluid-structure interaction simulation of aortic valves. Comput. Mech. 50 (6), 789–804.
Zeng, W., Liu, G.R., 2018. Smoothed Finite Element Methods (S-FEM): an overview and recent developments. Arch. Comput. Methods Eng. 25 (2), 397–435.

Journal of Biomechanics 157 (2023) 111691

Contents lists available at ScienceDirect

Journal of Biomechanics

journal homepage: www.elsevier.com/locate/jbiomech

Short communication

Smoothed finite element methods in simulation of active contraction of myocardial tissue samples

Denisa Martonová [a,*], David Holz [a], Minh Tuan Duong [a,b], Sigrid Leyendecker [a]

[a] Friedrich-Alexander-Universität Erlangen-Nürnberg, Institute of Applied Dynamics, Immerwahrstraße 1, 91058 Erlangen, Germany
[b] School of Mechanical Engineering, Hanoi University of Science and Technology, 1 DaiCoViet Road, Hanoi, Vietnam

ARTICLE INFO

Keywords:
Heart
Cardiac mechanics
Smoothed finite element method
Volumetric locking
Abaqus

ABSTRACT

In modelling and simulation of cardiac mechanics, tetrahedral meshes are often used due to the easy availability of efficient meshing algorithms. This is beneficial in particular when complex geometries such as cardiac structures are considered. The gold standard in simulating the cardiac cycle is to solve the mechanical balance equations with the finite element method (FEM). However, using linear shape functions in the FEM in combination with nearly-incompressible material models is known to produce overly stiff approximations, whereas higher order elements are computationally more expensive.

To overcome these problems, smoothed finite element methods (S-FEMs) have been proposed by Liu and co-workers. So far, S-FEMs in 3D have been utilised only in simulations of passive mechanics. In the present work, different S-FEMs are for the first time used for simulation of an active cardiac contraction on three-dimensional myocardial tissue samples. Further, node-based S-FEM (NS-FEM), face-based S-FEM (FS-FEM) and selective FS/NS-FEM are for the first time implemented as user subroutine in the commercial software Abaqus.

Our results confirm that all S-FEMs perform softer than linear FEM and volumetric locking is reduced. The FS/NS-FEM produces solutions with the relative error in maximum displacement and rotation being less than 5% with respect to the reference solution obtained by the quadratic FEM for all considered mesh sizes, although linear shape functions are used. We therefore conclude that in particular FS/NS-FEM is an efficient and accurate numerical method in the simulation of an active cardiac muscle contraction.

1. Introduction

In the last decades, mathematical modelling and simulation have been solidly established in the field of biomechanics. In particular, the application in cardiology is of great interest, since cardiovascular diseases remain the leading cause of death worldwide (WHO, 2020).

To numerically solve the addressed electromechanical problem, most commonly, finite element method (FEM) is used (Lopez-Perez et al., 2015; Niederer et al., 2019; Peirlinck et al., 2021). It initially requires a discretisation of the domain which may be very complex. For such complex geometries, tetrahedral meshes (TET) can be generated automatically, e.g. with Delaunay triangulation (Duong and Staat, 2014). However, TET, in particular in combination with nearly-incompressible materials and linear shape functions, are very stiff and lead to volumetric locking (Jiang et al., 2014; Liu, 2019; Kadapa, 2019). Using higher order elements can overcome this problem, but the computations become significantly more expensive. Instead of TET, more accurate hexahedral elements are often used. However, a high-quality hexahedral mesh is a demanding and time-consuming task for complex geometries such as cardiac structures.

As an alternative numerical technique, a group of smoothed finite element methods (S-FEMs), has been proposed by Liu and co-workers (Liu et al., 2007). These methods combine FEM and specific techniques from meshless methods, in particular strain smoothing over a designed smoothing domain (SD). Depending on the SD type, one can distinguish cell-based S-FEM (CS-FEM) (Liu et al., 2007), node-based S-FEM (NS-FEM) (Liu et al., 2009a), edge-based S-FEM (ES-FEM) for both 2D and 3D problems (Liu et al., 2009b) and face-based S-FEM (FS-FEM) for 3D problems (Nguyen-Thoi et al., 2009; Duong and Staat, 2014). Additionally, a selective FS/NS-FEM and ES/NS-FEM are proposed for nearly incompressible materials, where FS-FEM is used for the isochoric part and NS-FEM for the volumetric part (Nguyen et al., 2007; Jiang et al., 2014). Recently, Wu et al. (2021) introduced a unified-implementation of S-FEM (UI-S-FEM) allowing to use different types of SDs for different materials.

* Corresponding author.
E-mail address: denisa.martonova@fau.de (D. Martonová).

https://doi.org/10.1016/j.jbiomech.2023.111691
Accepted 14 June 2023
Available online 24 June 2023

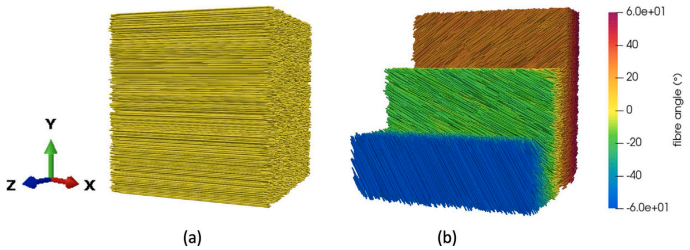

Fig. 1. Schematic representation of the geometries and fibre orientations considered in the numerical examples. (a) Globally aligned fibre orientation on cube, (b) fibre orientation from −60° to +60° on cube, mimicking the fibre rotation from the epicardium to the endocardium of a left ventricle.

Liu (2019) and Zeng and Liu (2018) review the advantages and applications of S-FEMs in detail. The most important benefits are: First, S-FEMs are softer than liner FEM using the same mesh size and therefore resistant to volumetric locking. Second, they are less sensitive to mesh distortion which often occurs in presence of large deformations. Third, they are primarily developed for TET which can be generated automatically. However, recently, S-FEM for arbitrary n-sided polygonal elements (nS-FEM) has been proposed in Wu et al. (2022, 2023a).

In the last years, S-FEMs have been applied in different fields of mechanics. Recently, biomechanics became a promising field of application of S-FEMs for reasons corresponding the S-FEMs' benefits mentioned above: First, biological tissues are often modelled as nearly incompressible materials, suffering from volumetric locking. Second, large deformations often need to be simulated. Third, geometries are usually complex and need to be meshed with TET.

To date, S-FEMs have been used in biomechanical simulations for the growth of soft biological tissue (Duong and Staat, 2014; Duong et al., 2015), aortic valve opening (Yao et al., 2012), biomechanical responses of brain tissue (Wu et al., 2020), dynamic analysis of the human annulus fibrosus (Yan et al., 2022), the artery wall, cervical spine (Wu et al., 2023b) multi-material in orthodontics (Wu et al., 2021). Jiang et al. (2015a,b) have utilised FS/NS-FEM in passive cardiac mechanics. In the recent work related to S-FEMs (Martonová et al., 2021b), the NS-FEM approach has been extended towards active cardiac mechanics. Previously mentioned works have demonstrated that S-FEMs perform accurate, are able to overcome volumetric-locking, insensitive to mesh distortion and computationally efficient. The latter three works (Jiang et al., 2015a,b; Martonová et al., 2021b) conclude that S-FEMs are a promising alternative in cardiac modelling and simulation. However, S-FEMs have only been applied to passive cardiac mechanics (Jiang et al., 2015a) and only NS-FEM for active cardiac mechanics on 2D geometries (Martonová et al., 2021b). So far, S-FEMs have mostly been implemented within in-house solvers. Additionally, CS-FEM in 3D (Cui et al., 2018; Bhowmick and Liu, 2018a,b; Kumbhar et al., 2020; Guan et al., 2021) and NS-FEM in 2D (Kshrisagar et al., 2019; Martonová et al., 2021b) have been implemented as user element subroutines (UELs) within the commercial software Abaqus.

In the present work, a 3D model for active cardiac mechanics using NS-FEM, FS-FEM as well as FS/NS-FEM is developed. The objective is to extend S-FEMs for the first time for an active cardiac mechanics using a 3D geometry. Further, NS-FEM, FS-FEM and FS/NS-FEM are implemented as UELs in Abaqus and performance of these numerical methods is compared.

2. Methods

2.1. Balance equation and constitutive model

In the following, we consider a geometrically and materially nonlinear 3D problem. Let an undeformed domain $\Omega_0 \subseteq \mathbb{R}^3$ bounded by Γ be discretised with TET. The balance of linear momentum in the reference configuration reads as

$$\begin{aligned} \boldsymbol{0} &= \mathrm{Div}[\mathbf{F}\cdot\mathbf{S}] + \boldsymbol{F}^{\varphi} \quad \text{in } \Omega_0, \\ \boldsymbol{\varphi}(\boldsymbol{X},t) &= \bar{\boldsymbol{\varphi}} \text{ in } \Gamma_{\varphi}, \quad \boldsymbol{T}(\boldsymbol{X},t) = \bar{\boldsymbol{T}} \quad \text{in } \Gamma_T, \end{aligned} \tag{1}$$

where $\mathbf{F}$ is the deformation gradient, $\mathbf{S}$ is the second Piola–Kirchhoff stress tensor (PK2), $\boldsymbol{F}^{\varphi}$ is the external mechanical body force, $\boldsymbol{\varphi}$ is the displacement and $\boldsymbol{T}$ the surface traction vector. The prescribed values on the boundaries are marked with bars. Let the total stress be additively decomposed into the passive part $\mathbf{S}_{pas}$ and the active part $\mathbf{S}_{act}$ according to the widely used stress-approach (Göktepe and Kuhl, 2010; Eriksson et al., 2013; Sack et al., 2018; Martonová et al., 2022b), namely

$$\mathbf{S} = \mathbf{S}_{pas} + \mathbf{S}_{act}. \tag{2}$$

The passive PK2 is obtained as

$$\mathbf{S}_{pas}(\mathbf{C}) = 2\frac{\partial \Psi}{\partial \mathbf{C}}, \tag{3}$$

where $\mathbf{C}$ is the right Cauchy stress tensor and Ψ is a strain energy function of a nearly-incompressible material. The latter is decomposed as

$$\Psi = \Psi_{iso} + \Psi_{vol}, \tag{4}$$

$$\Psi = \Psi_{iso}(\mathbf{C}^{\circ}) + \Psi_{vol}(J), \tag{5}$$

where Ψ_{iso} is the isochoric part and $\Psi_{vol} = \kappa(J-1)^2$ the volumetric part with the bulk modulus κ. $\mathbf{C}^{\circ} = \mathbf{F}^{\circ T}\mathbf{F}^{\circ}$ and $\mathbf{F}^{\circ} = J^{-1/3}\mathbf{F}$ denote the isochoric right Cauchy–Green tensor and deformation gradient, respectively, i.e. $\det \mathbf{C}^{\circ} = \det \mathbf{F}^{\circ} = 1$. In the following numerical examples, Holzapfel-Ogden orthotropic strain energy function is considered which is commonly used to model myocardium (Göktepe et al., 2011; Eriksson et al., 2013; Baillargeon et al., 2014; Martonová et al., 2021a), see Appendix A or the original work (Holzapfel and Ogden, 2009) for the constitutive law.

The active part is modelled following the approach used in Pfaller et al. (2019) and Martonová et al. (2022a) as

$$\mathbf{S}_{act} = T(\boldsymbol{f}_0 \otimes \boldsymbol{f}_0), \tag{6}$$

where $\boldsymbol{f}_0$ represents the local orientation in the reference configuration which is schematically shown in Fig. 1. The time-dependent scalar active tension T, plotted in Fig. 2, is obeying the differential equation

$$\dot{T}(t) = -|a(t)|T(t) + T_{max}|a(t)|_+ \tag{7}$$

with the activation function a (for details see Appendix B or the original work Pfaller et al., 2019), the maximum value of the active stress T_{max} and the function $|a(t)|_+ = \max(a(t);0)$. For material parameters used in the simulation, see Table 3.

Table 1
Summary of numerical methods used in simulations.

method\discretisation	C3D10	C3D4	node-based SD	face-based SD
quadratic FEM	$\Psi_{iso}, \Psi_{vol}, \mathbf{S}_{act}$			
linear FEM		$\Psi_{iso}, \Psi_{vol}, \mathbf{S}_{act}$		
NS-FEM			$\Psi_{iso}, \Psi_{vol}, \mathbf{S}_{act}$	
FS-FEM				$\Psi_{iso}, \Psi_{vol}, \mathbf{S}_{act}$
FS/NS-FEM vol			$\Psi_{vol}, \mathbf{S}_{act}$	Ψ_{iso}
FS/NS-FEM iso			Ψ_{vol}	$\Psi_{iso}, \mathbf{S}_{act}$

For each numerical method listed in the first column, the table identifies on which finite element or SD, the passive isochoric Ψ_{iso}, passive volumetric Ψ_{vol} and active $\mathbf{S}_{act}$ parts of the constitutive law are computed.

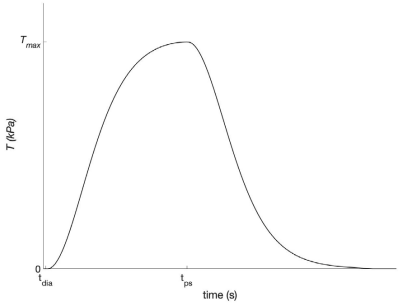

Fig. 2. Temporal evolution of the active tension T according to (7). End-diastolic and peak-systolic times are denoted with t_{dia} and t_{ps}, respectively. T_{max} is the maximum value of the active tension.

2.2. Idea of S-FEM in 3D for non-linear problems

The balance equation (1) is solved numerically using the following numerical methods: linear FEM discretised with four-node tetrahedral elements (C3D4), quadratic FEM discretised with ten-node tetrahedral elements (C3D10), NS-FEM, FS-FEM, NS-FEM for the volumetric part and active part and FS-FEM for the isochoric part (FS/NS-FEM vol), NS-FEM for the volumetric part and FS-FEM for the isochoric and active part (FS/NS-FEM iso). A summary of these numerical methods is given in Table 1. We note that while Jiang et al. (2014) proposed to use NS-FEM for the volumetric and FS-FEM for the isochoric part of a passive material law, an active contraction solved with FS/NS-FEM has not been investigated yet. We therefore compare both above possibilities (FS/NS-FEM iso and FS/NS-FEM vol).

All mentioned S-FEMs are based on the strain smoothing over a designed SD. First, using an automatic meshing algorithm, the computational domain Ω_0 is discretised into non-overlapping tetrahedral elements Ω_e with the reference volume V_e. Second, it is subdivided into a finite number of non-overlapping SDs Ω_k with the boundary Γ_k and the reference volume V_k, i.e. $\Omega_0 = \cup_{k=1}^{n_{sd}} \Omega_k$ and n_{sd} is the number of SDs. We refer to Fig. 3(a) and (b) for the illustration of SDs in 3D for NS-FEM and FS-FEM, respectively. Further, let $\boldsymbol{X} \in \Omega_0$ be a material point, $\boldsymbol{x}$ a spatial point and $\mathbf{I}$ the identity tensor. The deformation gradient $\mathbf{F}$ is smoothed by multiplication with a smoothing function Φ_k, namely

$$\Phi_k(\boldsymbol{X}) = \begin{cases} 1/V_k & \text{if } \boldsymbol{X} \in \Omega_k \\ 0 & \text{else} \end{cases} \quad \text{with } V_k = \int_{\Omega_k} \mathrm{d}\Omega, \tag{8}$$

which satisfies the unity property $\int_{\Omega_k} \Phi_k(\boldsymbol{X})\mathrm{d}\Omega = 1$. For tetrahedral discretisations and linear shape functions N_α for the node α on the tetrahedral element Ω_e, the smoothed deformation gradient $\bar{\mathbf{F}}^k$ is constant on the SD Ω_k and takes the form

$$\begin{aligned} \bar{\mathbf{F}}^k_{ij} &= \int_{\Omega_k} \frac{\partial u_i(\boldsymbol{X})}{\partial X_j} \Phi_k(\boldsymbol{X})\mathrm{d}\Omega_0 + \delta_{ij} = \frac{1}{4}\sum_{e=1}^{n^e_k} \int_{\Omega_e} \frac{\partial u_i(\boldsymbol{X})}{\partial X_j} \Phi_k(\boldsymbol{X})\mathrm{d}\Omega_0 + \delta_{ij} \\ &= \frac{1}{4V_k}\sum_{e=1}^{n^e_k} \frac{\partial u_i(\boldsymbol{X}_e)}{\partial X_j} V_e + \delta_{ij} = \frac{1}{4V_k}\sum_{e=1}^{n^e_k}\sum_{\alpha=1}^{4} \frac{\partial N_\alpha}{\partial X_j}(\boldsymbol{u}_\alpha)_i V_e + \delta_{ij} \end{aligned} \tag{9}$$

where n^e_k is the set of tetrahedrons connected to the node k in NS-FEM or face k in FS-FEM and δ_{ij} is the Kronecker delta. Consequently, the smoothed right Cauchy–Green tensor $\bar{\mathbf{C}}^k = \bar{\mathbf{F}}^{kT}\bar{\mathbf{F}}^k$ and the PK2 $\bar{\mathbf{S}}^k$ are computed on the SD Ω_k. Furthermore, the fibre orientation on the SD $\bar{\boldsymbol{f}}^k_0 = (\bar{x}^k_1, \bar{x}^k_2, \bar{x}^k_3)$ is given as

$$\bar{x}^k_i = \frac{1}{n^e_k}\sum_{e=1}^{n^e_k} x^e_i \quad i \in \{1,2,3\}, \tag{10}$$

where x^e_i is the ith component of the local fibre orientation on the element Ω_e. The stiffness matrix and the residual vector are computed analogously to the non-linear FEM, but integration is performed over the SDs rather than over elements.

2.3. Numerical examples

2.3.1. Cube – active contraction in fibre direction – globally aligned fibres

To exemplarily demonstrate the idea of S-FEMs and their relation to FEM, initially a cube ($a = 10$ mm) with globally aligned fibres in x-direction is considered, see Fig. 1(a). The (yz)-plane is fixed in x-direction, (xz)-plane is fixed in y-direction and (xy)-plane is fixed in z-direction. The active contraction ($T_{max} = 1$ kPa) is induced in the fibre direction.

2.3.2. Cube – active contraction in fibre direction – local fibre direction

To mimic the fibre, sheet and normal orientation in the left ventricle, the fibres rotate transmurally from −60° to +60° on the cube boundaries and sheet angle is set to 0° (Milne et al., 2019; Chen et al., 2005), see Fig. 1(b). Affine translated (xz)-plane of the cube at $y = 10$ mm is fixed in all directions, additionally (xz)-plane is fixed at $y = 0$ mm. We compare the maximum magnitude of the nodal displacement u^{max} and the maximum rotation of (xz)-plane u^{max}_R for linear and quadratic FEMs as well as for different S-FEMs. Further, $T_{max} = 1$ kPa in (7) is set such that the resulting cube rotation corresponds to the experimentally reported values of the ventricular twist, i.e. 0.15 to 0.35 rad (Nishikage et al., 2010; Thompson et al., 2010; Omar et al., 2015).

3. Results and discussion

In the first numerical example (cube with globally aligned fibres, volumetric locking-free contraction), all numerical methods produce the same maximum displacement in the fibre direction, i.e. $u^{max} = 1.65$ mm. Due to the parallel fibre contraction in x-direction, the cube changes its shape uniformly and therefore, the locking phenomenon is not present. The stress and strain in all elements are equal and consequently, the stress and strain smoothing (i.e. averaging) does not cause any difference between S-FEMs and FEM. Similar results have

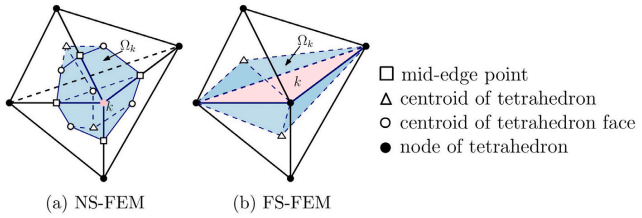

Fig. 3. Smoothing domains in 3D for NS-FEM (a) and FS-FEM (b). In blue, the SDs Ω_k around the node k respectively the face k are highlighted. (For interpretation of the references to colour in this figure legend, the reader is referred to the web version of this article.)

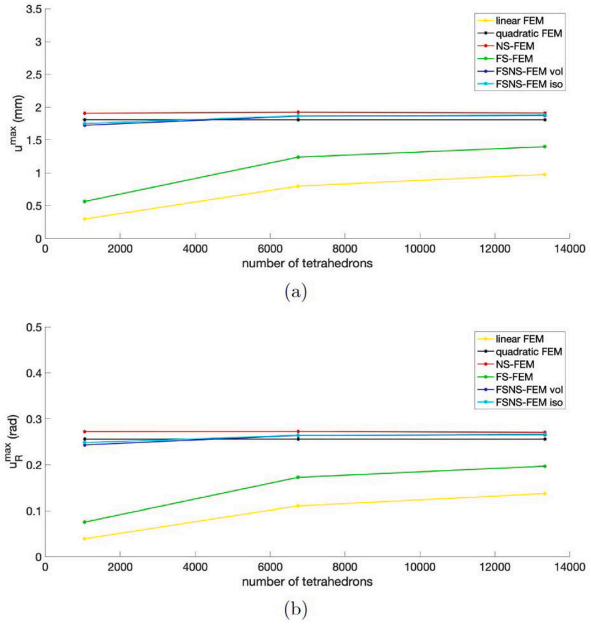

Fig. 4. (a) Maximum magnitude of the nodal displacement u^{max}, (b) maximum rotation of the (xz)-plane u_R^{max}, both for linear and quadratic FEMs using C3D4 and C3D10 elements from Abaqus, respectively, and for different S-FEMs.

been observed in a tensile test in x-direction performed on a cube (Wu et al., 2020).

In Table 2, Figs. 4 and 5, the simulation results for the second numerical example (cube with transmurally rotating fibre direction, contraction with volumetric locking), are shown for different mesh sizes. The results produced by quadratic FEM on the fine mesh (39 417 C3D10) serve as the reference solution. For linear FEM, the accuracy rapidly decreases with decreasing degrees of freedom, i.e. the relative error in the maximum rotation u_R^{max} increases from 46% to 85% from the finest (13338 C3D4) to the coarsest discretisation (1050 C3D4). This confirms the known phenomenon of high stiffness in linear FEM in combination with nearly-incompressible materials due to volumetric locking (Liu, 2019; Wu et al., 2020). Using all S-FEMs, volumetric locking is reduced. For FS-FEM, it is still present, i.e. the relative errors for the finest considered mesh are nearly 23%. Conversely, NS-FEM underestimates the stiffness for all mesh sizes which is in agreement with previous studies (Liu et al., 2009a; Zeng and Liu, 2018; Liu, 2019; Martonová et al., 2022b), see Table 2 for the relative errors ranging from 5.6% to 6.6%. The selective methods, FS/NS-FEM iso and FS/NS-FEM vol, produce solutions which are close to the reference solution, even for a relatively coarse mesh of 1050 C3D4, i.e. the magnitude of the relative error is less than 5%. We note that, if the active part $\mathbf{S}_{act}$ is included in the face-based SD (FS/NS-FEM iso), the material is softer than when it is included in the node-based SD (FS/NS-FEM vol). On the one hand, as linear shape functions are used in the S-FEM analysis, all S-FEMs are computationally more efficient compared to quadratic FEM on the same tetrahedral mesh. On the other hand, as the global stiffness matrix is less sparse than in FEM due to strain smoothing over adjacent elements, the computational time is higher than in linear FEM.

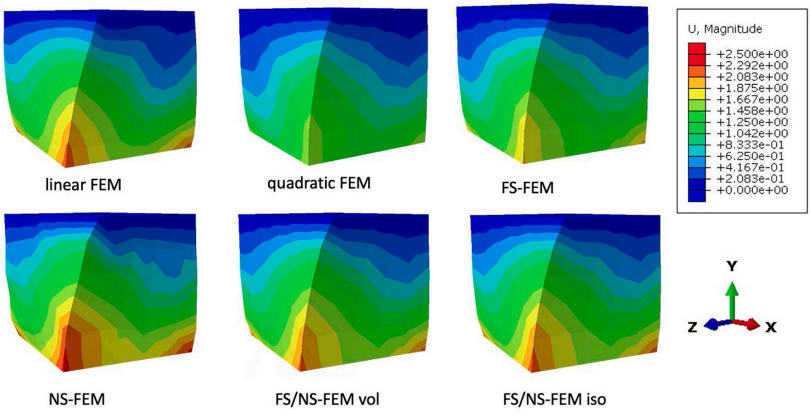

Fig. 5. Snapshots at $t = 61$ ms for an active contraction in fibre direction rotating from $+60°$ on (xy)-plane, representing the endocardium, to $-60°$ on the affine translated (xy)-plane, representing the epicardium. The cube is discretised with 6749 tetrahedral elements.

Table 2
Simulation results for an active contraction of a cube with Holzapfel-Ogden material.

no. of TET	13 338			6749			1050		
method	u_R^{max}	u^{max}	err	u_R^{max}	u^{max}	err	u_R^{max}	u^{max}	err
quadratic FEM	2.557	1.807	0.0/0.0	2.558	1.807	0.1/0.0	2.557	1.808	0.0/0.1
linear FEM	1.371	0.975	−46.3/−46.0	1.104	0.795	−56.8/−56.0	0.390	0.295	−84.7/−83.7
NS-FEM	2.705	1.911	5.9/5.8	2.724	1.923	6.6/6.5	2.720	1.907	6.5/5.6
FS-FEM	1.970	1.397	−22.9/−22.7	1.725	1.238	−32.5/−31.5	0.752	0.562	−70.6/−68.8
FS/NS-FEM vol	2.652	1.873	3.8/3.7	2.638	1.864	3.3/3.2	2.432	1.724	−4.8/−4.5
FS/NS-FEM iso	2.663	1.881	4.2/4.2	2.641	1.867	3.4/3.4	2.480	1.752	−2.9/−3.0

u_R^{max} = maximum rotation in 10^{-1} rad, u^{max} = maximum displacement in mm, err = relative error in u_R^{max}/u^{max} in % with respect to the reference solution computed with 39 417 C3D10 in Abaqus, $u_R^{ref} = 2.555 \cdot 10^{-1}$ rad, $u^{ref} = 1.806$ mm, $err = (\square^{max} - \square^{ref})/\square^{ref}$, $\square \in \{u_R^{max}, u^{max}\}$.

Table 3
Material parameters used in numerical examples.

passive part (HO)	$a = 1.665$ kPa, $b = 1.237$ (–), $a_f = 7.822$ kPa, $b_f = 0.008$ (–), $a_s = 0.0$ kPa, $b_s = 0.0$ (–), $a_{fs} = 1.342$ kPa, $b_{fs} = 9.178$ (–), $\kappa = 1000$ kPa
active part	$t_{ed} = 1$ ms, $t_{ps} = 61$ ms, $\alpha_{min} = -0.1$ m s^{-1}, $\alpha_{max} = 0.1$ m s^{-1}, $\gamma = 25$ ms

4. Conclusion

In this work, we extended for the first time several S-FEMs for the active cardiac mechanics using a 3D geometry, mimicking myocardial tissue including fibre orientation. NS-FEM, FS-FEM and the selective FS/NS-FEM are implemented within the commercial software Abaqus as UELs based on an automatically generated tetrahedral mesh. Using S-FEMs, the volumetric locking problem being present in linear FEM is reduced (FS-FEM) or even overcome (NS-FEM, FS/NS-FEM iso and FS/NS-FEM vol). If a coarse discretisation is used, FS/NS-FEM iso produces the most accurate solutions and it is therefore proposed as a suitable numerical method when active cardiac contraction is simulated at low computational cost.

CRediT authorship contribution statement

Denisa Martonová: Writing – original draft, Visualization, Software, Methodology, Formal analysis, Conceptualization. **David Holz:** Writing – review & editing, Visualization. **Minh Tuan Duong:** Writing – review & editing. **Sigrid Leyendecker:** Writing – review & editing, Supervision, Project administration, Methodology, Funding acquisition, Conceptualization.

Declaration of competing interest

The authors declare that they have no known competing financial interests or personal relationships that could have appeared to influence the work reported in this paper.

Acknowledgements

This work is funded by the Deutsche Forschungsgemeinschaft (DFG, German Research Foundation) project no. 496647562. The authors gratefully acknowledge the cooperation on this project with the Cardiac Surgery at the Friedrich-Alexander-Universität Erlangen-Nürnberg, in particular Dr. Muhannad Alkassar and the Institute of Medical Biotechnology at the Friedrich-Alexander-Universität Erlangen-Nürnberg, in particular Prof. Dr. Oliver Friedrich.

Appendix A. Passive constitutive law

In the numerical examples, the orthotropic Holzapfel-Ogden-strain energy (HO) is utilised, namely

$$\Psi_{iso}^{HO} = \frac{a}{2b}\exp\left[b(I_1^\circ - 3)\right] + \frac{a_f}{2b_f}\left(\exp\left[b_f(\max(I_{4f}^\circ, 1) - 1)^2\right] - 1\right) + \frac{a_s}{2b_s}\left(\exp\left[b_s(\max(I_{4s}^\circ, 1) - 1)^2\right] - 1\right) + \frac{a_{fs}}{2b_{fs}}\left(\exp\left[b_{fs}(I_{8fs}^\circ)^2 - 1\right]\right). \tag{11}$$

with the isochoric invariants of $\mathbf{C}$: $I_1^\circ, I_{4f}^\circ, I_{4s}^\circ, I_{8fs}^\circ$. The parameters $a, b, a_f, b_f, a_s, b_s, a_{fs}, b_{fs}$ are set according to Martonová et al. (2021a) for healthy rats, see Table 3.

Appendix B. Activation function

The activation function $a(t)$ in (7) is modelled as

$$a(t) = \alpha_{max} \cdot f(t) + \alpha_{min} \cdot (1 - f(t)) \tag{12}$$

with maximum and minimum activation rates α_{max} and α_{min}, respectively, and functions

$$f(t) = S^+(t - t_{ed}) \cdot S^-(t - t_{ps}), \tag{13}$$

$$S^\pm(\Delta t) = \frac{1}{2}(1 \pm \tanh(\frac{\Delta t}{\gamma})) \tag{14}$$

with steepness γ and descending and ascending sigmoid functions S^+ and S^-, respectively. The indicator function $f \in (0, 1)$ indicates systole. The times t_{ed} and t_{ps} model the end-diastolic and the peak-systolic times, respectively. The simulation parameters are given in Table 3 and the resulting temporal evolution of the active tension in Fig. 2.

References

Baillargeon, B., Rebelo, N., Fox, D.D., Taylor, R.L., Kuhl, E., 2014. The living heart project: A robust and integrative simulator for human heart function. Eur. J. Mech. A Solids 48, 38–47. http://dx.doi.org/10.1016/j.euromechsol.2014.04.001.

Bhowmick, S., Liu, G.R., 2018a. A phase-field modeling for brittle fracture and crack propagation based on the cell-based smoothed finite element method. Eng. Fract. Mech. 204, 369–387. http://dx.doi.org/10.1016/j.engfracmech.2018.10.026.

Bhowmick, S., Liu, G.R., 2018b. Three dimensional CS-FEM phase-field modeling technique for brittle fracture in elastic solids. Appl. Sci. 8 (2488), http://dx.doi.org/10.3390/app8122488.

Chen, J., Liu, W., Zhang, H., Lacy, L., Yang, X., Song, S.K., Wickline, S.A., Yu, X., 2005. Regional ventricular wall thickening reflects changes in cardiac fiber and sheet structure during contraction: Quantification with diffusion tensor MRI. Am. J. Physiol. Heart Circ. Physiol. 289, H1898–H1907. http://dx.doi.org/10.1152/ajpheart.00041.2005.

Cui, X., Han, X., Shuyong, D., Liu, G., 2018. An ABAQUS implementation of the cell-based smoothed finite element method (CS-FEM). Int. J. Comput. Methods (17), http://dx.doi.org/10.1142/S021987621850127X.

Duong, M.T., Staat, M., 2014. A face-based smoothed finite element method for hyperelastic models and tissue growth. In: 11th World Congress on Computational Mechanics.

Duong, M.T., Staat, M., Nguyen-Nhu, H., 2015. Modeling and simulation of a growing mass by the smoothed finite element method (SFEM). In: 3rd ECCOMAS Young Investigators Conference.

Eriksson, T.S.E., Prassl, A.J., Plank, G., Holzapfel, G.A., 2013. Modeling the dispersion in electromechanically coupled myocardium. Int. J. Numer. Methods Biomed. Eng. 29, 1267–1284. http://dx.doi.org/10.1002/cnm.2575.

Göktepe, S., Acharya, S.N.S., Wong, J., Kuhl, E., 2011. Computational modeling of passive myocardium. Int. J. Numer. Methods Biomed. Eng. 27, 1–12. http://dx.doi.org/10.1002/cnm.1402.

Göktepe, S., Kuhl, E., 2010. Electromechanics of the heart: A unified approach to the strongly coupled excitation–contraction problem. Comput. Mech. 45, 227–243. http://dx.doi.org/10.1007/s00466-009-0434-z.

Guan, W., Bhowmick, S., Gao, G., Liu, G.R., 2021. A phase-field modelling for 3D fracture in elasto-plastic solids based on the cell-based smoothed finite element method. Eng. Fract. Mech. 254, 107920. http://dx.doi.org/10.1016/j.engfracmech.2021.107920.

Holzapfel, G.A., Ogden, R.W., 2009. Constitutive modelling of passive myocardium: A structurally based framework for material characterization. Phil. Trans. R. Soc. A 367, 3445–3475. http://dx.doi.org/10.1098/rsta.2009.0091.

Jiang, C., Liu, G.R., Han, X., Zhang, Z.Q., Zeng, W., 2015a. A smoothed finite element method for analysis of anisotropic large deformation of passive rabbit ventricles in diastole. Int. J. Numer. Methods Biomed. Eng. 31, e02697. http://dx.doi.org/10.1002/cnm.2697.

Jiang, C., Zhang, Z.Q., Han, X., Liu, G.R., 2014. Selective smoothed finite element methods for extremely large deformation of anisotropic incompressible bio-tissues. Internat. J. Numer. Methods Engrg. 99, 587–610. http://dx.doi.org/10.1002/nme.4694.

Jiang, C., Zhang, Z.Q., Liu, G., Han, X., Zeng, W., 2015b. An edge-based/node-based selective smoothed finite element method using tetrahedrons for cardiovascular tissues. Eng. Anal. Bound. Elem. 59, 62–77. http://dx.doi.org/10.1016/j.enganabound.2015.04.019.

Kadapa, C., 2019. Novel quadratic Bézier triangular and tetrahedral elements using existing mesh generators: Applications to linear nearly incompressible elastostatics and implicit and explicit elastodynamics. Internat. J. Numer. Methods Engrg. 117, 543–573. http://dx.doi.org/10.1002/nme.5967.

Kshrisagar, S., Francis, A., Yee, J.J., Natarajan, S., Lee, C.K., 2019. Implementing the node based smoothed finite element method as user element in abaqus for linear and nonlinear elasticity. Comput. Mater. Continua 61, 481–502. http://dx.doi.org/10.32604/cmc.2019.07967.

Kumbhar, P.Y., Francis, A., Swaminathan, N., Annabattula, R.K., Natarajan, S., 2020. Development of user element routine (UEL) for cell-based smoothed finite element method (CSFEM) in abaqus. Int. J. Comput. Methods 17, 1850128. http://dx.doi.org/10.1142/S0219876218501281.

Liu, G.R., 2019. The smoothed finite element method (S-FEM): A framework for the design of numerical models for desired solutions. Front. Struct. Civ. Eng. 13, 456–477. http://dx.doi.org/10.1007/s11709-019-0519-5.

Liu, G.R., Dai, K.Y., Nguyen, T.T., 2007. A smoothed finite element method for mechanics problems. Comput. Mech. 39, 859–877. http://dx.doi.org/10.1007/s00466-006-0075-4.

Liu, G.R., Nguyen-Thoi, T., Lam, K.Y., 2009b. An edge-based smoothed finite element method (ES-FEM) for static, free and forced vibration analyses of solids. J. Sound Vib. 320, 1100–1130. http://dx.doi.org/10.1016/j.jsv.2008.08.027.

Liu, G., Nguyen-Thoi, T., Nguyen-Xuan, H., Lam, K., 2009a. A node-based smoothed finite element method (NS-FEM) for upper bound solutions to solid mechanics problems. Comput. Struct. 87, 14–26. http://dx.doi.org/10.1016/j.compstruc.2008.09.003.

Lopez-Perez, A., Sebastian, R., Ferrero, J.M., 2015. Three-dimensional cardiac computational modelling: Methods, features and applications. BioMed. Eng. OnLine 14, 35. http://dx.doi.org/10.1186/s12938-015-0033-5.

Martonová, D., Alkassar, M., Seufert, J., Holz, D., Duong, M.T., Reischl, B., Friedrich, O., Leyendecker, S., 2021a. Passive mechanical properties in healthy and infarcted rat left ventricle characterised via a mixture model. J. Mech. Behav. Biomed. Mater. 119, 104430. http://dx.doi.org/10.1016/j.jmbbm.2021.104430.

Martonová, D., Holz, D., Brackenhammer, D., Weyand, M., Leyendecker, S., Alkassar, M., 2022a. Support pressure acting on the epicardial surface of a rat left ventricle–a computational study. Front. Cardiovasc. Med. 9, 850274. http://dx.doi.org/10.3389/fcvm.2022.850274.

Martonová, D., Holz, D., Duong, M.T., Leyendecker, S., 2021b. Towards the simulation of active cardiac mechanics using a smoothed finite element method. J. Biomech. 115, 110153. http://dx.doi.org/10.1016/j.jbiomech.2020.110153.

Martonová, D., Holz, D., Seufert, J., Duong, M.T., Alkassar, M., Leyendecker, S., 2022b. Comparison of stress and stress–strain approaches for the active contraction in a rat cardiac cycle model. J. Biomech. 134, 110980. http://dx.doi.org/10.1016/j.jbiomech.2022.110980.

Milne, M.L., Schick, B.M., Alkhazal, T., Chung, C.S., 2019. Myocardial fiber mapping of rat hearts using apparent backscatter, with histological validation. Ultrasound Med. Biol. 45, 2075–2085. http://dx.doi.org/10.1016/j.ultrasmedbio.2019.05.002.

Nguyen, T.T., Liu, G.R., Dai, K.Y., Lam, K.Y., 2007. Selective smoothed finite element method. Tsinghua Sci. Technol. 12, 497–508. http://dx.doi.org/10.1016/S1007-0214(07)70125-6.

Nguyen-Thoi, T., Liu, G.R., Lam, K.Y., Zhang, G.Y., 2009. A face-based smoothed finite element method (FS-FEM) for 3D linear and geometrically non-linear solid mechanics problems using 4-node tetrahedral elements. Internat. J. Numer. Methods Engrg. 78, 324–353. http://dx.doi.org/10.1002/nme.2491.

Niederer, S.A., Lumens, J., Trayanova, N.A., 2019. Computational models in cardiology. Nature reviews. Cardiology 16, 100–111. http://dx.doi.org/10.1038/s41569-018-0104-y.

Nishikage, T., Takeuchi, M., Nakai, H., Otsuji, Y., Lang, R., 2010. Possible link between strain ST-T change on the electrocardiogram and subendocardial dysfunction assessed by two-dimensional speckle-tracking echocardiography. Eur. J. Echocardiogr.: J. Work. Group Echocardiogr. Eur. Soc. Cardiol. 11, 451–459. http://dx.doi.org/10.1093/ejechocard/jeq001.

Omar, A.M.S., Vallabhajosyula, S., Sengupta, P.P., 2015. Left ventricular twist and torsion. Circ.: Cardiovasc. Imaging 8, e003029. http://dx.doi.org/10.1161/CIRCIMAGING.115.003029.

Peirlinck, M., Costabal, F.S., Yao, J., Guccione, J.M., Tripathy, S., Wang, Y., Ozturk, D., Segars, P., Morrison, T.M., Levine, S., Kuhl, E., 2021. Precision medicine in human heart modeling: Perspectives, challenges, and opportunities. Biomech. Model. Mechanobiol. 20, 803–831. http://dx.doi.org/10.1007/s10237-021-01421-z.

Pfaller, M.R., Hörmann, J.M., Weigl, M., Nagler, A., Chabiniok, R., Bertoglio, C., Wall, W.A., 2019. The importance of the pericardium for cardiac biomechanics: From physiology to computational modeling. Biomech. Model. Mechanobiol. 18, 503–529. http://dx.doi.org/10.1007/s10237-018-1098-4.

Sack, K.L., Dabiri, Y., Franz, T., Solomon, S.D., Burkhoff, D., Guccione, J.M., 2018. Investigating the role of interventricular interdependence in development of right heart dysfunction during LVAD support: A patient-specific methods-based approach. Front. Physiol. (9), http://dx.doi.org/10.3389/fphys.2018.00520.

Thompson, R., Paterson, I., Chow, K., Cheng-Baron, J., Scott, J., Esch, B., Ennis, D., Haykowsky, M., 2010. Characterization of the relationship between systolic shear strain and early diastolic shear strain rates: Insights into torsional recoil. Am. J. Physiol. Heart Circ. Physiol. 299, H898–907. http://dx.doi.org/10.1152/ajpheart.00353.2010.

WHO, 2020. Global health estimates 2019: Disease burden by cause, age, sex, by country and by region, 2000–2019. https://www.who.int/data/gho/data/themes/mortality-and-global-health-estimates.

Wu, S.W., Jiang, C., Jiang, C., Liu, G.R., 2020. A selective smoothed finite element method with visco-hyperelastic constitutive model for analysis of biomechanical responses of brain tissues. Internat. J. Numer. Methods Engrg. 121, 5123–5149. http://dx.doi.org/10.1002/nme.6515.

Wu, S.W., Jiang, C., Jiang, C., Niu, R.P., Wan, D.T., Liu, G.R., 2021. A unified-implementation of smoothed finite element method (UI-SFEM) for simulating biomechanical responses of multi-materials orthodontics. Comput. Mech. 67, 541–565. http://dx.doi.org/10.1007/s00466-020-01947-6.

Wu, S.W., Jiang, C., Liu, G., Wan, D.T., Jiang, C., 2022. An n-sided polygonal selective smoothed finite element method for nearly incompressible visco-hyperelastic soft materials. Appl. Math. Model. 107, 398–428. http://dx.doi.org/10.1016/j.apm.2022.02.026.

Wu, S.W., Liu, G., Jiang, C., Liu, X., Liu, K., Wan, D.T., Yue, J.H., 2023a. Arbitrary polygon mesh for elastic and elastoplastic analysis of solids using smoothed finite element method. Comput. Methods Appl. Mech. Engrg. 405, 115874. http://dx.doi.org/10.1016/j.cma.2022.115874.

Wu, S.W., Wan, D.T., Jiang, C., Liu, X., Liu, K., Liu, G.R., 2023b. A finite strain model for multi-material, multi-component biomechanical analysis with total Lagrangian smoothed finite element method. Int. J. Mech. Sci. 243, 108017. http://dx.doi.org/10.1016/j.ijmecsci.2022.108017.

Yan, X., Wan, D., Hu, D., Han, X., Liu, G.R., 2022. A selective smoothed finite element method for 3D explicit dynamic analysis of the human annulus fibrosus with modified composite-based constitutive model. Eng. Anal. Bound. Elem. 134, 49–65. http://dx.doi.org/10.1016/j.enganabound.2021.09.021.

Yao, J., Liu, G.R., Narmoneva, D.A., Hinton, R.B., Zhang, Z.Q., 2012. Immersed smoothed finite element method for fluid–structure interaction simulation of aortic valves. Comput. Mech. 50, 789–804.

Zeng, W., Liu, G.R., 2018. Smoothed finite element methods (S-FEM): An overview and recent developments. Arch. Comput. Methods Eng. 25, 397–435. http://dx.doi.org/10.1007/s11831-016-9202-3.

PLOS ONE

RESEARCH ARTICLE

Effects of PTH glandular and external dosing patterns on bone cell activity using a two-state receptor model—Implications for bone disease progression and treatment

Denisa Martonová[1,2]*, Maxence Lavaill[1], Mark R. Forwood[3], Alexander Robling[4], David M. L. Cooper[5], Sigrid Leyendecker[1,2], Peter Pivonka[1]*

1 Mechanical, Medical and Process Engineering, Queensland University of Technology, Brisbane, Queensland, Australia, **2** Institute of Applied Dynamics, Friedrich-Alexander-Universität Erlangen-Nürnberg, Erlangen, Germany, **3** School of Pharmacy and Medical Sciences, Griffith University, Gold Coast, Queensland, Australia, **4** Anatomy, Cell Biology & Physiology, School of Medicine, Indiana University, Indianapolis, Indiana, United States of America, **5** Department of Anatomy, Physiology and Pharmacology, University of Saskatchewan, Saskatoon, Canada

* denisa.martonova@fau.de (DM); peter.pivonka@qut.edu.au (PP)

Citation: Martonová D, Lavaill M, Forwood MR, Robling A, Cooper DML, Leyendecker S, et al. (2023) Effects of PTH glandular and external dosing patterns on bone cell activity using a two-state receptor model—Implications for bone disease progression and treatment. PLoS ONE 18(3): e0283544. https://doi.org/10.1371/journal.pone.0283544

Editor: Mohammadreza Hadizadeh, Central State University, UNITED STATES

Received: October 7, 2022

Accepted: March 10, 2023

Published: March 30, 2023

Data Availability Statement: All relevant data are within the paper and its Supporting information files.

Funding: The work of DM and SL was supported by a fellowship within the IFI programme of the German Academic Exchange Service (DAAD), the Bavarian funding programme BayIntAn and Deutsche Forschungsgemeinschaft (DFG, German Research Foundation) no. 496647562, which are

Abstract

Temporal aspects of ligand specificity have been shown to play a significant role in the case of pulsatile hormone secretion, as exemplified by parathyroid hormone (PTH) binding to its receptor (PTH1R), a G-protein-coupled receptor expressed on surfaces of osteoblasts and osteocytes. The latter binding reaction regulates intracellular signalling and subsequently modulates skeletal homeostasis via bone remodelling. PTH glandular secretion patterns dictate bone cellular activity. In healthy humans, 70% of PTH is secreted in a tonic fashion, whereas 30% is secreted in low-amplitude and high-frequency bursts occurring every 10–20 min, superimposed on the tonic secretion. Changes in the PTH secretion patterns have been associated with various bone diseases. In this paper, we analyse PTH glandular secretion patterns for healthy and pathological states and their link to bone cellular responsiveness (α_R). We utilise a two-state receptor ligand binding model of PTH to PTH1R together with a cellular activity function which is able to distinguish various aspects of the stimulation signal including peak dose, time of ligand exposure, and exposure period. Formulating and solving several constrained optimisation problems, we investigate the potential of pharmacological manipulation of the diseased glandular secretion and via clinical approved external PTH injections to restore healthy bone cellular responsiveness. Based on the mean experimentally reported data, our simulation results indicate cellular responsiveness in healthy subjects is sensitive to the tonic baseline stimulus and it is 28% of the computed maximum responsiveness. Simulation results for pathological cases of glucocorticoid-induced osteoporosis, hyperparathyroidism, initial and steady state hypocalcemia clamp tests indicate α_R values significantly larger than the healthy baseline (1.7, 2.2, 4.9 and 1.9-times, respectively). Manipulation of the pulsatile glandular secretion pattern, while keeping the mean PTH concentration constant, allowed restoration of healthy baseline values from these catabolic bone diseases. Conversely, PTH glandular diseases that led to

gratefully acknowledged. PP and ML would like to gratefully acknowledge funding received through the Australian Research Council (ARC) Industrial Transformation Training Centre for Joint Biomechanics (IC190100020). This work was supported, in part, by a New Frontiers in Research Fund Exploration stream grant (NFRFE-2020-00866) awarded to DMLC and PP.

Competing interests: The authors have declared that no competing interests exist.

maximum bone cellular responsiveness below the healthy baseline value can't be restored to baseline via glandular manipulation. However, external PTH injections allowed restoration of these latter cases.

1 Introduction

Calcium is the most abundant mineral in all vertebrates [1]. Most of the body's calcium (99%) is stored in the bones and teeth, with only 1% stored in blood and other tissues. Calcium serves as a critical regulator of multiple physiological processes, including blood coagulation, nerve conduction, membrane permeability, muscle contraction, enzyme activity and hormone release [2]. Therefore, maintenance of extracellular fluid (ECF) free calcium concentrations in the normal physiological range is tightly regulated in all organisms [3].

As outlined in the recent review by Hernandez-Castellano et al. [1], the classic calciotropic hormones—parathyroid hormone (PTH), calcitriol and calcitonin—regulate calcium homeostasis under normal physiological conditions in mammals by coordinating the availability of ECF free calcium in the blood at the level of the bones, intestine and kidneys. In humans ECF free calcium is regulated by dynamic secretion of PTH by the parathyroid gland and to a lesser contribution from calcitriol and calcitonin [4].

In the following, we focus on PTH secretion patterns of the human parathyroid gland which targets the parathyroid hormone/parathyroid hormone-related protein receptor (PTH/PTHrP type 1 receptor), also commonly known as PTH1R. As highlighted in the review of Cheloha et al. [5], PTH1R is a G-protein-coupled receptor (GPCR) that regulates skeletal development, bone turnover and mineral homeostasis. PTH1R transduces stimuli from PTH and PTH-related-peptide (PTHrP) into the interior of target cells (i.e. cells of the osteoblastic lineage) to promote several divergent signalling cascades. This receptor is able to exist in at least 2 distinct conformation states (R0 and RG) that differ in their signalling response [6]. Ligands that bind selectively to the RG state result in a shorter signalling response, whereas ligands that bind selectively to the R0 state result in prolonged signalling response [7]. The downstream cyclic adenosine monophosphate (cAMP) signalling response is considered to be the primary signalling cascade that mediates the effect of the PTH receptor. PTH1R can modulate a ligand's biological activity depending of the preferential binding to either state [7]. Since most PTH analogues have some affinity for both states of the PTH/PTHrP receptor, the behaviour of a given PTH vis à vis duration of effect is determined by the ratio of binding affinities to each of these receptor states.

As reviewed by Chiavistelli et al. [8], PTH secretion is characterised by an ultradian rhythm with tonic and pulsatile components. In healthy subjects, the majority of PTH is secreted in a tonic fashion (70%), whereas approximately 30% is secreted in low-amplitude and high-frequency bursts occurring every 10–20 min, superimposed on the tonic secretion. Changes in the ultradian PTH secretion pattern have been associated with various diseases including primary and secondary osteoporosis, and hyperparathyroidism. Depending on the dual modifications of pulsatile and tonic components the latter diseases may have different severity of skeletal complications. Furthermore, the pulsatile component can be selectively activated as part of the PTH glandular immediate response to changes in ECF free calcium concentrations [9]. Acute hypocalcemia induces a selective, several-fold increase in bursts frequency and amplitude, whereas hypercalcemia suppresses the PTH pulsatile secretion component, as does prolonged calcitriol therapy.

In the mid 80's, the development of mathematical tools such as heuristic pulse detection methods including Pulsar [10], Cluster [11] and the algorithm of Santen and Bardin [12], allowing decomposition of hormonal release patterns into tonic and pulsatile components, has paved the way for identifying the biological importance of dynamic hormonal secretion. Current theory suggests that biological information in hormonal systems is encoded as a dynamic hormone concentration in the circulating blood. Variations of the concentration are determined by glandular secretion rate and hormonal metabolism. It is now well established that most hormones exhibit a dynamic pattern of episodic secretory and metabolic events. Furthermore, cell biology experiments suggest that pulsatile secretory patterns govern most appropriately the dynamic modulation of the hormone-receptor-interaction, namely receptor de- and resensitisation.

Endocrine diseases are typically defined by comparing serum levels of endocrine factors with the 'normal (or reference) range'. This reference range is used to discern hyper- and hypofunction of respective glands. Dynamic diseases evolve within the normal range and are characterised by increased or decreased secretory dynamics [8]. These high or low dynamic functional states govern cellular responses at the target organs and a disturbed function of a gland can lead to development of progressive diseases. Development of skeletal diseases such as osteoporosis might be linked to the PTH1R signalling pathway and, consequently, it is crucial to understand the dynamics of PTH-PTH1R binding and subsequent signal transduction. Furthermore, osteoporosis therapies such as intermittent PTH(1–34) can also be targeted to PTH1R signalling inducing an osteoanabolic effect [13].

In this paper we utilise a two-state receptor model of PTH-PTH1R originally proposed in [14]. This model is an extension of the work of Potter et al. [15] with respect of introducing a (osteoblastic) *cellular responsiveness* function which is able to distinguish different dynamic PTH dosing patterns. The *cellular responsiveness* has been originally proposed by Li and Goldbeter for pulsatile (square-wave) stimuli [16] applied to gonadotropin-releasing hormone. Using the experimental data of Harms et al. [17, 18] of PTH glandular secretion patterns, we first investigate the reference range of cellular activity representing normal bone homeostasis. We then introduce perturbations of both the tonic and pulsatile components of PTH secretion to mimic various disease states including osteoporosis and hyperparathyroidism. To assess the possibility to achieve a certain *cellular responsiveness* for a given dynamic PTH dosing pattern, we solve a constrained optimisation problem, where the area under the curve (AUC) representing the evolution of the PTH concentration in time (i.e. the mean PTH concentration) is kept constant. These simulations are motivated by the fact that drugs that target calcium-sensing receptors on parathyroid cells can directly affect PTH glandular secretion patterns [19, 20].

In a subsequent analysis, we investigate the effects of an external PTH dose in the form of a subcutaneous (sc) injection on the *cellular responsiveness* for a given disease state. The latter simulations are motivated by the fact that intermittent PTH sc daily injections are used for osteoporosis treatment. The additional PTH dose contributes to an additional *cellular responsiveness* and so has the ability to modify bone cellular activity. We first use the currently clinically approved dose of 20μg daily PTH injections and subsequently, we optimise the dosing pattern to obtain firstly, the maximal *cellular responsiveness* and secondly, the *cellular responsiveness* of a healthy person.

In contrast to previous works [14, 16] presenting an analytical solution for a special case of the optimisation of the *cellular responsiveness*, we make use of numerical approximation methods. The numerical approach is much more flexible in the sense that there are no special case restrictions on the parameters in the model and one can easily consider different scenarios by formulation constrained optimisation problems with various objective functions and constraints.

In Section 2, we introduce the two-state receptor ligand binding model for PTH. This section includes an introduction of various theoretical measures of bone cellular activity (Subsection 2.1) and a representation of PTH plasma concentration (Subsection 2.2). In Section 3, the considered optimisation problems are introduced. In Sections 4 and 5, the results are presented and discussed.

2 Two-state receptor ligand binding model for PTH

Receptor kinetics models have been developed for many different receptor systems, ranging from general models for entire classes of receptors to specific models for a particular receptor expressed in a specific type of cell (see [21, 22] for reviews of existing models). GPCRs such as the PTH1R, are known to exist in various conformations that have different affinities for processes such as binding, activation, and phosphorylation [23, 24]. It has been shown that PTH1R undergoes multiple conformational changes as it binds to ligands and becomes activated [25, 26]. Most commonly, these multiple conformational states can be conceptually grouped into two functional states: active and inactive. A widely accepted model for the activation of GPCRs is the two-state receptor ligand binding model first proposed by Segel et al. in the study of exact sensory adaptation [14]. This model was subsequently employed by Li and Goldbeter to study frequency specificity in intercellular communication [16] and further discussed in [27].

Based on the ability of PTH1R to change conformation independent of a ligand, it is assumed that the two receptor conformational states can transform into each other regardless of its binding to its ligand. This can be achieved either through covalent modification of PTH1R or through simple conformational change. In either case, these correspond to active (or nondesensitised) receptor states, R_a, and inactive (or desensitised) receptor states, R_i, which differ by their capability of eliciting a cellular response upon binding of the ligand. Both receptor states combine with the PTH ligand L to form active and inactive ligand-receptor complexes C_a and C_i (see Fig 1 for a schematic of the model kinetics). This creates a distribution among the four receptor species with the total concentration of receptor $R_T (= [R_a] + [C_a] + [C_i] + [R_i])$.

The ordinary differential equations (ODEs) for the two-state receptor model can be summarised in matrix notation as [14]:

$$\frac{d\mathbf{C}}{dt} = \mathbf{K}(L(t))\mathbf{C}(t), \tag{1}$$

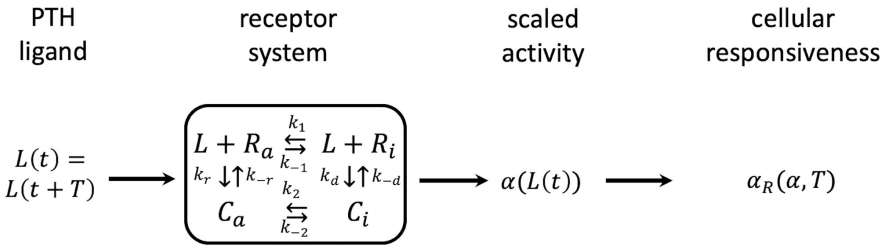

Fig 1. Schematic of the two-state receptor model representing PTH to PTH1R binding based on [16]. $L(t)$ = PTH concentration; t = time; T = period; R_a = active receptor concentration; R_i = inactive receptor concentration; C_a = active ligand-receptor complex concentration, C_i = inactive ligand-receptor complex concentration, $k_{\pm i}$ = kinematic parameters ($i \in \{1, 2, d, r\}$); α = scaled activity; α_R = *cellular responsivenes.*

https://doi.org/10.1371/journal.pone.0283544.g001

where the vector of unknown time-dependent concentration C(t) for the receptor states is given in its scaled form as

$$\mathbf{C} = \begin{bmatrix} r_a \\ c_a \\ c_i \\ r_i \end{bmatrix}, \tag{2}$$

with $r_a = R_a/R_T$, $c_a = C_a/R_T$, $c_i = C_i/R_T$, and $r_i = R_i/R_T$. The constant coefficient matrix describing the ligand-receptor binding kinetics is given as

$$\mathbf{K}(L) = \begin{bmatrix} -k_1 - k_r L & k_{-r} & 0 & k_{-1} \\ k_r L & -k_2 - k_{-r} & k_{-2} & 0 \\ 0 & k_2 & -k_{-2} - k_{-d} & k_d L \\ k_1 & 0 & k_{-d} & -k_{-1} - k_d L \end{bmatrix} \tag{3}$$

see Table 1 for details on the specific parameters. As the above coefficient matrix has not full rank, the system of ODEs reduces to

$$\begin{bmatrix} \dot{r}_a \\ \dot{c}_a \\ \dot{c}_i \end{bmatrix} = \begin{bmatrix} -k_1 - k_r L & k_{-r} & 0 & k_{-1} \\ k_r L & -k_2 - k_{-r} & k_{-2} & 0 \\ 0 & k_2 & -k_{-2} - k_{-d} & k_d L \end{bmatrix} \begin{bmatrix} r_a \\ c_a \\ c_i \\ 1 - (r_a + c_a + c_i) \end{bmatrix} \tag{4}$$

with the conservation condition

$$r_a + c_a + c_i + r_i = 1 \tag{5}$$

being automatically fullfilled by solution of Eq 1. In Eqs (3) and (4), L denotes the ligand concentration, i.e. PTH in plasma (or bone fluid) which binds to PTH1R expressed on osteoblastic cells. We note that, unlike in the paper of [15], we do not compute the PTH concentration from an additional ODE. We assume that this can be approximated by a simple square-wave stimulus characterised by the the peak ligand concentration γ_1, duration of the on-phase τ_1 and period T, see [16]. For the physiological gland pulses, these quantities are derived from experimental data, whereas for the PTH injection, we compute the PTH concentration in plasma from a one compartment pharmacokinetic (PK) model of PTH sc injection in humans

Table 1. Parameter values for the two-state receptor model of PTH-PTH1R as illustrated in Fig 1.

Parameter	Rate constant description	Value	Source
k_1	conversion receptors: $R_a \to R_i$	0.012 min^{-1}	[31]
k_{-1}	conversion receptors: $R_i \to R_a$	0.104 min^{-1}	[31]
k_2	conversion complexes: $C_a \to C_i$	0.222 min^{-1}	[31]
k_{-2}	conversion complexes: $C_i \to C_a$	0.055 min^{-1}	[31]
$K_r = k_{-r}/k_r$	dissociation constant for active complex	1 nM	[29, 30]
$K_d = k_{-d}/k_d$	dissociation constant for inactive complex	10^3 nM	condition of detailed balance [16]

https://doi.org/10.1371/journal.pone.0283544.t001

[28]. This model delivers the periodic ligand stimulus, $L(t) = L(t + T)$. Binding of the ligand to the respective receptor induces a cellular response. As was pointed out by Segel and co-workers [14], the nature of this response as well as the precise manner by which it is linked to ligand binding differ from one particular system to another. In the context of PTH binding to its receptor, PTH1R, the dissociation constant is approximately 1nM [15, 29, 30]. For the kinetic parameters k_1, k_{-1}, k_2, k_{-2}, we adopted the experimentally derived parameters published by [31] for cAMP signalling which uses a GPCR, too. Table 1 summarises the model parameters used for the two-state receptor model.

2.1 Definition of bone cellular responses: Activity functions

Bone cellular response is induced by binding of PTH to PTH1R. Following the work of Segel et al. [14], we assume that the effect induced by the PTH stimulus is measured by a quantity, the so-called scaled activity α, which can be defined as a weighted linear combination of receptors and complexes normalised concentrations as [14]:

$$\alpha(L) = a_1 r_a + a_2 c_a + a_3 c_i + a_4 r_i, \tag{6}$$

where a_i can be viewed as association constants and are hence non-negative [14]:

$$a_i \geq 0, \quad i = 1, 2, 3, 4 \tag{7}$$

The activity defined in Eq (6) should be regarded as a loose measure of how strongly ligand binding to the receptor is contributing to the induction of a physiological cell response.

The choice of affinity coefficients (a_i) is not arbitrary, but based on a particular biological system response. Here, we utilise the *exact adaptation* response defined by Segel et al. [14] as the systems response to a constant stimulus. For the case of *exact adaptation*, the scaled activity α returns to the same value at steady state regardless of the concentration of constant stimulus. The coefficients a_1, a_3 and a_4 are chosen according to [16] with the scaling factor $s = 100$ due to smaller concentration of PTH compared to that work. a_2 is computed such that the exact adaptation condition is satisfied, i.e. $a_2 = ((a_1K_1 + a_4)/(K_1 + 1)(K_2 + 1) - a_3)/K_2$ with $K_1 = k_{-1}/k_1$ and $K_2 = k_{-2}/k_2$ [14].

2.1.1 Dose-response curves for periodic stimuli. As discussed in detail in [16], the aim is to define a meaningful measure of activity for the long-term effect of periodic stimuli. Implicitly, we assume that the cell response can be linked to this quantity. Here, we consider the case of *exact adaptation* for which the steady state value of activity (α_s) equals the basal activity value (α_0). Under these conditions, the basal activity α_0 provides a unique reference value.

2.2.2 Cellular responsiveness. As pointed out in [16], the definition of *cellular responsiveness* is incomplete in terms of the integrated activity $\alpha_T := \int_0^T (\alpha(t) - \alpha_0)dt$ from a physiological point of view. *Cellular responsiveness* should take into account the magnitude of integrated activity as well as the number of activity pulses in a given time interval. Li et al. [16] define the *cellular responsiveness* as the product of two terms:

$$\alpha_R = \frac{\alpha_T}{\alpha_{T_{step}}} \frac{\alpha_T}{T} \tag{8}$$

where $\alpha_{T_{step}}$ is defined as the integrated activity in response to a corresponding step increase in ligand from γ_0 to γ_1:

$$\alpha_{T_{step}}(\gamma_0, \gamma_1) = \tau_a(\gamma_1)\alpha_{M_{step}}(\gamma_0, \gamma_1) \tag{9}$$

In Eq (9), $\alpha_{M_{step}}$ denotes the maximum activity in response to a step increase in ligand from γ_0

to γ_1, while $\tau_a(\gamma_1)$ denotes the adaptation time to a constant stimulus γ_1. The first term in Eq (8) is related to the magnitude of the integrated activity, i.e. $\alpha_T/\alpha_{T_{step}}$, which scales the integrated activity during one pulse of the periodic stimulus with respect to the integrated activity corresponding to a step increase in ligand of the same amplitude. Note $\alpha_{T_{step}} \gg \alpha_T$. The second term is the period (or intrinsic) average of the integrated activity α_T/T, which takes not only the on-phase τ_1, but also the off-phase τ_0 into account. As noted in [16], the latter quantity will equate to a total integrated activity $n\alpha_T$ over a certain time interval $t = nT$.

2.2 PTH ligand concentration in plasma

We note the subscript and superscript *gl* refers to quantities connected to PTH gland secretion.

2.2.1 Physiological parathyroid gland secretion. In humans, plasma PTH fluctuates periodically at a frequency of 3–7 bursts per hour, see S1 Table. Approximately 30% of circulating PTH results from pulsatile secretion and the remaining 70% from tonic secretion [32–34]. The plasma PTH concentration in the latter studies is approximated by a convolution model [35]. In the present study, however, we follow the simplified approach from [14, 16] in which the plasma ligand concentration L_{gl} is approximated by a square-wave stimulus as

$$L_{gl}(\tau_1, T, \gamma_0, \gamma_1, t) = \begin{cases} \gamma_1 & \text{if} \quad (n-1)T \le t \le (n-1)T + \tau_1 \\ \gamma_0 & \text{if} \quad (n-1)T + \tau_1 \le t \le (n-1)T + \tau_1 + \tau_0 \end{cases} \tag{10}$$

where $n = 1, 2, 3, \ldots, N$ represent successive pulses in the repetitive square-wave stimulation. τ_0 and τ_1 denote the off- and on-phase of the signal respectively, while the period T is defined as $T = \tau_0 + \tau_1$, see Fig 2. We note that as the equation system Eq (1) is solved numerically, in contrast to the original work [14], there is no need to introduce dimensionless signal function. Hence, γ_1 and γ_0 denote the concentrations (in pM/L) of PTH in plasma. Further, the model

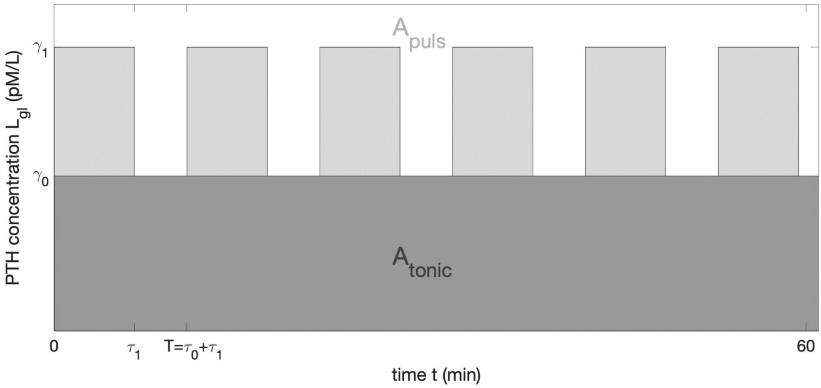

Fig 2. Schematic representation of the square-wave PTH ligand concentration L_{gl} (in plasma) vs. time. γ_1 is the peak PTH concentration due to pulsatile glandular secretion, γ_0 is the PTH concentration due to tonic glandular secretion, and τ_0 and τ_1 are the off- and on-phases of pulsatile component. Dark grey area A_{tonic} represents the plasma concentration resulting from a tonic secretion whereas the light grey area A_{puls} represents the plasma concentration resulting from the pulsatile secretion.

https://doi.org/10.1371/journal.pone.0283544.g002

for the ligand concentration is not restricted to a square-wave stimulus and more complex functions can be used. In order to conserve the dose input signal [36], commonly referred to as AUC, we introduce the integrated concentration per an arbitrary time interval $[0, s]$ as

$$A = A_{tonic} + A_{puls} = \int_0^s L_{gl}(\tau_1, T, \gamma_0, \gamma_1, t)\ \mathrm{d}t, \tag{11}$$

where A_{tonic} and A_{puls} are the AUC of the tonic and pulsatile secretions of PTH, respectively and their ratio is given as $r = \frac{A_{puls}}{A}$.

The mean plasma concentration is assumed to be $\bar{L}_{gl} = 1/T \int_0^T L_{gl}(t)\mathrm{d}t$. As the quantity of our interest is the plasma PTH concentration, see Eq (1), in the subsequent numerical examples, the experimental data from [17, 18] are used, see S1 Table. In these studies, the total plasma concentration was measured.

2.2.2 Additional drug administration. We note the subscript and superscript *inj* refers to quantities connected to an external sc PTH injection. An additional time-dependent PTH dose $D(t)$ can be added in form of a sc injection. To model the resulting plasma concentration, we follow the approach taken by Pivonka and co-workers, i.e. we use a one-compartment PK model of PTH [28, 37] which is given by two ODEs

$$\frac{\mathrm{d}D}{\mathrm{d}t} = -k_a F D(t) \quad \text{and} \quad \frac{\mathrm{d}L_{inj}^{PK}}{\mathrm{d}t} = F V_d k_a D(t) - k_e L_{inj}^{PK}(t), \tag{12}$$

where L_{inj}^{PK} is the ligand plasma concentration, the absorption rate constant k_a represents the drug absorption process from the sc site of injection into the blood stream, and the elimination rate constant k_e represents the drug elimination process from blood, V_d is the distribution volume and F is the bioavailability. Fig 3 shows PTH plasma concentration for the non-linear case and the simplified square-wave stimulus.

Assuming that the peak PTH drug concentration is the same for the square-wave stimulus and the PK model and assuming that the AUC in the (L, t)-plots representing the integrated

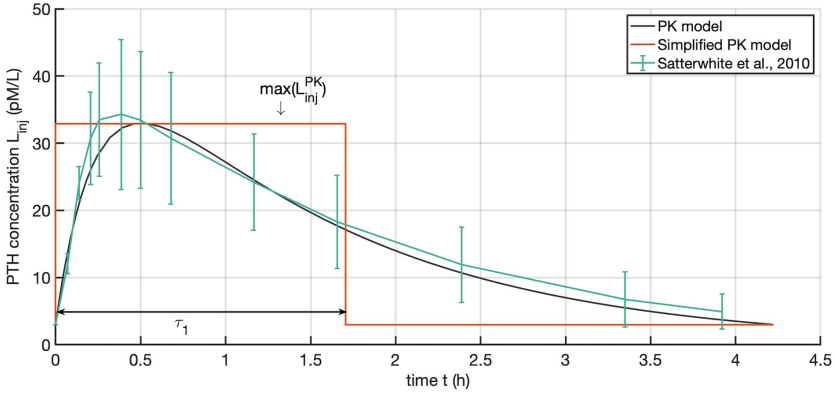

Fig 3. PTH plasma concentration obtained from the PTH PK model and the simplified square-wave stimulus characterised by the maximum PTH concentration $\max(L_{inj}^{PK})$ and the on-phase τ_1.

https://doi.org/10.1371/journal.pone.0283544.g003

drug concentration are equal between these two models ($A_{inj}^{PK} = A_{inj}$), we can calculate the on-phase of the square-wave signal as

$$\tau_1 = \frac{A_{inj}^{PK}}{\max(L_{inj}^{PK}) - \gamma_0}, \tag{13}$$

where γ_0 is the PTH concentration resulting from the tonic secretion, see Eq (10). The PTH drug concentration L_{inj} can be then approximated as

$$L_{inj}(D, T, \gamma_0, t) = \begin{cases} \gamma_1 & \text{if} \quad (n-1)T \le t \le (n-1)T + \tau_1 \\ \gamma_0 & \text{if} \quad (n-1)T + \tau_1 \le t \le (n-1)T + \tau_1 + \tau_0 \end{cases} \tag{14}$$

To compute the resulting *cellular responsiveness*, two models are investigated:

- model 1: we assume that the resulting PTH ligand concentration in Eq (1) is $L = L_{gl} + L_{inj}$, solve Eq (1) numerically and obtain the scaled activity from Eq (6) (blue curve in Fig 4(a)). Subsequently, the *cellular responsivenesses* α_R^{gl} and α_R^{inj} are computed separately by integrating over different parts of the scaled activity and scaling them with T_{gl} and T_{inj} for α_R^{gl} and α_R^{inj} in Eq (8), respectively. The resulting *cellular responsiveness* is computed as $\alpha_R = \alpha_R^{gl}(L) + \alpha_R^{inj}(L)$.
- model 2: Eq (1) is solved separately for both, L_{gl} and L_{inj}. Then, the *cellular responsiveness* is computed as $\alpha_R = \alpha_R^{gl}(L_{gl}) + \alpha_R^{inj}(L_{inj})$, see Fig 4b.

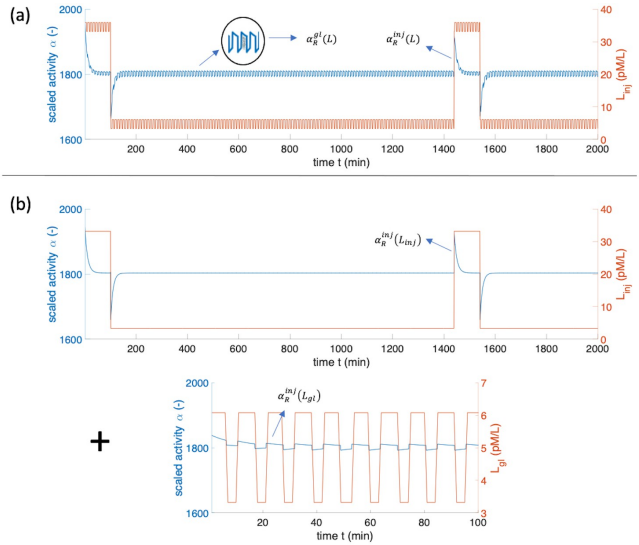

Fig 4. Computational simulation results of two models used to compute scaled activity α and *cellular responsiveness* α_R for the case of combined PTH glandular secretion and external sc daily PTH injection ($D = 20\mu g$). (a) refers to model 1 whereas (b) refers to model 2.

https://doi.org/10.1371/journal.pone.0283544.g004

Table 2. Computed *cellular responsiveness* for different PTH doses using model 1 and model 2.

daily drug dose D	healthy	idiopathic osteoporosis	hyperparathyroidism
0μg	0.939/0.939 (0)	0.497/0.497 (0)	2.105/2.105 (0)
10μg	1.358/1.398 (0.459)	0.957/0.957 (0.459)	2.376/2.443 (0.338)
20μg	1.778/1.818 (0.879)	1.375/1.376 (0.879)	2.694/2.835 (0.730)
30μg	2.143/2.183 (1.244)	1.759/1.741 (1.244)	3.042/3.179 (1.074)

Computed *cellular responsiveness* for different PTH doses administered via sc daily injections (model 1/model 2) superposed to baseline glandular secretion patterns. The results are given in form model 1 /model 2 (α_R^{inj}). For example, considering a healthy person and a PTH dose of 20μg, α_R computed from model 2 is obtained as a sum 0.939 + 0.879 = 1.818.

https://doi.org/10.1371/journal.pone.0283544.t002

Table 2 indicates that both models produce nearly the same *cellular responsiveness* α_R results for different doses and illnesses. Therefore, in the following computation, the computationally less expensive model 2 is utilised.

3 Optimal pulsatile regimes to reach maximal or targeted *cellular responsiveness*

We note that in the original work [16], a non-constrained optimisation for a square-wave signal with constant γ_0 and γ_1 was utilised. This is based on an analytical formula for an optimal τ_1 and T. However, as the numerical solution is available, different dosing patterns, i.e. combination of glandular and drug contribution (see Section 3.2) and different optimisation questions in addition to the maximisation of the *cellular responsiveness* can be answered. After transformation of the constrained optimisation problems to equivalent unconstrained ones, all optimisation problems are solved with the function *fminsearch* in MATLAB. In the following, we describe the formulation of different optimisation problems.

3.1 Baseline PTH secretion

As described earlier, the tonic secretion makes up approximately 70% and the pulsatile secretion the remaining 30%. Based on the data in [17, 18], the integrated concentration remain in the same range and hence we assume that the AUC in the (L, t)-plot can be rewritten as $A = A_{tonic} + A_{puls}$. To fix the mean plasma concentration at the reference value obtained from experimental data, we enforce that $A = A^{ref}$. In order to predict the optimal pulsatile pattern to reach the maximum *cellular responsiveness* α_R^{max}, we consider the following constrained optimisation problem

$$\max_{(\tau_1,T,\gamma_0,\gamma_1)} \alpha_R(L_{gl}(\tau_1, T, \gamma_0, \gamma_1, t)) \text{ with the constraints } \begin{cases} A(s, L_{gl}) = A^{ref}(s, L_{gl}) \\ A_{puls} = rA \end{cases} \tag{15}$$

where r is the ratio of pulsatile integrated concentration to total integrated concentration (see S1 Table), $A(s) = \int_0^s L_{gl}(\tau_1, T, \gamma_0, \gamma_1, t)\mathrm{d}t$ is the AUC in a (L_{gl}, t)-plot during an arbitrary time interval $[0, s]$ and the superscript *ref* refers to the quantities based on the experimental data for a healthy person [17, 18]. With the assumed square-wave stimulus in Eq (10) follows $A(s) = \gamma_0 s + \frac{(\gamma_1-\gamma_0)\tau_1 s}{T}$. The constraints in Eq (15) yield then

$$\gamma_0 = \gamma_0^{ref} \tag{16}$$

$$T = s\tau_1(\gamma_1 - \gamma_0)/rA^{ref} \tag{17}$$

Therefore, the constrained optimisation problem in Eq (15) can be reduced to a non-constrained optimisation problem

$$\boxed{\max_{(\gamma_1,\tau_1)} \alpha_R(L_{gl}(\tau_1, T, \gamma_0, \gamma_1, t))} \tag{18}$$

with γ_0 and T according to Eqs (16) and (17).

Another important question that can be addressed using the proposed optimisation method is "Can a healthy *cellular responsiveness* α_R^{ref} be reached by manipulating the glandular secretion pattern?". Note that the case of external PTH injection is considered below. Here, we explore the possibility of modulating a pathological glandular secretion pattern such that one would obtain α_R close to the healthy case. To answer the question if it is possible to reach the *cellular responsiveness* of the healthy person solely by changing the pulsatile pattern and keeping the area A constant, the following minimisation problem is to be solved

$$\boxed{\min_{(\gamma_1,\tau_1)}(\alpha_R(L_{gl}(\tau_1, T, \gamma_0, \gamma_1, t) - \alpha_R^{ref}))^2} \tag{19}$$

3.2 PTH injection

The previous concept can be applied to the investigation of the optimal dosing regimes for sc PTH injection and furthermore extended to other drugs. Here, we remark that τ_1 and γ_1 are not independent as they are given by the injected dose of the ligand and the experimentally measured pharmacokinetics. This is approximated by a function $f_{PK}(\gamma_0, D)$ determining the corresponding values, i.e. $(\gamma_1, \tau_1) = f_{PK}(\gamma_0, D)$. For different PTH daily doses ($D \in \{10\mu g, 20\mu g, 30\mu g\}$), *cellular responsiveness* is computed exemplarily for healthy person and patients with idiopathic osteoporosis and hyperparathyroidism.

3.2.1 Maximising the *cellular responsiveness*. Let A_{inj} be the AUC in the (L, t)-plot resulting from the sc injection of PTH (see Fig 4) and A_{inj}^{ref} the reference area corresponding the clinically used doses of 20μg once daily. The optimisation problem becomes

$$\boxed{\max_{(D,T)} \alpha_R^{inj}(D, T, \gamma_0) \text{ with the constraint } A_{inj}(D, T, \gamma_0) = A_{inj}^{ref}.} \tag{20}$$

which again is equivalent to a non-constrained optimisation

$$\boxed{\max_{D} \alpha_R^{inj}(D, T, \gamma_0)} \tag{21}$$

with $T = \tau_1(\gamma_1 - \gamma_0)/A_{inj}^{ref}$ and $(\gamma_1, \tau_1) = f_{PK}(\gamma_0, D)$ are given by the PK model [37].

3.2.2 Targeting healthy *cellular responsiveness* using external PTH injections. Suppose that α_R^{ill} denotes an altered *cellular responsiveness* compared to a healthy reference value α_R^{ref}, e.g. for patients with osteoporosis. Note that this could be higher or lower than α_R^{ref}. We are aiming to find a dose D such that the *cellular responsiveness* of the healthy person is reached, i.e. we solve the following optimisation problem

$$\boxed{\min_{D}(\alpha_R^{inj}(D, T, \gamma_0) - (\alpha_R^{ref} - \alpha_R^{ill}))^2.} \tag{22}$$

This gives the optimal dose to normalise the PTH *cellular responsiveness* by keeping the dosing period unchanged ($T = 24$ h).

4 Results of numerical simulations

4.1 Basal secretion

Table 3, first row, shows computed α_R using the mean experimental data [8, 17, 18] for healthy people and patients with different types of osteoporosis, hyperparathyroidism as well as under hyper- and hypocalcemia conditions. We note that if the tonic secretion is reduced in a healthy person, then the *cellular responsiveness* is slightly higher than the reference value. The corresponding scaled activity α computed according to Eq (6) is displayed in Fig 5, exemplarily for three cases with reference, reduced and increased α values—healthy, idiopathic osteoporosis and hyperparathyroidism, respectively.

In Table 3, solutions of the optimisation problems given in Eqs (18) and (19) are summarised. Superscript *max* denotes the values yielding the maximal *cellular responsiveness* by conserving the area A. Superscript * refers to the optimal values needed to reach the *cellular responsivenesss* of a healthy person. We note that this is possible only if $\alpha_R^{max} \geq \alpha_R^{ref}$.

Fig 6 shows surface plots where α_R for a healthy person is a function of two variables of the triplet (τ_1, T, γ_1). The third component is computed from Eq (17). The maximal *cellular responsiveness* is in each plot labelled with a red star. Its value $\alpha_R^{max} = 3.35$ is for all three cases identical because the same constrained optimisation problem given in Eq (15) is solved.

4.2 PTH external injection

In the following, simulation results for various PTH dosing patterns are presented with the aim of identifying optimal dosing regimes leading to maximum cellular responsiveness. Further, an optimal PTH dose of 9.61μg daily has been computed in order to reach the target *cellular responsiveness* of a patient with osteoporosis, see Table 4. The intersection of the red and black dashed lines in Fig 7 visually confirms that the optimal dose is close to 10μg. The latter figure also indicated that the *cellular responsiveness* increases nearly linearly as the daily dose increases.

Table 3. *Cellular responsiveness* for gland secretion.

parameter	healthy [17], r	OP	PMO [38, 39]	GIO	HP	hypocal 1	hypocal 2	hypercal
α_R	0.939/0.957	0.497	0.939/0.856	1.607	2.105	4.645	1.814	0.174
α_R^{max}	3.345/3.384	0.649	3.345/2.757	5.689	9.983	27.653	6.798	0.466
τ_1^{max} (min)	12.92/12.89	11.77	12.92/12.64	13.49	14.78	15.67	14.24	11.33
T^{max} (min)	54.94/54.31	65.94	55.94/55.57	51.23	55.04	50.01	55.12	65.78
γ_1^{max} (pm/L)	10.41/9.68	4.98	10.41/8.52	12.67	38.73	78.18	25.63	1.99
τ_1^* (min)	6.40/6.54	-	6.40/6.46	6.33	7.80	-	6.42	-
T^* (min)	10.60/10.69	-	10.60/11.50	8.94	9.80	-	8.84	-
γ_1^* (pm/L)	6.08/5.38	-	6.08/5.02	5.71	22.21	-	15.45	-

Cellular responsiveness α_R for gland secretion computed according to Eq (8), α_R and the corresponding τ_1, T, γ_1 are denoted with the superscripts *max* and * as solutions of the optimisation problems in Eqs (18) and (19), respectively. Coding: healthy = healthy person [17], r = healthy with reduced (by 20%) tonic secretion, OP = idiopathic osteoporosis [17], PMO = postmenopausal osteoporosis based on [38, 39], GIO = glucorticoid-induced osteoporosis [40], HP = hyperparathyroidism [18], hypocal 1 = hypocalcemia initial state [32], hypocal 2 = hypocalcemia steady state [32], hypercal = hypercalcemia steady state [32]. - optimisation problem (19) has no solution within the tolerance. Simulation parameters are given in Table 1 and S2 Table.

https://doi.org/10.1371/journal.pone.0283544.t003

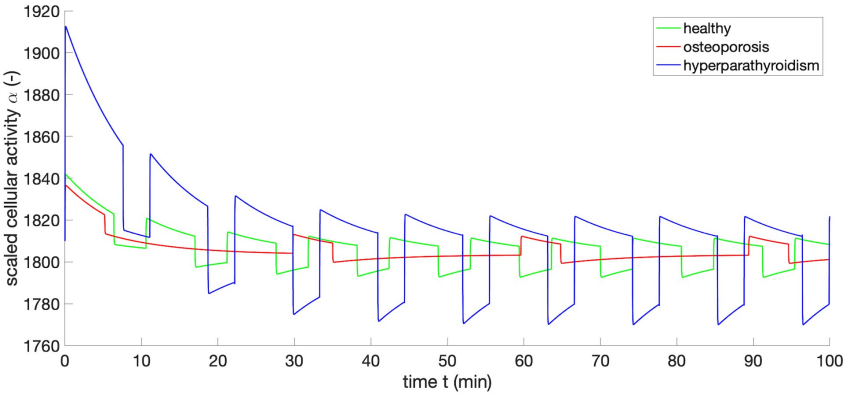

Fig 5. Scaled activity α for healthy person, patient with idiopathic osteoporosis and hyperparathyroidism. Simulation parameters are given in Table 1 and S2 Table.

https://doi.org/10.1371/journal.pone.0283544.g005

5 Discussion

In this paper, we utilised a two-state receptor model to investigate bone cellular responses due to PTH glandular secretion patterns together with external administration of PTH. We considered five different types of glandular secretion patterns corresponding to healthy subjects and patients with osteoporosis, hyperparathyroidism, hypercalcemia and hypocalcemia. Our model a priori prescribes a particular glandular PTH secretion pattern reported in the literature and then calculates the corresponding cellular activity. We note that the PTH glandular secretion plays a pivotal role in calcium and phosphorus homeostasis and, consequently,

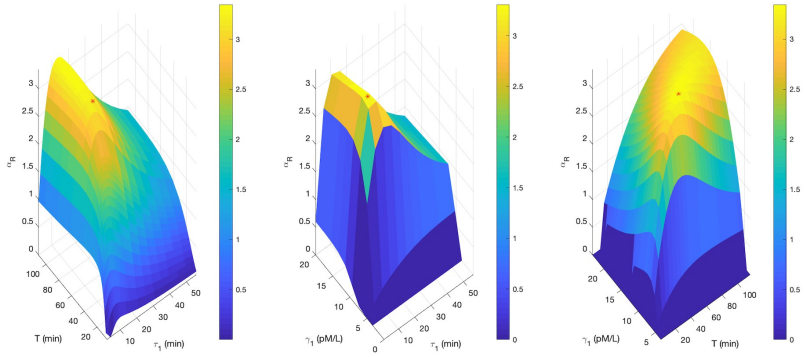

Fig 6. *Cellular responsiveness* for a healthy person as function of T and τ_1; γ_1 and τ_1; γ_1 and T. The third quantity of the triplet (γ_1, τ_1, T) results from the optimisation constraint given in Eq (15). Simulation parameters are given in Table 1 and S2 Table.

https://doi.org/10.1371/journal.pone.0283544.g006

Table 4. Maximum *cellular responsiveness* for PTH doses administered via sc daily injections.

parameter	10μg	20μg	30μg	optimised dose according to Eq (22)	
α_R^{max}	1.455	2.183	2.817	$\alpha_R^{ref}/\alpha_R^{ill}$	0.939/0.497
D^{max} (μg)	1.606	2.866	4.049	D^*	9.61
τ_1^{max} (min)	43.30	58.76	67.67	τ_1^*	87.90
T^{max} (min)	79.18	98.56	107.60	T	1440
γ_1^{max} (pM/L)	6.63	8.51	10.32	γ_1^*	17.16

Maximum *cellular responsiveness* for PTH doses administered via sc daily injections given to a patient with osteoporosis. Model 2 is used for optimisation. Superscript *max* denotes values leading to maximum *cellular responsiveness* α_R^{max} by keeping the daily drug dose, i.e. the area A_{inj} unchanged. Superscript * denotes the optimal values to reach the reference *cellular responsiveness* α_R^{ref}.

https://doi.org/10.1371/journal.pone.0283544.t004

factors that affect the different organs involved in controlling mineral balance can also influence the glandular secretion patterns. Major factors that can affect PTH glandular secretion are dietary conditions (i.e., calcium and phosphorus intake), lifestyle (i.e., physical activity), and genetics (i.e., vitamin D system). However, it is beyond the scope of the current study to investigate the effects of these factors on glandular PTH secretion patterns.

Using an efficient numerical approach to solve the ODEs allowed us to formulate a variety of optimisation problems which aimed at restoring the perturbed bone cellular response due to different disease back to the healthy baseline state. We note that the computation of the *cellular responsiveness* based on a two-state receptor model is for the first time computed numerically. The numerical approach is much more flexible in the sense that there are no special case restrictions on the parameters in the model and one can easily consider different scenarios by formulating constrained optimisation problems with various objective functions and constraints. The MATLAB codes are provided on request.

Below, we discuss first how the different bone cell response values can be interpreted in a bone remodelling context. Then, we discuss the manipulation of glandular secretion patterns

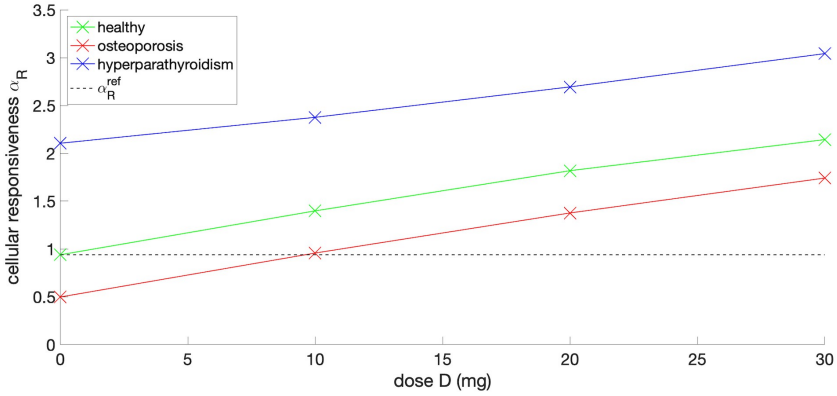

Fig 7. *Cellular responsiveness* computed with model 2 for healthy person, patients with idiopathic osteoporosis and hyperparathyroidism after different doses of PTH sc injection are applied once daily.

https://doi.org/10.1371/journal.pone.0283544.g007

and the superposition of an external PTH injections. Finally, we will also discuss the limitations of the current study.

5.1 Comparison of healthy versus disease states

While the bone cellular response parameter (α_R) of the current two-state receptor model is not linked to any (downstream) catabolic or anabolic bone cell responses, it is instructive to view this parameter's action on the bone remodelling process. In the bone remodelling models of Lemaire et al. and Pivonka et al. [41–43], a single monovalent binding reaction function was used to simulate the catabolic action of PTH on bone remodelling. This was achieved by introducing a PTH activator function which was a sigmoidal function of the PTH serum concentration mapped on the interval 0 and 1. Using this function, the catabolic ligand (RANKL) expressed on osteoblastic cells was monotonously increased for pathological cases of increased PTH serum concentration. We note that serum PTH concentration was assumed constant in these models and based on the rather simplistic receptor ligand binding model, it was emphasised that these models are not able to capture pulsatile effects of PTH such as the anabolic response due to external intermittent PTH injections. Hence, a reduction in serum PTH concentration gave rise to reduced bone remodelling with modest to no anabolic bone gains.

In the following, we interpret the decrease or increase of α_R with respect to catabolic actions of bone cells on the remodelling process. Hence, an increased value of the bone cellular response parameter (compared to the healthy baseline value) indicates a catabolic response, while a decreased value of α_R indicates a moderate anabolic bone response. With this in mind, the simulation results for hyperparathyroidism and hypocalcemia indicate that for the given pattern of glandular PTH secretion, a catabolic bone response is obtained. Hence, for these pathological conditions, net increase in bone resorption will occur. Primary hyperparathyroidism is due to a benign overgrowth of parathyroid tissue either as single gland (80% of cases) or as a multiple gland disorder. For symptomatic cases, it is associated with bone loss. The latter can be treated by using antiresorptive drugs, but more often hyperparathyroidism can be cured by removing the parathyroid gland(s) [6].

For the hypocalcemia simulations representing the hypocalcemic clamp tests reported in [32], we found that the PTH glandular secretion pattern in the transitional period of hypocalcemia (i.e., hypocalcemia 1) gave rise to a very high α_R value indicating high bone resorption, while the α_R value for the steady state period was significantly lower indicating lower bone resorption. Based on the tight regulation of calcium homeostasis, these results are meaningful, i.e. the immediate reduction of calcium due to the clamp test is rapidly compensated for by high bone resorption followed by a more modest bone resorption period.

For the hypercalcemia simulations representing the hypercalcemic clamp test reported in [32], we found that the PTH glandular secretion pattern led to a lower value of α_R and consequently reducing bone remodelling. During bone remodelling calcium is released from the bone matrix and, consequently, reducing bone remodelling avoids release of calcium into the plasma [44].

For the case of the osteoporosis simulations, lower, approximately similar and higher α_R values compared to healthy baseline were obtained for the idiopathic osteoporosis (OP), postmenopausal osteoporosis (PMO) and glucocorticoid-induced osteoporosis (GIO) case, respectively. Below we interpret these results in more detail. The results for the idiopathic OP seem to be not physiologically meaningful given that osteoporosis is associated with bone loss (i.e., catabolic bone response) [45]. However, there are quite a number of things to consider for interpretation of this result. The OP data [17] are based on only three male patients with idiopathic OP (mean age, 37 yr; range, 31–42 yr). This is an extremely low sample number. Also,

research into establishing a link between PTH patterns and other types of osteoporosis indicate that PTH modulation may be only a secondary effect, but that other catabolic bone regulators (such as RANKL) could directly be affected by the disease. Below, we discuss some of these findings.

For cases of PMO, our simulation results indicate that α_R is equal or slightly reduced compared to the reference value. These results are based on qualitative data provided in [8] for describing the PTH glandular secretion pattern in PMO. However, the data on this pattern are not conclusive as discussed next. Samuels et al. [38] compared PTH glandular secretion patterns from healthy young subjects with postmenopausal women of various oestrogen levels and bone mineral density (BMD). They found there were no differences in the amplitude or frequency of pulsatile PTH secretory parameters between the pathological cases and the healthy group. They concluded that different types of PMO do not alter PTH secretory patterns and temporal organisation. Based on these findings, the authors suggested that abnormalities in orderly pulsatile PTH secretion are unlikely to play a major role in driving PMO related osteoporosis. We note that oestrogen deficiency, i.e. a hallmark of PMO, has been directly linked with increased RANKL production.

For the case of GIO, which is the largest cause of secondary osteoporosis, some studies have not found an association between GIO and increased PTH concentration. On the other hand, other studies have shown that patients with GIO did exhibit elevated PTH serum concentrations [46]. However, as pointed out in [8], the PTH serum levels have little meaning in identifying a role of PTH in driving GIO, but it is the glandular pulsatile secretory pattern of PTH that might provide a link. However, only a few studies have investigated this pattern in a very small population of men. Bonadonna et al. [40] evaluated spontaneous PTH pulsatile secretion in patients chronically treated with pharmacological amounts of glucocorticoids. Their findings indicate that in the glucocorticoid-treated group, the PTH tonic secretory rate was reduced, while there was an increase in the fractional pulsatile PTH secretion in glucocorticoid-treated vs normal subjects. Mean overall PTH concentration, as well as mean integrated area, was similar among normal and glucocorticoid-treated subjects. Therefore, it can be concluded that chronic glucocorticoid treatment induces a redistribution of spontaneous PTH secretory dynamics by reducing the amount released in tonic fashion and increasing the amount released as pulses. In this study, GIO is simulated by scaling the parameters τ_1, T, γ_0 and γ_1 according to the data provided in [40], see S2 Table. In particular, the tonic secretion is nearly halved while the pulsatile pattern remains similar as the reference values. Our simulation produces α_R value significantly larger than in the healthy case. This indicates bone resorption which is in agreement with the obtained findings.

5.2 Optimisation of glandular dosing patterns to restore healthy cell response

Our simulation results for some of the PTH glandular disease states indicate that it may be possible to pharmacologically manipulate the PTH secretion pattern such as to restore similar values for *cellular responsiveness* as for healthy subjects. This would indicate a similar bone remodelling behaviour. We note that this could only be achieved for pathological cases that led to $\alpha_R^{max}/\alpha_R^{min}$ values higher/lower than the healthy baseline value, i.e. PMO, hyperparathyroidism, hypocalemia clamp test, and GIO. These cases, except PMO, could be restored towards the healthy α_R^{ref} by manipulating the pulsatile profile to a more continuous pattern which desensitises the active receptors and ligand complexes and leads to lower values of α_R. For PMO, solely the manipulation of the pulsatile pattern leads to an elevation of α_R up to the reference value. On the other hand, PTH glandular diseases that led to maximum bone *cellular*

responsiveness below the healthy baseline value such as the idiopathic osteoporosis case reported by Harms et al. [17], can't be restored to baseline via glandular manipulation. For such cases, external PTH injections are a viable solution which is further discussed below. Moreover, in the case of the initial hypercalcemia, the minimum *cellular responsiveness* α_R^{min} is higher than α_R^{ref} and therefore a lowering to the targeted level is not possible, too.

5.3 Effects of external PTH injections

To simulate the effect of external sc once daily PTH administration, as it is currently clinically available, one had to superpose the external PTH injection with the glandular PTH secretion. We explored two modelling approaches: In model 1, we assume that the resulting PTH ligand concentration in Eq (1) becomes $L = L_{gl} + L_{inj}$. Subsequently, Eq (1) is solved numerically. In model 2, Eq (1) is solved separately for both, L_{gl} and L_{inj}. Then, the α_R is given as a sum of the *cellular responsiveness* of the gland and a sc injection. Comparison of the simulation results for these two models indicated that the final values for α_R are very similar. Given that the computational efficiency of model 2 was significantly higher than model 1, all optimisations were performed for model 2. A general observation is, that superposing external PTH injections onto a baseline glandular secretion gave rise to increased values of α_R. The increase of the *cellular responsiveness* scaled nearly linearly with respect to the external PTH dose. Hence, for the case of osteoporosis, optimum external PTH dose of $D = 10\mu$g daily injections, that would give a *cellular responsiveness* close to the healthy state.

5.4 Limitations of the current study

The current study has a number of limitations. The receptor ligand PTH-PTH1R binding constants are taken from the open literature. We note that we deliberately did not use the constants that were proposed in [15] for several reasons. Firstly, the constants are not experimentally determined and do not fulfil the condition of the detailed balance as proposed [16]. Secondly, using the constants suggested in [15] gives several orders of magnitude difference between the active complexes and inactive complexes, which seems physiologically not realistic.

Another limitation of our study is that we discussed mainly the action of PTH on RANKL expression on cells of the osteoblastic lineage with no discussions of potential feedback mechanisms in the organs responsible for mineral metabolism. One such factor is fibroblast growth factor 23 (FGF-23) which is most highly expressed in bone, predominantly in osteocytes [47, 48]. In healthy subjects FGF-23 is expressed at low levels in osteocytes, but is significantly increased in osteocytes in patients with hypophosphatemic rickets [49] and in patients with chronic kidney disease [50]. It has been suggested that circulating FGF-23 directly acts on parathyroid glands to modify PTH dosing pattern [51].

We acknowledge that the current study exclusively focused on the PTH-PTH1R system that is most relevant for regulation of bone metabolism. We note that PTH also binds to its second receptor PTH2R together with its Ligand Tuberoinfundibular Peptide of 39 Residues (TIP39) to particularly regulate skin function via differentiation of keratocytes [52].

6 Conclusions

We developed a novel two-state PTH-PTH1R receptor binding model to analyse the effects of PTH glandular secretion patterns on bone *cellular responsiveness*. In particular, we explored differences between healthy and pathological glandular secretion patterns and their effect on bone cellular responsiveness. We explored the potential of (pharmacological) manipulation of

pathological glandular secretion patterns back to its normal baseline bone cellular responsiveness. Also, we investigated the effect of (external) once daily PTH injections on bone cellular responsiveness. For this purpose, we formulated a variety of constrained optimisation problems with and without keeping the area under the curve constant. Based on our numerical simulations, we found the following:

- Bone *cellular responsiveness* in healthy subjects is sensitive to the tonic baseline stimulus and is significantly below the maximum responsiveness;
- Bone *cellular responsiveness* greatly varies between healthy and pathological glandular secretions patterns;
- Catabolic bone diseases, as defined by $\alpha_R^{ill} > \alpha_R^{ref}$, (with exception of very high hypocalcemia) could be restored to normal by manipulating the pulsatile component of glandular secretion of the pathological gland;
- Bone diseases characterised by $\max(\alpha_R^{ill}) < \alpha_R^{ref}$ with a maximum *cellular responsiveness* value below healthy baseline can't be restored to baseline.
- External once daily PTH injections can restore the above cases back to normal.
- Superposition of glandular PTH secretion and external PTH injections can be effectively achieved by additive superposition;
- Based on the numerical formulation of the two-state receptor model, constrained optimisation problems can be efficiently formulated and solved;

In conclusion, the current two-state receptor model seems to capture major aspect of PTH glandular secretion and associated skeletal pathologies. In the future, this type of model could be used for analysing pharmacological drug effects on glandular secretion.

Supporting information

S1 Table. Experimental data. Experimental data for PTH, based on the cited literature. The values are given as mean ± sd or median (minimum—maximum).
(PDF)

S2 Table. Simulation parameters. Simulation parameters for cases: healthy person [17]/ healthy with reduced (by 20%) tonic secretion, idiopathic osteoporosis (OP), postmenopausal osteoporosis (PMO), glucocorticoid induced osteoporosis (GIO), initial hypocalcemia (hypocal 1), steady state hypocalcemia (hypocal 2) and hypercalcemia (hypercal) and glucocorticoid induced osteoporosis (GIO). The parameters for healthy person, OP and HP are based on the experimental provided in [17] which are shown in S1 Table. The remaining parameters are obtained via scaling the experimental data for healthy people [17] with relative changes presented in [38–40, 53] for PMO, GIO and different calcium levels, respectively.
(PDF)

Author Contributions

Conceptualization: Denisa Martonová, Sigrid Leyendecker, Peter Pivonka.

Funding acquisition: Sigrid Leyendecker, Peter Pivonka.

Investigation: Peter Pivonka.

Methodology: Denisa Martonová, Maxence Lavaill, Sigrid Leyendecker, Peter Pivonka.

Resources: Sigrid Leyendecker, Peter Pivonka.

Software: Denisa Martonová, Maxence Lavaill.

Supervision: Sigrid Leyendecker, Peter Pivonka.

Visualization: Denisa Martonová.

Writing – original draft: Denisa Martonová, Peter Pivonka.

Writing – review & editing: Maxence Lavaill, Mark R. Forwood, Alexander Robling, David M. L. Cooper, Sigrid Leyendecker, Peter Pivonka.

References

1. Hernández-Castellano LE, Hernandez LL, Bruckmaier RM. Review: Endocrine Pathways to Regulate Calcium Homeostasis around Parturition and the Prevention of Hypocalcemia in Periparturient Dairy Cows. Animal. 2020; 14(2):330–338. https://doi.org/10.1017/S1751731119001605 PMID: 31337460
2. Wendelaar Bonga SE, Pang PK. Control of Calcium Regulating Hormones in the Vertebrates: Parathyroid Hormone, Calcitonin, Prolactin, and Stanniocalcin. International Review of Cytology. 1991; 128:139–213. https://doi.org/10.1016/S0074-7696(08)60499-4 PMID: 1917377
3. Brown EM. Extracellular Ca2+ Sensing, Regulation of Parathyroid Cell Function, and Role of Ca2+ and Other Ions as Extracellular (First) Messengers. Physiological Reviews. 1991. https://doi.org/10.1152/physrev.1991.71.2.371 PMID: 2006218
4. Mundy GR, Martin TJ. Physiology and Pharmacology of Bone. vol. 107 of Handbook of Experimental Pharmacology. Berlin, Heidelberg: Springer Berlin Heidelberg; 1993.
5. Cheloha RW, Gellman SH, Vilardaga JP, Gardella TJ. PTH receptor-1 signalling—mechanistic insights and therapeutic prospects. Nature Reviews Endocrinology. 2015; 11(12):712–724. https://doi.org/10.1038/nrendo.2015.139 PMID: 26303600
6. Bilezikian JP, Bandeira L, Khan A, Cusano NE. Hyperparathyroidism. Lancet (London, England). 2018; 391(10116):168–178. https://doi.org/10.1016/S0140-6736(17)31430-7 PMID: 28923463
7. Dean T, Vilardaga JP, Potts J J T, Gardella TJ. Altered Selectivity of Parathyroid Hormone (PTH) and PTH-Related Protein (PTHrP) for Distinct Conformations of the PTH/PTHrP Receptor. Molecular Endocrinology. 2008; 22(1):156–166. https://doi.org/10.1210/me.2007-0274 PMID: 17872377
8. Chiavistelli S, Giustina A, Mazziotti G. Parathyroid Hormone Pulsatility: Physiological and Clinical Aspects. Bone Research. 2015; 3(1):1–5. https://doi.org/10.1038/boneres.2014.49 PMID: 26273533
9. Schmitt CP, Hömme M, Schaefer F. Structural Organization and Biological Relevance of Oscillatory Parathyroid Hormone Secretion. Pediatric Nephrology (Berlin, Germany). 2005; 20(3):346–351. https://doi.org/10.1007/s00467-004-1767-7 PMID: 15700141
10. Merriam GR, Wachter KW. Algorithms for the Study of Episodic Hormone Secretion. The American Journal of Physiology. 1982; 243(4):E310–318. PMID: 6889816
11. Veldhuis JD, Johnson ML. Cluster Analysis: A Simple, Versatile, and Robust Algorithm for Endocrine Pulse Detection. American Journal of Physiology-Endocrinology and Metabolism. 1986; 250(4):E486–E493. https://doi.org/10.1152/ajpendo.1986.250.4.E486 PMID: 3008572
12. Santen RJ, Bardin CW. Episodic Luteinizing Hormone Secretion in Man. Pulse Analysis, Clinical Interpretation, Physiologic Mechanisms. The Journal of Clinical Investigation. 1973; 52(10):2617–2628. https://doi.org/10.1172/JCI107454 PMID: 4729055
13. Tay D, Cremers S, Bilezikian JP. Optimal dosing and delivery of parathyroid hormone and its analogues for osteoporosis and hypoparathyroidism—translating the pharmacology. British Journal of Clinical Pharmacology. 2018; 84(2):252–267. https://doi.org/10.1111/bcp.13455 PMID: 29049872
14. Segel LA, Goldbeter A, Devreotes PN, Knox BE. A Mechanism for Exact Sensory Adaptation Based on Receptor Modification. Journal of Theoretical Biology. 1986; 120(2):151–179. https://doi.org/10.1016/S0022-5193(86)80171-0 PMID: 3784578
15. Potter LK, Greller LD, Cho CR, Nuttall ME, Stroup GB, Suva LJ, et al. Response to Continuous and Pulsatile PTH Dosing: A Mathematical Model for Parathyroid Hormone Receptor Kinetics. Bone. 2005; 37(2):159–169. https://doi.org/10.1016/j.bone.2005.04.011 PMID: 15921971

16. Li Y, Goldbeter A. Frequency Specificity in Intercellular Communication. Influence of Patterns of Periodic Signaling on Target Cell Responsiveness. Biophysical Journal. 1989; 55(1):125–145. https://doi.org/10.1016/S0006-3495(89)82785-7 PMID: 2930817

17. Harms HM, Kaptaina U, Külpmann WR, Brabant G, Hesch RD. Pulse Amplitude and Frequency Modulation of Parathyroid Hormone in Plasma*. The Journal of Clinical Endocrinology & Metabolism. 1989; 69(4):843–851. https://doi.org/10.1210/jcem-69-4-843 PMID: 2778038

18. Harms HM, Schlinke E, Neubauer O, Kayser C, Wüstermann PR, Horn R, et al. Pulse Amplitude and Frequency Modulation of Parathyroid Hormone in Primary Hyperparathyroidism. 1994; p. 5.

19. Silverberg SJ, Bone HG, Marriott TB, Locker FG, Thys-Jacobs S, Dziem G, et al. Short-Term Inhibition of Parathyroid Hormone Secretion by a Calcium-Receptor Agonist in Patients with Primary Hyperparathyroidism. The New England Journal of Medicine. 1997; 337(21):1506–1510. https://doi.org/10.1056/NEJM199711203372104 PMID: 9366582

20. Trivedi R, Mithal A, Chattopadhyay N. Recent Updates on the Calcium-Sensing Receptor as a Drug Target. Current Medicinal Chemistry. 2008; 15(2):178–186. https://doi.org/10.2174/092986708783330601 PMID: 18220773

21. Weiss JA, Makerc BN, Govindjee S. Finite Element Implementation of Incompressible, Transversely Isotropic Hyperelasticity. Comput Methods Appl Mech Engrg. 1996; 135(1-2):107–128. https://doi.org/10.1016/0045-7825(96)01035-3

22. Lauffenburger DA, Linderman J. Receptors: Models for Binding, Trafficking, and Signaling. Revised edition ed. New York, NY: Oxford University Press; 1996.

23. Structure and Function of 7-TM G-Protein Coupled Receptors. In: Foreman JC, Johansen T, Gibb AJ, editors. Textbook of Receptor Pharmacology. 3rd ed. CRC Press; 2010.

24. Waelbroeck I. Kinetics versus Equilibrium: The Importance of GTP in GPCR Activation. Trends in Pharmacological Sciences. 1999; 20(12):477–481. https://doi.org/10.1016/S0165-6147(99)01394-2 PMID: 10603489

25. Parfitt AM. Parathyroid Hormone and Periosteal Bone Expansion. Journal of Bone and Mineral Research. 2002; 17(10):1741–1743. https://doi.org/10.1359/jbmr.2002.17.10.1741 PMID: 12369776

26. Gardella TJ, Jüppner H. Molecular Properties of the PTH/PTHrP Receptor. Trends in endocrinology and metabolism: TEM. 2001; 12(5):210–217. https://doi.org/10.1016/S1043-2760(01)00409-X PMID: 11397646

27. Leff P. The two-state model of receptor activation. Trends in Pharmacological Sciences. 1995; 16 (3):89–97. https://doi.org/10.1016/S0165-6147(00)88989-0 PMID: 7540781

28. Trichilo S, Scheiner S, Forwood M, Cooper DML, Pivonka P. Computational Model of the Dual Action of PTH—Application to a Rat Model of Osteoporosis. Journal of Theoretical Biology. 2019; 473:67–79. https://doi.org/10.1016/j.jtbi.2019.04.020 PMID: 31009612

29. Yasuoka T, Kawashima M, Takahashi T, Iwata A, Oka N, Tanaka K. Changes in Parathyroid Hormone Receptor Binding Affinity during Egg Laying: Implications for Calcium Homeostasis in Chicken. Journal of Bone and Mineral Research. 2010; 11(12):1913–1920. https://doi.org/10.1002/jbmr.5650111212

30. Hoare SRJ, Usdin TB. Quantitative Cell Membrane-Based Radioligand Binding Assays for Parathyroid Hormone Receptors. Journal of Pharmacological and Toxicological Methods. 1999; 41(2-3):83–90. https://doi.org/10.1016/S1056-8719(99)00024-6 PMID: 10598679

31. Martiel JL, Goldbeter A. A Model Based on Receptor Desensitization for Cyclic AMP Signaling in Dictyostelium Cells. Biophysical Journal. 1987; 52(5):807–828. https://doi.org/10.1016/S0006-3495(87)83275-7 PMID: 19431710

32. Schmitt CP, Schaefer F, Bruch A, Veldhuis JD, Schmidt-Gayk H, Stein G, et al. Control of Pulsatile and Tonic Parathyroid Hormone Secretion by Ionized Calcium. The Journal of Clinical Endocrinology and Metabolism. 1996; 81(12):4236–4243. https://doi.org/10.1210/jcem.81.12.8954021 PMID: 8954021

33. Schaefer F. Pulsatile Parathyroid Hormone Secretion in Health and Disease. In: Chadwick DJ, Goode JA, editors. Novartis Foundation Symposia. Chichester, UK: John Wiley & Sons, Ltd; 2008. p. 225–243.

34. Samuels MH, Veldhuis J, Cawley C, Urban RJ, Luther M, Bauer R, et al. Pulsatile Secretion of Parathyroid Hormone in Normal Young Subjects: Assessment by Deconvolution Analysis. 1993; p. 5.

35. Veldhuis JD, Carlson ML, Johnson ML. The Pituitary Gland Secretes in Bursts: Appraising the Nature of Glandular Secretory Impulses by Simultaneous Multiple-Parameter Deconvolution of Plasma Hormone Concentrations. Proceedings of the National Academy of Sciences. 1987; 84(21):7686–7690. https://doi.org/10.1073/pnas.84.21.7686 PMID: 2823271

36. Fletcher PA, Clément F, Vidal A, Tabak J, Bertram R. Interpreting Frequency Responses to Dose-Conserved Pulsatile Input Signals in Simple Cell Signaling Motifs. PLoS ONE. 2014; 9(4):e95613. https://doi.org/10.1371/journal.pone.0095613 PMID: 24748217

37. Lavaill M, Trichilo S, Scheiner S, Forwood MR, Cooper DML, Pivonka P. Study of the Combined Effects of PTH Treatment and Mechanical Loading in Postmenopausal Osteoporosis Using a New Mechanistic PK-PD Model. Biomechanics and Modeling in Mechanobiology. 2020; 19(5):1765–1780. https://doi.org/10.1007/s10237-020-01307-6 PMID: 32100180

38. Samuels MH, Veldhuis JD, Kramer P, Urban RJ, Bauer R, Mundy GR. Episodic Secretion of Parathyroid Hormone in Postmenopausal Women: Assessment by Deconvolution Analysis and Approximate Entropy. Journal of Bone and Mineral Research. 1997; 12(4):616–623. https://doi.org/10.1359/jbmr.1997.12.4.616 PMID: 9101373

39. Harms HM, Neubauer O, Kayser C, Wüstermann PR, Horn R, Brosa U, et al. Pulse Amplitude and Frequency Modulation of Parathyroid Hormone in Early Postmenopausal Women before and on Hormone Replacement Therapy. The Journal of Clinical Endocrinology and Metabolism. 1994; 78(1):48–52. https://doi.org/10.1210/jcem.78.1.8288712 PMID: 8288712

40. Bonadonna S, Burattin A, Nuzzo M, Bugari G, Rosei EA, Valle D, et al. Chronic Glucocorticoid Treatment Alters Spontaneous Pulsatile Parathyroid Hormone Secretory Dynamics in Human Subjects. European Journal of Endocrinology. 2005; 152(2):199–205. https://doi.org/10.1530/eje.1.01841 PMID: 15745926

41. Lemaire V, Tobin FL, Greller LD, Cho CR, Suva LJ. Modeling the Interactions between Osteoblast and Osteoclast Activities in Bone Remodeling. Journal of Theoretical Biology. 2004; 229(3):293–309. https://doi.org/10.1016/j.jtbi.2004.03.023 PMID: 15234198

42. Pivonka P, Zimak J, Smith DW, Gardiner BS, Dunstan CR, Sims NA, et al. Model Structure and Control of Bone Remodeling: A Theoretical Study. Bone. 2008; 43(2):249–263. https://doi.org/10.1016/j.bone.2008.03.025 PMID: 18514606

43. Pivonka P, Zimak J, Smith DW, Gardiner BS, Dunstan CR, Sims NA, et al. Theoretical Investigation of the Role of the RANK-RANKL-OPG System in Bone Remodeling. Journal of Theoretical Biology. 2010; 262(2):306–316. https://doi.org/10.1016/j.jtbi.2009.09.021 PMID: 19782692

44. Rowe P, Koller A, Sharma S. Physiology, Bone Remodeling. In: StatPearls. Treasure Island (FL): StatPearls Publishing; 2022.

45. Sözen T, Özışık L, Başaran NÇ. An Overview and Management of Osteoporosis. European Journal of Rheumatology. 2017; 4(1):46–56. https://doi.org/10.5152/eurjrheum.2016.048 PMID: 28293453

46. Rubin MB, Bodner SR. A Three-Dimensional Nonlinear Model for Dissipative Response of Soft Tissue. International Journal of Solids and Structures. 2002; 39:5081–5099. https://doi.org/10.1016/S0020-7683(02)00237-8

47. Shimada T, Kakitani M, Yamazaki Y, Hasegawa H, Takeuchi Y, Fujita T, et al. Targeted Ablation of Fgf 23 Demonstrates an Essential Physiological Role of FGF 23 in Phosphate and Vitamin D Metabolism; 2004.

48. Bonewald LF, Wacker MJ. FGF23 Production by Osteocytes. Pediatric nephrology (Berlin, Germany). 2013; 28(4):563–568. https://doi.org/10.1007/s00467-012-2309-3 PMID: 22983423

49. Liu S, Rowe PSN, Vierthaler L, Zhou J, Quarles LD. Phosphorylated Acidic Serine-Aspartate-Rich MEPE-associated Motif Peptide from Matrix Extracellular Phosphoglycoprotein Inhibits Phosphate Regulating Gene with Homologies to Endopeptidases on the X-chromosome Enzyme Activity. The Journal of Endocrinology. 2007; 192(1):261–267. https://doi.org/10.1677/joe.1.07059 PMID: 17210763

50. Pereira RC, Juppner H, Azucena-Serrano CE, Yadin O, Salusky IB, Wesseling-Perry K. Patterns of FGF-23, DMP1, and MEPE Expression in Patients with Chronic Kidney Disease. Bone. 2009; 45(6):1161–1168. https://doi.org/10.1016/j.bone.2009.08.008 PMID: 19679205

51. Courbebaisse M, Lanske B. Biology of Fibroblast Growth Factor 23: From Physiology to Pathology. Cold Spring Harbor Perspectives in Medicine. 2018; 8(5):a031260. https://doi.org/10.1101/cshperspect.a031260 PMID: 28778965

52. Dobolyi A, Dimitrov E, Palkovits M, Usdin T. The Neuroendocrine Functions of the Parathyroid Hormone 2 Receptor. Frontiers in Endocrinology. 2012; 3. https://doi.org/10.3389/fendo.2012.00121 PMID: 23060860

53. Schmitt P, Veldhuis D. PTH Secretion Patterns in Patients with Secondary Hyperparathyroidism. 1998; p. 13.